Lattice thermal conductivity and anharmonic phonon properties in the mode coupling approach

José Pedro Alvarinhas Batista

Nanomat Group

Q-MAT Unit, Département de Physique

Faculté des Sciences

Université de Liège, Belgique

Supervised by:

Prof. Dr. Matthieu Verstraete

Submitted to the University of Liège for the degree of

Doctorat en Sciences

Année académique 2024-2025

Lattice thermal conductivity and anharmonic phonon properties in the mode coupling approach

José Pedro Alvarinhas Batista

Nanomat Group

Q-MAT Unit, Département de Physique

Faculté des Sciences

Université de Liège, Belgique

Supervised by:

Prof. Dr. Matthieu Verstraete

Submitted to the University of Liège for the degree of

Doctorat en Sciences

Année académique 2024-2025

Supervisor:	Prof. Matthieu Verstraete
	Department of Physics, Faculty of Sciences
	University of Liège, Belgium
	Role: Member
Internal Examiner:	Prof. Stéphane Dorbolo
	Department of Physics, Faculty of Sciences
	University of Liège, Belgium
	Role: Secretary
External Examiner:	Dr. François Bottin
	Laboratoire Matière en Conditions Extremes
	CEA Paris, France
	Role: Member
External Examiner:	Prof. Giorgia Fugallo
	Laboratoire de Physique
	École Normale Supérieure, France
	Role: Member
External Examiner:	Prof. Pascal Gehring
	Institute of Condensed Matter and Nanociences
	Université Catholique de Louvain, Belgium
	Role: Member
Chair:	Prof. Alejandro Silhanek
	Department of Physics, Faculty of Sciences
	University of Liège, Belgium
	Role: President

Day of the defence: September 3rd 2023

Abstract

Cette thèse traite du domaine de la dynamique du réseau anharmonique, avec un accent particulier sur la précision des calculs et des grandeurs associées. Une attention spéciale est portée à la conductivité thermique du réseau et aux systèmes bidimensionnels, en raison de leur importance dans les applications de gestion thermique et d'efficacité énergétique.

Nous commençons par dériver une nouvelle théorie de la dynamique du réseau anharmonique fondée sur le formalisme de l'opérateur de projection de Mori-Zwanzig et la théorie du couplage de modes. Cette dérivation est formellement exacte, inclut les effets quantiques nucléaires et l'anharmonicité selon les choix de l'utilisateur, et reste exacte en pratique pour la partie conservative de la dynamique, ne nécessitant des approximations que pour la partie dissipative. Une théorie du transport thermique basée sur cette formulation de la dynamique du réseau est également développée, fournissant un cadre cohérent pour comprendre et prédire le transport thermique médié par les phonons dans les solides. Des applications sont proposées pour plusieurs systèmes, avec un accent particulier sur le nitrure de bore hexagonal en monocouche qui, en raison de ses propriétés de symétrie, nécessite la prise en compte d'interactions à quatre phonons. Une dérivation supplémentaire de conditions de conservation de l'énergie compatibles avec le théorème fluctuation-dissipation est proposée, constituant un changement de paradigme dans la compréhension de la conductivité thermique dans des systèmes possédant de grandes bandes interdites phononiques, tels que l'arséniure de bore.

Enfin, les propriétés diélectriques dépendantes de la température ainsi que la conductivité thermique du réseau dans le nitrure de bore hexagonal massif sont étudiées. Nous trouvons à nouveau un accord qualitatif avec les expériences, en améliorant les résultats existants de deux manières : les propriétés diélectriques sont calculées sans interactions à quatre phonons grâce à l'utilisation de phonons renormalisés, et la conductivité thermique est trouvée en accord à la fois pour les composantes dans le plan et hors du plan, où les interactions à quatre phonons jouent un rôle crucial.

Par ce travail, nous faisons progresser de manière significative le domaine de la dynamique du réseau anharmonique, en fournissant non seulement des cadres théoriques, mais aussi des exemples concrets où nos améliorations par rapport aux approches actuelles s'avèrent précieuses, mettant en lumière les avantages de nos méthodes théoriques et computationnelles novatrices.

Abstract

This thesis addresses the field of anharmonic lattice dynamics, with particular focus on the accuracy of these calculations and their related quantities. Special attention is given to the lattice thermal conductivity and 2D systems, due to its importance in heat management and energy efficiency applications.

We start by deriving a novel theory of anharmonic lattice dynamics based on the Mori-Zwanzig projection operator formalism and mode-coupling theory. This derivation is formally exact, includes nuclear quantum effects and anharmonicity to the user's discretion, and remains exact in practice for the conservative part of the dynamics, only requiring approximations to be made on the dissipative part. A theory of thermal transport based on this formulation of lattice dynamics is also derived, providing a consistent framework for understanding and predicting phonon-mediated heat transport in solids. Applications are provided for several systems, with particular focus on monolayer hexagonal boron nitride which due to its symmetry properties requires up to 4-phonon scattering to be taken into account. A further derivation of fluctuation-dissipation theorem compliant energy conservation conditions is given, providing a change of paradigm in the understanding of the thermal conductivity in systems with wide phonon band-gaps such as boron arsenide.

Finally, the temperature dependent dielectric properties and lattice thermal conductivity of bulk hexagonal boron nitride are studied. We again find qualitative agreement with experiments, improving existing results in two ways: the dielectric properties are computed without 4-phonon interactions due to the use of renormalized phonons, and the thermal conductivity is found to be in agreement both in the in-plane and the out-of-plane components, where the 4-phonon interactions are of great importance.

With this work we advance the field of anharmonic lattice dyanmics significantly, providing not only frameworks but also concrete examples where our improvements on the state of the art approaches are of great value, showcasing the advantages of our novel theoretical and computational methods.

Contents

Part I

Introduction

The field of lattice dynamics, which focuses on the many-body atomic problem in crystals, is fundamental to understand and predict several important physical quantities. Despite originating over a century ago and having been understood for about as long, its great degree of complexity has led the scientific community to develop new theories and methods on how to tackle it at an increasing rate over the last decades. Phonon-centric methods in particular have been greatly improved in comparison to the longstanding harmonic theory, with new approaches capable of including the effects of temperature and anharmonicity in great detail, substantially closing the gap between theoretical predictions and experimental measurements. Combined with the ever-increasing accessibility of powerful computers, the ability to perform simulations of large and complex structures with great accuracy has revolutionized the scope of applications of lattice dynamics' many sub-fields.

One major sub-field of interest is thermal transport. With the lattice thermal conductivity as its central property, it is extremely important to a broad range of relevant applications in current energetic and heat management problems. These require a fundamental understanding of phonon behaviour as the main quasi-particles carrying heat in solids. While the theoretical foundations of thermal transport were laid with those of lattice dynamics, the computational advancements and techniques allowing for predictive simulations of the lattice thermal conductivity have been developed only in the XXIst century. Since then, the field has evolved quickly, and currently benefits from the numerous sophisticated molecular dynamics and phonon simulation techniques, enabling unprecedented precision in predicting and tailoring thermal properties for materials design. In particular, the ability to include 4-phonon scattering in thermal conductivity simulations has only become possible in the past few years. This has led to a completely new understanding of paradigmatic materials such as graphene, but also a critical re-evaluation of established thermal conductivity models, and a more robust predictive capability for disordered and high-temperature systems.

The aim of this thesis is to explore thermal transport and anharmonic phonon properties, through the lens of a new approach to lattice dynamics, the mode-coupling theory. Based on the Mori-Zwanzig projection operator formalism and using results from linear response theory, it formulates a generalized Langevin

equation separating the phonon dynamics into a static and a memory-dependent dynamic part. This approach leads to an exact formulation of the anharmonic phonon spectral functions. This enables the construction of a systematic perturbative expansion of the renormalized interatomic force constant via a mode-coupling approach: each successive order is built in a way that minimizes the following ones. This formalism is of particular importance as it provides for a formal framework for the temperature dependent effective potential (TDEP), one of the methods in the forefront of renormalized phonon calculations. It also extends TDEP to include nuclear quantum effects, a previously unjustified level of approximation for its molecular dynamics based formulation.

The manuscript is organized as follows. In the first part, an overview of phonons and anharmonicity is provided, from the harmonic theory and its perturbative expansion to the two most prominent approaches to renormalized phonon simulations: the self consistent harmonic approximation (SCHA) and TDEP. A review of thermal transport theory follows in the quasiparticle picture through the relaxation time approximation (RTA) and the iterative solution to the Boltzmann transport equation (IBTE) and in the Green-Kubo approach, when this picture is allowed to break. A discussion of the thermal conductivity in two-dimensional systems is provided, exploring the intricacies specific to these systems in detail.

In the second part, the results of this thesis are presented. In the first four sections, the articles associated to this work are provided. The first, titled "Mode-coupling theory of lattice dynamics for classical and quantum crystals" deals with the derivation of the aforementioned approach to lattice dynamics. The second, "Mode-coupling formulation of heat transport in anharmonic materials", establishes a framework based on mode-coupling theory that allows for thermal conductivity to be accurately computed in this approach. The third, "Fluctuation-dissipation and virtual processes in interacting phonon systems", builds on the fact that standard energy conservation conditions based on Dirac delta functions break the fluctuation-dissipation theorem, and derives new conditions based on self-consistent Lorentzians that ensure its global instead of microscopic conservation. In the fourth, "Thermal Conductivity Of Monolayer Hexagonal Boron Nitride: Four-Phonon Scattering And Quantum Sampling Effects", path integral molecular dynamics (PIMD) and 4-phonon scattering are used to explore

the temperature dependence of thermal conductivity in this system, as well as the degree of impact these effects have. Finally, a fifth section is included comprising a study of the temperature dependent dielectric properties and thermal conductivity of bulk hexagonal boron nitride, and is unpublished work.

After discussing our results, a conclusion with a summary of the thesis and future outlooks on the subject is provided. Lastly, two appendixes are included, in order to provide supporting text on the topics of machine-learning interatomic potentials (MLIPs) and molecular dynamics.

1

Phonons And Anharmonicity

1.1 Harmonic Phonons And Perturbative Expansion

In the absence of external perturbations, the Hamiltonian for a many-body system in quantum mechanics is given by

$$\hat{H} = \hat{T}_e + \hat{V}_{ee} + \hat{V}_{en} + \hat{T}_n + \hat{V}_{nn} \; , \tag{1.1}$$

where the indices e correspond to the electrons involvement in the operator and the n to the nuclei. The electron's kinetic energy operator is given by

$$\hat{T}_e = \sum_i \frac{\hat{p}_i^2}{2m_e} \; , \tag{1.2}$$

with p_i and m_e the electron's momentum and mass respectively, while the Coulomb potential responsible for the electron repulsion phenomena is given by

$$\hat{V}_{ee} = \sum_{i \neq j} \frac{e^2}{|\vec{r}_i - \vec{r}_j|} \; , \tag{1.3}$$

where $\vec{r}_I$ and $\vec{r}_J$ are the electron's position operators. Similarly, the nuclei's kinetic energy operator is given by

$$\hat{T}_n = \sum_I \frac{\hat{p}_I^2}{2m_I} \; , \tag{1.4}$$

where the capital indices now represent the sum over all nuclei instead, while the corresponding Coulomb repulsion is now modified by the nuclear charge:

$$\hat{V}_{nn} = \sum_{I \neq J} \frac{Z_I Z_J e^2}{|\vec{r}_I - \vec{r}_J|} \ . \tag{1.5}$$

Finally, the Coulomb attraction potential between electrons and nuclei is given by

$$\hat{V}_{en} = -\sum_{i \neq J} \frac{Z_J e^2}{|\vec{r}_i - \vec{r}_J|} \ . \tag{1.6}$$

Given the large difference between the electron and nuclei masses, we can for most problems apply the Born Oppenheimer approximation to the many-body problem [9], and thus consider the dynamics of the electrons to be independent to that of the nuclei. In practice, this implies first separating the full Hamiltonian into an electronic and nuclear components

$$\hat{H} = \hat{H}_e + \hat{H}_n \ , \tag{1.7}$$

with $\hat{H}_e = \hat{T}_e + \hat{V}_{ee} + \hat{V}_{en}$ and $\hat{H}_n = \hat{T}_n + \hat{V}_{nn}$, and then solving the electronic many-body problem for a fixed geometry, with the nuclei's positions $\vec{r}_J$ being parameters of the electron wavefunction:

$$\hat{H}_e(\vec{r}_i, \vec{r}_J)\Psi_e(\vec{r}_i, \vec{r}_J) = E_e(\vec{r}_J)\Psi_e(\vec{r}_i, \vec{r}_J) \ . \tag{1.8}$$

With the electronic energy in hand, one can then finally solve the many-body problem within the Born-Oppenheimer approximation:

$$\left(\hat{H}_n(\vec{r}_I) + E_e(\vec{r}_I) \right) \Psi_n(\vec{r}_I) = \left(\hat{T}_n + \hat{V}_{nn}(\vec{r}_I) + E_e(\vec{r}_I) \right) \Psi_n(\vec{r}_I) = E_{tot}\Psi_n(\vec{r}_I) \ . \tag{1.9}$$

By solving equation 1.8 and 1.9 for a set of nuclear configurations, one obtains the nuclei's dynamics as governed by their kinetic energy T_n and an *effective* Born-Oppenheimer potential energy surface (PES):

$$V_{BO}(\vec{r}_I) = E_e(\vec{r}_I) + V_{nn}(\vec{r}_I) \tag{1.10}$$

While in general this is a very complicated operator, a simple starting point is easy to find. Given that we are interested in crystalline systems, where each nuclei vibrates around an equilibrium position, we can begin by assuming that the nuclear displacement around this position is small, and expand the PES in a Taylor series:

$$V_{BO}(\vec{r}) \approx V_{BO}(\vec{r}^0) + \sum_I \left(\frac{\partial V_{BO}}{\partial \vec{r}_I} \right)_{\vec{r}^0} \vec{u}_I + \frac{1}{2} \sum_{IJ} \left(\frac{\partial^2 V_{BO}}{\partial \vec{r}_I \partial \vec{r}_J} \right)_{\vec{r}^0} \vec{u}_I \vec{u}_J + ... \quad (1.11)$$

where the derivatives are evaluated around the equilibrium positions $\vec{r}^0$ and $\vec{u}_{I,J}$ are the displacements of each nuclei around this configuration. Since the equilibrium position represents at least a local minimum of the Born-Oppenheimer PES, the first derivative of the Taylor expansion is zero. If one then truncates 1.11 at second-order, V_{BO} is then approximated by a harmonic potential and can be simplified to

$$V_{BO}(\vec{r}) \approx V_{BO}(\vec{r}_0) + \frac{1}{2} \sum_{IJ} \phi_{IJ}^{(2)} \vec{u}_I \vec{u}_J \; , \quad (1.12)$$

with the $\phi_{IJ}^{(2)}$ the second-order interatomic force-constants (IFCs), governing the strength of the coupling between nuclei in their motion. Within this harmonic approximation, we can now write the nuclear Hamiltonian as

$$H = \sum_I \frac{\vec{p}_I^2}{2m_I} + \frac{1}{2} \sum_{IJ} \phi_{IJ}^{(2)} \vec{u}_I \vec{u}_J \; . \quad (1.13)$$

At this point we drop the index n from the Hamiltonian, as this will be our Hamiltonian of interest from here on out. The index BO will also be dropped from V_{BO}, as that will be the potential energy operator of interest moving forward as well. It is worth noting, however, that this need not be the case as one can go beyond the Born-Oppenheimer approximation and work instead with a non-adiabatic PES in which coupling between electronic and nuclear wavefunctions is included via derivative terms. An example is electron-phonon coupling when computed from time-dependent density functional theory (TDDFT) [66] where the matrix-element

$$\Lambda_\mu^{kk'} = \left\langle \Psi_e^k \left| \frac{\partial V_{\text{el}}}{\partial u_{q,s}} \right| \Psi_e^{k'} \right\rangle \tag{1.14}$$

defines the strength of this coupling, and which are essential to study phenomena such as superconductivity or polarons.

As the Hamiltonian in 1.13 represents a system of coupled harmonic oscillators, our goal is to simplify it into an uncoupled one through a normal mode projection. This is done in two steps: first, by introducing mass-weighted coordinates, i.e. by defining

$$U_I = \sqrt{m_I} u_I \tag{1.15}$$

$$P_I = \sqrt{m_I} p_I \tag{1.16}$$

$$\Phi_{IJ} = \frac{1}{\sqrt{m_I m_J}} \phi_{IJ} \ , \tag{1.17}$$

and therefore re-writing the Hamiltonian as [8, 106]

$$H = \sum_I \frac{\vec{P}_I^2}{2} + \frac{1}{2} \sum_{IJ} \Phi_{IJ}^{(2)} \vec{U}_I \vec{U}_J \ ; \tag{1.18}$$

then, by decoupling the system and solving the eigenvalue problem for $\Phi_{IJ}^{(2)}$, i.e. by re-writing the second-order IFCs in their normal mode decomposition

$$\Phi_{IJ}^{(2)} = \sum_{\vec{\lambda}} \Omega_{\vec{\lambda}}^2 \vec{\varepsilon}_{I,\vec{\lambda}} \vec{\varepsilon}_{J,\lambda} \ , \tag{1.19}$$

where the super-index $\vec{\lambda} = (\vec{q}, s)$ represents both the phonon's crystal momentum and mode. By performing this projection, our system is now decoupled into independent harmonic oscillators, represented by the normal modes of the second-order IFCs, and the Hamiltonian is now written as their sum:

$$H = \frac{1}{2} \sum_{\vec{\lambda}} \left(P_{\vec{\lambda}}^2 + \Omega_{\vec{\lambda}}^2 U_{\vec{\lambda}}^2 \right) \ . \tag{1.20}$$

This is the simplest form of the phonon Hamiltonian, its harmonic form, where each quasiparticle is represented as a normal mode s with momentum $\mathbf{q}$ and frequency $\Omega_{\vec{\lambda}}$.

This fact is made clearer when one quantizes the phonon Hamiltonian. First, we introduce the phonon annihilation and creation operators

$$a_{\vec{\lambda}} = \sqrt{\frac{\Omega_{\vec{\lambda}}}{2}} U_{\vec{\lambda}} - \frac{i}{\sqrt{2\Omega_{\vec{\lambda}}}} P_{\vec{\lambda}} \tag{1.21}$$

$$a_{\vec{\lambda}}^{\dagger} = \sqrt{\frac{\Omega_{\vec{\lambda}}}{2}} U_{\vec{\lambda}} + \frac{i}{\sqrt{2\Omega_{\vec{\lambda}}}} P_{\vec{\lambda}} \ , \tag{1.22}$$

and their inverse transformations

$$U_{\vec{\lambda}} = \frac{1}{\sqrt{2\Omega_{\vec{\lambda}}}} \left(a_{\vec{\lambda}} + a_{-\vec{\lambda}}^{\dagger} \right) \tag{1.23}$$

$$P_{\vec{\lambda}} = -i\sqrt{\frac{\Omega_{\vec{\lambda}}}{2}} \left(a_{\vec{\lambda}} - a_{-\vec{\lambda}}^{\dagger} \right) \ , \tag{1.24}$$

where we define $-\vec{\lambda} = (-\vec{q}, s,)$and then we substitute them into the Hamiltonian, obtaining

$$H = \sum_{\vec{\lambda}} \Omega_{\vec{\lambda}} \left(\frac{1}{2} + a_{\vec{\lambda}}^{\dagger} a_{\vec{\lambda}} \right) = \sum_{\vec{\lambda}} \Omega_{\vec{\lambda}} \left(\frac{1}{2} + N_{\vec{\lambda}} \right) \ , \tag{1.25}$$

with $N_{\vec{\lambda}} = a_{\vec{\lambda}}^{\dagger} a_{\vec{\lambda}}$ the number operator, which counts the number of phonons in mode λ with momentum $\mathbf{q}$, and $\frac{1}{2}\Omega_{\vec{\lambda}}$ the zero-point energy of each mode.

While extremely simple and surprisingly successful, the harmonic theory of phonons is obviously not sufficient to describe all properties of solids, and in fact *cannot* predict some of them for very fundamental reasons. The lattice thermal conductivity, for example, is infinite under this approximation, as phonons are considered as non-interacting and without scattering they have infinite lifetimes. Another example is the temperature dependence of the phonon frequencies, an experimentally observed phenomenon that impacts all phonon properties and even their interaction with other quasiparticles. This effect, however, cannot be captured in the harmonic theory, as they are temperature independent at that level. In order to reconcile with experimental observation, one needs to go beyond the harmonic theory and introduce phonon anharmonicity.

1. PHONONS AND ANHARMONICITY

We start by recalling the Taylor expansion of the potential energy, and now add an extra term explicitly:

$$V_{BO}(\vec{r}) \approx V_{BO}(\vec{r}^0) + \frac{1}{2} \sum_{IJ} \left(\frac{\partial^2 V_{BO}}{\partial \vec{r}_I \partial \vec{r}_J} \right)_{\vec{r}^0} \vec{u}_I \vec{u}_J + \tag{1.26}$$

$$+ \frac{1}{6} \sum_{IJK} \left(\frac{\partial^3 V_{BO}}{\partial \vec{r}_I \partial \vec{r}_J \vec{r}_K} \right)_{\vec{r}^0} \vec{u}_I \vec{u}_J \vec{u}_K \ldots .$$

All extra terms after the quadratic one are known as anharmonic, with the third-order derivative of the potential known as the first of the higher-order IFCs, now governing the interaction strength of triplets of atoms. In the same fashion as for the harmonic case, one can write in mass-weighted coordinates

$$H = \sum_I \frac{\vec{P}_I^2}{2} + \frac{1}{2} \sum_{IJ} \Phi_{IJ}^{(2)} \vec{U}_I \vec{U}_J + \frac{1}{6} \sum_{IJK} \Phi_{IJK}^{(3)} \vec{U}_I \vec{U}_J \vec{U}_K \tag{1.27}$$

and in phonon operator terms

$$H = \sum_{\vec{\lambda}} \Omega_{\vec{\lambda}} \left(\frac{1}{2} + a_{\vec{\lambda}}^\dagger a_{\vec{\lambda}} \right) + \sum_{\vec{\lambda}_1, \vec{\lambda}_2, \vec{\lambda}_3} \Phi_{vec\lambda_1 \vec{\lambda}_2 \vec{\lambda}_3}^{(3)} \left(a_{\vec{\lambda}_1} + a_{\vec{\lambda}_1}^\dagger \right) \left(a_{\vec{\lambda}_2} + a_{\vec{\lambda}_2}^\dagger \right) \left(a_{\vec{\lambda}_2} + a_{\vec{\lambda}_3}^\dagger \right) , \tag{1.28}$$

where the $\Phi^{(3)}$ are given by

$$\Phi_{\vec{\lambda}_1 \vec{\lambda}_2 \vec{\lambda}_3}^{(3)} = \sum_{IJK} \sum_{\alpha\beta\gamma} \frac{\varepsilon_{I,\vec{\lambda}_1}^\alpha \varepsilon_{J,\vec{\lambda}_2}^\beta \varepsilon_{K,\vec{\lambda}_3}^\gamma}{\sqrt{m_I m_J m_K} \sqrt{\Omega_{\vec{\lambda}_1} \Omega_{\vec{\lambda}_2} \Omega_{\vec{\lambda}_3}}} \Phi_{IJK}^{\alpha\beta\gamma} e^{i(\vec{q}_1 \cdot \vec{r}_I + \vec{q}_2 \cdot \vec{r}_J + \vec{q}_3 \cdot \vec{r}_K)} . \tag{1.29}$$

Inspecting 1.1, one can easily see the extra processes that are being included. While the harmonic term simply counts the number of phonons for each mode and sums their energies together with the zero-point energy, the anharmonic term allows for dissociation processes (for example $a_{\vec{\lambda}_1}^\dagger a_{\vec{\lambda}_2} a_{\vec{\lambda}_3}$ where phonon $\vec{\lambda}_1$ is created and phonons $\vec{\lambda}_2$ and $\vec{\lambda}_3$ are annihilated) and coalescence processes (for example $a_{\vec{\lambda}_1}^\dagger a_{\vec{\lambda}_2} a_{\vec{\lambda}_3}$ where phonons $\vec{\lambda}_2$ and $\vec{\lambda}_3$ are annihilated and give origin to phonon $\vec{\lambda}_1$). These two kinds of cases are both parts of the umbrella of three-phonon scattering processes, and constitute the lowest order of phonon-phonon

interactions. With this level of theory, we are now able to obtain finite phonon lifetimes and therefore a finite thermal conductivity, as well as a renormalization of the phonon frequencies as the phonon self-energy is now non-zero. Considering that the perturbations are small in order for the expansion to hold, the phonon spectral function is Lorentzian in shape, and its self energy is given by

$$\Sigma_{\vec{\lambda}} = \Delta_{\vec{\lambda}} + i\Gamma_{\vec{\lambda}} \, , \tag{1.30}$$

with $\Delta_{\vec{\lambda}}$ and $\Gamma_{\vec{\lambda}}$ its real and imaginary parts respectively. Using the Fermi golden rule, the imaginary part of the self-energy can be obtained at a 3-phonon scattering level as

$$\Gamma_{\vec{\lambda}_1} = \frac{\hbar\pi}{16} \sum_{\vec{\lambda}_2 \vec{\lambda}_3} \left| \Phi^{(3)}_{\vec{\lambda}_1 \vec{\lambda}_2 \vec{\lambda}_3} \right|^2 \left[\left(n_{\vec{\lambda}_2} + n_{\vec{\lambda}_3} + 1 \right) \delta \left(\Omega_{\vec{\lambda}_1} - \Omega_{\vec{\lambda}_2} - \Omega_{\vec{\lambda}_3} \right) \right.$$
$$\left. + 2 \left(n_{\vec{\lambda}_2} - n_{\vec{\lambda}_3} \right) \delta \left(\Omega_{\vec{\lambda}_1} - \Omega_{\vec{\lambda}_2} + \Omega_{\vec{\lambda}_3} \right) \right] \, , \tag{1.31}$$

where $n_{\vec{\lambda}} = (\exp(\beta H) - 1)^{-1}$ is the Bose-Einstein distribution for the phonon thermal occupations and the delta functions ensure energy conservation in individual scattering processes. Phonon lifetimes can then be obtained as

$$\tau_{\vec{\lambda}} = \frac{1}{2\Gamma_{\vec{\lambda}}} \, . \tag{1.32}$$

The real part of the self-energy, on the other hand, is obtained by performing a Kramers-Kronig transformation on the imaginary part.

In the same fashion as third-order scattering was included in the phonon Hamiltonian, successive higher-order terms can be incorporated as well. These share the same functional form, but involve higher-order IFCs and extra sums of phonon creation and annihilation operators for increasing numbers of modes. If the Taylor expansion is extended to infinite order one then recovers an exact theory of phonon dynamics, so long as the nuclei vibrate along their equilibrium positions and the expansion holds. One could then compute the IFCs to any order by simply performing finite differentiation of the Born-Oppenheimer potential energy surface, with the order-N finite differences corresponding to the order-N IFC.

1. PHONONS AND ANHARMONICITY

While seemingly simple and, as we will see shortly, superseded, finite differences approaches are still in widespread use and constitute a major workhorse in many phonon calculations to this day. They are, however, not without drawbacks.

While perturbation theory is a very powerful tool for dealing with phonon anharmonicity, it faces systematic issues when applied to realistic systems. For starters, a perturbative approach to an interacting particle problem always assumes that the perturbation is small when compared to the non-interacting Hamiltonian (in the phonon case, the harmonic one). This assumption, however, breaks down when the systems being studied exhibit strong anharmonicity, like the cases of chalcogenides or perovskites even near room temperature, or many other systems at large temperatures where atomic displacements around their equilibrium positions become very large [27, 58, 92, 98]. Furthermore, harmonic perturbative theories are not equipped to handle structural or dynamical instabilities that some systems possess (for example when near phase transitions), as they are built to compute real-valued frequencies around a stable minimum of the potential energy surface. When the harmonic ground state is unstable and phonon frequencies become imaginary, the perturbative approach is no longer valid and other approaches need to be applied that in some capacity are able to capture the correct stable configuration [29, 87, 93].

Finally, perturbation theory fails to account for the inherent temperature dependence of phonons and instead works off of a $T = 0K$ potential energy surface to compute all properties. In reality, temperature impacts all phonon dependent quantities, either implicitly via the thermal expansion of the unit-cell and super-cell, which impacts the phonon frequencies with its contraction or expansion due to the asymmetry of the potential energy surface, or explicitly in the frequency shifts and finite lifetimes and their explicit dependence on temperature. In order to properly capture these effects, a proper sampling of the phase space for the system needs to be employed, either via a molecular dynamics (MD) based approach where the true anharmonic potential drives the dynamics and thus all orders of anharmonicity and temperature are implicitly included, or self-consistent phonon theories where the best effective potential that can include the aforementioned effects is computed instead using the $T= 0K$ one. These approaches will be the subject of the next section.

1.2 Renormalized Phonon Theories

1.2.1 Self Consistent Harmonic Approximation

The Self Consistent Harmonic Approximation (SCHA)[51] , most commonly used in its stochastic form (sSCHA) [7, 67], is a non-perturbative theory of phonon renormalization that relies on the minimization of the Helmholtz free energy in order to find the best effective harmonic Hamiltonian for a given system at finite temperature. Within this approach, not only is anharmonicity included taking temperature into account, but also nuclear quantum effects, allowing for a rigorous treatment even for systems at low temperatures or containing light atoms.

At its core, the SCHA is rooted on the Gibbs-Bogoliubov variational principle, where the exact Helmholtz free energy F of the system bounds all trial free energies from below. As such, given a trial density-matrix ρ', at fixed volume, temperature and number of atoms we have that

$$F_\rho \leq F_{\rho'} = E_{\rho'} - TS_{\rho'} \ , \tag{1.33}$$

where ρ and ρ' are the true and the trial density matrices respectively, and $E_{\rho'} = \mathrm{Tr}\,(\rho'H)$ is the total energy. This inequality implies that if one chooses any trial density-matrix, one can then optimize it in order to minimize the free-energy, and the parameters of ρ' such as the atomic positions will be the optimal ones for a fixed finite temperature. In the SCHA, a constraint is imposed such that ρ' is a gaussian distribution, thus mapping the system at equilibrium to a trial harmonic Hamiltonian:

$$\tilde{H}_0 = \sum_I \frac{\vec{P}_I^2}{2} + \frac{1}{2}\sum_{IJ} \tilde{\Phi}_{IJ}^{(2)}(\vec{r}_I - \vec{\mathcal{R}}_I)(\vec{r}_J - \vec{\mathcal{R}}_J) \tag{1.34}$$

In the SCHA trial Hamiltonian $\vec{\mathcal{R}}$ and $\tilde{\Phi}^{(2)}$ correspond to the trial effective equilibrium positions of the system's atoms and the trial harmonic IFCs, and are parameters that uniquely define the trial density-matrix ρ'. The SCHA Helmholtz free energy is then

$$F_{SCHA}[\{\vec{\mathcal{R}}\}, \{\tilde{\Phi}^{(2)}\}] = E_{\rho'_{\vec{\mathcal{R}}, \tilde{\Phi}(2)}} - TS_{\rho'_{\vec{\mathcal{R}}, \tilde{\Phi}(2)}} = K_{\rho'_{\vec{\mathcal{R}}, \tilde{\Phi}(2)}} + V(\{\vec{\mathcal{R}}\})_{\rho'_{\vec{\mathcal{R}}, \tilde{\Phi}(2)}} - TS_{\rho'_{\vec{\mathcal{R}}, \tilde{\Phi}(2)}} \; .$$
$$(1.35)$$

By applying 1.33, the best SCHA free energy is given by minimizing 1.35 with respect to the trial density-matrix's parameters $\{\vec{\mathcal{R}}\}$ and $\{\tilde{\Phi}^{(2)}\}$. As the trial Hamiltonian is harmonic, the kinetic energy and entropy are analytic functions of the trial harmonic IFCs $\{\tilde{\Phi}^{(2)}\}$. This means that the only unknown in 1.35 is the exact potential energy evaluated at the trial harmonic ensemble, which needs to be computed in an *ab-initio* fashion.

The minimum of F_{SCHA} is finally obtained when it is stationary with respect to the trial parameters, i.e. when

$$\frac{\partial F_{SCHA}}{\partial \vec{\mathcal{R}}_I} = \left\langle -\frac{\partial V(\{\vec{\mathcal{R}}\})}{\partial \vec{r}_I} \right\rangle_{\rho'_{\vec{\mathcal{R}}, \tilde{\Phi}(2)}} = 0 \qquad (1.36)$$

$$\frac{\partial F_{SCHA}}{\partial \tilde{\Phi}_{IJ}^{(2)}} = 0 \rightarrow \left\langle \frac{\partial^2 V(\{\vec{\mathcal{R}}\})}{\partial \vec{r}_I \vec{r}_J} \right\rangle_{\rho'_{\vec{\mathcal{R}}, \tilde{\Phi}(2)}} = \tilde{\Phi}_{IJ}^{(2)} \; . \qquad (1.37)$$

The first equation states that the thermal average of the forces on each atom vanish at the optimal trial $\mathcal{R}$. This establishes the equilibrium structure of the system at finite temperature, and will therefore include not only the effect of thermal expansion but also any kind of structural deformations. The second equation, on the other hand, establishes the harmonic IFCs as the thermal average of the second derivative of the full anharmonic potential energy surface evaluated at the trial density-matrix. This allows for both temperature and anharmonicity to renormalize the phonon frequencies, no longer constraining them to be the curvature at the minimum of the T=0K Born-Oppenheimer potential energy surface, and now implicitly absorbing higher-order effects due to quantum and thermal fluctuations. For pathological cases where the harmonic theory predicts imaginary phonon frequencies, the SCHA will systematically renormalize them to be real and stable, as well as incorporate thermal expansion in a natural fashion, and therefore overcoming harmonic theory's major limitations. It is however important to note that while the frequencies that arise from the SCHA

16

trial IFCs are renormalized, they do not hold physical meaning by themselves, and further corrections need to be made before being able to compare them to experiments. By themselves, they are simply a parameter required for the free energy minimization. This topic will be addressed later in this section.

1.37 establishes a self consistent equation that gives name to the theory, and allow for a procedural solution as follows. First, one starts with an initial guess for the trial parameters, such as the T=0K positions for the atoms and the corresponding harmonic IFCs, phonon frequencies and eigenvectors. The thermal averages at these trial parameters are then computed. In the standard SCHA approach, this is the most challenging bottleneck to overcome, as it requires multi-dimensional integration to be performed, either an explicitly or numerically. The trial parameters are then updated to satisfy 1.36 and 1.37, for example via a gradient descent approach, giving rise to new trial atomic positions and trial IFCs. The process is then repeated until self-consistency is obtained.

Compared to the traditional SCHA, the sSCHA provides an improvement on the thermal averaging step of the self-consistent procedure, by employing a stochastic sampling approach. Instead of analytical thermal integration, a Monte Carlo scheme is used, where a number of super-cell configurations are generated to perform the averaging according to the Gaussian functional form of the density-matrix. The atomic displacements for a thermalized configuration are then given by

$$\vec{u}_I = \sum_{\vec{\lambda}} \varepsilon_{I,\vec{\lambda}} \langle A_{\vec{\lambda}} \rangle \chi \ , \tag{1.38}$$

where χ is a uniform randomly distributed number and $\langle A_{\vec{\lambda}} \rangle$ is the thermal prefactor, classically

$$\langle A_{\vec{\lambda}} \rangle = \frac{1}{\Omega_{\vec{\lambda}}} \sqrt{\frac{1}{\beta m}} \ , \tag{1.39}$$

where $\beta = \frac{1}{k_B T}$ and k_B is the Boltzmann constant, and in the quantum case

$$\langle A_{\vec{\lambda}} \rangle = \sqrt{\frac{2n_{\vec{\lambda}} + 1}{2m\Omega_{\vec{\lambda}}}} \tag{1.40}$$

1. PHONONS AND ANHARMONICITY

In order to improve the accuracy of the integration, the displacement in the inverse direction can also be generated and it will be a valid configuration as well, since the Gaussian distribution is a symmetric one. By stochastically generating the canonical ensemble, the computational requirement for the thermal integrations reduces drastically, and the SCHA becomes a reliable, accurate method for obtaining the thermal expansion and temperature-dependent phonon properties from the free energy of the system.

Within the SCHA approach there is, however, the caveat that the optimized trial IFC does not lead to the physical renormalized phonon frequencies, and the $\tilde{\Phi}^{(2)}$ obtained at the end of the self-consistent procedure are simply the optimized trial force-constants required to minimize the free energy. It is, however, possible to show that one can obtain these quantities by instead relying on the Hessian of the free-energy at the equilibrium configuration, making this quantity the generalized harmonic dynamical matrix in the SCHA context, which now includes both anharmonic and nuclear quantum effects.

Up to this point we have dealt with the SCHA purely as an approach that improves upon the harmonic theory's limitations by providing an accurate thermal expansion, renormalized phonon frequencies, and the Helmholtz free energy. It is possible, however, to also expand the SCHA in a perturbative way and thus obtain other important quantities that rely on higher-order IFCs like the phonon lifetimes. This is done just like in the harmonic theory's case, with improved results coming from the fact that at a basic level the SCHA's renormalization ensures that the higher-order terms are smaller than in the former's case, making perturbation theory more reliable and well grounded. This means that quantities like the lattice thermal conductivity will be more accurate by using the SCHA, providing another advantage over the harmonic theory.

The SCHA is not, however, without limitations. While the assumption of a Gaussian canonical ensemble is reliable and often produces good results, this functional form does not hold for all systems. In particular, extremely anharmonic or high temperature systems, where the baseline effective harmonic approach is not sufficient, and the density matrix strongly deviates from a normal distribution, are pathological for such an approach. Furthermore, the fact that higher-order IFCs are required to obtain the Hessian of the free energy, and consequently the

renormalized phonon frequencies, is an expensive procedure, and one would prefer to stay at the harmonic level to compute the effective harmonic properties. An alternative approach to renormalized phonons that combats these problems is the subject of the next section.

1.2.2 Temperature Dependent Effective Potential

The temperature dependent effective potential (TDEP) method [41, 42, 43], similarly to the SCHA, is an alternative approach to phonon renormalization. First introduced by Hellman *et al.* in 2011, its goal is to use MD simulations, whether *ab initio* or driven by MLIPs, in order to sample phase space with temperature dependency and phonon anharmonicity to all orders. By doing so, the density-matrix is no longer constrained to a Gaussian distribution as in the SCHA, allowing for systems with larger and more complex anharmonicity to be handled without sacrificing accuracy. Furthermore, effective harmonic properties like the renormalized phonon frequencies are obtained without having to resort to higher than second-order IFCs. In contrast to the SCHA, however, the approach was introduced purely for classical MD simulations, thus not allowing for the inclusion of nuclear quantum effects, making it less reliable for systems where the simulation temperature is much lower than their Debye temperature. Relaxing this constraint is not a trivial matter, and is thoroughly explored in 3.1 .

In order to derive TDEP's formalism, our starting point is again an effective harmonic Hamiltonian:

$$\tilde{H}_0 = U_0 + \sum_I \frac{\vec{P}_I^2}{2} + \frac{1}{2} \sum_{IJ} \Theta_{IJ}^{(2)} \vec{U}_I \vec{U}_J \; , \tag{1.41}$$

where the TDEP effective harmonic IFCs are written as $\Theta_{IJ}^{(2)}$. The corresponding effective harmonic forces f_I are then

$$\vec{f}_I = -\sum_J \Theta_{IJ}^{(2)} \vec{U}_J \; . \tag{1.42}$$

The TDEP IFCs $\Theta^{(2)}$ are then obtained by minimizing the difference between the effective harmonic forces and those from the MD simulation:

$$\Theta^{(2)} = \min_{\Theta^{(2)}} \left\{ \frac{1}{N_{\text{tot}}} \sum_{t=1}^{N_{\text{tot}}} \left| \vec{f}_t^{\text{MD}} + \Theta^{(2)} \vec{U}_t \right|^2 \right\} . \tag{1.43}$$

Equation 1.43 is solved via the least-squares method

$$\Theta^{(2)} = -\frac{\langle U, f \rangle}{\langle U, U \rangle} , \tag{1.44}$$

yielding the $\Theta^{(2)}$ that minimize the force difference. An important detail about the TDEP approach is that the symmetry relations of the IFCs are applied before the least-squares method is employed. This means that, for example, a bcc crystal structure with 128 atoms that would have 147456 second order coefficients can be uniquely determined by computing the 11 unknowns that remain after all symmetry operations are applied. This makes the TDEP IFC computation extremely cheap when compared to other phonon renormalization methods.

After obtaining the effective harmonic IFCs, their higher-order counterparts are obtained in a similar fashion. If one considers a Taylor expansion of the effective Hamiltonian to third-order

$$\tilde{H} = U_0 + \sum_I \frac{\vec{P}_I^2}{2} + \frac{1}{2} \sum_{IJ} \Theta_{IJ}^{(2)} \vec{U}_I \vec{U}_J + \frac{1}{6} \sum_{IJK} \Theta_{IJK}^{(3)} \vec{U}_I \vec{U}_J \vec{U}_K , \tag{1.45}$$

and compute $\Theta^{(2)}$ according to equations 1.43 and 1.44, the third-order IFCs are computed from the residuals of the forces $\delta \vec{f}$ from that procedure. That is, if

$$\delta \vec{f}_t = \vec{f}_t^{MD} + \Theta^{(2)} \vec{U}_t , \tag{1.46}$$

then

$$\Theta^{(3)} = \min_{\Theta^{(3)}} \left\{ \frac{1}{N_{\text{tot}}} \sum_{t=1}^{N_{\text{tot}}} \left| \vec{f}_t^{\text{MD}} + \Theta^{(2)} \vec{U}_t + \Theta^{(3)} \vec{U}_t \vec{U}_t \right|^2 \right\} , \tag{1.47}$$

where $\Theta^{(2)}$ is now fixed by 1.44, and

$$\Theta^{(3)} = -\frac{\langle UU, \delta f \rangle}{\langle UU, UU \rangle} . \tag{1.48}$$

The procedure for higher than third-order IFCs is identical. Just like in the SCHA, TDEP is by construction a better basis for perturbation theory than the traditional harmonic theory, as it maximizes the amount of information in the lowest-order IFCs in comparison to the higher-order ones is exactly the grounding needed for it to work consistently. Consequently, TDEP is not only more adequate than the harmonic theory at describing quantities like phonon frequencies, but also anharmonic properties like thermal expansion and lattice thermal conductivity.

As mentioned previously, an inherent advantage of TDEP is the fact that all orders of anharmonicity are included in the phonon renormalization. That is made evident by equations 1.43 and 1.47, where the IFCs are computed from the forces and displacements from a MD simulation. These will therefore contain information about the exact temperature dependent dynamics of the system, and that will consequently be reflected in all IFCs. This means that, for example, the phonon frequencies will not only be temperature dependent, but also renormalized to all orders of anharmonicity and therefore only limited by the quality of the MD simulation.

The TDEP approach as demonstrated above is not, however, without limitations. Firstly, the lack of nuclear quantum effects is clear, as the molecular dynamics being considered is explicitly classical in nature with respect to the ionic motion. While one can hypothesize (and as is shown in [16]) the extension of the method to path-integral molecular dynamics (PIMD) as to include these effects, that is beyond the scope of the original introduction and almost entire usage of TDEP in the literature. Secondly, while the utilization of an effective anharmonic Hamiltonian, minimization of the difference between MD and (an)harmonic model and consequent computation of IFCs from least-squares fits are straightforward and intuitive, they lack both a more formal motivation and derivation. Finally, as presented TDEP is a purely static phonon theory, with the dynamical extension being done *a posteriori* in a Markovian fashion via the Fermi golden rule. While many phonon properties of interest are static, some are not, and in order to properly describe e.g. spectral functions and related quantities, one needs a theory that is also capable of including frequency dependency

no matter its complexity, and especially in cases where the quasiparticle picture breaks down. All of these limitations are addressed and solved in [16].

As a final note, it is important to mention that TDEP is not limited to sample phase space from MD. Indeed, it is possible to derive a SCHA based theory that works exactly like the sSCHA, but instead of determining the second-order IFCs by a gradient descent, doing so using the TDEP least-squares fit. This method, known as sTDEP [84], is identical to the sSCHA as it also generates configurations from a Monte Carlo approach and assumes a Gaussian distribution shaped density-matrix. Unsurprisingly, it suffers from the same limitations as the sSCHA, as even the renormalized phonon frequencies in sTDEP are computed from the Hessian of the free-energy and need to be corrected by terms involving higher order IFCs. Furthermore, it is also possible to derive TDEP up to second-order from the Helmholtz free energy resulting from MD sampling [14]. Like the SCHA, this approach is also grounded on the Gibbs-Bogoliubov inequality. However, the TDEP free energy is instead bounded from above compared to the exact one, making the variational problem in this case a maximization one. While laying out a solid foundation for TDEP as an effective harmonic theory, this derivation still fails to properly motivate and derive TDEP for an effective Hamiltonian beyond second-order, and therefore does not fully address the concerns previously highlighted.

2

Lattice Thermal Conductivity

The lattice thermal conductivity (κ) is the intrinsic property of a system that characterizes its ability to carry heat. While in general heat can be carried by several different quasiparticles, in insulators and semiconductors heat is carried predominantly by phonons. These systems are the focus of this manuscript.

When a temperature gradient is applied, heat conduction is described by Fourier's law

$$\vec{J} = -\kappa \vec{\nabla} T, \tag{2.1}$$

where $\vec{J}$ is the heat flux and $\vec{\nabla} T$ is the temperature gradient. Considering phonons to be the only quasiparticles that carry heat, the heat current is given by

$$\vec{J} = \frac{1}{V} \sum_{\vec{\lambda}} \hbar \Omega_{\vec{\lambda}} \vec{v}_{\vec{\lambda}} N_{\vec{\lambda}} , \tag{2.2}$$

where $\hbar \Omega_{\vec{\lambda}}$ are the phonon energies and $\vec{v}_{\vec{\lambda}}$ is the respective group velocity. From Eq. 2.2, we will thus be interested in the evolution of occupations $n_{\vec{\lambda}}$ over time as dictated by the phonon Boltzmann transport equation (BTE). In the absence of external forces, the phonon BTE is [1]

$$\frac{\partial n_{\vec{\lambda}}}{\partial t} + \vec{v}_{\vec{\lambda}} \cdot \vec{\nabla}_{\vec{r}} n_{\vec{\lambda}} = \left(\frac{\partial n_{\vec{\lambda}}}{\partial t} \right)_{coll} , \tag{2.3}$$

The second term in 2.3 corresponds to the phonon drift, while the last term is the collision integral, accounting for all the changes in $n_{\vec{\lambda}}$ due to all sources of scattering, and is the most complex and computationally expensive part of the phonon BTE.

2.1   Relaxation Time Approximation

If one considers the distribution to be in a steady-state, the first term $\frac{\partial n_{\vec{\lambda}}}{\partial t} = 0$ and the equation simplifies to

$$\vec{v}_{\vec{\lambda}} \cdot \vec{\nabla}_{\vec{r}} n_{\vec{\lambda}} = \left(\frac{\partial n_{\vec{\lambda}}}{\partial t} \right)_{coll} . \tag{2.4}$$

If one further takes the temperature gradient to be a small perturbation, the phonon BTE can then be linearized. By assuming that the $n_{\vec{\lambda}}$ deviates only slightly from the equilibrium occupations $n_{\vec{\lambda}}^0$, i.e. $n_{\vec{\lambda}} = n_{\vec{\lambda}}^0 + \delta n_{\vec{\lambda}}$, the drift term becomes

$$\vec{\nabla}_{\vec{r}} n_{\vec{\lambda}} = \vec{\nabla}_{\vec{r}} n_{\vec{\lambda}}^0 + \vec{\nabla}_{\vec{r}} \delta n_{\vec{\lambda}} . \tag{2.5}$$

The first term can be re-written as

$$\vec{\nabla}_{\vec{r}} n_{\vec{\lambda}}^0 = \frac{\partial n_{\vec{\lambda}}^0}{\partial T} \vec{\nabla}_{\vec{r}} T , \tag{2.6}$$

such that the left side of 2.4 reads

$$\vec{v}_{\vec{\lambda}} \cdot \vec{\nabla}_{\vec{r}} n_{\vec{\lambda}} = \vec{v}_{\vec{\lambda}} \cdot \left(\frac{\partial n_{\vec{\lambda}}^0}{\partial T} \vec{\nabla}_{\vec{r}} T + \vec{\nabla}_{\vec{r}} \delta n_{\vec{\lambda}} \right) . \tag{2.7}$$

In order to simplify the collision integral, a further approximation can be made. If one assumes that $n_{\vec{\lambda}}$ relaxes back to $n_{\vec{\lambda}}^0$ after a characteristic relaxation time $\tau_{\vec{\lambda}}$, then

$$\left(\frac{\partial n_{\vec{\lambda}}}{\partial t} \right)_{coll} = -\frac{n_{\vec{\lambda}} - n_{\vec{\lambda}}^0}{\tau_{\vec{\lambda}}} = -\frac{\delta n_{\vec{\lambda}}}{\tau_{\vec{\lambda}}} . \tag{2.8}$$

This is known as the relaxation time approximation [88], and is common in lattice thermal conductivity simulations both as a standalone and a starting point to

more complex approaches. Finally, one can take the phonon occupations to be spatially homogeneous, and therefore $\vec{\nabla}_{\vec{r}} \delta n_{\vec{\lambda}} \approx 0$. Eq. 2.4 then reduces to

$$\delta n_{\vec{\lambda}} = -\tau_{\vec{\lambda}} \vec{v}_{\vec{\lambda}} \cdot \frac{\partial n^0_{\vec{\lambda}}}{\partial T} \vec{\nabla}_{\vec{r}} T \ . \tag{2.9}$$

Inserting this into Eq. 2.2 and recognizing that the equilibrium distribution carries no heat, we obtain

$$\vec{J} = -\frac{1}{V} \sum_{\vec{\lambda}} \hbar \Omega_{\vec{\lambda}} \frac{\partial n^0_{\vec{\lambda}}}{\partial T} \vec{v}_{\vec{\lambda}} \otimes \vec{v}_{\vec{\lambda}} \tau_{\vec{\lambda}} \vec{\nabla}_{\vec{r}} T \ . \tag{2.10}$$

Since $\hbar \Omega_{\vec{\lambda}} \frac{\partial n^0_{\vec{\lambda}}}{\partial T}$ is the definition of the harmonic specific heat capacity per mode $C_{\vec{\lambda}}$, the final form of the heat current in the RTA is

$$\vec{J} = -\frac{1}{V} \sum_{\vec{\lambda}} C_{\vec{\lambda}} \vec{v}_{\vec{\lambda}} \otimes \vec{v}_{\vec{\lambda}} \tau_{\vec{\lambda}} \vec{\nabla}_{\vec{r}} T \ . \tag{2.11}$$

By inserting Eq. 2.11 into 2.2, the lattice thermal conductivity at the RTA level is

$$\kappa = \frac{1}{V} \sum_{\vec{\lambda}} C_{\vec{\lambda}} \vec{v}_{\vec{\lambda}} \otimes \vec{v}_{\vec{\lambda}} \tau_{\vec{\lambda}} \ . \tag{2.12}$$

Within the RTA, κ will only depend on the phonon frequencies and group velocities, which are harmonic quantities, and the relaxation times, which are an anharmonic quantity. Since at the harmonic level phonons don't interact, $\tau \to \infty$ and from 2.12 $\kappa \to \infty$, demonstrating one of the harmonic approximation's limitations mentioned previously. If 3-phonon scattering is included, for example, the lifetimes are computed from 1.31 and 1.32.

As simple and accurate as the RTA can be, it comes with very clear limitations from its many approximations. For one, the core RTA of the collision integral can be a very strong simplification, as it treats all scattering processes as resistive in nature. In reality, phonon scattering is more complex, with both resistive and additive processes contributing to κ. If the latter kind are non-negligible, the RTA is not well-grounded and an improved approximation is required. Furthermore, it fails at addressing how phonon modes can deviate from equilibrium in

complex ways. Indeed, by using a single relaxation time $\tau_{\vec{\lambda}}$ for each mode, we ignore the influence other modes exert on the chosen phonon with momentum and mode $\vec{\lambda} = (\vec{q}, s)$ and how their occupations are interconnected. Finally, $n_{\vec{\lambda}}$ is considered to only relax to the equilibrium distribution $n_{\vec{\lambda}}^0$, bypassing possible intermediate states. All these limitations turn the intricacies of scattering events and the non-locality of the collision integrals into a local, independent quasiparticle problem that is often insufficient for an accurate prediction of the lattice thermal conductivity. In short, the RTA fails to account for collective phonon effects.

2.2 Iterative Boltzmann Transport Equation

The standard approach to go beyond the RTA and have a full solution of the collision integral is the iterative Boltzmann transport equation (IBTE) [32, 74]. Within the IBTE, the lattice thermal conductivity is given by

$$\kappa = \frac{1}{V} \sum_{\vec{\lambda}_1 \vec{\lambda}_2} c_{\vec{\lambda}} \vec{v}_{\vec{\lambda}_1} \otimes \vec{v}_{\vec{\lambda}_2} (\Xi)^{-1}_{\vec{\lambda}_1 \vec{\lambda}_2} , \tag{2.13}$$

where $\Xi_{\vec{\lambda}_1 \vec{\lambda}_2}$ is the scattering matrix, a generalization of the previously derived lifetimes. Relative to the RTA, Ξ not only contains the phonon scattering rates in its diagonal elements, but the coupling between phonon modes in its off-diagonal components as well, while also accounting for the detailed balance.

While general, this scattering matrix is a very complicated object (see the appendix of [17] for more details), and the required matrix inversion presents a serious computational challenge to perform directly. Instead, within the IBTE one first considers only the components diagonal in $\vec{\lambda}$ and slightly re-defines κ to be

$$\kappa = \frac{1}{V} \sum_{\vec{\lambda}} c_{\vec{\lambda}} \vec{v}_{\vec{\lambda}} \otimes \vec{F}_{\vec{\lambda}} , \tag{2.14}$$

where

$$\vec{F}_{\vec{\lambda}_1} = \sum_{\vec{\lambda}_2} \Xi^{-1}_{\vec{\lambda}_1 \vec{\lambda}_2} \vec{v}_{\vec{\lambda}_2} \tag{2.15}$$

is a generalized phonon mean free path. If we now assume that the off-diagonal components of Ξ are smaller than the diagonal ones and take advantage of the Neumann series for matrix inversion, we obtain

$$\vec{F}_{\vec{\lambda}_1} = \sum_{\vec{\lambda}_2} \left[\sum_{k=0}^{n} \left(-\Xi_{\vec{\lambda}_1 \vec{\lambda}_1}^{-1} \Xi_{\vec{\lambda}_1 \vec{\lambda}_2} \right)^k \right] \Xi_{\vec{\lambda}_2 \vec{\lambda}_2}^{-1} \vec{v}_{\vec{\lambda}_2} \ . \tag{2.16}$$

This series converges when $\left| \Xi_{\vec{\lambda}_1 \vec{\lambda}_1}^{-1} \Xi_{\vec{\lambda}_1 \vec{\lambda}_2} \right| < 1$, and thus for sufficiently large k will allow for a solution of the IBTE by iteratively solving for $\vec{F}_{\vec{\lambda}}$:

$$\vec{F}_{\vec{\lambda}_1}^{k+1} = \vec{F}_{\vec{\lambda}_1}^{0} - \tau_{\vec{\lambda}_1} \sum_{\vec{\lambda}_2} \Xi_{\vec{\lambda}_1 \vec{\lambda}_2} \vec{F}_{\vec{\lambda}_2}^{k}$$

$$\vec{F}_{\vec{\lambda}_1}^{0} = \tau_{\vec{\lambda}_1} \vec{v}_{\vec{\lambda}_1} \ . \tag{2.17}$$

If we take $\vec{F}_{\vec{\lambda}} = \vec{F}_{\vec{\lambda}}^{0}$, then we recover the RTA.

The IBTE, especially when coupled with coherence contributions, is a very successful theory for lattice thermal conductivity simulations. It not only is able to account for both resistive and additive scattering but also more complex coupling between different phonon modes. A classic example of IBTE's success is that of diamond, for which an increase of about 50% is found when compared to the RTA due to it's improper treatment of normal scattering [99].

While a well grounded and incredibly successful theory, the IBTE is still reliant on the quasiparticle picture being preserved to be applicable, with phonons having well defined momenta and being described by sharp Lorentzian distributions. For example, in systems near phase transitions some phonon modes can soften to the point where their lifetimes become comparable to or smaller than their frequencies. In this case, commonly called an "overdamped" regime, the notion of a harmonic oscillator is no longer valid, and the quasiparticle picture is broken [26, 56, 105]. This can lead in turn to more complex spectral functions, generally non-Lorentzian and often including satellites. In order to overcome these limitations, one works within the Green-Kubo formalism, which is will be the topic of the next section.

2.3 Green-Kubo Thermal Conductivity

The Green-Kubo formula is a general expression from linear response theory that relates transport coefficients to time correlations of their respective currents. In the thermal conductivity case, it reads

$$\kappa = \frac{V}{k_B T^2} \int_0^\infty \langle \vec{J}(t) \otimes \vec{J}(0) \rangle dt \; , \tag{2.18}$$

where $\vec{J}(t)$ is the microscopic heat current vector at time t, and $\langle \vec{J}(t) \otimes \vec{J}(0) \rangle$ is the corresponding autocorrelation function. This relation dictates that even near equilibrium there are fluctuations in the microscopic current $\vec{J}$ that determine the macroscopic response function κ. The slower these fluctuations decay, the more efficient heat transport will be in response to a small thermal gradient.

Up to lowest order, the microscopic heat current is given by

$$\vec{J}_{ha} = \frac{1}{2V} \sum_{\vec{\lambda}_1 \vec{\lambda}_2} \vec{v}_{\vec{\lambda}_1 \vec{\lambda}_2} \Omega_{\vec{\lambda}_1} B_{\vec{\lambda}_1} A_{\vec{\lambda}_2} \; , \tag{2.19}$$

with $A_{\vec{\lambda}} = a_{\vec{\lambda}} + a^\dagger_{-\vec{\lambda}}$ and $B_{\vec{\lambda}} = a_{\vec{\lambda}} - a^\dagger_{-\vec{\lambda}}$. These quantities can be seen as displacements and momenta in the phonon picture via the relations 1.24. This is a generalization of Eq. 2.11, where the phonon picture is relaxed and a non-diagonal group velocity is considered. Eq. 2.19 reduces to Eq. 2.11 if $\vec{\lambda}_1 = \vec{\lambda}_2$.

First introduced by Peierls in [76] for a nearest neighbours case and systematically derived by Hardy in [40], the heat current is subject to the heat-gauge invariance principle [28, 64, 65]. This conditions the heat current, which can be expressed generally in terms of local energies ϵ_I, equilibrium positions $\vec{\mathcal{R}}_I$ and displacements u_I as

$$\vec{J} = \sum_I \vec{\mathcal{R}}_I \epsilon_I + \frac{d}{dt} \sum_I \vec{u}_I \epsilon_I \; , \tag{2.20}$$

to be independent of a time derivative of a stationary process in the absence atoms diffusing in the crystal. The heat current then reduces to

$$\vec{J} = \sum_I \vec{\mathcal{R}}_I \epsilon_I \; , \tag{2.21}$$

and in the harmonic limit to 2.19 in terms of phonon operators.

By inserting 2.19 into 2.18, we obtain the thermal conductivity in the harmonic heat-current limit:

$$
\kappa = \frac{1}{4Vk_BT^2} \sum_{\vec{\lambda}_1\ldots\vec{\lambda}_4} \Omega_{\vec{\lambda}_1} \Omega_{\vec{\lambda}_3} \vec{v}_{\vec{\lambda}_1\vec{\lambda}_2} \otimes \vec{v}_{\vec{\lambda}_3\vec{\lambda}_4} \int_0^\infty dt \langle B_{\vec{\lambda}_1}(t) A_{\vec{\lambda}_2}(t) B_{\vec{\lambda}_3}(0) A_{\vec{\lambda}_4}(0) \rangle \; .
$$
(2.22)

This expression showcases the Green-Kubo formalism's generality, as it not only allows for off-diagonal group velocities and therefore mode-mixing to occur, but also holds when the phonon picture is broken, since the correlation function on the right-hand side does not presume any functional form. Furthermore, the phonon operators $A_{\vec{\lambda}}$ and $B_{\vec{\lambda}}$ can be anharmonic and temperature dependent in nature, further expanding the scope of application. It is also important to note that the quantum nature of phonons can be included naturally in 2.22, both at the quasiparticle level by including quantum effects in the frequencies, group velocities and phonon displacements and momenta, and at the level of the correlation functions, by using Kubo correlation functions (KCFs) instead of classical ones:

$$
\int_0^\infty dt \langle B_{\vec{\lambda}_1}(t) A_{\vec{\lambda}_2}(t) B_{\vec{\lambda}_3}(0) A_{\vec{\lambda}_4}(0) \rangle \rightarrow \frac{1}{\beta} \int_0^\infty dt \int_0^\beta d\Lambda \langle B_{\vec{\lambda}_1}(t) A_{\vec{\lambda}_2}(t) B_{\vec{\lambda}_3}(i\hbar\Lambda) A_{\vec{\lambda}_4}(i\hbar\Lambda) \rangle \; .
$$
(2.23)

In the above, the inverse-temperature integration variable Λ connects the quantum average to the high-temperature classical canonical ensemble. This variable turns the classical correlation function into one that is properly symmetric, and the integration from 0 to β effectively sums all possible thermal orderings [55].

The crucial part of computing κ in the Green-Kubo formalism lies in the correlation function. Since the general form presented in 2.22 involves the 2-phonon correlation function, it is very complicated to calculate, and requires some level of simplification. If one neglects collective effects (the so-called dressed-bubble approximation) and applies Wick's theorem to the 4-point correlation function, we can re-write it in terms of products of 2-point correlators:

2. LATTICE THERMAL CONDUCTIVITY

$$\langle B_{\vec{\lambda}_1}(t)A_{\vec{\lambda}_2}(t)B_{\vec{\lambda}_3}(0)A_{\vec{\lambda}_4}(0)\rangle \approx \langle B_{\vec{\lambda}_1}(t)B_{\vec{\lambda}_3}(0)\rangle\langle A_{\vec{\lambda}_2}(t)A_{\vec{\lambda}_4}(0)\rangle$$
$$+ \langle B_{\vec{\lambda}_1}(t)A_{\vec{\lambda}_4}(0)\rangle\langle A_{\vec{\lambda}_2}(t)B_{\vec{\lambda}_3}(0)\rangle . \qquad (2.24)$$

If one further assumes the phonon self-energies to be diagonal in momentum only then so are the group velocities and spectral functions, and this expression simplifies to

$$\langle B_{\vec{\lambda}_1}(t)A_{\vec{\lambda}_2}(t)B_{\vec{\lambda}_3}(0)A_{\vec{\lambda}_4}(0)\rangle \approx \langle B_{\vec{q}_1 s_1}(t)B_{-\vec{q}_1 s_3}(0)\rangle\langle A_{\vec{q}_2 s_2}(t)A_{-\vec{q}_2 s_4}(0)\rangle$$
$$+ \langle B_{\vec{q}_1 s_1}(t)A_{-\vec{q}_1 s_4}(0)\rangle\langle A_{\vec{q}_2 s_2}(t)B_{-\vec{q}_2 s_3}(0)\rangle , \qquad (2.25)$$

which when injected into 2.22 yields (after some algebra, see e.g. [6, 25])

$$\kappa = \frac{\pi}{2V}\sum_{\vec{q}}\sum_{s_1\dots s_4}\vec{v}_{\vec{q}s_1 s_2}\otimes\vec{v}_{\vec{q}s_3 s_4}\int_{-\infty}^{+\infty}c_v(\omega)\chi''_{\vec{q}s_1 s_3}(\omega)\chi''_{\vec{q}s_2 s_4}(\omega)d\omega , \qquad (2.26)$$

where $\chi''(\omega)$ is the phonon spectral function. If one takes $\chi''(\omega)$ to be Lorentzian in 2.26 and the collective effects to be negligible in 2.13 such that $\vec{F}_{\vec{\lambda}} = \vec{F}^0_{\vec{\lambda}} = \tau_{\vec{\lambda}}\vec{v}_{\vec{\lambda}}$, both approaches are under the same constraints and reduce to the RTA. If off-diagonal contributions are considered, we can also recover the results from [45] or [86] and obtain

$$\kappa = \frac{1}{2V}\sum_{\vec{\lambda}_1 \vec{\lambda}_2}\vec{v}_{\vec{\lambda}_1 \vec{\lambda}_2}\otimes\vec{v}_{\vec{\lambda}_1 \vec{\lambda}_2}\left(c_{\vec{\lambda}_1} + c_{\vec{\lambda}_2}\right)\frac{\Gamma_{\vec{\lambda}_1} + \Gamma_{\vec{\lambda}_2}}{\left(\Omega_{\vec{\lambda}_1} - \Omega_{\vec{\lambda}_2}\right)^2 + \left(\Gamma_{\vec{\lambda}_1} + \Gamma_{\vec{\lambda}_2}\right)^2} . \qquad (2.27)$$

Here, $\vec{v}_{\vec{\lambda}_1 \vec{\lambda}_2}$ are the generalized group velocities [40, 45, 86], off-diagonal in momentum and defined as

$$\vec{v}_{\vec{\lambda}_1 \vec{\lambda}_2} = \frac{i}{\sqrt{2\Omega_{\vec{\lambda}_1}\Omega_{\vec{\lambda}_2}}}\sum_{IJ}\left(\mathcal{R}_I^\alpha - \mathcal{R}_J^\alpha\right)\Phi_{IJ}^{\beta\gamma}\varepsilon^\beta_{I,\vec{\lambda}_1}\varepsilon^\gamma_{J,\vec{\lambda}_2} , \qquad (2.28)$$

and reduce to the standard group velocities in the diagonal components, i.e. when $\vec{\lambda}_1 = \vec{\lambda}_2$.

Eq. 2.26 presents major differences when compared to the thermal conductivity obtained from the IBTE in 2.13. While the group velocity outer product is the same if one considers the same diagonal self-energy approximation, the heat capacity is now frequency dependent and the scattering loses collective effects but gains the ability to include non-Lorentzian phonon spectral functions, and thus to work in the overdamped regime. These results exemplify the main difference between both approaches: Green-Kubo under the dressed-bubble approximation is well equipped to deal with non-Lorentzian phonons but not collective effects, and vice-versa for the IBTE. The best approach to use in the calculation of the lattice thermal conductivity is therefore dependent on the system.

While this chapter is focused on computing the Green-Kubo thermal conductivity in the phonon picture, it is possible to obtain it directly from 2.18 via MD [4, 12, 49, 52]. In this case, the non-perturbative dynamics of the nuclei are included in the heat currents, making them inherently anharmonic to all orders, and keeping the ability to handle both collective effects and phonon picture breaking cases. If MLIPs are used to drive the MD, this approach provides a way to compute κ that, all else being equal, is inherently more accurate than both the IBTE and Green-Kubo approaches. By directly computing the autocorrelation function integral, however, one also suffers some disadvantages, the first of these being the lack of interpretability: if one never transitions into the phonon picture there is no distinction between contributions. If one has, for example, the case of isotopically pure diamond, the IBTE is able to distinguish between the RTA level contributions and those coming from collective effects, and is therefore able to show that the latter are fundamental to an accurate thermal conductivity. Direct autocorrelation function integration, on the other hand, yields a value for κ that while similar to that of the IBTE shows no such distinction.

A second limitation of this approach is the ability to include impurity scattering, in particular due to isotopes where mass disorder causes thermal resistance and acts to decrease κ. For both phonon picture based methods this type of scattering can be trivially included via a model like the Tamura one [94] where the isotopes are assumed to be randomly distributed along the lattice sites, with the mass deviations leading to a source of scattering. The contribution to the scattering rates from this model is then given by

$$\Gamma_{\vec{\lambda}_1}^{\text{iso}} = \frac{\pi}{4} \sum_{\vec{\lambda}_2} \Omega_{\vec{\lambda}_1} \Omega_{\vec{\lambda}_2} \sum_I g_I \left| \varepsilon_{I,\vec{\lambda}_1}^{\dagger} \varepsilon_{I,\vec{\lambda}_2} \right|^2 \delta \left(\Omega_{\vec{\lambda}_1} - \Omega_{\vec{\lambda}_2} \right) \;, \tag{2.29}$$

where g_I is the mass variance parameter

$$g_I = \sum_J c_I^J \left(\frac{m_I^J - \bar{m}_I}{\bar{m}_I} \right)^2 \;, \tag{2.30}$$

with c_I^J the concentration of the J isotope of atom I, m_I^J its mass and $\bar{m}$ the average mass of all isotopes present for that species. The scattering rates given by 2.29 can then be simply added to the ones from 3-phonon scattering, 4-phonon scattering, etc. in the imaginary part of the phonon self-energy to further improve the accuracy of κ. This effect has been shown to be extremely important in several cases, such as diamond, where isotopically enriched ^{12}C is found to have 50% larger thermal conductivity than natural occurring one [44], or graphene, where a similar result is observed [20, 33]. While isotopes can be included in MD studies by directly changing atomic masses according to the desired distribution, the computational cost rises severely with them as the simulation cell's size needs to be large enough to allow for the proper statistics, and often averaging over several simulations is required in order to correct for sample size induced errors.

Finally, in the particular case where MLIPs are used to drive the MD, direct autocorrelation integration methods is affected by the error in ML predicted forces compared to the *ab-initio* ones [101, 103]. While they are able to be corrected, this requires a significant computational effort and that the functional form for the errors is Gaussian, which holds for the most commonly used MLIPs but is by no means a guarantee. On the other hand, quasiparticle based approaches such as TDEP are unaffected by the force error so long as it's distribution has zero mean and finite variance. In the TDEP case, for example, the least-squares fit can be shown to be the maximum likelihood estimator when these conditions are met as the peak of the force distribution is unaffected by them.

2.4   Thermal Conductivity In 2D Systems

While formally similar to the 3-dimensional (3D) cases, thermal conductivity in 2-dimensional (2D) systems shows fundamental differences due to the reduced dimensionality both at the phonon and scattering level.

The clearest of these lies in the phonon dispersion, where the atoms' in-phase out of plane motion gives rise to a flexural acoustic mode (ZA). This phonon mode shows a distinct characteristic when compared to other acoustic modes, as its dispersion is quadratic in the long wavelength limit, i.e. $\omega \propto q^2$ for $q \to 0$. The ZA mode is present in all 2D systems, and compared to the linear dispersion of the other acoustic modes it has a higher density of states at lower frequencies. In order to properly recover this quadratic dispersion, both the Born-Huang rotational invariance conditions, arising from the fact that 2D crystals are invariant under a rotation around the perpendicular axis, and the Huang equilibrium conditions, which require a vanishing stress tensor for a unit cell at equilibrium, need to be imposed. If both constraints are not present, it has been shown that the ZA mode's dispersion can not only deviate from a quadratic behaviour, but also become imaginary close to the zone center [60].

The impact of the ZA mode on the lattice thermal conductivity can be easily seen from a symmetry analysis. If one considers, for example, a 3-phonon scattering process $\lambda_1 + \lambda_2 \to \lambda_3$, in order for it to be valid it has to respect both energy and momentum conservation, as well as the system's crystal symmetries. For perfectly planar 2D crystals, mirror plane symmetry is enforced and invariance under reflection across the z-plane is imposed. While simple, this symmetry implies major limitations on phonon scattering as it enforces that the process as a whole preserves it. While in-plane phonons transform symmetrically under reflection across the xy-plane, and are therefore not limited by it, ZA phonons transform anti-symmetrically, and can therefore only enter scattering events in even numbers. Consequently, for the aforementioned 3-phonon scattering case, interactions involving 1 or 3 flexural phonons are frozen by mirror-plane symmetry. While present for all orders of scattering processes, the limitation imposed by mirror-plane symmetry is particularly relevant for the 3-phonon case. Being the lowest order of anharmonicity in the perturbative expansion, as well as having

the smallest combinatorial number of possible processes, the amount of interactions involving odd numbers of flexural phonons is the highest relative to the total possible. This leads to an overestimation of phonon lifetimes and the lattice thermal conductivity for the flexural modes, and the need for higher-order phonon scattering for these systems, as their relative impact grows due the reduction of 3-phonon interactions.

The paradigmatic and most studied planar 2D system regarding their thermal conductivity is graphene, with several theoretical and experimental studies pointing towards a record high thermal conductivity, with the ZA mode's extremely large lifetimes being the main driver [2, 11, 20, 33, 34, 38, 62, 63, 71, 72, 81]. Most theoretical work, however, includes only 3-phonon and isotope scattering, which as previously mentioned are strongly restricted by mirror-plane symmetry. More recent studies [31, 39], however, include 4-phonon scattering as well, and show a reduction of nearly 50% in the lattice thermal conductivity at room temperature, clearly demonstrating how crucial they are. Furthermore, while all phonon modes are impacted by the increased level of scattering, the ZA mode is by far the one whose lifetimes are reduced the most. Another example of such a system is monolayer hexagonal boron nitride (h-BN), also a planar 2D system with a reported large lattice thermal conductivity [19, 21, 30, 50, 61, 69, 70, 82, 104]. Just like in graphene, most reported values point towards a large thermal conductivity including 3-phonon and isotope scattering. A drastic reduction is also observed at room temperature when 4-phonon interactions are included [90].

While the effect of mirror-plane symmetry is clear on planar 2D systems, it is important to highlight that the constraint is only dramatic in these cases, and does not impact other 2D systems as visibly. As an example one can take the case of MoS_2, a layered 2D material whose semiconducting monolayer structure is trigonal prismatic (2H), with every molybdenum atom sandwiched between two sulfur atoms giving rise to a structure that, while 2D, is not planar. Consequently, despite $MosS_2$ having mirror-plane symmetry, its phonon eigenvectors are now no longer strictly in-plane or out-of-plane, but instead linear combinations of both, making it much easier to combine them in a way that preserves the mirror plane symmetry at any order of phonon scattering. As such, 4-phonon interactions are often not essential for these systems and staying at a 3-phonon + isotope

scattering level is sufficient for an accurate calculation of the lattice thermal conductivity.

Another peculiarity of thermal transport in 2D system is the presence of so-called hydrodynamic effects. In order to understand them, it is useful to distinguish scattering processes that dissipate the heat current, usually referred to as resistive ($\mathcal{R}$), and those that do not, usually referred to as normal ($\mathcal{N}$). Isotope scattering is included in the first, since it acts resistively with respect to the heat current and therefore decreases the thermal conductivity. For extremely low temperatures where the phonon mean free path is larger than crystal's size, extrinsic scattering ($\mathcal{E}$) is also relevant as it becomes the dominant mechanism to dissipate the heat current.

For a typical crystal, four different transport regimes can be identified as a function of the dominant scattering mechanism:

- a ballistic regime, where $\mathcal{E} \gg \mathcal{N}$ and $\mathcal{E} \gg \mathcal{R}$ and thermal conductivity becomes sample size dependent due to the lack of internal scattering mechanisms;

- a Poiseuille regime, with $\mathcal{N} \gg \mathcal{E} \gg \mathcal{R}$ and where, despite predominance of normal processes, extrinsic scattering ultimately dissipates the heat current and there is therefore still size dependence on the thermal conductivity;

- a Ziman regime, where $\mathcal{N} \gg \mathcal{R} \gg \mathcal{E}$, which is similar to the Poiseuille one but with resistive scattering acting as the main dissipative source;

- a ballistic regime, with $\mathcal{R} \gg \mathcal{E}$ and $\mathcal{R} \gg \mathcal{N}$, which is the standard thermal transport regime where the heat current dissipates at most scattering events.

These are ordered with respect to increasing temperature, with the ballistic, Poiseuille and Ziman regimes only found at cryogenic temperatures for most systems, with the latter two often not present at any temperature. Commonly denominated as hydrodynamic regimes, they are analogues of the phonon gas to a viscous fluid (the viscosity being analogue to $\mathcal{N}$ processes, and the internal resistance of the fluid to $\mathcal{R}$ processes) running through a pipe (whose friction with

the fluid represents $\mathcal{E}$ processes). In the Poiseuille flow, while the fluid's internal viscosity allows it to flow coherently (predominance of $\mathcal{N}$ scattering), the pipe's radius is small enough that the friction of its walls dissipates the flow (representing the condition $\mathcal{E} \gg \mathcal{R}$). In the Ziman regime, the pipe's radius is taken to be large enough that the internal resistance becomes the relevant dissipation mechanism ($\mathcal{R} \gg \mathcal{E}$).

2D crystals like graphene and monolayer h-BN, unlike standard systems, have been found to have predominant $\mathcal{N}$ scattering at all temperatures, and therefore only occupy the two hydrodynamic regimes [19]. This means that for these systems the RTA is a bad approximation for the thermal conductivity, as it presumes that all scattering is dissipative, and an improved approach such as the IBTE is fundamental to capture the correct scattering physics. Furthermore, it implies that these systems are able to showcase second-sound [78, 80], making them even more interesting testbeds for exotic phonon transport phenomena.

Finally, it is worth noting that thermal transport in 2D systems has a systematic issue due to the differences in definition of effective thickness used in the literature to construct a volume that ensures the same units as the 3D case. While usually grounded in physical reason, such as the interlayer distance between two layers in the corresponding bulk system, this choice is ultimately arbitrary and its only purpose is to enable the comparison between different materials regardless of dimensionality. Furthermore, if one uses the interlayer distance of the bulk crystal as the effective thickness, this value becomes system dependent and inevitably biases the κ values, as two systems that carry the same amount of heat in the monolayer but have different interlayer distances in the bulk will misleadingly report different thermal conductivities. In summary, the only unbiased approach that ensures that the units are $\mathrm{Wm}^{-1}\mathrm{K}^{-1}$ is to use a constant value for all systems regardless of potential differences in the bulk. Alternative approaches that circumvent this problem have been proposed [100], but rely on re-defining the quantity as a thermal sheet conductance which is an intensive 2D property instead and explicitly remove the effective thickness from the equation. While seemingly simple, this problem has severe ramifications in the field of thermal conductivity, as great care has to be taken to convert all values to the same effective thickness in order to not provide incorrect comparisons and conclusions.

Part II

Results and Discussion

3

Published Work

The full list of publications produced in this thesis is the following:

- A. Castellano, J. P. A. Batista, and M. J. Verstraete, Mode-coupling theory of lattice dynamics for classical and quantum crystals, The Journal of Chemical Physics 159, 10.1063/5.0174255 (2023)*;

- F. Knoop, N. Shulumba, A. Castellano, J. P. A. Batista, R. Farris, M. J. Verstraete, M. Heine, D. Broido, D. S. Kim, J. Klarbring, I. A. Abrikosov, S. I. Simak, and O. Hellman, Tdep: Temperature dependent effective potentials, Journal of Open Source Software 9, 6150 (2024);

- A. Canetta, S. Volosheniuk, S. Satheesh, J. P. Alvarinhas Batista, A. Castellano, R. Conte, D. G. Chica, K. Watanabe, T. Taniguchi, X. Roy, H. S. J. van der Zant, M. Burghard, M. J. Verstraete, and P. Gehring, "Impact of spin-entropy on the thermoelectric properties of a 2d magnet", Nano Letters 24, 6513–6520 (2024);

- A. Castellano, J. P. A. Batista, O. Hellman, and M. J. Verstraete, "Mode-coupling formulation of heat transport in anharmonic materials", Physical Review B 111, 10.1103/physrevb.111.094306 (2025)*;

- N. G. Erhardt, A. Castellano, J. P. A. Batista, R. Bianco, I. Loncaric, M. J. Verstraete, and D. Novko, "Electron-mediated anharmonicity and its role

in the Raman spectrum of graphene", npj Computational Materials 11, 10.1038/s41524-025-01610-9 (2025);

- A. Castellano, J. P. A. Batista, and M. J. Verstraete, "Fluctuation-dissipation and virtual processes in interacting phonon systems", 10.48550/ARXIV.2502.03362 (2025)*;

- J. P. A. Batista, M. J. Verstraete, and A. Castellano, "Thermal conductivity of monolayer hexagonal boron nitride: four-phonon scattering and quantum sampling effects", 10.48550/ARXIV. 2506.14547 (2025)*.

Publications followed by an asterisk are included in this manuscript as part of the results and discussion section.

Paper I

3.1 Mode-coupling theory of lattice dynamics for classical and quantum crystals

Aloïs Castellano, JP Batista, Matthieu J Verstraete

Publication Report

Contributions Summary:*Contributed to conceptualization, theory derivations, physical understanding and manuscript review*

Abstract

The dynamical properties of nuclei, carried by the concept of phonon quasiparticles , are central to the field of condensed matter. While the harmonic approximation can reproduce a number of properties observed in real crystals, the inclusion of anharmonicity in lattice dynamics is essential to accurately predict properties such as heat transport or thermal expansion. For highly anharmonic systems, non-perturbative approaches are needed, which result in renormalized theories of lattice dynamics. In this article, we apply the Mori–Zwanzig projector formalism to derive an exact generalized Langevin equation describing the quantum dynamics of nuclei in a crystal. By projecting this equation on quasiparticles in reciprocal space, and with results from linear response theory, we obtain a formulation of vibrational spectra that fully accounts for the anharmonicity. Using a mode-coupling approach, we construct a systematic perturbative expansion in which each new order is built to minimize the following ones. With a truncation to the lowest order, we show how to obtain a set of self-consistent equations that can describe the lineshapes of quasiparticles. The only inputs needed for the resulting set of equations are the static Kubo correlation functions, which can be computed using (fully quantum) path-integral molecular dynamics or approximated with (classical or ab initio) molecular dynamics. We illustrate the theory with an application on fcc ^{4}He, an archetypal quantum crystal with very strong anharmonicity.

Aloïs Castellano ✉ iD ; J. P. Alvarinhas Batista iD ; Matthieu J. Verstraete iD

Check for updates

View Online   Export Citation

25 June 2025 05:47:22

Mode-coupling theory of lattice dynamics for classical and quantum crystals (F)

Aloïs Castellano,[a) (iD)] J. P. Alvarinhas Batista, [(iD)] and Matthieu J. Verstraete [(iD)]

AFFILIATIONS

Nanomat Group, QMAT Center, CESAM Research Unit and European Theoretical Spectroscopy Facility, Université de Liège, Allée du 6 Août, 19, B-4000 Liège, Belgium

Note: This paper is part of the 2023 JCP Emerging Investigators Special Collection.
[a)]Author to whom correspondence should be addressed: alois.castellano@uliege.be

ABSTRACT

The dynamical properties of nuclei, carried by the concept of phonon quasiparticles, are central to the field of condensed matter. While the harmonic approximation can reproduce a number of properties observed in real crystals, the inclusion of anharmonicity in lattice dynamics is essential to accurately predict properties such as heat transport or thermal expansion. For highly anharmonic systems, non-perturbative approaches are needed, which result in renormalized theories of lattice dynamics. In this article, we apply the Mori–Zwanzig projector formalism to derive an exact generalized Langevin equation describing the quantum dynamics of nuclei in a crystal. By projecting this equation on quasiparticles in reciprocal space, and with results from linear response theory, we obtain a formulation of vibrational spectra that fully accounts for the anharmonicity. Using a mode-coupling approach, we construct a systematic perturbative expansion in which each new order is built to minimize the following ones. With a truncation to the lowest order, we show how to obtain a set of self-consistent equations that can describe the lineshapes of quasiparticles. The only inputs needed for the resulting set of equations are the static Kubo correlation functions, which can be computed using (fully quantum) path-integral molecular dynamics or approximated with (classical or *ab initio*) molecular dynamics. We illustrate the theory with an application on fcc ^{4}He, an archetypal quantum crystal with very strong anharmonicity.

Published under an exclusive license by AIP Publishing. https://doi.org/10.1063/5.0174255

I. INTRODUCTION

In the condensed phases of matter, many physical properties are profoundly related to the vibrations of nuclei. The understanding of thermodynamical, dynamical, or transport phenomena in crystals requires the inclusion of the correlated motion of atoms around their equilibrium positions. To describe such dynamics, the cornerstone of modern theories is the harmonic approximation.[1] Using a second-order Taylor expansion of the Born–Oppenheimer surface (BOS), this model describes the lattice vibrations as a non-interacting quantum gas of quasiparticles called phonons. Despite its simplicity, the harmonic approximation has been tremendously successful in explaining a large number of phenomena observed in the solid state, including excitation spectra, the phase stability of various materials, elastic properties, or even zero point motion.[2,3] Consequently, it naturally became one of the most important tools in the field of condensed matter. Nevertheless, the early truncation of the BOS Taylor expansion can be a severe limitation to the accuracy of the harmonic approximation.[3–5] In some cases,

these inaccuracies are only quantitative, but many phenomena cannot be described even qualitatively with a purely harmonic theory of lattice dynamics. Indeed, the higher order terms of the Taylor expansion, which are denoted as anharmonic, are responsible for a number of properties that cannot be predicted at all with the non-interacting phonon picture. Two of the most striking examples of these limitations are probably the dynamical stabilization of some structures,[6] and the computation of the thermal conductivity, which diverges in the harmonic approximation.[2] These limitations are a good illustration of the intrinsic problem with the non-interacting phonon picture. Indeed, within the harmonic approach, phonons are quasiparticles with temperature-independent energies and infinite lifetimes. Such features are incompatible with the frequency changes associated with a dynamical stabilization or the finite lifetimes associated with a finite thermal conductivity. In order to reconcile the temperature-dependent frequencies with a harmonic approximation, the quasi-harmonic approximation is often used,[3,7] in which the temperature evolution is included indirectly through a volume dependence. Unfortunately, this approach is biased in the

type of anharmonicity it includes,[8] is often insufficient to accurately describe the frequency evolution, and is still unable, by construction, to incorporate a linewidth.[9]

Nevertheless, a quasiparticle picture still seems to be an adequate representation of the finite temperature vibrational excitations for most solids. As a matter of fact, in most vibrational spectroscopy measurements on pure crystals, one can observe reasonably sharp Lorentzian-like resonances.[10] These resonances can be associated with vibrational quasiparticles, and it is these excitations that are approximated with harmonic phonons. However, in contrast with the harmonic picture, these quasiparticles have temperature-dependent frequencies $\Omega_v(T)$, as well as a linewidth $\Gamma_v(T)$, which can be interpreted as a manifestation of their finite lifetimes.

In recent years, a number of frameworks have been developed to account for the anharmonicity of materials. For example, it is nowadays common to use perturbation theory[11–13] to describe the effects of finite temperature on phonons within an *ab initio* setting.[14–17] In this approach, the anharmonic contributions to the BOS are responsible for phonon–phonon interactions, which leads to temperature-dependent frequencies as well as the finite lifetimes missing in the harmonic approximation. However, if perturbation theory can improve the agreement between harmonic phonons and more realistic vibrational QP, it is based on the assumption that the higher order anharmonic contributions will be of progressively lower importance, the (T = 0 K) harmonic contribution being dominant. This hypothesis is often too drastic, and perturbative approaches are consequently known to fail in some cases.[18–21] Moreover, a significant drawback of such approaches is that they cannot be applied at all in strongly anharmonic systems with unstable harmonic-level phonons. These failures suggest that approaches beyond standard perturbation theory are necessary to obtain a satisfactory description of vibrational properties of materials.

Starting from this observation, a significant number of works have focused on developing non-perturbative methods to treat anharmonicity without the drawbacks of the perturbative expansion. Most of these approaches are constructed on the idea of renormalized phonons and phonon–phonon interactions. The foremost non-perturbative theory of anharmonicity is the Self-Consistent Harmonic Approximation (SCHA),[22–31] also known as self-consistent phonons, first imagined by Born and since then rederived several times.[4] The idea behind the SCHA is that interactions between harmonic phonons renormalize their frequencies. Using the Gibbs–Bogoliubov free energy inequality,[23,30,32] a Dyson equation for the Green function,[27] or even a path-integral formalism,[33] the SCHA can be derived as a set of self-consistent equations, which uses the density matrix of an effective harmonic Hamiltonian. In essence, the renormalized phonons are obtained from an average computed on the distribution associated with the converged Hamiltonian. However, the quadratic form of the effective Hamiltonian means that the average is always computed on a multivariate Gaussian distribution, which can differ substantially from the true distribution. For instance, the renormalized phonons obtained as a result of the self-consistent equations still need a correction to approximate the QP frequencies.[29,32]

Fortunately, there exists a clear way to lift the multivariate Gaussian distribution approximation. Indeed, given a potential $V(\mathbf{R})$, which can be computed using *ab initio* methods, such as

density functional theory (DFT) or a classical model, it is possible to sample the exact canonical distribution in the classical limit for a given temperature T with methods such as molecular dynamics (MD) or Markov-chain Monte Carlo. Consequently, it seems natural to use these methods to obtain a non-perturbative description of lattice dynamics to go beyond the effective harmonic distribution of the SCHA. For instance, it has been proposed to use the displacements covariance tensor computed from MD to map it on an effective harmonic model through effective interatomic force constants (IFC).[34–36] However, the prevailing MD-based lattice dynamics method is probably the temperature dependent effective potential (TDEP).[37–39] This method uses configurations extracted from MD to fit an effective harmonic potential as well as third and sometimes fourth order anharmonic terms.[39] An important feature of this potential is that each new order is fitted on the residual forces from the previous order.[40] The goal of this procedure is to minimize the importance of high order contributions compared to the effective harmonic one. By using perturbation theory on top of this effective anharmonic Hamiltonian, TDEP has proven its ability to describe anharmonic properties with a great number of applications on the free energy and transport of materials.[37–39,41–43] Unfortunately, the renormalized anharmonic Hamiltonian at the heart of TDEP lacks a theoretical justification. This feature hinders a clear vision of its limits and raises questions on the justification for the use of perturbation theory with the effective Hamiltonian.

For instance, an important question raised by this approach is the easily overlooked problem of going from the classical description of MD to the quantum description of perturbation theory. Indeed, the QP description of a many-body system is intrinsically constructed on correlation functions. However, while the definition of classical correlation functions is unambiguous, this is not the case for a quantum system, where there exist an infinite number of ways to define them.[44] Consequently, the classical to quantum transformation of correlation functions is a non-trivial task that needs strong justifications.[45–47] It would seem that to dispose of this problem, a solution could be to use the true quantum distribution of displacements using, for example, path-integral molecular dynamics. Unfortunately, the freedom of choice in how to define quantum correlation functions is still an obstacle to a clear vision of how to apply TDEP. Indeed, from all the different types of quantum correlation functions, which one should be used as input for the least-squares problem? In a recent publication, it has been proposed to use the standard correlation functions.[48] However, this choice was justified with the goal of having a good description of the BOS, which unfortunately does not answer the remaining questions on how to approximate the QP with the effective Hamiltonian.

A more satisfying answer comes from the recent method introduced by Morresi *et al.*,[49,50] which uses the static Kubo correlation function (KCF) as input to obtain the QP. With simple manipulations, the authors were able to show that QPs computed this way match the exact zero frequency of the Matsubara QP Green's function. While their QPs feature an infinite lifetime, this result is a strong suggestion that the KCF might be an answer to the questions raised previously. From this type of correlation functions, the missing step is how to obtain the dynamical QP properties, but the use of the KCF points to the field of linear response theory, in which established theoretical tools exist to solve such problems.

In this work, we build a foundation for an exact non-perturbative theory of lattice dynamics that can describe strongly anharmonic quantum systems. With this objective, we derive a dynamical theory for solids based on the Mori–Zwanzig projector formalism of linear response theory.[51–57] This approach projects the dynamics on the slow variables of the system, resulting in a generalized Langevin equation (GLE) and thus splitting the equation of motion for the KCF into a conservative and in a memory-dependent dissipative part. After defining a projection on quasiparticle operators in reciprocal space, we use linear response theory to obtain an exact formulation of the spectral function. By using a mode-coupling theory[58–61] to approximate the memory kernel inherent to the Mori–Zwanzig formalism, we derive a theory in which the renormalized interatomic force constants of all orders appear naturally. This approximation allows us to obtain a set of self-consistent equations to compute vibrational spectra, for which we also propose a simplification based on a scattering approximation. Moreover, we show how our findings can justify a theory of temperature dependent phonons, thus giving an explanation of the success of renormalized phonon methods. We also discuss the implications of the method, showing, for instance, how it can be used to approximate nuclear quantum effects (NQE) on classical simulations, while alleviating ambiguities related to the multiple definitions of quantum correlation functions. We show that well established methods, such as perturbation theory or the SCHA, can be recovered as approximations of our mode-coupling theory, and that TDEP, used with (PI)MD [(Path-integral) Molecular Dynamics], is a direct application of our approach. Another interesting result of the present theory is that it shows that the often-used Lorentzian approximation of spectral lineshapes can never be an exact representation.

This paper is organized as follows. In Sec. II, we introduce the notation used throughout the paper as well as the Kubo correlation functions (KCF), before deriving the generalized Langevin equation for the displacement KCF, using the Mori–Zwanzig projector formalism. We then construct the projection in reciprocal space in Sec. III, before using the GLE to derive exact equations describing the spectral properties in Sec. IV. Using a mode-coupling approach, we then derive in Sec. V a set of approximations to the memory kernel appearing in the GLE. Next, we discuss how to compute from *ab initio* calculations the quantities needed as input for the method in Sec. VI. Section VII is devoted to the discussion of the classical limit as well as the comparison to other theories of anharmonicity. We illustrate the theory with an application on ^{4}He in Sec. VIII before concluding in Sec. IX.

II. DERIVATION OF THE GENERALIZED LANGEVIN EQUATION

A. Notations

In this work, we consider a three-dimensional crystal in the Born–Oppenheimer approximation so that the Hamiltonian governing the dynamics of the system is taken with the general form

$$H = \sum_i \frac{p_i^2}{2M_i} + V(\mathbf{R}),\tag{1}$$

where $\mathbf{R}$ and $\mathbf{p}$ are, respectively, the position and momentum operators, and $V(\mathbf{R})$ is the potential. In this work, we will consider

that there is no atomic diffusion in the system so that we can use the displacements $\mathbf{u}_i = \mathbf{R}_i - \langle \mathbf{R}_i \rangle$ as dynamical variables. In this definition, $\langle O(t) \rangle$ is the thermal average of the operator O, meaning that $\langle \mathbf{R} \rangle$ are the equilibrium positions. It should be noted that with this definition, the equilibrium positions, and consequently the definitions of displacements, are temperature dependent. While it is common to expand the potential in Eq. (1) in a Taylor expansion, here we make no assumptions on its form, apart from its time independence.

To describe the time evolution of the system, we use the Heisenberg representation, where the time dependence and derivatives of operators are obtained with

$$A(t) = e^{\frac{i}{\hbar}Ht} A e^{-\frac{i}{\hbar}Ht} = e^{i\mathcal{L}t} A,$$
$$\dot{A}(t) = \frac{i}{\hbar}[H, A(t)] = i\mathcal{L}A(t),\tag{2}$$

where $A = A(0)$ and $\mathcal{L} = \frac{1}{\hbar}[H, \cdot]$ is the quantum Liouville operator. We will denote $p_i(t) = M_i \dot{u}_i(t)$ the time derivative of the displacement of atom i with mass M_i. Furthermore, we will define mass scaled coordinates $\tilde{u}_i = \sqrt{M_i} u_i$ and $\tilde{p}_i = \frac{1}{\sqrt{M_i}} p_i$.

B. Kubo correlation function

Given the many-body nature of atomic vibrations in a crystal, a natural tool to describe the dynamics are correlation functions. In this work, we will be using the Kubo correlation function (KCF), which, for two operators A and B, is defined as

$$\begin{aligned} G_{AB}(t) &= k_B T \int_0^\beta d\lambda \langle A^\dagger(i\lambda\hbar) B(t) \rangle \\ &= \frac{k_B T}{\mathcal{Z}} \int_0^\beta d\lambda \operatorname{Tr}\left[e^{-(\beta-\lambda)H} A^\dagger e^{-\lambda H} B(t) \right] \\ &= (A, B(t)), \end{aligned}\tag{3}$$

where $\beta = \frac{1}{k_B T}$ is the inverse temperature and $\mathcal{Z}$ is the partition function. This correlation function, which can be derived from linear response theory,[53,62] has the advantage of being easily approximated in the path-integral molecular dynamics formalism.[49,63] Moreover, the KCF has a number of properties which simplify its manipulation. First, similarly to classical correlation functions, it is a real and even function of time and it obeys the relations $G_{AB}(t) = G_{AB}(-t)$ as well as $G_{AB}(t) = G_{BA}(t)$. Using the Lehmann representation, it can also be shown that derivatives of the static Kubo correlation function are related[64]

$$\frac{d^k}{dt^k}(A, B(t))|_{t=0} = (-1)^k \frac{d^k}{dt^k}(B, A(t))|_{t=0},\tag{4}$$

$$\frac{d^k}{dt^k}(A, A(t))|_{t=0} = 0 \quad \forall k = 1, 3, 5, \ldots.\tag{5}$$

Naturally, all the different quantum correlation functions are related by simple relations[47,53] so that knowledge of any type of correlation function allows to obtain any other one. Finally, we will note that the KCF, as the standard or any other quantum correlation function, reduces to the classical correlation function in the limit $\hbar \to 0$.

25 June 2025 05:47:22

In this work, the KCF of interest is the mass-weighted displacement KCF, which is a $3N_{at} \times 3N_{at}$ symmetric matrix defined with

$$
\begin{aligned}
G_{ij}(t) &= \sqrt{M_i M_j} \frac{k_B T}{\mathcal{Z}} \int_0^\beta d\lambda \, \mathrm{Tr}\left[e^{-(\beta-\lambda)H} u_i^\dagger e^{-\lambda H} u_j(t) \right] \\
&= \sqrt{M_i M_j}\, (u_i, u_j(t)) \\
&= (\tilde{u}_i, \tilde{u}_j(t))
\end{aligned}
\tag{6}
$$

with an equation of motion given by

$$
\begin{aligned}
\ddot{G}_{ij}(t) &= \sqrt{M_i M_j}\, (u_i, \ddot{u}_j(t)) \\
&= (\tilde{u}_i, \dot{\tilde{p}}_j(t)).
\end{aligned}
\tag{7}
$$

Our goal in this work is to derive a solution for this equation of motion.

C. The generalized Langevin equation

Presented in the form of Eq. (7), solving for the dynamics of the many-body system is an intractable problem. Fortunately, the projection operator formalism derived by Mori[51] and Zwanzig[52] allows to express Eq. (7) in a form amenable to approximations. This formalism is based on operators $\mathcal{P}$ and $\mathcal{Q}$, which project an observable $O(t)$ onto the subspace of "slow" dynamical variables of interest. In this work, we will use the mass scaled coordinates as "slow" variables, so that the projectors are defined as

$$
\mathcal{P}O(t) = \sum_{ij} \frac{(\tilde{u}_j, O(t))}{(\tilde{u}_i, \tilde{u}_j)} \tilde{u}_i + \sum_{ij} \frac{(\tilde{p}_j, O(t))}{(\tilde{p}_i, \tilde{p}_j)} \tilde{p}_i,
\tag{8}
$$

$$
\mathcal{Q}O(t) = (1 - \mathcal{P})O(t).
\tag{9}
$$

By construction, it should be noted that the projectors $\mathcal{P}$ and $\mathcal{Q}$ are orthogonal, in the sense that they follow $\mathcal{P} + \mathcal{Q} = 1$ and $\mathcal{P}\mathcal{Q} = \mathcal{Q}\mathcal{P} = 0$. Being projection operators, it is natural that $\mathcal{P}$ and $\mathcal{Q}$ are idempotent so that $\mathcal{P}\mathcal{P} = \mathcal{P}$ and $\mathcal{Q}\mathcal{Q} = \mathcal{Q}$. Moreover, it can be shown that these projectors, as the Liouville operators, are Hermitian with respect to the static Kubo correlation function,[55] which results in the properties

$$
(X, \mathcal{P}Y) = (\mathcal{P}X, Y),
\tag{10}
$$

$$
(X, \mathcal{Q}Y) = (\mathcal{Q}X, Y).
\tag{11}
$$

Equipped with these operators, we can now express the equation of motion of the mass scaled momentum of atom i,

$$
\begin{aligned}
\dot{\tilde{p}}_i(t) &= e^{i\mathcal{L}t} i\mathcal{L}\tilde{p}_i \\
&= e^{i\mathcal{L}t}(\mathcal{P} + \mathcal{Q})i\mathcal{L}\tilde{p}_i \\
&= e^{i\mathcal{L}t}\mathcal{P}i\mathcal{L}\tilde{p}_i + e^{i\mathcal{Q}\mathcal{L}t}\mathcal{Q}i\mathcal{L}\tilde{p}_i + \int_0^t ds\, e^{i\mathcal{L}(t-s)}\mathcal{P}i\mathcal{L}e^{i\mathcal{Q}\mathcal{L}s}\mathcal{Q}i\mathcal{L}\tilde{p}_i,
\end{aligned}
\tag{12}
$$

where we used the Dyson identity[55,59] to expand the $\mathcal{Q}$ projection.

To simplify the notation of Eq. (12), we introduce the frequency matrix $\mathbf{\Theta}$ (note that it is not in mass scaled coordinates)

$$
\Theta_{ij} = -\sum_k \frac{(u_k, f_i)}{(u_j, u_k)},
\tag{13}
$$

where $f_i = M_i \mathcal{L}^2 u_i$ is the force acting on atom i, as well as $\delta\mathbf{f}(t)$, which is often called the random force,

$$
\delta f_i(t) = e^{i\mathcal{Q}\mathcal{L}t}\left(f_i + \sum_j \Theta_{ij} u_j \right)
\tag{14}
$$

and the memory kernel $\mathbf{K}(t)$

$$
K_{ij}(t) = \frac{(\delta f_i, \delta f_j(t))}{\sqrt{M_i M_j}}
\tag{15}
$$

so that the equations of motion for the momentum can be written as[58-61]

$$
\dot{\tilde{p}}_i(t) = -\sum_j \frac{\Theta_{ij}}{\sqrt{M_i M_j}} \tilde{u}_j(t) - \frac{\delta f_i(t)}{\sqrt{M_i}} - \beta \sum_j \int_0^t ds K_{ij}(s) \tilde{p}_j(t-s).
\tag{16}
$$

Formally, the Mori–Zwanzig projection splits the evolution of the dynamical variables into a "slow" contribution, driven by the frequency matrix and a "fast" one, given by the random force and the memory kernel. As depicted in Fig. 1, the "slow" part of the dynamics represents a subspace of the full Hilbert space of the dynamical variables. Thus, the goal of the operator $\mathcal{P}$ is to project any dynamical variable into this subspace. The random forces, which account for the effects of other degrees of freedom, evolve in the "fast" orthogonal subspace, as indicated by the evolution operator $e^{i\mathcal{Q}\mathcal{L}t}$, and its orthogonal nature is recovered thanks to the property $(\tilde{u}_i, \delta f_i(t)) = 0$. It should be noted that the randomness of this term is only apparent. By contracting information through the projector $\mathcal{Q}$, the time evolution of this term is more difficult to apprehend and its dynamics appears "random,"[55] though this is not the case.

We can now inject $\dot{\tilde{p}}_i(t)$ into the equations of motion of Eq. (7) to obtain the generalized Langevin equation of motion of the mass weighted displacement KCF

$$
\ddot{\mathbf{G}}(t) = -\frac{\mathbf{\Theta}}{\sqrt{\mathbf{M}^T \mathbf{M}}} \mathbf{G}(t) - \beta \int_0^t ds \mathbf{K}(s)\dot{\mathbf{G}}(t-s).
\tag{17}
$$

An interesting result of this formulation is the separation of the dynamics into two parts. The first one, driven by the static frequency matrix, is conservative, while the second part, driven by
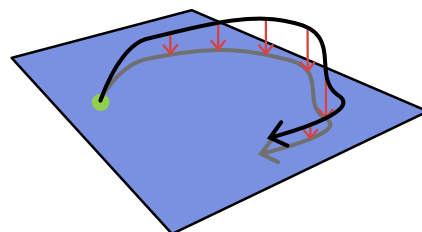
FIG. 1. Schematic illustration of the Mori–Zwanzig projection operator formalism. Within this formalism, the dynamics of a dynamical variable, represented here with a black arrow, happen in the full Hilbert space. The operators $\mathcal{P}$, represented as the red arrows, projects this dynamic onto a "slow" subspace depicted here as a blue rectangle. By construction, the starting point of the dynamics, visualized with the green dot, is located on the projected subspace.

the memory kernel, is dissipative.[61] The formulation of the memory kernel as the autocorrelation of the random forces is a result of the equilibrium state of the system and is known as the second fluctuation–dissipation theorem.[53] It is important to note that there is no approximation leading to Eq. (17) so that it is an exact description of the dynamics of the system. However, the main difficulty in solving this equation comes from the memory kernel of Eq. (15), for which the dynamics is not generated by the Liouville operator, but by its orthogonal projection.

III. THE GLE IN QP SPACE

Up to this point, we have been working in real space. To formulate the problem in reciprocal space, there is a freedom of choice for the basis set into which we will project the dynamical variables. A natural projection is one where the conservative part of the GLE is block diagonal in momentum and completely diagonal in vibrational modes, all while taking advantage of the periodicity of the crystal. Such a transformation can be achieved using concepts from the toolkit of harmonic phonon theory.

With this goal, we define a generalized dynamical matrix $\mathbf{D}(\mathbf{q})$ as the Fourier transform of the mass weighted $\boldsymbol{\Theta}$,

$$\mathbf{D}_{ij}(\mathbf{q}) = \sum_{\tau} \frac{\Theta_{0,i}^{\tau,j}}{\sqrt{M_i M_j}} e^{i\mathbf{q}(\langle \mathbf{R}_{\tau j}\rangle - \langle \mathbf{R}_{0 i}\rangle)}, \quad (18)$$

where we introduced a unit cell based notation $i \to (\tau, i)$ so that $\Theta_{\delta,i}^{\tau,j}$ is the frequency matrix relating atom i in the unit cell δ to the atom j in unit cell τ. Similarly to the harmonic phonon case, we can now obtain QP polarization vectors $\boldsymbol{\epsilon}^{\nu}(\mathbf{q})$ and frequencies $\Omega_{\mathbf{q},\nu}$ by diagonalizing $\mathbf{D}(\mathbf{q})$,

$$\mathbf{D}(\mathbf{q})\boldsymbol{\epsilon}^{\nu}(\mathbf{q}) = \Omega_{\nu}^2(\mathbf{q})\boldsymbol{\epsilon}^{\nu}(\mathbf{q}), \quad (19)$$

where ν is a QP mode. Without loss of generality, we can now express the mass-weighted atomic displacements as

$$\tilde{u}_i(t) = \sum_{\mathbf{q},\lambda} \rho_{\mathbf{q},\lambda} \epsilon_i^{\lambda}(\mathbf{q}) A_{\lambda}(\mathbf{q}, t), \quad (20)$$

where $A_{\lambda}(\mathbf{q}, t)$ are unitless quasiparticle operators with the property $\left(A_{\lambda}(\mathbf{q}), A_{\lambda'}(\mathbf{q}')\right) = \frac{2k_B T}{\hbar \Omega_{\lambda}(\mathbf{q})}\delta_{\lambda\lambda'}\delta_{\mathbf{q},\mathbf{q}'}$ [65] and $\rho_{\mathbf{q},\lambda}$ is a prefactor determined below. Using the static solution of Eq. (17) as well as the property $\ddot{G}_{ij}(0) = -k_B T/M_i \delta_{ij}$ [66,67] we can express the static mass-weighted displacement covariance tensor as

$$\left(\tilde{u}_i, \tilde{u}_j\right) = k_B T \sqrt{M_i M_j}\Theta_{ij}^{-1}. \quad (21)$$

Injecting Eq. (20) into this equation and with some reorganization, it can be shown that $\rho_{\mathbf{q},\lambda} = \sqrt{\hbar/\Omega_{\lambda}(\mathbf{q})}$ so that the displacements can be expressed as

$$u_i(t) = \sqrt{\frac{\hbar}{2M_i}}\sum_{\mathbf{q},\lambda} \frac{\epsilon_i^{\lambda}(\mathbf{q})}{\sqrt{\Omega_{\lambda}(\mathbf{q})}} A_{\lambda}(\mathbf{q}, t). \quad (22)$$

We can now define a Kubo transformed QP Green's function

$$\mathbf{G}_{\lambda,\mu}(\mathbf{q}, t) = \left(A_{\lambda}(\mathbf{q}), A_{\mu}(\mathbf{q}, t)\right). \quad (23)$$

To obtain the expression of the memory kernel projected on the QP, we note that from Eq. (22), the force acting on nucleus i can be expressed as

$$f_i = \sqrt{\frac{\hbar M_i}{2}}\sum_{\mathbf{q}\lambda} \frac{\epsilon_i^{\lambda}(\mathbf{q})}{\sqrt{\Omega_{\lambda}(\mathbf{q})}} \ddot{A}_{\lambda}(\mathbf{q}). \quad (24)$$

The part of the random forces involving the frequency matrix has a structure resembling mass-scaled harmonic forces, which can be written in terms of quasiparticle operators as

$$\sum_{j\beta} \frac{\Theta_{ij}^{\alpha\beta}}{\sqrt{M_i M_j}} u_j^{\beta} = \sqrt{\frac{\hbar M_i}{2}}\sum_{\mathbf{q}\lambda} \frac{\epsilon_i^{\lambda}(\mathbf{q})}{\sqrt{\Omega_{\lambda}(\mathbf{q})}} \Omega_{\lambda}^2(\mathbf{q})A_{\lambda}(\mathbf{q}). \quad (25)$$

Consequently, we can define the random forces in terms of QP operators as

$$\delta f_i = \sqrt{\frac{\hbar M_i}{2}}\sum_{\mathbf{q},\lambda} \frac{\epsilon_i^{\lambda}(\mathbf{q})}{\sqrt{\Omega_{\lambda}(\mathbf{q})}}\left(\ddot{A}_{\lambda}(\mathbf{q}) - \Omega_{\lambda}^2(\mathbf{q})A_{\lambda}(\mathbf{q})\right)$$
$$= \sqrt{\frac{\hbar M_i}{2}}\sum_{\mathbf{q},\lambda} \frac{\epsilon_i^{\lambda}(\mathbf{q})}{\sqrt{\Omega_{\lambda}(\mathbf{q})}}\delta A_{\lambda}(\mathbf{q}), \quad (26)$$

where we defined the QP random forces operator $\delta A_{\lambda}(\mathbf{q}) = \ddot{A}_{\lambda}(\mathbf{q}) - \Omega_{\lambda}^2(\mathbf{q})A_{\lambda}(\mathbf{q})$, which follows orthogonal time dynamics

$$\delta A_{\lambda}(\mathbf{q}, t) = e^{i\mathcal{QL}t}\delta A_{\lambda}(\mathbf{q}). \quad (27)$$

We are now able to define the memory kernel in reciprocal space

$$\mathbf{K}(\mathbf{q}, t) = \frac{\hbar}{k_B T}\boldsymbol{\Omega}(\mathbf{q})^{-1}\left(\delta\mathbf{A}(\mathbf{q}), \delta\mathbf{A}(\mathbf{q}, t)\right), \quad (28)$$

which allows us to write the GLE for the Kubo transformed Green's function as

$$\ddot{\mathbf{G}}(\mathbf{q}, t) = -\boldsymbol{\Omega}^2(\mathbf{q})\mathbf{G}(\mathbf{q}, t) - \int_0^t ds\,\mathbf{K}(\mathbf{q}, s)\dot{\mathbf{G}}(\mathbf{q}, t - s). \quad (29)$$

The dynamical properties of the many-body system can now be obtained by solving Eq. (29) with the initial conditions

$$G_{\lambda\mu}(\mathbf{q}, 0) = \frac{2k_B T}{\hbar\Omega_{\lambda}(\mathbf{q})}\delta_{\lambda,\mu}, \quad (30)$$

$$\dot{G}_{\lambda\mu}(\mathbf{q}, 0) = 0. \quad (31)$$

IV. VIBRATIONAL SPECTRA FROM THE KUBO CORRELATION FUNCTION

From linear response theory, it is known that the correlations of an unperturbed system are related to its response to a perturbation.[53,62,68] For a perturbation applied to an observable A, the response of the system through the observable B can be computed using the response function Φ_{AB}, which we define as

$$\Phi_{AB}(t) = -\frac{i}{\hbar}\langle [A, B(t)]\rangle, \quad (32)$$

25 June 2025 05:47:22

where the average of the commutator of A and $B(t)$ is called the symmetrized correlation function. The dynamical susceptibility of the system is then simply given by the Laplace transform of the response function

$$\chi_{AB}(\omega) = \int_0^\infty dt \Phi_{AB}(t) e^{-i\omega t}. \qquad (33)$$

It should be noted that the use of a Laplace transform with the definition Eq. (32) allows to include causality in the response of the system. This formulation is equivalent to more common definitions of the susceptibility where causality is introduced with the use of the Heaviside function. To connect the preceding derivation to the response function, we need to express $\Phi_{AB}(t)$ as a function of the KCF. This can be achieved using the cyclic property of the trace, which gives a classical-like formulation of the response function

$$\begin{aligned}
\Phi_{AB}(t) &= -\frac{i}{\hbar}\frac{1}{\mathcal{Z}}\Big(\text{Tr}\big[e^{-\beta H} A B(t) \big] - \text{Tr}\big[e^{-\beta H} B(t) A \big] \Big) \\
&= \frac{i}{\hbar}\frac{1}{\mathcal{Z}}\Big(\text{Tr}\big[e^{-\beta H} e^{\beta H} A e^{-\beta H} B(t) \big] - \text{Tr}\big[e^{-\beta H} A B(t) \big] \Big) \\
&= \int_0^\beta d\lambda \frac{1}{\mathcal{Z}} \text{Tr}\big[e^{-\beta H} \dot{A}(i\hbar\lambda) B(t) \big] \\
&= \beta \dot{G}_{AB}(t),
\end{aligned} \qquad (34)$$

where $\dot{A} = i[H, A]/\hbar$ is the time derivative of A at $t = 0$.

From this response function, the dynamical susceptibility of the system is simply obtained by applying a Laplace transform

$$\begin{aligned}
\chi_{AB}(\omega) &= \beta \int_0^\infty dt \big(\dot{A}, B(t)\big) e^{-i\omega t} \\
&= \beta \widetilde{\dot{G}}_{AB}(i\omega) \\
&= i\beta\omega \widetilde{G}_{AB}(i\omega) - \beta G_{AB}(0),
\end{aligned} \qquad (35)$$

with $\widetilde{G}_{AB}(i\omega)$ the Laplace transform of the KCF of A and B, and $\widetilde{\dot{G}}_{AB}(i\omega)$ is the Laplace transform of its time derivative. The dynamical susceptibility can be decomposed into a real and imaginary part $\chi_{AB}(\omega) = \chi'_{AB}(\omega) + i\chi''_{AB}(\omega)$, where $\chi'_{AB}(\omega)$ and $\chi''_{AB}(\omega)$ are related by a Kramers–Kronig transform, meaning that the knowledge of one is sufficient to recover the dynamical response of the system. From Eq. (35), we see that the imaginary part of the dynamical susceptibility, which corresponds to the dissipative part of the response, is simply proportional to the real part of $\widetilde{G}_{AB}(\omega)$. Since the KCF is an even and real function of time, this real part is proportional to the power spectrum $G_{AB}(\omega)$, which corresponds to the Fourier transform of $G_{AB}(t)$, so that the dissipative part of the response, also called the spectral function, can be written as

$$\chi''_{AB}(\omega) = \frac{\omega}{2k_B T} G_{AB}(\omega). \qquad (36)$$

This equation is simply the fluctuation–dissipation theorem, written using the Kubo transformed correlation function. The trace of the dissipation $\chi''(\mathbf{q}, \omega)$ is particularly important since this quantity can be linked to the cross section $d^2\sigma/d\Omega dE$ from spectroscopy

measurements, allowing thus a direct comparison between theory and experiment. For the QP KCF, using the initial conditions [Eqs. (30) and (31)], the Laplace transform is expressed as

$$\widetilde{\mathbf{G}}(\mathbf{q}, i\omega) = \frac{2k_B T}{\hbar\Omega(\mathbf{q})} \frac{-i\omega - \tilde{\mathbf{K}}(\mathbf{q}, i\omega)}{\omega^2 - \Omega^2(\mathbf{q}) - i\omega\tilde{\mathbf{K}}(\mathbf{q}, i\omega)}. \qquad (37)$$

To obtain a formula for the Fourier transform of $\mathbf{G}(\mathbf{q}, \omega)$, we start by separating the memory kernel into a real and an imaginary part as $\tilde{\mathbf{K}}(\mathbf{q}, i\omega) = \tilde{\mathbf{\Gamma}}(\mathbf{q}, \omega) - i\tilde{\mathbf{\Delta}}(\mathbf{q}, \omega)$. Since $\mathbf{K}(\mathbf{q}, t)$ is a real and even function of time, the real part $\tilde{\mathbf{\Gamma}}(\mathbf{q}, \omega)$ of its Laplace transform is proportional to its Fourier transform $\mathbf{\Gamma}(\mathbf{q}, \omega)$, with $\tilde{\mathbf{\Gamma}}(\mathbf{q}, \omega) = 2\mathbf{\Gamma}(\mathbf{q}, \omega)$. Moreover, $\tilde{\mathbf{\Gamma}}(\mathbf{q}, \omega)$ and $\tilde{\mathbf{\Delta}}(\mathbf{q}, \omega)$ are not independent, and one can recover the other using Kramers–Kronig relations.[69] For instance, $\tilde{\mathbf{\Delta}}(\mathbf{q}, \omega)$ can be computed with

$$\tilde{\mathbf{\Delta}}(\mathbf{q}, \omega) = \frac{1}{\pi} \int d\omega' \frac{\tilde{\mathbf{\Gamma}}(\mathbf{q}, \omega')}{\omega' - \omega}, \qquad (38)$$

where the absence of the usual minus sign comes from the previous definition of the memory kernel. This allows us to take the real part of Eq. (37) and obtain the power spectrum as

$$\mathbf{G}(\mathbf{q}, \omega) = \frac{k_B T}{\pi\hbar} \frac{8\Omega(\mathbf{q})\mathbf{\Gamma}(\mathbf{q}, \omega)}{(\omega^2 - \Omega^2(\mathbf{q}) - 2\omega\Delta(\mathbf{q}, \omega))^2 + 4\omega^2\mathbf{\Gamma}^2(\mathbf{q}, \omega)}. \qquad (39)$$

Finally, the dissipative part of the response function can be computed using the fluctuation–dissipation theorem of Eq. (36), giving

$$\chi''(\mathbf{q}, \omega) = \frac{1}{\pi\hbar} \frac{4\omega\Omega(\mathbf{q})\mathbf{\Gamma}(\mathbf{q}, \omega)}{(\omega^2 - \Omega^2(\mathbf{q}) - 2\omega\Delta(\mathbf{q}, \omega))^2 + 4\omega^2\mathbf{\Gamma}^2(\mathbf{q}, \omega)}. \qquad (40)$$

In the end, the dynamical response of the system can be entirely characterized using $\Omega(\mathbf{q})$, $\mathbf{\Gamma}(\mathbf{q}, \omega)$, and $\Delta(\mathbf{q}, \omega)$. Consequently, at this point, the only missing ingredient needed to compute the dynamical properties of the system is the real part of the memory kernel.

V. MODE-COUPLING APPROXIMATION FOR THE MEMORY KERNEL

For the moment, the formulation is exact and consists only in a rewriting of the dynamical problem, by framing the unsolvable part into a memory kernel. The exact computation of $\mathbf{K}(t)$ is a formidable task and we have to resort to approximations to be able to apply the theory to real simulations. To obtain a tractable formulation of the memory kernel, we use a cluster expansion of the random forces. With this goal, we define the nth order projection operators $\mathcal{P}_n$,[70] which project an operator $O(t)$ on the subspace of n QP operators, as well as the corresponding orthogonal projection $\mathcal{Q}_n$,

$$\mathcal{P}_n O(t) = \frac{1}{n!} \sum_{\substack{\lambda_1 \ldots \lambda_n \\ \lambda'_1 \ldots \lambda'_n}} \frac{\big(A_{\lambda'_1} \ldots A_{\lambda'_n}, O(t)\big)}{\big(A_{\lambda_1} \ldots A_{\lambda_n}, A_{\lambda'_1} \ldots A_{\lambda'_n}\big)} A_{\lambda_1} \ldots A_{\lambda_n}, \qquad (41)$$

$$\mathcal{Q}_n = 1 - \mathcal{P}_n, \qquad (42)$$

where the prefactor $1/n!$ is here to account for all the permutations of A_λ operators so that $\mathcal{P}_n \mathcal{P}_n = \mathcal{P}_n$. Going up to order N and inserting several times the identity $\mathcal{P}_n + \mathcal{Q}_n = 1$, we can rewrite the random forces

$$\begin{aligned}
\delta A_\lambda &= (\mathcal{P}_2 + \mathcal{Q}_2)\delta A_\lambda \\
&= \mathcal{P}_2 \delta A_\lambda + (\mathcal{P}_3 + \mathcal{Q}_3)\mathcal{Q}_2 \delta A_\lambda \\
&= \sum_n^N \mathcal{P}_n \delta_{n-1} A_\lambda + \delta_N A_\lambda,
\end{aligned} \tag{43}$$

$$\delta_N A_\lambda = \mathcal{Q}_N \mathcal{Q}_{N-1} \ldots \mathcal{Q}_2 \delta A_\lambda, \tag{44}$$

where each successive application of $\mathcal{Q}_n$ will produce an ever smaller $\delta_n A_\lambda$, and $\delta_N A_\lambda$ is the final residual random force we will neglect. We can now inject this expression into the memory kernel to obtain

$$\begin{aligned}
K^{\lambda,\lambda'}(t) &= (\delta A_\lambda, \delta A_{\lambda'}(t)) \\
&= \sum_{n=2}^N \sum_{n'=2}^N (\mathcal{P}_n \delta_{n-1} A_\lambda, \mathcal{P}_{n'} \delta_{n'-1} A_{\lambda'}(t)) \\
&\quad + (\delta_N A_{\lambda'}, \delta_N A_{\lambda'}(t)) \\
&= \sum_{n=2}^N \sum_{n'=2}^N K_{nn'}^{\lambda,\lambda'}(t) + (\delta_N A_\lambda, \delta_N A_{\lambda'}(t)),
\end{aligned} \tag{45}$$

where we define the (n, n') order memory kernel

$$\begin{aligned}
K_{n,n'}^{\lambda,\lambda'}(t) &= (\mathcal{P}_n \delta_{n-1} A_\lambda, \mathcal{P}_{n'} \delta_{n'-1} A_{\lambda'}(t)) \\
&= \sum_{\substack{\lambda_1,\ldots,\lambda_n \\ \lambda'_1,\ldots,\lambda'_{n'}}} \Psi_n(\lambda, \lambda_1, \ldots, \lambda_n) \Psi_{n'}(\lambda', \lambda'_1, \ldots, \lambda'_{n'}) \\
&\quad \times (A_{\lambda_1} \ldots A_{\lambda_n}, e^{i\mathcal{QL}t} A_{\lambda'_1} \ldots A_{\lambda'_{n'}})
\end{aligned} \tag{46}$$

as well as the vertex

$$\Psi_n(\lambda_1, \ldots, \lambda_n) = \frac{1}{n!} \sum_{\mu_1,\ldots,\mu_n} \frac{(A_{\mu_1} \ldots A_{\mu_n}, \delta_{n-1} A_\lambda)}{(A_{\lambda_1} \ldots A_{\lambda_n}, A_{\mu_1} \ldots A_{\mu_n})}. \tag{47}$$

The preceding manipulations serve to shift the orthogonal space time dependence from the random forces into multiple displacement Kubo correlation functions. By subtracting the contributions up to order n, the $\mathcal{Q}_n$ projectors minimize the corresponding contribution of the random forces $\delta_n A_\lambda$. Consequently, this "clustering" procedure ensures that the contribution of each new order in the memory kernel is less important than the previous one. While this is still impossible to solve in practice, this rewriting opens a way to approximate $\mathbf{K}(\mathbf{q}, t)$.

As a first approximation, we truncate the expansion of the memory kernel at some order N and we neglect the Nth order correlation of the random forces. The second approximation consists in decoupling the n point correlations in orthogonal time into $n/2$ products of two point correlations in real time.[58,59,61] For instance, a four point correlation function is given by

$$\begin{aligned}
(A_{\lambda_1} A_{\lambda_2}, e^{i\mathcal{QL}t} A_{\lambda_3} A_{\lambda_4}) &\approx (A_{\lambda_1}, A_{\lambda_3}(t))(A_{\lambda_2}, A_{\lambda_4}(t)) \\
&\quad + (A_{\lambda_1}, A_{\lambda_4}(t))(A_{\lambda_2}, A_{\lambda_3}(t)).
\end{aligned} \tag{48}$$

These two approximations are at the foundation of the mode-coupling theory of the liquid–glass transition.[58,59]

In this work, we will limit ourselves to the second order in the memory kernel expansion. To simplify further the expression of the memory kernel, we will neglect its off-diagonal terms ($n \neq n'$, $\lambda \neq \lambda'$). We note that this approximation does not remove mode coupling [the sum in Eq. (46) runs over all the other modes] and would not prevent the inclusion of off-diagonal velocity terms in the thermal conductivity as in Ref. 71. Finally, taking into account the conservation of crystal momentum (with the $-\lambda$), our approximation for the memory kernel is given by

$$K_\lambda(t) \approx \frac{\hbar}{2k_B T \Omega_\lambda} \sum_{\mu,\nu} |\Psi(-\lambda, \mu, \nu)|^2 G_\mu(t) G_\nu(t). \tag{49}$$

The only inputs are contained in the vertex Ψ. We define the third-order tensor Θ as

$$\Theta_{ijk} = -\frac{1}{2} \frac{\sum_{l,m}(u_l u_m, \delta f_i)}{\sum_{l,m}(u_j u_k, u_l u_m)}. \tag{50}$$

Using the projection of displacements and random forces on QP, the vertex can then be expressed as

$$\begin{aligned}
\Psi(\lambda, \mu, \nu) &= \sqrt{\frac{\hbar}{2} \frac{\Omega_\lambda}{\Omega_\mu \Omega_\nu}} \sum_{i,j,k} \frac{\epsilon_i^\lambda \epsilon_j^\mu \epsilon_k^\nu}{\sqrt{M_i M_j M_k}} \Theta_{ijk} \\
&\quad \times e^{i(\mathbf{R}_i \mathbf{q}_\lambda + \mathbf{R}_j \mathbf{q}_\mu + \mathbf{R}_k \mathbf{q}_\nu)} \delta_\mathbf{G}(\mathbf{q}_\lambda + \mathbf{q}_\mu + \mathbf{q}_\nu),
\end{aligned} \tag{51}$$

where $\delta_\mathbf{G}(\mathbf{q}_\lambda + \mathbf{q}_\mu + \mathbf{q}_\nu) = 1$ if $\mathbf{q}_\lambda + \mathbf{q}_\mu + \mathbf{q}_\nu$ is 0 modulo a reciprocal lattice vector $\mathbf{G}$.

With the preceding approximation of $\mathbf{K}$, we now have all the ingredients to compute the power spectrum. Fourier transforming Eq. (49) in frequency domain, and using Eqs. (38) and (39), we obtain the following set of self-consistent equations:

$$\Gamma_\lambda(\omega) = \frac{\hbar}{2k_B T \Omega_\lambda} \sum_{\mu,\nu} |\Psi(-\lambda, \mu, \nu)|^2 (G_\mu * G_\nu)(\omega), \tag{52}$$

$$\Delta_\lambda(\omega) = \frac{1}{\pi} \int d\omega' \frac{\Gamma_\lambda(\omega')}{\omega' - \omega}, \tag{53}$$

$$G_\lambda(\omega) = \frac{k_B T}{\pi \hbar} \frac{8\Omega_\lambda \Gamma_\lambda(\omega)}{(\omega^2 - \Omega_\lambda^2 - 2\omega\Delta_\lambda(\omega))^2 + 4\omega^2 \Gamma_\lambda^2(\omega)}. \tag{54}$$

In order to obtain a starting point to the self-consistent cycle, we introduce an approximation inspired by scattering theory. We begin by defining a bare Green's function as the solution of a memory-less GLE

$$\ddot{G}_{\lambda,0}(t) = -\Omega_\lambda^2 G_{\lambda,0}(t), \tag{55}$$

which is simply given by $G_{\lambda,0}(t) = \frac{k_B T}{\hbar \Omega_\lambda} \cos(\Omega_\lambda t)$. The scattering theory approximation is obtained by replacing the Green's function in Eq. (52) by $G_{\lambda,0}(\omega)$, which allows to obtain the linewidth

$$\Gamma_\lambda^s(\omega) = \frac{\pi k_B T}{\hbar \Omega_\lambda \Omega_\mu \Omega_\nu} \sum_{\mu,\nu,s,s'} |\Psi(-\lambda, \mu, \nu)|^2 \delta(\omega + s\Omega_\mu + s'\Omega_\nu) \tag{56}$$

with $s, s' = \pm 1$. From this result, a first approximation to the power spectrum can be obtained by using Eqs. (53) and (54) with $\Gamma_\lambda^s(\omega)$ as an input.

VI. COMPUTING THE FREQUENCIES AND VERTEX FROM (PI)MD SIMULATIONS

One advantage of the formalism derived previously is that only static averages are needed as input. This is particularly interesting for applications given that the static KCF of two variables A and B can be computed exactly in the path-integral molecular dynamics framework as[49,63]

$$G_{AB}(0) = \lim_{P \to \infty} \lim_{t \to \infty} \int_0^t \frac{e^{-\beta H(t)}}{\mathcal{Z}} \left(\sum_p^P A_p(t) \right) \left(\sum_p^P B_p(t) \right) dt$$
$$\approx \frac{1}{N} \sum_n^N \bar{A}(t_n) \bar{B}(t_n), \qquad (57)$$

where P is the number of beads in the classical polymer, and $\bar{A}(t) = \sum_p A_p(t)$ is the mean of the property A over the classical polymer. The second line of Eq. (57) corresponds to the approximation with a finite number of configurations and beads from path integral molecular dynamics.

The static correlation function of classical MD simulations corresponds to the limit $P = 1$ and can be computed as

$$G_{AB}(0) \approx \frac{1}{N} \sum_n^N A(t_n) B(t_n). \qquad (58)$$

We note that this can be used as a way to approximate the static KCF, as will be discussed on the next section.

In the limit of a finite number N of configurations, the frequency matrix can be computed with

$$\Theta_{ij} = -\frac{\sum_n^N \sum_k \bar{u}_k(t_n) \bar{f}_i(t_n)}{\sum_n^N \sum_k \bar{u}_k(t_n) \bar{u}_j(t_n)}, \qquad (59)$$

where we used the property $(u_i, f_j) = -k_B T \delta_{ij}$ to decouple the sums in the numerator and denominator of Eq. (13). In this equation, one can recognize the least squares solution $\boldsymbol{\Theta}$ of the linear problem $\boldsymbol{\Theta u} = -\mathbf{f}$. This implies that the computation of the frequency matrix can be mapped to the problem of fitting an effective harmonic Hamiltonian using the distribution of forces and displacements at the studied temperature. This corresponds to the TDEP method at second order,[37] for which our framework offers an exact formal justification and a path for generalization. In practice, the average needed in the computation of $\boldsymbol{\Theta}$ might necessitate long simulations, which could become prohibitive. Fortunately, $\boldsymbol{\Theta}$ is a sparse matrix, with many coefficients related by symmetry, as it must be invariant under the symmetry group of the crystal. Moreover, since the displacements and forces are invariant with respect to global translation and rotation of the system, their static KCF should also respect these invariances. This means that, by definition, $\boldsymbol{\Theta}$ follows the usual symmetries found in the IFC tensor of the harmonic approximation for phonons. Consequently, imposing them on $\boldsymbol{\Theta}$ before applying Eq. (59) will considerably decrease the length of the simulations needed, similarly to what is done in lattice dynamic fitting

methods.[38,72–74] A similar analysis can be done for the second order vertex in real space, which can be computed as

$$\Theta_{ijk} = -\frac{1}{2} \sum_n^N \frac{\sum_{l,m} \bar{u}_l(t_n) \bar{u}_m(t_n) \delta \bar{f}_i(t_n)}{\sum_{l,m} \bar{u}_l(t_n) \bar{u}_m(t_n) \bar{u}_j(t_n) \bar{u}_k(t_n)} \qquad (60)$$

with $\delta f_i = f_i + \sum_j \Theta_{ij} u_j$. A simple variable transformation allows to rewrite this equation as a least-squares solution of the equation $\boldsymbol{\Theta}^T \mathbf{U} = \delta \mathbf{f}$, where $\mathbf{U} = \mathbf{u} \mathbf{u}^T$.[39,74] As in the frequency matrix case, this means that this interaction can be constructed exactly as the third-order IFC in the TDEP method. It can be shown that this TDEP-like construction arises naturally for every order, by definition of the nth order projectors $\mathcal{P}_n$.

VII. DISCUSSION

A. Classical-like correlation functions and classical limit

Looking at the main results in the preceding derivation, it would be easy to miss the quantum character of the dynamics described, since most of the equations seem to lack the usual quantum-related prefactors. The quantum behavior of the system is hidden in the Kubo correlation function, as can be inferred from its Lehmann representation given by

$$G_\lambda(\omega) = k_B T \sum_{jk} p_j \frac{|\langle j|A_\lambda|k\rangle|^2}{\hbar \omega (n(\omega) + 1)} \delta\left(\omega - \frac{E_j - E_k}{\hbar}\right), \qquad (61)$$

where $p_j = e^{-\beta E_j}/\mathcal{Z}$ is the Boltzmann weight associated with state j of energy E_j and $n(\omega) = 1/(e^{\beta \hbar \omega} - 1)$ is the Bose–Einstein distribution. Consequently, our approach allows to alleviate any ambiguity related to the type of quantum correlation functions one should use in PIMD simulations, all while giving a consistent formulation of the dynamics of the system.

Interestingly, the classical limit of this mode-coupling approach is completely analogous to its quantum counterpart.[60] Indeed, the classical version of the Mori–Zwanzig formalism is obtained by simply replacing the KCF with classical correlation functions. Using the similarity between the properties of Kubo and classical correlation functions, the same derivation can be used to obtain the classical version of the set of self-consistent Eq. (52)–(54). Therefore, the only difference between the quantum and classical description comes from the type of correlation functions used to compute the frequency matrix $\boldsymbol{\Theta}$ and the vertex. This classical-like behavior is particularly visible in the KCF formulation of the quantum fluctuation–dissipation theorem given by Eq. (36), which is exactly the same as its classical limit.[62] This observation brings a new justification to the interpretation of classical correlation functions as approximated KCF.[47] From a practical point of view, and as discussed in the previous section, this means that the same set of equations can be used in the two limits, the only difference stemming from the type of simulation used to compute the correlation functions.

Furthermore, our approach allows for a simple inclusion of quantum behavior when doing classical simulations. For this, we

introduce the lesser Green's function $G_\lambda^<(t) = \langle A_\lambda^\dagger(t) A_\lambda \rangle$, given in the Lehmann representation by

$$G_\lambda^<(\omega) = \sum_{jk} p_j e^{-\beta \hbar \omega} |\langle j|A_\lambda|k\rangle|^2 \delta\left(\omega - \frac{E_j - E_k}{\hbar}\right). \qquad (62)$$

From this representation, it is easy to see that the Kubo and lesser Green's functions are related by $G_\lambda^<(\omega) = \frac{\hbar\omega}{k_BT} n(\omega) G_\lambda(\omega)$. Replacing the Kubo Green's functions in Eq. (52) with the lesser Green's functions makes the Bose–Einstein distributions visible in the following equation:

$$\Gamma_\lambda(\omega) = \frac{\hbar}{2k_BT\Omega_\lambda} \sum_{\mu,\nu} |\Psi(-\lambda, \mu, \nu)|^2$$
$$\times \int_{-\infty}^\infty d\omega' \frac{k_BT}{\hbar(\omega - \omega') n(\omega - \omega')} G_\lambda^<(\omega - \omega')$$
$$\times \frac{k_BT}{\hbar\omega' n(\omega')} G_\lambda^<(\omega'). \qquad (63)$$

In the scattering theory approximation, $G_\lambda^<(t) = n(\Omega_\lambda)\cos(\Omega_\lambda t)$ so that $\Gamma_\lambda^s(\omega)$ reduces to

$$\Gamma_\lambda^s(\omega) = \frac{\hbar\pi}{4k_BT\Omega_\lambda} \sum_{\mu,\nu} |\Psi(-\lambda, \mu, \nu)|^2 F(\omega, \mu, \nu), \qquad (64)$$

$$F(\omega, \mu, \nu) = \sum_{s=\pm1} \left[(n_\mu + n_\nu + 1)\delta(\omega + s\Omega_\mu + s\Omega_\nu) \right.$$
$$\left. + (n_\mu - n_\nu)\delta(\omega + s\Omega_\mu - s\Omega_\nu) \right] \qquad (65)$$

with $n_\mu = n(\Omega_\mu)$, and where we used $\lim_{\omega\to0} 1/[\hbar\omega n(\omega)] = \beta$. Once Ψ has been calculated, using Eq. (64) to process inputs from MD simulations is a simple zero-cost and legitimate way to approximate quantum effects without needing to do expensive PIMD simulations. Such an approximation should be valid for systems with low anharmonicity or at high temperature.

B. Interpretation of the static quasiparticles

With the previous discussions, we focused on dynamical properties. It is interesting to also consider static properties associated with the formalism, in particular the quasiparticle frequencies. Interestingly, these temperature-dependent frequencies have often been compared with great success to experiments,[35,37,43] but these comparisons lacked a rigorous theoretical justification. It has been proposed to interpret these frequencies as an approximation of the first excitation of the system.[49,75] While such an approximation would be accurate at low temperature, it does not hold for high temperature and completely misses the exact character associated with the quantity.[75]

Taking the $\omega \to 0$ limit of Eq. (35), the static susceptibility can be written as $\chi = -\beta G(0)$. From Eq. (13) and using the property $(u_i, f_j) = -k_BT\delta_{ij}$, we obtain a proportionality relation between the frequency matrix and the inverse static susceptibility in real space

$$\frac{\Theta}{\sqrt{\mathbf{M}^T \mathbf{M}}} = \chi^{-1}, \qquad (66)$$

meaning that the frequency matrix is directly related to the instantaneous response of the system to an external perturbation. By doing

the transformation in Sec. III, and due to the Hermitian character of the matrices involved, we can conclude that the quasiparticle polarizations $\epsilon_\lambda(\mathbf{q})$ are also eigenvectors of the Fourier transform of the susceptibility matrix, with eigenvalues $\hbar\Omega_\lambda^{-2}(\mathbf{q})$. From this observation, we can interpret the eigenvectors $\epsilon^\lambda(\mathbf{q})$ of the quasiparticles as displacement patterns associated with a perturbation with a momentum $\mathbf{q}$. The $A_\lambda(\mathbf{q})$ are thus the amplitude of these displacement patterns, which can be seen as a temperature-dependent generalization of the normal modes of the harmonic theory.

To have a better understanding of the meaning of these frequencies, it is useful to focus on the second order time derivative of the KCF. From the relation $\ddot{G}_{ij} = k_BT$, and using Eqs. (22) and (24), we have $\ddot{G}_\lambda(\mathbf{q})/G_\lambda(\mathbf{q}) = \Omega_\lambda^2(\mathbf{q})$. Using then the Lehmann representation of the KCF $G_\lambda(\mathbf{q})$ and $\ddot{G}_\lambda(\mathbf{q})$,

$$G_\lambda(\mathbf{q}) = k_BT \sum_{jk} \frac{|\langle j|A_\lambda(\mathbf{q})|k\rangle|^2 (p_k - p_j)}{\omega_{jk}}, \qquad (67)$$

$$\ddot{G}_\lambda(\mathbf{q}) = k_BT \sum_{jk} \frac{\langle j|A_\lambda(\mathbf{q})|k\rangle\langle k|\ddot{A}_\lambda(\mathbf{q})|j\rangle (p_k - p_j)}{\omega_{jk}}$$
$$= k_BT \sum_{jk} \frac{\omega_{jk}^2 |\langle j|A_\lambda(\mathbf{q})|k\rangle|^2 (p_k - p_j)}{\omega_{jk}} \qquad (68)$$

with $\omega_{jk} = (E_j - E_k)/\hbar$, and where we used $\langle j|\ddot{A}_\lambda(\mathbf{q})|k\rangle = -\omega_{jk}^2\langle j|A_\lambda(\mathbf{q})|k\rangle$, we obtain a formulation of the frequencies in terms of a complete set of eigenstates of the Hamiltonian

$$c_{jk}(\lambda, \mathbf{q}) = \frac{|\langle j|A_\lambda(\mathbf{q})|k\rangle|^2 (p_k - p_j)}{\omega_{jk}}, \qquad (69)$$

$$\Omega_\lambda(\mathbf{q}) = \sqrt{\frac{\sum_{jk} \omega_{jk}^2 c_{jk}(\lambda, \mathbf{q})}{\sum_{jk} c_{jk}(\lambda, \mathbf{q})}}. \qquad (70)$$

This result shows that the quasiparticle frequencies correspond to a thermodynamic average of the transitions between states of the system projected on the displacement patterns.

It should be noted that these frequencies do not necessarily align with peaks in the spectral functions. Indeed, the relation between the static frequencies and the spectral function is given by the sum rule

$$\int_0^\infty d\omega \chi_\lambda''(\mathbf{q}, \omega)\omega = \Omega_\lambda(\mathbf{q}). \qquad (71)$$

Consequently, the peaks and the static frequencies should be aligned only in the case of a symmetric lineshape or at least in cases where the spectral weight is evenly distributed around Ω_λ.

C. Comparison with other methods

To help understanding the implication of the mode-coupling theory of lattice dynamics, it is informative to compare it to well established methods. In this section, we show that the perturbation theory, the SCHA and the TDEP method can be understood as different approximations of the mode-coupling approach, that we summarize in Table I.

25 June 2025 05:47:22

TABLE I. Summary of different approach of anharmonic lattice dynamics.

	Perturbation theory	SCHA	Mori–Zwanzig
Sampling of displacements	Perturbative through finite difference or DFPT	Effective harmonic (multivariate Gaussian)	Exact through MD (classical case) or PIMD (quantum case)
Static quasiparticles	Harmonic phonons	Effective harmonic phonons or eigenstates of the inverse susceptibility	Eigenstates of the inverse susceptibility
Vertex in the bubble contribution	Perturbative	Gaussian approximation	Exact
Implementations	Phono3py[15] ShengBTE[16]	SSCHA[30] Alamode[27,28] sTDEP[76] qSCAILD[31]	MD-TDEP[37,38]

1. The harmonic limit

A good theory of lattice dynamics should reduce to the exactly known harmonic limit. This can be trivially shown to be true for the mode-coupling theory. Indeed, for a harmonic system, the frequency matrix presented in Eq. (13) is equal to the harmonic force constants so that the random forces cancel out. Consequently, the GLE reduces to the expected memory-less harmonic equations of motion.

2. Perturbation theory

More interestingly, it can be shown that the perturbative limit of the mode-coupling approach allows us to retrieve the usual linewidth formulation obtained from a diagrammatic expansion.[11,13] To show this, we suppose that the potential energy of the system can be approximated by an anharmonic potential truncated to third order

$$V(\mathbf{R}) \approx \frac{1}{2} \sum_{ij} \Theta_{ij}^{\mathrm{pt}} u_i u_j + \frac{1}{3!} \sum_{ijk} \Psi_{ijk}^{\mathrm{pt}} u_i u_j u_k, \tag{72}$$

$$\Theta_{ij}^{\mathrm{pt}} = \frac{\partial^2 V(\mathbf{R})}{\partial R_i \partial R_j}, \tag{73}$$

$$\Psi_{ijk}^{\mathrm{pt}} = \frac{\partial^3 V(\mathbf{R})}{\partial R_i \partial R_j \partial R_k}, \tag{74}$$

where we assume that contributions from Ψ_{ijk}^{pt} are perturbations with respect to $\Theta_{ij}^{\mathrm{pt}}$ so that averages can be taken with respect to the harmonic contribution. In this approximation, the frequency matrix is equal to the second order force constants Θ^{pt} and the memory kernel can be written

$$K_{ij}^{\mathrm{pt}}(t) = \sum_{klmn} \Psi_{ikl}^{\mathrm{pt}} \Psi_{jmn}^{\mathrm{pt}} \left(u_k u_l, e^{-i\mathcal{Q}\mathcal{L}t} u_m u_n \right), \tag{75}$$

which corresponds to the $(2, 2)$-order memory kernel defined in real space, but with third-order force constants instead of the full vertex. From this observation, the derivation of the phonon quasiparticles follows the same route as the more general Mori–Zwanzig theory. In the end, the main difference between the perturbation and mode-coupling theories lies in the definition of the quasiparticles and in the strength of the vertex $\Psi(\lambda, \mu, \nu)$. In order to quantitatively reconcile experimental observations and theoretical predictions for properties such as thermal conductivity, these renormalizations are important. Indeed, while the temperature dependence of QP frequencies is known to have a large impact on this kind of quantity,[77] the deviations brought by scattering renormalization can be of similar magnitude and have the potential to remove the expected high temperature trend $\kappa \propto T^{-\alpha}$, as shown in Refs. 78–80.

From a diagrammatic derivation to lowest-order, this dynamical contribution is given by the bubble diagram represented in Fig. 2(a). Doing a naive comparison, it would seem that the other lowest-order diagrams, known as the tadpole [Fig. 2(b)] and the loop [Fig. 2(c)], are missing from the mode-coupling theory. However, the absence of these diagrams is correct, and a consequence of some exact properties of this approach. By construction, the Mori–Zwanzig projection formalism used in Sec. II C results in a conservative contribution that gives the *exact* static part of the Kubo Green's function. The tadpole and loop diagrams are purely real so that their contributions to the Green's function only result in a shift of the static terms.[11,28] From this observation, one can infer that the frequencies $\Omega_\lambda(\mathbf{q})$ already include all static diagrams to all orders. Adding any static diagram, such as the loop or the tadpole, would result in an over-correction, thus explaining their absence from the lowest-order mode-coupling approximation.
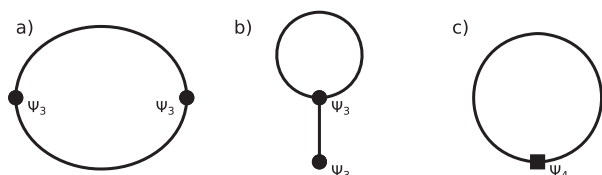
FIG. 2. Feynman diagrams appearing in the self-energy in perturbation theory to lowest order. Each line represents a propagator, while dots and squares are, respectively, third and fourth order vertices. (a) The bubble, (b) the tadpole, and (c) the loop. In the mode-coupling approach presented here, we observe only bubble-like contributions in the memory kernel.

25 June 2025 05:47:22

Even if the approaches are quite similar, we should expect the mode-coupling theory to have a wider range of validity than bare perturbation theory. Indeed, being constructed on a truncated expansion of the Hamiltonian with respect to displacements, perturbation theory is known to fail for systems with strong anharmonicity. In these systems, the high-order contributions to the Hamiltonian can be of similar—or even higher—magnitude than the harmonic contribution. This is because the perturbative nature of the high order contributions is only a supposition, and there is no guarantee that this holds in general.[17,21,81] On the contrary, the projection operators of Eqs. (8) and (41) are constructed so that effects of higher order correlations are minimized. Such a construction allows the mode-coupling theory to be valid even in strongly anharmonic systems. One should note that the use of linear response theory for this kind of system is not a problem for the Mori–Zwanzig approach, as the linearity is assumed in the response of the system to a weak probe, not in the behavior of the system itself.

3. Self-consistent harmonic approximation

The self-consistent harmonic approximation is a workhorse for the study of anharmonic crystals. The method is based on the minimization of the Gibbs–Bogoliubov free energy $\widetilde{\mathcal{F}}$ defined as

$$\widetilde{\mathcal{F}} = \widetilde{\mathcal{F}}_0 + \langle V(\mathbf{R}) - \widetilde{V}(\mathbf{R}) \rangle_0, \tag{76}$$

where $\widetilde{V}(\mathbf{R})$ is an effective potential, $\widetilde{\mathcal{F}}_0$ is its associated free energy, and $\langle O \rangle_0$ is an average computed within the distribution associated with $\widetilde{V}(\mathbf{R})$. As the name of the method implies, the effective potential has a harmonic form

$$\widetilde{V}(\mathbf{R}) = (\mathbf{R} - \mathcal{R})^{\mathrm{T}} \Theta^{\mathrm{SCHA}} (\mathbf{R} - \mathcal{R}), \tag{77}$$

where the effective force constants Θ^{SCHA} and equilibrium positions $\mathcal{R}$ are parameters to optimize. The advantage of such a potential is that the distribution of displacements around $\mathbf{R}$ is a multivariate Gaussian. Consequently, the sampling of atomic positions to compute averages is greatly simplified compared to the true potential. Using Jensen's inequality, it can be shown that the Gibbs–Bogoliubov is an upper bound to the real free energy $\mathcal{F} < \widetilde{\mathcal{F}}$[82] so that optimizing the parameters means minimizing $\widetilde{\mathcal{F}}$. For the effective force constants, the minimum is obtained when

$$\Theta_{ij}^{\mathrm{SCHA}} = \left\langle \frac{\partial^2 V(\mathbf{R})}{\partial u_i \partial u_j} \right\rangle_0, \tag{78}$$

while the effective equilibrium positions are optimized when the average difference of true and harmonic forces is zero. In practice, the minimization is done self-consistently, and several approaches and implementations can be found in the literature.[26–31,76]

After the minimization, while the effective force constants can be used to approximate quasiparticles, a more consistent result is obtained by using the Hessian Ξ of the free energy[29,30]

$$\Xi_{ij} = \frac{\partial^2 \widetilde{\mathcal{F}}}{\partial \mathcal{R}_i \partial \mathcal{R}_j}. \tag{79}$$

By seeing the Gibbs–Bogoliubov free energy as a Landau expansion with an order parameter $\mathcal{R}$, the free energy Hessian Ξ can be understood as the inverse static susceptibility. However, compared to the

mode-coupling approach, where this quantity is exact, χ^{-1} is approximated in the SCHA, as only the contribution from the first-order free energy cumulant enters in $\widetilde{\mathcal{F}}$.

On top of the quasiparticles computed from the free energy Hessian, the dynamical susceptibility can be obtained with a bubble-like contribution[29,30] in which the vertices are computed using the average of the third-order derivative of the potential energy

$$\Psi_{ijk}^{\mathrm{SCHA}} = \frac{1}{\sqrt{M_i M_j M_k}} \left\langle \frac{\partial^3 V(\mathbf{R})}{\partial R_i \partial R_j \partial R_k} \right\rangle_0$$
$$= -\frac{1}{\sqrt{M_i M_j M_k}} \sum_{lm} \frac{\langle u_l u_m f_k \rangle_0}{\langle u_i u_l \rangle_0 \langle u_j u_m \rangle_0}, \tag{80}$$

where the second line can be derived with an integration by parts. This procedure can also be compared with our mode-coupling theory. To show this, we start by assuming that we can approximate the real distribution with the Gaussian associated with Θ^{SCHA}. With this assumption, the frequency matrix is actually given by the SCHA force constants Θ^{SCHA}, and the random forces are given with by $\delta f_i = f_i + \sum_j \Theta_{ij}^{\mathrm{SCHA}} u_j$. Applying the mode-coupling decomposition of Sec. V to approximate $\mathbf{K}^{\mathrm{SCHA}}(t)$, it is then simple to show that the vertex appearing in the (2,2)-order memory kernel in real space is given by Eq. (80), as the average of an odd number of displacements cancels out with the Gaussian average. From this observation, we can conclude that the bubble-like dynamical contribution in the SCHA is an approximation of the mode-coupling theory.

To summarize, two approximations enter in the SCHA compared to the mode-coupling theory. The first one concerns the static frequencies, which are approximated by the effective harmonic frequencies corrected by a first-order cumulant of the free energy. The second one is in the vertices in the bubble contribution, which are computed on the basis of a Gaussian approximation. From a computational point-of-view, the SCHA bears the important advantage of a lower cost due to its simplified sampling compared to (PI)MD. This is particularly true for the inclusion of nuclear quantum effects, which can be added in a simple way. However higher-order corrections and applications to strongly anharmonic (and hence non-Gaussian) systems are more delicate to justify.

4. Average of the Hessian

In the literature, it has been proposed to define a generalization of the harmonic force constants through an average of the potential energy Hessian[49]

$$\Pi_{ij} = \left\langle \frac{\partial^2 V(\mathbf{R})}{\partial R_i \partial R_j} \right\rangle, \tag{81}$$

where the only difference with the SCHA force constants of Eq. (78) lies in the Hamiltonian used to compute the average. From the harmonic limit, where Π_{ij} reduces to the harmonic force constants, and the similarity with Eq. (78), this generalization seems like a sensible choice. However, it is constructed on the equality $\Pi_{ij} = \Theta_{ij}$ that only holds in a harmonic system.

To highlight the differences between this formulation and the mode-coupling theory, the potential energy Hessian average can be expanded in terms of force–force KCF,[49]

$$\Pi_{ij} = \frac{(f_i, f_j)}{k_B T}. \tag{82}$$

Using this equation, the static part of memory kernel can be formulated as

$$K_{ij}(0) = \Pi_{ij} - \Theta_{ij}. \tag{83}$$

Since $\mathbf{K}$ is a positive definite matrix,[69] this equation tells us that $\mathbf{\Pi}$ is greater that $\mathbf{\Theta}$, meaning that frequencies computed from the diagonalization of the average Hessian will overestimate the Ω_λ. This result shows that while formulations based on the SCHA and on the true distribution by means of (PI)MD are similar, they are not interchangeable.

5. Temperature dependent effective potential

TDEP is a method based on the construction of an effective anharmonic potential of the form (here presented up to third order)

$$\widetilde{V}(\mathbf{R}) = \frac{1}{2} \sum_{ij} \Theta_{ij}^{\text{TDEP}} u_i u_j + \frac{1}{3!} \sum_{ijk} \Psi_{ijk}^{\text{TDEP}} u_i u_j u_k. \tag{84}$$

The temperature dependence in this potential is introduced through a successive fitting of each order. First, using a set of positions and forces distributed according to a given temperature, the second order interatomic force constants Θ_{ij} are fit using ordinary least-squares. Then, the third order force constants Ψ_{ijk} are fit on the residual of the forces. In principle, this successive fitting can be continued to any order, though usual applications of the method truncate the potential at the third or fourth order.

In applications of TDEP, two approaches have been used to generate the set of positions and forces. In the original works,[37,38] which we will call MD-TDEP, MD simulations are used. In the second one, sometimes called sTDEP (for stochastic TDEP), the displacements are computed from an effective harmonic model. In the latter case, the set of forces and displacements have to be constructed self-consistently by refitting the second order potential from the set of the previous iteration.

It is important to differentiate the approaches. On one hand, sTDEP is simply an implementation of the SCHA, since the self-consistent least-squares fit allows to minimize the Gibbs–Bogoliubov free energy in Eq. (77). On the other hand, by using the real distribution, MD-TDEP is an implementation of the mode-coupling theory. Indeed, as has already been discussed in Sec. VI, the force constants Θ^{TDEP} and Ψ^{TDEP} computed from the TDEP methods are equal to the frequency matrix Θ and the real space vertex Ψ. Consequently, the perturbation theory usually applied to compute the spectral function is equivalent to the scattering approximation of mode-coupling theory [Eq. (64)] if only the bubble term is used. As this is the case for most applications of TDEP in the literature, we have a large number of examples showing the accuracy of the mode-coupling approach. For instance, the method has been used successfully to explain the anomalous neutron scattering of SnTe and PbTe,[83] to study the phase transition of GeTe[84] or the phase diagram of uranium[85,86] as well as many other phenomena for highly anharmonic systems.[40,87–89] Our work provides

a theoretical justification for the results of these studies, as well as a generalization, allowing to include quantum effects through the use of PIMD and to include higher order corrections.

D. Markovian approximation and Lorentzian lineshape

In the limit of small anharmonicity, the spectral lineshapes are often approximated with Lorentzians.[7,15,90] An interesting conclusion to be taken from the presented theory is that such a solution cannot be an exact representation of the dynamics of the nuclei. In the Lorentzian approximation, the frequency dependency of the lifetime is neglected and $\Gamma(\omega)$ is approximated with a constant given by $\Gamma_\lambda = \Gamma_\lambda(\Omega_\lambda)$.[15] In the Mori–Zwanzig formalism presented here, such Lorentzian spectra would appear in the context of a Markovian approximation of the memory kernel.[54] In this case, where it is assumed that $\mathbf{K}(t)$ decays very quickly compared to $\mathbf{G}(t)$, the memory kernel can be replaced by a constant friction term $\mathbf{\Gamma}^M(\mathbf{q}) = \beta \int_0^\infty dt \mathbf{K}(\mathbf{q}, t)$ so that the Kubo transformed Green's function is written as

$$\ddot{\mathbf{G}}(\mathbf{q}, t) = -\mathbf{\Omega}^2(\mathbf{q})\mathbf{G}(\mathbf{q}, t) - \mathbf{\Gamma}^M(\mathbf{q})\dot{\mathbf{G}}(\mathbf{q}, t) \tag{85}$$

with solutions

$$\mathbf{G}(\mathbf{q}, t) = \cos(\mathbf{\Omega}(\mathbf{q})t) e^{-\mathbf{\Gamma}^M(\mathbf{q})t}. \tag{86}$$

However, it can be observed that this solution is not an even function of time, as requested for the KCF. For instance, in a Markovian approximation, the property $\frac{d\mathbf{G}(t)}{dt}\big|_{t=0} = 0$ would not be respected. This means that a Markovian approximation, and consequently a Lorentzian approximation, will never fully represent the dynamics of the system.

Nevertheless, for mildly anharmonic systems, the Markovian limit of the GLE should still be a reliable approximation, and Lorentzian-like lineshapes are frequently observed in spectroscopy measurements. Consequently, a derivation of the inputs needed for such an approximation is of interest in order to provide an efficient way to compute the dynamical properties of a system of nuclei from (PI)MD.

VIII. APPLICATIONS

To demonstrate the accuracy of the theory developed here, we apply it to the fcc phase of ^{4}He. Due to its very small atomic mass, helium is known to show strong nuclear quantum effects (NQE) making it an archetypal example of a quantum crystal.[92] Indeed, the zero-point motion in solid helium is large enough to make the system explore the BOS far beyond the range of applicability of the harmonic approximation. This unusual behavior manifests itself in the largest Lindemann ratio (i.e., $\sqrt{\langle u^2 \rangle}/a$ with $\langle u^2 \rangle$ the mean squared atomic displacement and a the lattice parameter) of any material observed at cryogenic temperature.[92] The high anharmonicity in helium, which can be found in other rare gas solids, is what started the field of anharmonic lattice dynamics and spawned the development of theories, such as the SCHA.[4,22,23,93]

Given these properties, this system represents a perfect case to illustrate that both NQE and strong anharmonicity can be captured with our mode-coupling approach. To emphasize this point, we

performed numerical simulations in a fully quantum setting using PIMD as well as classical MD simulations. For the sake of comparison, we also performed simulations using both the SCHA and perturbation theory. To allow for a comparison with inelastic neutron scattering results,[91] all simulations were run at a temperature of 38 K and with a molar volume of 9.03 mol^3/mol, which correspond to a lattice parameter of 3.915 Å.

To describe the BOS of helium, we use the Aziz pair potential,[94] as it offers an accurate representation of the solid phases of helium at low pressure.[92] PIMD and MD simulations were done using the implementation of the Langevin thermostat in Large-scale Atomic/Molecular Massively Parallel Simulator (LAMMPS)[95] for a duration of 125 ps with a timestep of 0.5 fs in both cases and 64 beads for the PIMD. To compute the frequency matrix and

the second order vertex in real space, we used the recursive least-square fit presented in Sec. VI. After projecting these tensors on QP following Subsection III, we solved the mode-coupling theory equations in the scattering approximation using the greater and lesser Green's function formalism of Subsection VII A. For this step, a $12 \times 12 \times 12$ **q**-point grid was sufficient to obtain converged results. We note that for both PIMD and MD results, the memory kernel is obtained within a quantum formalism, though NQE are included in the frequency matrix and second order vertex only in the PIMD case. For the SCHA, we used the stochastic TDEP approach presented in Subsection VII C 5 with Bose–Einstein occupations in order to capture NQE.

Before presenting the spectral properties of ^{4}He, we first assess the anharmonicity of the system. To this end, we adopt a
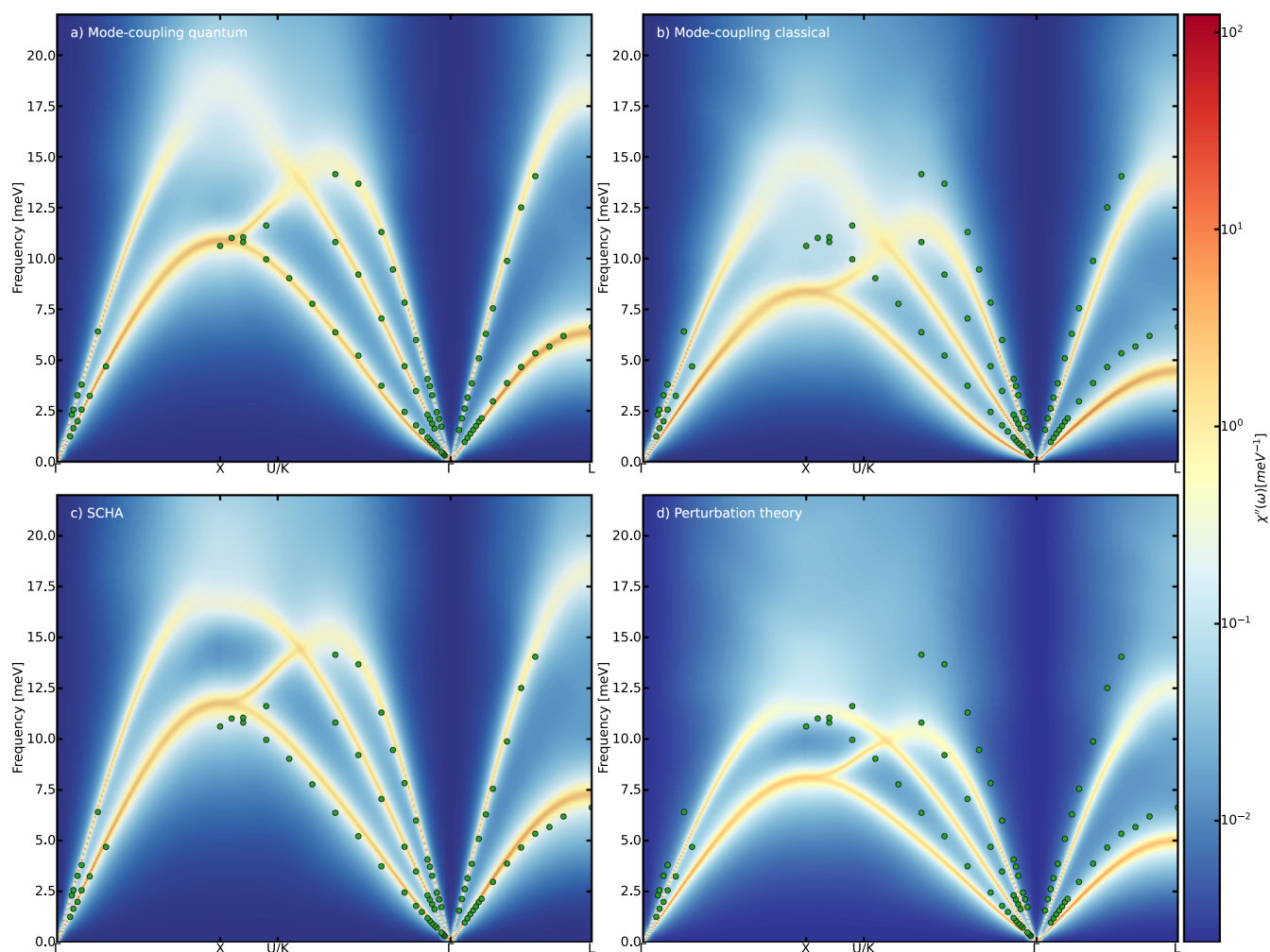
FIG. 3. Spectral function $\chi''(\omega)$ of fcc ^{4}He at 9.03 cm^3/mol and 38 K computed with the mode-coupling approach in the scattering-like approximation. The frequency matrix and second order vertex were computed using PIMD for (a), classical MD for (b), the SCHA for (c), and through perturbation theory for (d). The green dots are from inelastic neutrons scattering experiment.[91]

recently proposed measure of anharmonicity[5] to our Mori–Zwanzig formalism as

$$\sigma^A = \sqrt{\frac{\sum_i \langle \delta f_i^2 \rangle}{\sum_i \langle f_i^2 \rangle}}. \tag{87}$$

We note, however, that used in this way σ^A is not strictly a measure of anharmonicity since the frequency matrix already goes beyond the harmonic contribution of the BOS. It is more accurate to see σ^A as a measure of the dissipative contribution to the dynamics of the system. For fcc ^{4}He, we find $\sigma^A = 0.62$ when computed with PIMD, which would indicate a very dissipative system. Similarly, using a formulation based on the frequency matrix,[74] we find a Debye temperature of 174 K, close to the indirect experimental estimation of 154 K.[91] At 38 K, this means that zero-point motion is expected to be important. Coupled with the high σ^A, this confirms that the He system is a stringent test for the ability of the mode-coupling theory to capture both NQE and anharmonicity.

For each of the simulations, the theoretical spectra are presented in Fig. 3 where they are compared with inelastic neutron scattering results.[91] Among all the results, PIMD mode coupling presents the best agreement with experiment, with peaks of the theoretical spectral function fully aligning with the experimental phonon frequencies. On the contrary, the classical MD case severely underestimates phonon frequencies for all reciprocal space directions. This underestimation is even more important when using (harmonic, 0 K based) perturbation theory, showing the need to go to nonperturbative methods for an accurate description of this system. The spectra computed with the SCHA presents a good agreement with experimental data, even though a slight overestimation is observed compared to the PIMD mode-coupling results, especially for the transverse modes in the $\Gamma - U$ and $\Gamma - L$ directions.

It is interesting to ask why, even with the strong Gaussian approximation, the SCHA still gives an accurate description of the quasiparticle frequencies, while the classical MD completely disagrees with experimental results. To answer this question, we plot in Fig. 4 the density of first neighbor distances computed with MD, PIMD and the SCHA. This figure allows us to highlight the effects of NQE on the system. Indeed, comparing MD and PIMD results, the former presents a high skewness directed to large distances, while the inclusion of zero-point motion in the latter results in a
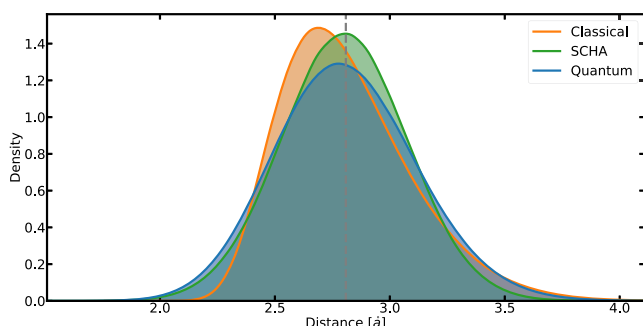
FIG. 4. Distribution of first neighbor distances in fcc ^{4}He at 38 K. The vertical grey bar corresponds to the equilibrium distance.
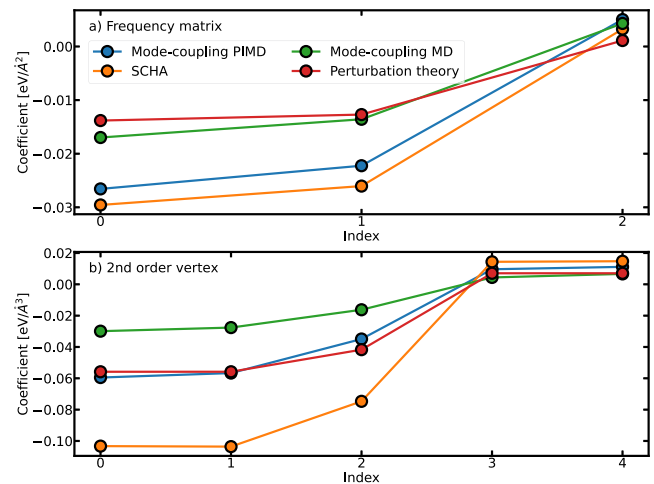
FIG. 5. Coefficients entering the (a) frequency matrix and (b) the second order vertex in the first shell of interactions computed with PIMD, MD, SCHA, and perturbation theory.

partial re-symmetrization of the density. Because of this, the tails of the PIMD and SCHA densities are similar, even though their areas differ, indicating a close to symmetric yet non-Gaussian distribution for the displacements in PIMD. In the end, the differences in exploration of the BOS strongly impact the generalized IFC. This is illustrated in Fig. 5 which compares the symmetry-irreducible coefficients entering the frequency matrix and second order vertex in the first shell of interactions. If the SCHA and PIMD frequency matrix coefficients are quite close, their magnitudes are almost twice those computed with MD, which explains the softer frequencies observed within the classical mode-coupling theory. The difference of ensemble sampling used is even more marked for the second order vertex. Comparing the vertex coefficients for the PIMD and SCHA cases, we observe that the harmonic perturbation theory is coincidentally close to the full PIMD results, while the SCHA has an almost doubled magnitude compared to PIMD. This implies that even if the SCHA has extended validity for effective QP frequencies thanks to NQE, higher order quantities will still be strongly biased by the Gaussian starting point.

From this application, it is clear that the method used to compute the frequency matrix and the interaction vertex significantly impact the resulting generalized susceptibility. In future works, it will be interesting to meticulously compare the effects of the sampling strategies in different regimes of anharmonicity. Moreover, while we limited ourselves to the scattering-like approximation, it remains to test the effects of the self-consistent solution of the mode-coupling equations, especially on systems where the QP picture is broken and the spectral function is strongly non-Lorentzian in shape.

IX. CONCLUSION

In summary, we have developed a non-perturbative theory of lattice dynamics based on the Mori–Zwanzig projection oper-

ator formalism. We derived a generalized Langevin equation for the displacement Kubo correlation functions, resulting in an exact description of the dynamics of the system in terms of a conservative part, driven by the frequency matrix Θ, and a dissipative part, driven by the memory kernel $\mathbf{K}(t)$. From the real space formulation of the dynamics, we were able to project this GLE into a quasiparticle basis, thus giving an equation of motion in reciprocal space. Using linear response theory, we then derived an exact formulation for the vibrational spectrum, in terms of the spectral function $\chi''(\omega)$. In order to approximate the memory kernel, we developed a systematic expansion inspired by mode-coupling theory, in which every new order is constructed to minimize higher-order contributions. By truncating this expansion to lowest order, we obtain a set of self-consistent equations for the memory kernel. Within this mode coupling approach, the only inputs needed are the *static* KCFs, and we show how to compute them from path-integral or classical molecular dynamics simulations.

Our Mori–Zwanzig approach to lattice dynamics, being based on the KCF, takes into account the quantum nature of nuclei. Consequently, this derivation demonstrates how to obtain vibrational properties of quantum systems from PIMD. Moreover, the classical-like nature of the equations derived allows us to justify the use of classical MD to perform vibrational spectroscopy when quantum effects are not relevant, for instance for systems with heavy nuclei or at high temperature. We also compare our mode-coupling scheme to more standard perturbation theory, which allows us to derive a scattering-like approximation to the memory kernel. Our approach gives physical meaning to the temperature-dependent phonons that appear in numerous recent works. Moreover, we are able to relate the mode-coupling theory to other approaches for anharmonic lattice dynamics. Notably, we show that in the perturbative limit, the presented theory is equivalent to the usual diagrammatic formulation to lowest order, and that the SCHA can be seen as a Gaussian averaged approximation of it. We also showed that the TDEP method used in conjunction with (PI)MD is a direct application of the mode-coupling theory, provided that static corrections to the frequencies are *not* applied, as they would double-count interactions. These comparisons treat all of the main theories for anharmonic lattice dynamics in a unified formalism, and give a better vision of their inter-relationships, strengths, and limits. The Mori–Zwanzig formalism also allows us to show that while the commonly used Lorentzian approximation for lineshapes can be a useful approximation, it can never be an exact description of the lattice dynamics. Finally, we apply the mode-coupling theory on fcc ^{4}He to demonstrate its ability to describe both strong anharmonicity and NQE in quantum crystals, in comparison with other theories of anharmonic lattice dynamics.

The mode-coupling theory of lattice dynamics should apply to a more general class of strongly anharmonic and/or quantum systems, where standard methods are known to fail. For instance, while we limited ourselves here to crystalline materials, the formalism only requires well defined equilibrium positions so that it would be straightforward to adapt the theory to disordered solids such as alloys or glasses. This framework can serve as a starting point for new formulations of related properties such as the thermal conductivity,[57,71,90,96,97] which will be the focus of future work.

AUTHOR DECLARATIONS

Conflict of Interest

The authors have no conflicts to disclose.

Author Contributions

Aloïs Castellano: Investigation (equal); Methodology (equal); Software (equal); Writing – original draft (equal); Writing – review & editing (equal). **J. P. Alvarinhas Batista**: Methodology (equal); Writing – original draft (equal); Writing – review & editing (equal). **Matthieu J. Verstraete**: Methodology (supporting); Writing – original draft (supporting); Writing – review & editing (equal).

DATA AVAILABILITY

The data that support the findings of this study are openly available in github at https://github.com/OrbitalC/ModeCouplingTheoryPhononsData.

REFERENCES

[1] M. Born and K. Huang, *Dynamical Theory of Crystal Lattices* (Oxford University Press, 1954).

[2] M. T. Dove, *Introduction to Lattice Dynamics* (Cambridge University Press, 1993).

[3] B. Fultz, Prog. Mater. Sci. **55**, 247 (2010).

[4] M. L. Klein and G. K. Horton, J. Low Temp. Phys. **9**, 151 (1972).

[5] F. Knoop, T. A. R. Purcell, M. Scheffler, and C. Carbogno, Phys. Rev. Mater. **4**, 083809 (2020).

[6] G. Grimvall, B. Magyari-Köpe, V. Ozoliņš, and K. A. Persson, Rev. Mod. Phys. **84**, 945 (2012).

[7] P. B. Allen, Mod. Phys. Lett. B **34**, 2050025 (2019).

[8] A. Glensk, B. Grabowski, T. Hickel, and J. Neugebauer, Phys. Rev. Lett. **114**, 195901 (2015).

[9] D. S. Kim, O. Hellman, N. Shulumba, C. N. Saunders, J. Y. Y. Lin, H. L. Smith, J. E. Herriman, J. L. Niedziela, D. L. Abernathy, C. W. Li, and B. Fultz, Phys. Rev. B **102**, 174311 (2020).

[10] P. B. Allen, Phys. Rev. B **92**, 064106 (2015).

[11] A. A. Maradudin and A. E. Fein, Phys. Rev. **128**, 2589 (1962).

[12] K. N. Pathak, Phys. Rev. **139**, A1569 (1965).

[13] R. A. Cowley, Rep. Prog. Phys. **31**, 123 (1968).

[14] D. A. Broido, A. Ward, and N. Mingo, Phys. Rev. B **72**, 014308 (2005).

[15] A. Togo, L. Chaput, and I. Tanaka, Phys. Rev. B **91**, 094306 (2015).

25 June 2025 05:47:22

[16] W. Li, J. Carrete, N. A Katcho, and N. Mingo, Comput. Phys. Commun. **185**, 1747 (2014).

[17] N. K. Ravichandran and D. Broido, Phys. Rev. X **10**, 021063 (2020).

[18] T. Sun, X. Shen, and P. B. Allen, Phys. Rev. B **82**, 224304 (2010).

[19] T. Sun and P. B. Allen, Phys. Rev. B **82**, 224305 (2010).

[20] Y. Xia, V. I. Hegde, K. Pal, X. Hua, D. Gaines, S. Patel, J. He, M. Aykol, and C. Wolverton, Phys. Rev. X **10**, 041029 (2020).

[21] X. Yang, T. Feng, J. Li, and X. Ruan, Phys. Rev. B **105**, 115205 (2022).

[22] T. R. Koehler, Phys. Rev. Lett. **17**, 89 (1966).

[23] N. R. Werthamer, Phys. Rev. B **1**, 572 (1970).

[24] N. K. Ravichandran and D. Broido, Phys. Rev. B **98**, 085205 (2018).

[25] K. Esfarjani and Y. Liang, *Nanoscale Energy Transport* (IOP Publishing, 2020), pp. 7-1–7-35.

[26] P. Souvatzis, O. Eriksson, M. Katsnelson, and S. Rudin, Comput. Mater. Sci. **44**, 888 (2009).

[27] T. Tadano and S. Tsuneyuki, Phys. Rev. B **92**, 054301 (2015).

[28] T. Tadano and S. Tsuneyuki, J. Phys. Soc. Jpn. **87**, 041015 (2018).

[29] R. Bianco, I. Errea, L. Paulatto, M. Calandra, and F. Mauri, Phys. Rev. B **96**, 014111 (2017).

[30] L. Monacelli, R. Bianco, M. Cherubini, M. Calandra, I. Errea, and F. Mauri, J. Phys.: Condens. Matter **33**, 363001 (2021).

[31] A. van Roekeghem, J. Carrete, and N. Mingo, Comput. Phys. Commun. **263**, 107945 (2021).

[32] P. Choquard, *The Anharmonic Crystal* (WA Benjamin, 1967).

[33] V. Samathiyakanit and H. R. Glyde, J. Phys. C: Solid State Phys. **6**, 1166 (1973).

[34] R. M. Levy, A. R. Srinivasan, W. K. Olson, and J. A. McCammon, Biopolymers **23**, 1099 (1984).

[35] L. T. Kong, G. Bartels, C. Campañá, C. Denniston, and M. H. Müser, Comput. Phys. Commun. **180**, 1004 (2009).

[36] L. T. Kong, Comput. Phys. Commun. **182**, 2201 (2011).

[37] O. Hellman, I. A. Abrikosov, and S. I. Simak, Phys. Rev. B **84**, 180301(R) (2011).

[38] O. Hellman, P. Steneteg, I. A. Abrikosov, and S. I. Simak, Phys. Rev. B **87**, 104111 (2013).

[39] O. Hellman and I. A. Abrikosov, Phys. Rev. B **88**, 144301 (2013).

[40] J. Klarbring, O. Hellman, I. A. Abrikosov, and S. I. Simak, Phys. Rev. Lett. **125**, 045701 (2020).

[41] A. B. Mei, O. Hellman, N. Wireklint, C. M. Schlepütz, D. G. Sangiovanni, B. Alling, A. Rockett, L. Hultman, I. Petrov, and J. E. Greene, Phys. Rev. B **91**, 054101 (2015).

[42] A. H. Romero, E. K. U. Gross, M. J. Verstraete, and O. Hellman, Phys. Rev. B **91**, 214310 (2015).

[43] D. Chaney, A. Castellano, A. Bosak, J. Bouchet, F. Bottin, B. Dorado, L. Paolasini, S. Rennie, C. Bell, R. Springell, and G. H. Lander, Phys. Rev. Mater. **5**, 035004 (2021).

[44] T. J. H. Hele, Mol. Phys. **115**, 1435 (2017).

[45] P. Schofield, Phys. Rev. Lett. **4**, 239 (1960).

[46] S. A. Egorov, K. F. Everitt, and J. L. Skinner, J. Phys. Chem. A **103**, 9494 (1999).

[47] R. Ramírez, T. López-Ciudad, P. Kumar P, and D. Marx, J. Chem. Phys. **121**, 3973 (2004).

[48] H. Y. Geng, J. Phys. Chem. C **126**, 19355 (2022).

[49] T. Morresi, L. Paulatto, R. Vuilleumier, and M. Casula, J. Chem. Phys. **154**, 224108 (2021).

[50] T. Morresi, R. Vuilleumier, and M. Casula, Phys. Rev. B **106**, 054109 (2022).

[51] H. Mori, Prog. Theor. Phys. **33**, 423 (1965).

[52] R. Zwanzig, Phys. Rev. **124**, 983 (1961).

[53] R. Kubo, Rep. Prog. Phys. **29**, 255 (1966).

[54] C. Hijón, P. Español, E. Vanden-Eijnden, and R. Delgado-Buscalioni, Faraday Discuss. **144**, 301 (2010).

[55] A. Carof, R. Vuilleumier, and B. Rotenberg, J. Chem. Phys. **140**, 124103 (2014).

[56] Z. Li, X. Bian, X. Li, and G. E. Karniadakis, J. Chem. Phys. **143**, 243128 (2015).

[57] A. Fiorentino and S. Baroni, "From Green-Kubo to the full Boltzmann kinetic approach to heat transport in crystals and glasses," Phys. Rev. B **107**, 054311 (2022).

[58] J. Bosse, W. Götze, and M. Lücke, Phys. Rev. A **17**, 434 (1978).

[59] D. R. Reichman and P. Charbonneau, J. Stat. Mech.: Theory Exp. **2005**, P05013.

[60] T. E. Markland, J. A. Morrone, K. Miyazaki, B. J. Berne, D. R. Reichman, and E. Rabani, J. Chem. Phys. **136**, 074511 (2012).

[61] L. M. C. Janssen, Front. Phys. **6**, 97 (2018).

[62] R. Kubo, M. Toda, and N. Hashitsume, *Statistical Physics II* (Springer, Berlin, Heidelberg, 1991).

[63] I. R. Craig and D. E. Manolopoulos, J. Chem. Phys. **121**, 3368 (2004).

[64] E. B. Brown, Phys. Rev. B **49**, 4305 (1994).

[65] While the choice of prefactor here can seem arbitrary, we use it to simplify comparison with other methods of anharmonic lattice dynamics.

[66] B. J. Braams and D. E. Manolopoulos, J. Chem. Phys. **125**, 124105 (2006).

[67] M. Rossi, M. Ceriotti, and D. E. Manolopoulos, J. Chem. Phys. **140**, 234116 (2014).

[68] R. Zwanzig, *Nonequilibrium Statistical Mechanics* (Oxford University Press, 2001).

[69] B. J. Berne and G. D. Harp, *Advances in Chemical Physics* (John Wiley and Sons, Inc., 1970), pp. 63–227.

[70] G. Szamel, J. Chem. Phys. **127**, 084515 (2007).

[71] M. Simoncelli, N. Marzari, and F. Mauri, Nat. Phys. **15**, 809 (2019).

[72] F. Eriksson, E. Fransson, and P. Erhart, Adv. Theory Simul. **2**, 1800184 (2019).

[73] F. Zhou, W. Nielson, Y. Xia, and V. Ozoliņš, Phys. Rev. B **100**, 184308 (2019).

[74] F. Bottin, J. Bieder, and J. Bouchet, Comput. Phys. Commun. **254**, 107301 (2020).

[75] R. Ramírez and T. López-Ciudad, J. Chem. Phys. **111**, 3339 (1999).

[76] N. Shulumba, O. Hellman, and A. J. Minnich, Phys. Rev. B **95**, 014302 (2017).

[77] Y. Xia, K. Pal, J. He, V. Ozoliņš, and C. Wolverton, Phys. Rev. Lett. **124**, 065901 (2020).

[78] Y. Zhu, Y. Xia, Y. Wang, Y. Sheng, J. Yang, C. Fu, A. Li, T. Zhu, J. Luo, C. Wolverton, G. J. Snyder, J. Liu, and W. Zhang, Research **2020**, 4589786.

[79] Z. Zeng, C. Zhang, Y. Xia, Z. Fan, C. Wolverton, and Y. Chen, Phys. Rev. B **103**, 224307 (2021).

[80] X. Yang, J. Tiwari, and T. Feng, Mater. Today Phys. **24**, 100689 (2022).

[81] T. Feng, L. Lindsay, and X. Ruan, Phys. Rev. B **96**, 161201(R) (2017).

[82] A. Decoster, J. Phys. A: Math. Gen. **37**, 9051 (2004).

[83] C. W. Li, O. Hellman, J. Ma, A. F. May, H. B. Cao, X. Chen, A. D. Christianson, G. Ehlers, D. J. Singh, B. C. Sales, and O. Delaire, Phys. Rev. Lett. **112**, 175501 (2014).

[84] D. Dangić, O. Hellman, S. Fahy, and I. Savić, npj Comput. Mater. **7**, 57 (2021).

[85] J. Bouchet and F. Bottin, Phys. Rev. B **95**, 054113 (2017).

[86] V. Ladygin, P. Korotaev, A. Yanilkin, and A. Shapeev, Comput. Mater. Sci. **172**, 109333 (2020).

[87] J. Ding, T. Lanigan-Atkins, M. Calderón-Cueva, A. Banerjee, D. L. Abernathy, A. Said, A. Zevalkink, and O. Delaire, Sci. Adv. **7**, eabg1449 (2021).

[88] L. Xie, J. H. Feng, R. Li, and J. Q. He, Phys. Rev. Lett. **125**, 245901 (2020).

[89] X. He, D. Bansal, B. Winn, S. Chi, L. Boatner, and O. Delaire, Phys. Rev. Lett. **124**, 145901 (2020).

[90] L. Isaeva, G. Barbalinardo, D. Donadio, and S. Baroni, Nat. Commun. **10**, 3853 (2019).

[91] J. Eckert, W. Thomlinson, and G. Shirane, Phys. Rev. B **16**, 1057 (1977).

[92] C. Cazorla and J. Boronat, Rev. Mod. Phys. **89**, 035003 (2017).

[93] V. Goldman, G. Horton, and M. Klein, Phys. Rev. Lett. **21**, 1527 (1968).

[94] R. A. Aziz, V. P. S. Nain, J. S. Carley, W. L. Taylor, and G. T. McConville, J. Chem. Phys. **70**, 4330 (1979).

[95] A. P. Thompson, H. M. Aktulga, R. Berger, D. S. Bolintineanu, W. M. Brown, P. S. Crozier, P. J. in 't Veld, A. Kohlmeyer, S. G. Moore, T. D. Nguyen, R. Shan, M. J. Stevens, J. Tranchida, C. Trott, and S. J. Plimpton, Comput. Phys. Commun. **271**, 108171 (2022).

[96] M. Simoncelli, N. Marzari, and F. Mauri, Phys. Rev. X **12**, 041011 (2022).

[97] G. Caldarelli, M. Simoncelli, N. Marzari, F. Mauri, and L. Benfatto, Phys. Rev. B **106**, 024312 (2022).

Paper II

3.2 Mode-coupling formulation of heat transport in anharmonic materials

Aloïs Castellano, JP Alvarinhas Batista, Olle Hellman, Matthieu J Verstraete

Publication Report

Contributions Summary:*Contributed to theory derivations, physical understanding and manuscript review*

Abstract

Temperature-dependent harmonic approximations generalize the ground-state phonon picture, and have found widespread use in computing the thermal properties of materials. However, applying these approaches to access the thermal conductivity still lacks a formal justification, in particular due to the use of perturbation theory. In this work, we derive a theory of heat transport in anharmonic crystals, using the mode-coupling theory of anharmonic lattice dynamics. Starting from the Green-Kubo formula, we develop the thermal conductivity tensor based on the system's dynamical susceptibility, or spectral function. Our results account for both the diagonal and off-diagonal contributions of the heat current, with and without collective effects. We implement our theory in the temperature-dependent effective potential (tdep) package, and have notably introduced a Monte Carlo scheme to compute phonon scattering due to third- and fourth-order interactions, achieving a substantial reduction in computational cost which enables full convergence of such calculations. We apply our methodology to systems with varying regimes of anharmonicity and thermal conductivity to demonstrate its universality. These applications highlight the importance of the phonon renormalization, and their interactions beyond the harmonic order. Overall, our work advances the understanding of thermal conductivity in anharmonic crystals and provides a theoretically robust framework for predicting heat transport in complex materials.

Mode-coupling formulation of heat transport in anharmonic materials

Aloïs Castellano [1], J. P. Alvarinhas Batista [1], Olle Hellman [2], and Matthieu J. Verstraete [1,3]

[1] *Nanomat Group, Q-MAT Research Center and European Theoretical Spectroscopy Facility, Université de Liège, allée du 6 août, 19, B-4000 Liège, Belgium*

[2] *Department of Molecular Chemistry and Materials Science, Weizmann Institute of Science, Rehovoth 76100, Israel*

[3] *ITP, Physics Department, Utrecht University 3508 TA Utrecht, The Netherlands*

Temperature-dependent harmonic approximations generalize the ground-state phonon picture, and have found widespread use in computing the thermal properties of materials. However, applying these approaches to access the thermal conductivity still lacks a formal justification, in particular due to the use of perturbation theory. In this work, we derive a theory of heat transport in anharmonic crystals, using the mode-coupling theory of anharmonic lattice dynamics. Starting from the Green-Kubo formula, we develop the thermal conductivity tensor based on the system's dynamical susceptibility, or spectral function. Our results account for both the diagonal and off-diagonal contributions of the heat current, with and without collective effects. We implement our theory in the temperature-dependent effective potential (TDEP) package, and have notably introduced a Monte Carlo scheme to compute phonon scattering due to third- and fourth-order interactions, achieving a substantial reduction in computational cost which enables full convergence of such calculations. We apply our methodology to systems with varying regimes of anharmonicity and thermal conductivity to demonstrate its universality. These applications highlight the importance of the phonon renormalizations, and their interactions beyond the harmonic order. Overall, our work advances the understanding of thermal conductivity in anharmonic crystals and provides a theoretically robust framework for predicting heat transport in complex materials.

I. INTRODUCTION

Fourier's law asserts that heat transport is characterized by the thermal conductivity which is an intrinsic material property relating the temperature gradient and heat current. This property is essential for selecting candidate materials in many technological applications, each requiring a specific range of thermal conductivity, either high, low, or "just right." For instance, the development of thermoelectric devices and barrier coatings demands materials with extremely low thermal conductivity [1,2]. Conversely, in applications which generate heat, such as electronic devices, batteries, or nuclear reactors, ensuring safe and controllable operating conditions necessitates the efficient removal of excess heat [3,4]. This can be achieved passively through the high thermal conductivity of the contact and heat sink materials. A theoretical understanding of the mechanisms underlying heat transport in materials is thus critical for fundamental science but also many applications.

In electrically insulating solids, the pioneering works of Hardy and Peierls have shown that heat is primarily transported by the vibrations of nuclei around their equilibrium positions. Within the harmonic approximation, these vibrations are quantized as quasiparticles called phonons. The Peierls-Boltzmann theory describes phonons as heat carriers that diffuse through materials collectively, with their transport limited by scattering due to other quasiparticles, boundaries, or defects [5,6]. Recently, the importance of another transport mechanism has been highlighted, where heat is carried through the wavelike tunneling of phonons to quasidegenerate

states. This mechanism, derivable from both the Hardy [7–10] and Wigner [11,12] formulations of the heat current, is particularly significant for systems with low thermal conductivity and complex crystal structures.

Accurately predicting a material's thermal conductivity thus ultimately comes down to the precise description of atomic vibrations and phonons. The harmonic approximation relies on a Taylor expansion of the Born-Oppenheimer surface, assuming that displacements around equilibrium positions are relatively small. Additionally, perturbation theory is often used to compute scattering mechanisms affecting phonon diffusion, and only converges if higher-order contributions to the potential energy are small compared to the harmonic part. However, these assumptions are not always valid in real materials [13,14]. This limits the predictive accuracy of the harmonic approximation. Recognizing this limitation, theories of temperature-dependent phonons have emerged, notably, the self-consistent harmonic approximation [15–18] and the temperature-dependent effective potential [19–21]. Both approaches involve renormalizing the bare harmonic phonons through nonperturbative interaction with a bath of all other phonons. These methods have been applied to many systems, showing significant improvement over harmonic or perturbative predictions, and highlighting the importance of including anharmonicity in the vibrational description of materials [22–27].

In recent work, we introduced the mode-coupling theory of anharmonic lattice dynamics [28], providing a formal justification for the temperature-dependent effective potential. This theory posits that the phonon bath originates from the full

dynamics of the many-body Hamiltonian. While applications of this methodology to compute thermal conductivity exist, they are based on formulas derived in a perturbative context, and a formal justification is still lacking.

In this work, we derive a theory of heat transport in anharmonic crystals based on the mode-coupling theory of anharmonic lattice dynamics. Our derivation applies heat current operators defined for anharmonic phonons in the Green-Kubo formula, allowing us to construct a theory founded on phonon correlation functions. Ultimately, we obtain a formulation of the thermal conductivity tensor that includes anharmonicity nonperturbatively, with both collective and coherent contributions. We describe the implementation of the theory in the open-source package temperature-dependent effective potential (TDEP) [29], emphasizing the reduction of computational cost, which is essential to be able to converge fully with complex unit cells and/or higher-order anharmonic coupling. Finally, we apply the method to several systems spanning different regimes of anharmonicity and thermal conductivity mechanisms.

The paper is organized as follows. In Sec. II, after introducing the mode-coupling theory of anharmonic lattice dynamics, we derive a heat current operator which is consistent with the theory. This operator is then injected in the Green-Kubo formula, enabling us to obtain formulations of the thermal conductivity tensor. We then discuss the improvement brought by our approach in Sec. III. Section IV presents our implementation of the theory in the TDEP package, focusing on approaches to reduce the computational cost. These methods include a linear algebra formulation of the scattering matrix elements, the irreducible representation of scattering triplets and quartets, and a Monte Carlo integration scheme for phonon scatterings. Finally, in Sec. V, we apply our formalism to several materials before concluding in Sec. VI.

II. DERIVATION

We consider a crystalline system within the framework of the Born-Oppenheimer approximation, where the system dynamics is described by the Hamiltonian

$$H = \sum_i \frac{\mathbf{P}_i^2}{2M_i} + V(\mathbf{R}), \tag{1}$$

where $\mathbf{R}$ and $\mathbf{P}$ are, respectively, the position and momentum operators and where $V(\mathbf{R})$ is the many-body potential. To incorporate quantum effects in the ionic motion, we utilize the quantum Liouvillian formalism, which describes the time evolution and derivative of an operator $\mathcal{O}$ as

$$\mathcal{O}(t) = e^{\frac{i}{\hbar} H t} \mathcal{O} e^{-\frac{i}{\hbar} H t} = e^{i\mathcal{L}t} \mathcal{O}, \tag{2}$$

$$\dot{\mathcal{O}}(t) = \frac{i}{\hbar}[H, \mathcal{O}(t)] = i\mathcal{L}\mathcal{O}(t), \tag{3}$$

where $\mathcal{L} = [H, \cdot]/\hbar$ is the Liouville superoperator.

We assume that ions oscillate around their equilibrium positions $\langle \mathbf{R} \rangle$, allowing us to introduce displacement operators $\mathbf{u}(t) = \mathbf{R}(t) - \langle \mathbf{R} \rangle$. In much of the literature, this assumption is used to define an approximate Hamiltonian obtained by truncating a Taylor expansion of the potential energy. Typically, this expansion is truncated at the third or fourth order,

implying small displacement from equilibrium positions. In our approach, we do not assume a specific amplitude for these displacements, other than ensuring that ions do not diffuse within the crystal, and remain localized around their equilibrium positions.

The focus of this work is the thermal conductivity tensor, which quantifies the heat flux $\mathcal{J}^\alpha$ in Cartesian direction α due to an applied temperature gradient in direction β:

$$\mathcal{J}^\alpha = -\kappa^{\alpha\beta} \nabla^\beta T. \tag{4}$$

In the regime where the applied gradient is small, linear response theory dictates that κ is an intrinsic equilibrium property expressed by the Green-Kubo formula

$$\kappa^{\alpha\beta} = \frac{1}{V k_\mathrm{B} T^2} \int_0^\infty dt (\mathcal{J}^\alpha, \mathcal{J}^\beta(t)), \tag{5}$$

where $(A, B(t)) = k_\mathrm{B} T \int_0^\beta d\lambda \langle A(-i\hbar\lambda), B^*(t) \rangle$ denotes the Kubo correlation function (KCF) [30]. From our initial considerations, the primary challenge lies in expressing heat current operators in terms of the dynamic variables of our systems, specifically the displacements. However, before addressing this task, it is crucial to establish a comprehensive description of ion dynamics.

A. Mode-coupling theory of anharmonic lattice dynamics

The many-body nature of the Hamiltonian governing ion motion renders an exact analytical description of the dynamics impossible. Fortunately, linear response theory offers effective tools for making accurate approximations in such scenarios. Recently, we introduced the mode-coupling theory of anharmonic lattice dynamics [28], which uses linear response theory to calculate the correlated motion of ions in crystals beyond standard perturbation theory. This formalism aims to describe the mass-weighted displacement-displacement KCF [30]:

$$G_{ij}^{\alpha\beta}(t) = \sqrt{M_i M_j} \big(u_i^\alpha, u_j^\beta(t) \big). \tag{6}$$

In this overview, we outline the key aspects of its derivation and refer interested readers to our previous work for comprehensive details.

The formalism is founded on a Mori-Zwanzig projection scheme [31,32], with the introduction of the projection operators

$$\mathcal{P} \cdot = \sum_{ij\alpha\beta} \frac{(u_j^\beta, \cdot)}{(u_i^\alpha, u_j^\beta)} u_i^\alpha + \sum_{ij\alpha\beta} \frac{(p_j^\beta, \cdot)}{(p_i^\alpha, p_j^\beta)} p_i^\alpha, \tag{7}$$

$$\mathcal{Q} = 1 - \mathcal{P}. \tag{8}$$

The operator $\mathcal{P}$ projects a dynamical variable on the subspace of the full dynamical variables defined by single displacements u_i and their momenta p_i, while its orthogonal projection $\mathcal{Q}$ projects on the rest of the full dynamical variable space. The first step of the derivation consists in projecting the time derivative of the momentum operator, the atomic force, on both $\mathcal{P}$ and $\mathcal{Q}$ which allows, after some steps, to formally write its equation of motion as the generalized

Langevin equation [30]

$$f_j^\alpha(t) = -\sum_{k\gamma} \Phi_{jk}^{\beta\gamma} u_k^\gamma(t)$$

$$- \sum_{k\gamma} \int_0^t ds\, K_{jk}^{\beta\gamma}(s)\dot{u}_k^\gamma(t-s) + \delta f_i(t), \quad (9)$$

where we introduced the temperature-dependent generalization of the second interatomic force constants (IFC)

$$\Phi_{ij}^{\alpha\beta} = -\frac{1}{\sqrt{M_i M_j}} \sum_{k\gamma} \frac{(u_k^\gamma, f_i^\alpha)}{(u_j^\beta, u_k^\gamma)} \quad (10)$$

as well as a memory matrix

$$K_{ij}^{\alpha\beta}(t) = \beta \frac{(\delta f_i^\alpha, \delta f_j^\beta(t))}{\sqrt{M_i M_j}} \quad (11)$$

and where $\delta f_i^\alpha(t) = e^{i\mathcal{QL}t}(f_i^\alpha + \sum_{j\beta} \Phi_{ij}^{\alpha\beta} u_j^\beta)$ is called the "random" force due to its projected dynamics outside of the space spanned by single displacements. Multiplying then by a displacement, taking the Kubo average, and using the property $(u_i^\alpha, \delta f_j(t)) = 0$, we obtain the generalized Langevin equation for the equation of motion of the displacement correlation function

$$\ddot{G}_{ij}^{\alpha\beta}(t) = -\sum_{k\gamma} \Phi_{jk}^{\beta\gamma} G_{ik}^{\beta\gamma}(t) - \sum_{k\gamma} \int_0^t ds\, K_{jk}^{\beta\gamma}(s)\dot{G}_{jk}^{\beta\gamma}(t-s). \quad (12)$$

As in the harmonic approximation, the Fourier transform of $\mathbf{\Phi}$ allows to define phonons with their associated phonon displacement operator $A_s(\mathbf{q})$, where s is the mode. The displacements can then be projected onto the phonon space using their eigenvectors $\boldsymbol{\varepsilon}_s(\mathbf{q})$:

$$u_i^\alpha(t) = \sqrt{\frac{\hbar}{2M_i}} \sum_\lambda \frac{\varepsilon_s^{i\alpha}(\mathbf{q})}{\sqrt{\Omega_s(\mathbf{q})}} A_s(\mathbf{q}, t). \quad (13)$$

To simplify the derivation of the heat current and ease the comparison with harmonic and perturbation theory, we will also introduce the phonon momentum operator

$$p_i^\alpha(t) = -i\sqrt{\frac{\hbar M_i}{2}} \sum_{s\mathbf{q}} \sqrt{\Omega_s(\mathbf{q})}\varepsilon_s^{i\alpha}(\mathbf{q})B_s(\mathbf{q}), \quad (14)$$

where we can recognize $B_s(\mathbf{q}, t) = -i\dot{A}_s(\mathbf{q}, t)/\Omega_s(\mathbf{q})$. The usefulness of the momentum operator comes from the relation between static correlation function involving $A_s(\mathbf{q})$ and $B_s(\mathbf{q})$, for instance,

$$(A_s(\mathbf{q}), A_{s'}(\mathbf{q}')) = (B_s(\mathbf{q}), B_{s'}(\mathbf{q}')) = \frac{k_B T}{\hbar\Omega_s(\mathbf{q})}\delta_{ss'}\delta_{\mathbf{qq}'}, \quad (15)$$

$$(A_s(\mathbf{q}), B_{s'}(\mathbf{q}')) = (B_s(\mathbf{q}), A_{s'}(\mathbf{q}')) = 0. \quad (16)$$

We can now define the phonon correlation function

$$G_s(\mathbf{q}, t) = (A_s(\mathbf{q}), A_s(\mathbf{q}, t)) \quad (17)$$

which follows the generalized Langevin equation

$$\ddot{G}_s(\mathbf{q}, t) = -\Omega_s^2(\mathbf{q})G_s(\mathbf{q}, t) - \int_0^t ds\, K_s(\mathbf{q}, s)\dot{G}_s(\mathbf{q}, t-s), \quad (18)$$

where $K_s(\mathbf{q}, t)$ is the projection of the memory kernel on phonon $(\mathbf{q}, s)$. Taking the real part of the Laplace transform of this equation, we obtain the phonon correlation function in frequency space

$$G_s(\mathbf{q}, \omega) = \frac{k_B T}{\pi\hbar}$$

$$\times \frac{8\Omega_s(\mathbf{q})\Gamma_s(\mathbf{q}, \omega)}{[\omega^2 - \Omega_s(\mathbf{q})^2 - 2\omega\Delta_s(\mathbf{q}, \omega)]^2 + 4\omega^2\Gamma_s^2(\mathbf{q}, \omega)}, \quad (19)$$

where $\Gamma_s(\mathbf{q}, \omega)$ and $\Delta_s(\mathbf{q}, \omega)$ are the real and imaginary parts of the memory kernel, which are related through a Kramers-Kronig transform

$$\Delta_s(\mathbf{q}, \omega) = \frac{1}{\pi}\int d\omega' \frac{\Gamma_s(\mathbf{q}, \omega')}{\omega' - \omega} \quad (20)$$

while $\Gamma_s(\mathbf{q}, \omega)$ is proportional to the Fourier transform of the memory kernel. It should be noted that up until this point, the only approximation made concerns the neglect in Eq. (17) of the off-diagonal component of the correlation function for a given $\mathbf{q}$ point. The correlation function in Eq. (19) is related to the phonon spectral function, which can be directly compared to experiments such as inelastic neutron or x-ray scattering and is obtained from the fluctuation-dissipation theorem $\chi_s''(\mathbf{q}, \omega) = \frac{\omega}{2k_B T} G_s(\mathbf{q}, \omega)$, resulting in

$$\chi_s''(\mathbf{q}, \omega) = \frac{1}{\pi\hbar}$$

$$\times \frac{4\omega\Omega_s(\mathbf{q})\Gamma_s(\mathbf{q}, \omega)}{[\omega^2 - \Omega_s(\mathbf{q})^2 - 2\omega\Delta_s(\mathbf{q}, \omega)]^2 + 4\omega^2\Gamma_s^2(\mathbf{q}, \omega)}. \quad (21)$$

The main difficulty in employing Eq. (19) or (21) lies in the *a priori* unknown expression of the memory kernel. In the mode-coupling approximation, this difficulty is alleviated by expanding the random forces using higher-order displacement projection operators. Up to fourth order, the random forces are then written as

$$\delta f_i^\alpha(t) = e^{i\mathcal{QL}t}\left[\frac{1}{2!}\sum_{jk}\sum_{\beta\gamma}\Psi_{ijk}^{\alpha\beta\gamma} u_j^\beta u_k^\gamma\right.$$

$$\left. + \frac{1}{3!}\sum_{jkl}\sum_{\beta\gamma\delta}\Psi_{ijkl}^{\alpha\beta\gamma\delta} u_j^\beta u_k^\gamma u_l^\delta + \delta_4 f_i^\alpha\right], \quad (22)$$

where $\delta_4 f_i^\alpha$ is the remainder of the force and the $\mathbf{\Psi}$ are the temperature-dependent generalizations of higher-order force constants. These can be computed as

$$\Psi_{ijk}^{\alpha\beta\gamma} = \sum_{k'l'}\sum_{\beta'\gamma'} \frac{(u_{j'}^{\beta'} u_{k'}^{\gamma'}, \delta f_i^\alpha)}{(u_{j'}^{\beta'} u_{k'}^{\gamma'}, u_j^\beta u_k^\gamma)}, \quad (23)$$

$$\Psi_{ijkl}^{\alpha\beta\gamma\delta} = \sum_{j'k'l'}\sum_{\beta'\gamma'\delta'} \frac{(u_{j'}^{\beta'} u_{k'}^{\gamma'} u_{l'}^{\delta'}, \delta_3 f_i^\alpha)}{(u_{j'}^{\beta'} u_{k'}^{\gamma'} u_{l'}^{\delta'}, u_j^\beta u_k^\gamma u_l^\delta)}, \quad (24)$$

where $\delta_3 f_i^\alpha = \delta f_i^\alpha - \sum_{jk}\sum_{\beta\gamma}\Psi_{ijk}^{\alpha\beta\gamma} u_j^\beta u_k^\gamma$. An approximation up to fourth order of the memory matrix can be computed by injecting Eq. (22) in (11) after the neglect of the $\delta_4 f_i^\alpha$ term and of the orthogonal projector $\mathcal{Q}$ in the time evolution. After

a projection on phonon modes, the memory kernel for mode $(s, \mathbf{q})$ can be decomposed as

$$\Gamma_s(\mathbf{q}, \omega) \approx \Gamma_s^{(3)}(\mathbf{q}, \omega) + \Gamma_s^{(4)}(\mathbf{q}, \omega). \tag{25}$$

After decoupling the various correlation functions appearing in $\Gamma_s(\mathbf{q})$ using the scheme presented in Appendix B, one

obtains a set of self-consistent equations for the memory kernel and $G_s(\mathbf{q}, \omega)$. This set can be replaced by a one-shot approximation, where the phonon correlation functions involved in the memory kernel are replaced by their memory-free counterparts. In this approximation, the three-phonon contribution is written

$$\Gamma_{s_1}^{(3)}(\mathbf{q}_1, \omega) = \sum_{\mathbf{q}_2 \mathbf{q}_3} \sum_{s_2 s_3} \Gamma_{s_1 s_2 s_3}^{(3)}(\mathbf{q}_1, \mathbf{q}_2, \mathbf{q}_3, \omega), \tag{26}$$

$$\Gamma_{s_1 s_2 s_3}^{(3)}(\mathbf{q}_1, \mathbf{q}_2, \mathbf{q}_3, \omega) = \frac{\pi}{16} \left| \Psi_{\mathbf{q}_1 \mathbf{q}_2 \mathbf{q}_3}^{s_1 s_2 s_3} \right|^2 \mathcal{S}^{(3)}(\omega, \Omega_{s_2}(\mathbf{q}_2), \Omega_{s_3}(\mathbf{q}_3)), \tag{27}$$

$$\mathcal{S}^{(3)}(\omega, \Omega_2, \Omega_3) = \sum_{s=1,-1} \{ s[n(\Omega_2) + n(\Omega_3) + 1]\delta(\omega + s\Omega_2 + s\Omega_3) + s[n(\Omega_2) - n(\Omega_3)]\delta(\omega + s\Omega_2 - s\Omega_3) \} \tag{28}$$

while the four-phonon interaction is given by

$$\Gamma_{s_1}^{(4)}(\mathbf{q}_1, \omega) = \sum_{\mathbf{q}_2 \mathbf{q}_3 \mathbf{q}_4} \sum_{s_2 s_3 s_4} \Gamma_{s_1 s_2 s_3 s_4}^{(4)}(\mathbf{q}_1, \mathbf{q}_2, \mathbf{q}_3, \mathbf{q}_4, \omega), \tag{29}$$

$$\Gamma_{s_1 s_2 s_3 s_4}^{(4)}(\mathbf{q}_1, \mathbf{q}_2, \mathbf{q}_3, \mathbf{q}_4, \omega) = \frac{\pi}{96} \left| \Psi_{\mathbf{q}_1 \mathbf{q}_2 \mathbf{q}_3 \mathbf{q}_4}^{s_1 s_2 s_3 s_4} \right|^2 \mathcal{S}^{(4)}(\omega, \Omega_{s_2}(\mathbf{q}_2), \Omega_{s_3}(\mathbf{q}_3), \Omega_{s_4}(\mathbf{q}_4)), \tag{30}$$

$$\mathcal{S}^{(4)}(\omega, \Omega_2, \Omega_3, \Omega_4) = \sum_{s=1,-1} \{ s[n(\Omega_2) + 1][n(\Omega_3) + 1][n(\Omega_4) + 1] - n(\Omega_2)n(\Omega_3)n(\Omega_4)\delta(\omega + s\Omega_2 + s\Omega_3 + s\Omega_4)$$

$$+ s\{3n(\Omega_2)[n(\Omega_3) + 1][n(\Omega_4) + 1] - [n(\Omega_2) + 1]n(\Omega_3)n(\Omega_4)]\delta(\omega + s\Omega_2 - s\Omega_3 - s\Omega_4) \}. \tag{31}$$

In these equations, the scattering matrix elements $\Psi_{\mathbf{q}_1 \mathbf{q}_2 \mathbf{q}_3}^{s_1 s_2 s_3}$ and $\Psi_{\mathbf{q}_1 \mathbf{q}_2 \mathbf{q}_3 \mathbf{q}_4}^{s_1 s_2 s_3 s_4}$ are the projections of the higher-order generalized IFCs on phonon modes. Introducing a unit-cell centered notation $\Psi_{ijk}^{\alpha\beta\gamma}(\mu, \nu)$, where i, j, and k are atoms in the unit cell and μ and ν denote the index of a unit cell in the crystal, the third-order scattering matrix elements are computed as

$$\Psi_{\mathbf{q}_1 \mathbf{q}_2 \mathbf{q}_3}^{s_1 s_2 s_3} = \sum_{ijk\alpha\beta\gamma\mu\nu} \frac{\Psi_{ijk}^{\alpha\beta\gamma}(\mu, \nu)e^{-i(\mathbf{q}_2 \mathbf{R}_{\mu,j} + \mathbf{q}_3 \mathbf{R}_{\nu,k})}}{\sqrt{M_i M_j M_k}}$$

$$\times \frac{\varepsilon_{s_1}^{i\alpha}(\mathbf{q}_1)\varepsilon_{s_2}^{j\beta}(\mathbf{q}_2)\varepsilon_{s_3}^{k\gamma}(\mathbf{q}_3)}{\sqrt{\Omega_\lambda \Omega_{\lambda'} \Omega_{\lambda''}}} \Delta(\mathbf{q}_1 + \mathbf{q}_2 + \mathbf{q}_3) \tag{32}$$

with $\mathbf{R}_{\mu,j}$ the distance between the atom i in a reference unit cell and the atom j in the unit cell μ and where $\Delta(\mathbf{q})$ is 1 if $\mathbf{q}$ is equal to a reciprocal lattice vector and 0 otherwise, to ensure conservation of the quasimomentum. The fourth-order scattering matrix elements are computed with a similar formula involving the fourth-order generalized IFC. The memory kernel in the mode-coupling approximation can be rationalized from a diagrammatic representation, pictured in Fig. 1. In this representation, the third-order contribution is analogous to the

third-order bubble diagram from perturbation theory, while the fourth order is equivalent to the sunset diagram.

It should be noted that to introduce the scattering of phonons due to isotopic effects, the following contribution can be added to the memory kernel:

$$\Gamma_s^{\text{iso}}(\mathbf{q}, \omega) = \sum_{\mathbf{q}_2 s_2} \Gamma_{ss_2}^{\text{iso}}(\mathbf{q}, \mathbf{q}_2, \omega)$$

$$= \sum_{\mathbf{q}_2 s_2} \sum_i g_i \left| \boldsymbol{\varepsilon}_s^i(\mathbf{q})\varepsilon_{s_2}^i(\mathbf{q}_2) \right|^2 \delta[\omega - \Omega_{s_2}(\mathbf{q}_2)]. \tag{33}$$

In this equation, corresponding to Tamura's model [33], the g_i measure the distribution of the isotope masses of element i and is computed as $g_i = \sum_n \frac{d_{i,n}}{N} (\frac{\Delta M_{i,n}}{M_i})^2$ where N is the number of isotopes, $d_{i,n}$ is the concentration of isotope n of element i, and $\Delta M_{i,n}$ is the mass difference between isotope n and the average mass of the element.

The generalized Langevin equation (12) describes phonons interacting with a bath made from all other phonons. When the interaction with this bath is weak, the time dependence of the memory kernel can be neglected, and the dissipative part of the dynamics can be reduced to a single value $\Gamma_s^M(\mathbf{q})$, given by $\Gamma_s(\mathbf{q}, \omega)$ evaluated at the frequency of the phonon $(s, \mathbf{q})$, as shown in Appendix C:

$$\Gamma_s^M(\mathbf{q}) = \Gamma_s(\mathbf{q}, \Omega_s(\mathbf{q})). \tag{34}$$

In this limit, known as Markovian, the spectral function reduces to a Lorentzian centered at the frequency $\Omega_s(\mathbf{q})$ and with a width $\Gamma_s(\mathbf{q})$:

$$\chi_s''^M(\mathbf{q}, \omega) = \frac{1}{\pi\hbar} \frac{\Gamma_s^M(\mathbf{q})}{[\omega - \Omega_s(\mathbf{q})]^2 + \left[\Gamma_s^M(\mathbf{q})\right]^2}. \tag{35}$$
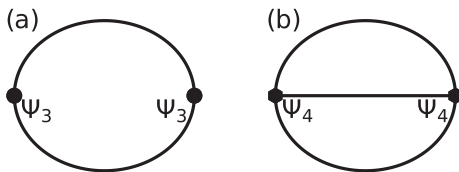

FIG. 1. Feynman diagrams for the memory kernel considered in this work. (a) The three-phonon bubble contribution. (b) The four-phonon sunset contribution.

The Markovian limit cannot be a complete description of the system since it breaks some sum rules that the correlation functions are supposed to follow [28]. Nevertheless, it remains a useful and often accurate approximation for systems where the quasiparticle picture is well founded. In this case, the phonons can be thought of as diffusing through the material with a lifetime $\tau_s(\mathbf{q}) = [2\Gamma_s^M(\mathbf{q})]^{-1}$. One can note that the Markovian limit is analogous to the use of Fermi's golden rule in perturbation theory.

B. Anharmonic heat current operator

To derive the thermal conductivity tensor using the Green-Kubo formula, it is essential to derive heat current operators which are consistent with the previously established mode-coupling theory. In an electrically insulating solid, with our prerequisite of absence of diffusion, the conductive component of the heat current operator, defined as [7,34]

$$\mathcal{J}(t) = \sum_i \langle \mathbf{R}_i \rangle \dot{E}_i(t) \tag{36}$$

is the only contributor the thermal conductivity. Here, $E_i(t)$ represents the local energy contribution from atom i to the system's total energy, a quantity that is inherently ambiguous. To circumvent the complexities associated with explicitly partitioning the potential energy, we instead focus directly on the time derivative $\dot{E}_i(t)$. Building on the approach of [35], the heat current operator can be expressed as

$$\mathcal{J}(t) = \frac{1}{V} \sum_{ij} (\langle \mathbf{R}_i \rangle - \langle \mathbf{R}_j \rangle) \mathbf{f}_{ij}(t) \dot{\mathbf{u}}_i(t), \tag{37}$$

where $\mathbf{f}_{ij}(t)$ denotes the forces exerted by atom j on atom i. To formally define this quantity, one would typically require an explicit formulation of the Hamiltonian. However, the Mori-Zwanzig projection scheme offers an alternative approach to perform the partitioning. Indeed, from the equation of motion for the forces [Eq. (9)], we can partition the force over atom pairs, resulting in the expression

$$\mathbf{f}_{ij}^\alpha(t) = -\Phi_{ij}^{\alpha\beta} u_j^\beta(t) - \int_0^\infty ds\, K_{ij}^{\alpha\beta}(s) p_j^\beta(t-s) + \delta f_j^\alpha(t) \delta_{ij} \tag{38}$$

which respects the condition $\mathbf{f}_i(t) = \sum_j \mathbf{f}_{ij}(t)$. Neglecting the contribution from the memory kernel and the random force, we can substitute this expression into the heat current operator, which yields

$$\mathcal{J}^\alpha(t) \approx \sum_{ij} \sum_{\beta\gamma} (\langle R_i^\alpha \rangle - \langle R_j^\alpha \rangle) \Phi_{ij}^{\beta\gamma} u_j^\gamma(t) \dot{u}_i^\beta(t) \tag{39}$$

which, in term of phonon operators, becomes

$$\mathcal{J}(t) = -\frac{1}{2} \sum_{\mathbf{q} s_1 s_2} \hbar \Omega_{s_2}(\mathbf{q}) \mathbf{v}_{\mathbf{q}}^{s_1 s_2} A_{s_1}(\mathbf{q}, t) B_{s_2}(\mathbf{q}, t) \tag{40}$$

with $\mathbf{v}_{\mathbf{q}}^{s_1 s_2}$ the generalized group velocities [7,12,36]. The heat current can be split as $\mathcal{J}(t) = \mathcal{J}^d(t) + \mathcal{J}^{nd}(t)$, where the first term is diagonal with respect to phonon branches

$$\mathcal{J}^d(t) = -\frac{1}{2} \sum_{\mathbf{q} s} \hbar \Omega_s(\mathbf{q}) \mathbf{v}_{\mathbf{q}}^s A_s(\mathbf{q}, t) B_s(\mathbf{q}, t) \tag{41}$$

with $\mathbf{v}_{\mathbf{q}}^s = \mathbf{v}_{\mathbf{q}}^{ss}$, and the other term is the off-diagonal contribution

$$\mathcal{J}^{nd}(t) = -\frac{1}{2} \sum_{\mathbf{q} s_1 \neq s_2} \hbar \Omega_{s_2}(\mathbf{q}) \mathbf{v}_{\mathbf{q}}^{s_1 s_2} A_{s_1}(\mathbf{q}, t) B_{s_2}(\mathbf{q}, t). \tag{42}$$

Neglecting the correlations between diagonal and off-diagonal heat current, the thermal conductivity can be separated in a similar manner

$$\kappa \approx \kappa^d + \kappa^{nd}, \tag{43}$$

$$\kappa^d = \frac{1}{VT} \int_0^\infty (\mathcal{J}^d, \mathcal{J}^d(t)), \tag{44}$$

$$\kappa^{nd} = \frac{1}{VT} \int_0^\infty (\mathcal{J}^{nd}, \mathcal{J}^{nd}(t)). \tag{45}$$

C. Diagonal thermal conductivity

We will begin with the diagonal part of κ,

$$\kappa^d = \frac{1}{4V k_B T^2} \sum_{\mathbf{q}_1 \mathbf{q}_2} \sum_{s_1 s_2} \Omega_{s_1}(\mathbf{q}_1) \Omega_{s_2}(\mathbf{q}_2) \mathbf{v}_{\mathbf{q}_1}^{s_1} \otimes \mathbf{v}_{\mathbf{q}_2}^{s_2}$$
$$\times \int_0^\infty dt (A_{s_1}(\mathbf{q}_1) B_{s_1}(\mathbf{q}_1), A_{s_2}(\mathbf{q}_2, t) B_{s_2}(\mathbf{q}_2, t)). \tag{46}$$

The main difficulty in this equation lies in the expression of the four-point correlation function. In Appendix D, we show how to obtain its equation of motion in the mode-coupling theory, which, after a Laplace transform and the application of the Markovian approximation, allows to express the diagonal contribution to κ as

$$\kappa^d = \frac{1}{V} \sum_{\mathbf{q}_1 \mathbf{q}_2} \sum_{s_1 s_2} \mathbf{v}_{\mathbf{q}_1}^{s_1} \otimes \mathbf{v}_{\mathbf{q}_2}^{s_2} c_{s_1}(\mathbf{q}_1) (\mathbf{\Xi}^{-1})(\mathbf{q}_1 s_1, \mathbf{q}_2 s_2), \tag{47}$$

where $c_s(\mathbf{q}) = \Omega_s^2(\mathbf{q}) n_s(\mathbf{q})[n_s(\mathbf{q}) + 1]/k_B T^2$ is the modal heat capacity and $\mathbf{\Xi}$ is the scattering matrix, given explicitly in Appendix D.

Neglecting the off-diagonal component of the scattering matrix, we obtain the single-mode approximation to the thermal conductivity tensor

$$\kappa^{d,SMA} = \frac{1}{V} \sum_{\mathbf{q} s} \mathbf{v}_{\mathbf{q}}^s \otimes \mathbf{v}_{\mathbf{q}}^s \frac{c_s(\mathbf{q})}{2\Gamma_s^M(\mathbf{q})}. \tag{48}$$

It is interesting to note that this result can also be obtained using the decoupling scheme of Kubo correlation functions, as we will use for the nondiagonal contribution.

D. Nondiagonal contribution to the thermal conductivity

The contribution stemming from the off-diagonal part of the heat current is written

$$\kappa^d = \frac{1}{4V k_B T^2} \sum_{\mathbf{q}_1 \mathbf{q}_2} {\sum_{s_1 s_2}}' {\sum_{s_3 s_4}}' \Omega_{s_2}(\mathbf{q}_1) \Omega_{s_4}(\mathbf{q}_2) \mathbf{v}_{\mathbf{q}_1}^{s_1 s_2} \otimes \mathbf{v}_{\mathbf{q}_2}^{s_3 s_4}$$
$$\times \int_0^\infty dt (A_{s_1}(\mathbf{q}_1) B_{s_2}(\mathbf{q}_1), A_{s_3}(\mathbf{q}_2, t) B_{s_4}(\mathbf{q}_2, t)), \tag{49}$$

where $\sum'_{s_1 s_2}$ indicates that $s_1 = s_2$ is excluded from the double sum. Using the rules presented in Appendix B, the four-point

Kubo correlation function can be decoupled as

$$\int_0^\infty dt (A_{s_1}(\mathbf{q}_1) B_{s_2}(\mathbf{q}_1), A_{s_3}(\mathbf{q}_2, t) B_{s_4}(\mathbf{q}_2, t))$$

$$\approx \delta_{\mathbf{q}_1 \mathbf{q}_2} \delta_{s_1 s_3} \delta_{s_2 s_4} \frac{\pi}{\Omega_{s_1}(\mathbf{q}_1) \Omega_{s_2}(\mathbf{q}_1)}$$

$$\times \int_{-\infty}^\infty d\omega \, \chi''_{s_1}(\mathbf{q}, \omega) \chi''_{s_2}(\mathbf{q}, \omega) \omega^2 n(\omega)[n(\omega) + 1]. \quad (50)$$

Injecting this result in Eq. (49), and introducing the frequency-dependent heat capacity $c_v(\omega) = \hbar \omega^2 n(\omega)[n(\omega) + 1]/k_B T^2$, the off-diagonal contribution to the thermal conductivity tensor is

$$\boldsymbol{\kappa}^{nd} \approx \frac{\pi}{V} \sum_{\mathbf{q}} \sideset{}{'}\sum_{s_1 s_2} \mathbf{v}_{\mathbf{q}}^{s_1 s_2} \otimes \mathbf{v}_{\mathbf{q}}^{s_1 s_2}$$

$$\times \int_{-\infty}^\infty d\omega \, \chi''_{s_1}(\mathbf{q}, \omega) \chi''_{s_2}(\mathbf{q}, \omega) c_v(\omega). \quad (51)$$

Within the Markovian approximation, this equation involves the integral of two Lorentzians multiplied by the heat capacity of a harmonic oscillator. If we assume a regime of anharmonicity where the quasiparticle picture is valid, each Lorentzian approaches a Dirac delta, allowing us to take the approximation

$$\boldsymbol{\kappa}^{nd} \approx \frac{1}{V} \sum_{\mathbf{q}} \sideset{}{'}\sum_{s_1 s_2} \mathbf{v}_{\mathbf{q}}^{s_1 s_2} \otimes \mathbf{v}_{\mathbf{q}}^{s_1 s_2} \frac{c_{\mathbf{q}}^{s_1} + c_{\mathbf{q}}^{s_2}}{2} \Gamma_{s_1 s_2}^M(\mathbf{q}), \quad (52)$$

where we introduced the off-diagonal scattering

$$\Gamma_{s_1 s_2}^M(\mathbf{q}) = \frac{\Gamma_{s_1}^M(\mathbf{q}) + \Gamma_{s_2}^M(\mathbf{q})}{[\Omega_{s_1}(\mathbf{q}) - \Omega_{s_2}(\mathbf{q})]^2 + [\Gamma_{s_1}^M(\mathbf{q}) + \Gamma_{s_2}^M(\mathbf{q})]^2}. \quad (53)$$

One should note that by removing the restriction of s_1 and s_2 being different, the diagonal contribution in the single-mode approximation is recovered, as expected.

III. DISCUSSION

Our final formulation of the thermal conductivity tensor is expressed as $\kappa = \kappa^d + \kappa^{nd}$, with κ^d given by Eq. (47) and κ^{nd} by Eq. (52). This result bears some resemblance to previous derivations based on Hardys formulation of the heat current operator [7–10,12,37,38]. For instance, we show in Appendix E that the diagonal contribution of the thermal conductivity tensor κ^d is equivalent to that obtained through the solution of the phonon Boltzmann equation, providing a further proof with Ref. [38] of the equivalence between the phonon Boltzmann and Green-Kubo approaches. Thus, our derivation provides a unified framework that encompasses the collective, single-mode, and off-diagonal contributions to heat transport by phonons. Notably, for the single-mode and off-diagonal contributions, it captures the non-Markovian memory effects described in Eq. (51) through the inclusion of the full phonon dynamical susceptibility. As a result, our formulation can address any system with a crystalline reference structure, from highly harmonic crystals at low temperatures where collective effects dominate to complex crystals with large unit cells, where the off-diagonal components of κnd are essential.

A key distinction of our approach is its inherent inclusion of temperature-dependent phonon renormalization, setting it apart from standard formalisms. The latter rely on a Taylor expansion of the Born-Oppenheimer potential energy surface, treating anharmonic terms as a perturbative correction to a dominant second-order term. Consequently, the dynamical properties of the system are inferred indirectly, being reconstructed *a posteriori* from the effective potential energy surface. However, in order to use perturbation theory, these methods assume that the atoms vibrate closely around their equilibrium positions, an assumption that fails at elevated temperatures, in the presence of nuclear quantum effects, or when the Hessian of the Born-Oppenheimer surface is not positive definite. In these scenarios, high-order anharmonic interactions become significant, making perturbative corrections insufficient.

In contrast, our mode-coupling theory focuses directly on the atom dynamics, rather than on the underlying potential energy surface. Because of this, the framework naturally incorporates temperature-dependent interactions and avoids the limitations of perturbative expansions.

In the end, this difference in foundations is critical. To understand how the approaches diverge, it is useful to focus on their fundamental building blocks: the interatomic force constants and the phonons. In the harmonic case (and its perturbation expansion), the IFC are derivatives of the Born-Oppenheimer surface. At the second order, the effective Hamiltonian can be diagonalized, giving rise to eigenstates: the harmonic phonons. Interactions between these phonons are then introduced through the higher-order IFCs, with the magnitude of phonon-phonon interactions at a given temperature being proportional to these IFCs and to the phonon population.

However, in general, these harmonic phonons are a very rough approximation of the true dynamical quantities. Indeed, since the second-order term captures only part of the full potential energy landscape, the accuracy of the harmonic phonons as descriptors of atomic motion is inherently limited. For instance, it has been shown that, in some systems, the harmonic component can account for less than half of the forces acting on atoms [13]. In such cases, the validity of perturbation theory is compromised: not only does the noninteracting phonon baseline inadequately describe the dynamics, but the phonon-phonon interactions themselves are poorly captured and constrained by the finite order of the Taylor expansion.

In contrast, the mode-coupling theory is constructed to alleviate these shortcomings. For example, we have shown previously [28] that the second-order generalized IFCs are physically meaningful, being proportional to the inverse static susceptibility. As a result, in the static limit, the phonons defined by mode-coupling theory are exact, corresponding to the mass-weighted displacement covariance. Furthermore, the Mori-Zwanzig projection scheme ensures that these phonons provide a minimally interacting basis, representing the most accurate noninteracting phonons possible, with already exact static properties [28]. On top of this, each order of the mode-coupling approximation is built to minimize the amplitude of all subsequent orders.

Thus, mode-coupling theory provides a rigorous and systematic framework for capturing dynamical properties. For

the thermal conductivity tensor, this approach introduces two primary improvements. First, it enhances the accuracy of key parameters of the heat current [Eq. (40)], specifically the phonon frequencies and group velocities, due to the exactness of the second-order generalized IFCs. As a result, both the propagation (through $\mathbf{v}_{\mathbf{q}}^s$) and the amount of heat carried for each phonon mode [through $c_s(\mathbf{q})$] are more accurately represented. Second, the mode-coupling theory offers a refined treatment of phonon-phonon scattering, yielding a more precise dynamical description and leading to improved predictions of thermal conductivity. However, our work is a further demonstration that, even with the renormalization, heat transport is not mediated by individual phonons but is a collective effect, and reduces to phonons only if the coupling between phonons is negligible. Nevertheless, the refinement brought by the mode-coupling theory also holds in systems where these collective excitations (also known as relaxons [39]) are necessary for an accurate description. In this case, the equivalence between our derivation and the phonon Boltzmann equation shown in Appendix E further suggests that diagonalizing Ξ allows to obtain the temperature-renormalized counterpart of the relaxons from a perturbative approach.

A notable strength of the mode-coupling theory is that despite its dynamical foundation, its building blocks are real-space and time-independent properties. Specifically, the generalized IFCs are derived from static Kubo averages, offering distinct advantages over fully time-dependent approaches.

First, this formulation facilitates the evaluation of thermodynamic and long-range limits of correlation functions using relatively moderate simulation sizes and durations. In contrast, direct time-dependent methods often require significantly larger and more computationally intensive simulations to achieve convergence, making the mode-coupling approach both more efficient and less prone to size-related artifacts.

Additionally, nuclear quantum effects are naturally integrated within the mode-coupling framework, as the formalism is rooted in Kubo correlation functions. These quantum effects can be explicitly incorporated in practice through path-integral simulations to compute the generalized IFCs. This is a noticeable advantage since the path-integral molecular dynamics formalism is only exact in the static limit [40] and provides an approximation of the real Kubo correlation that can be spoiled by numerical artifacts such as spurious resonances or shifts in frequency-resolved spectra [41–43]. Finally, the the framework being grounded on Kubo correlation functions supports a rigorously justified semiclassical approximation [28,44]. By using classical simulations to compute the generalized IFCs, these quantities can then serve as inputs for the quantum equations of motion developed in this work, enabling a practical treatment of quantum nuclear effects.

IV. IMPLEMENTATION

The formalism derived above has been implemented in the TDEP code [29] and this section outlines the strategy used in this implementation. For high-order many-body calculations, the latter is not just a question of efficiency: it is crucial to obtain converged results at all. This has been an important and unrecognized problem in comparing different approaches in the literature.

The generalized IFC are fit using linear least squares on the forces, incorporating the symmetry reduction described in Ref. [20]. This ensures strict adherence to transposition and point-group symmetries, as well as the acoustic and rotational sum rules and Hermiticity [45]. A key point of the implementation is the successive fitting of the IFC, meaning that each order is fit on the residual forces from the previous order. As demonstrated previously [28], this method aligns with the definition of the generalized IFC in the mode-coupling theory, providing a crucial step beyond the harmonic approximation and perturbation theory. It should be noted that for systems exhibiting significant nuclear quantum effects, path-integral molecular dynamics can be used, the static KCF needed to compute the generalized IFC corresponding to correlations of the centroid of the quantum polymer.

At the beginning of the thermal conductivity computation, harmonic properties (frequencies, eigenvectors, and group velocities) are generated on a $\mathbf{q}$-point grid. At this point, the degeneracies are carefully treated following the process introduced in Appendix F. To ensure the conservation of the quasimomentum in the definition of the scattering matrix elements, we use regular grids of size $N_1 \times N_2 \times N_3$ where $\mathbf{q}$ points are defined as $\mathbf{q} = (i_1/a, i_2/b, i_3/c)$, i_x being integers from 0 to $N_x - 1$, and a, b, and c representing the lattice constants of the system [46,47]. This grid structure ensures that given two $\mathbf{q}$ points $\mathbf{q}_1$ and $\mathbf{q}_2$, it is always possible to find a third $\mathbf{q}$ point $\mathbf{q}_3$ in the grid, such that $|\mathbf{q}_3| = |\mathbf{q}_1 + \mathbf{q}_2|$, thereby enforcing the quasimomentum conservation. The same principle applies when three $\mathbf{q}$ points are summed to find a fourth one.

For the numerical approximation of the delta function, we employ an adaptive Gaussian method. In this scheme, the delta functions appearing in the scattering processes are approximated with Gaussians

$$\delta[\Omega_s(\mathbf{q}) - W] \rightarrow \frac{e^{-[\Omega_s(\mathbf{q})-W]^2/2\sigma^2}}{\sqrt{2\pi}\sigma} \tag{54}$$

at a frequency W, with a width σ estimated according to the scattering event being computed. In the original formulation of the method [48] and the subsequent adaptations [37,46,49], the width is obtained by expanding W linearly with respect to the $\mathbf{q}$ point of one of the phonons involved in the scattering. In this work, we opted for a different, more robust approach, where each phonon frequency involved in the scattering is expanded around its respective $\mathbf{q}$ point. To first order, this means that the frequency of a phonon at a point $\mathbf{q}$ in the neighborhood of $\mathbf{q}_0$ can be expressed as

$$\Omega_s(\mathbf{q}) \approx \Omega_s(\mathbf{q}_0) + \sum_\alpha \frac{\partial \Omega_s(\mathbf{q})}{\partial \mathbf{q}^\alpha}\big(\mathbf{q}^\alpha - \mathbf{q}_0^\alpha\big). \tag{55}$$

From this extrapolation, one can "blur" phonons around each $\mathbf{q}$ point using Gaussians with mean $\bar{\Omega}_s(\mathbf{q})$ and variance $\sigma_s(\mathbf{q})$ computed with

$$\bar{\Omega}_s(\mathbf{q}) = E[\Omega_s(\mathbf{q})] = \Omega_s(\mathbf{q}_0), \tag{56}$$

$$\sigma_s^2(\mathbf{q}) = E[(\Omega_s(\mathbf{q}) - \bar{\Omega}_s(\mathbf{q}))^2] \tag{57}$$

$$= \left| \frac{\partial \Omega_s(\mathbf{q})}{\partial \mathbf{q}} \right|^2 | \mathbf{q} - \mathbf{q}_0 |^2, \tag{58}$$

where $E[X]$ is the expectation of X. The width σ can then be obtained from the convolution of all "blurred" phonons involved in a specific process, giving

$$\sigma = \sqrt{\sigma_{s_1}^2(\mathbf{q}_1) + \sigma_{s_2}^2(\mathbf{q}_2) + \sigma_{s_3}^2(\mathbf{q}_3)} \quad (59)$$

for third-order processes, and

$$\sigma = \sqrt{\sigma_{s_1}^2(\mathbf{q}_1) + \sigma_{s_2}^2(\mathbf{q}_2) + \sigma_{s_3}^2(\mathbf{q}_3) + \sigma_{s_4}^2(\mathbf{q}_4)} \quad (60)$$

for fourth-order processes. Compared to the approach involving group velocity differences [37,46,48,49], our approach respects the symmetries of the scattering matrix, and allow to keep it symmetric positive definite. Moreover, the individual phonon broadening parameters $\sigma_s(\mathbf{q})$ can be precomputed at the beginning of the calculation with other harmonic properties.

A. Iterative solution to the collective diagonal contribution

The collective contribution to the thermal conductivity tensor poses a computational challenge, as it requires the diagonalization of the scattering matrix $\boldsymbol{\Xi}$. An alternative formulation of Eq. (47) proves to be advantageous [50]

$$\boldsymbol{\kappa}^{\mathrm{d}} = \frac{1}{V} \sum_{\mathbf{q}} \sum_{s} c_s(\mathbf{q}) \mathbf{v}_{\mathbf{q}}^s \otimes \mathbf{F}_s(\mathbf{q}), \quad (61)$$

where

$$\mathbf{F}_s(\mathbf{q}) = \boldsymbol{\Xi}^{-1} \mathbf{v}_{\mathbf{q}}^s. \quad (62)$$

This formulation circumvents direct matrix inversion, by focusing on computing the vectors $\mathbf{F}_s(\mathbf{q})$, which can be limited to irreducible $\mathbf{q}$ points. Using the Neumann series for matrix inversion, $(\mathbf{1} - \boldsymbol{\Xi})^{-1} = \sum_{n=0}^{\infty} \boldsymbol{\Xi}^n$, and suitable reordering, an iterative method for computing $\mathbf{F}_s(\mathbf{q})$ is obtained

$$\mathbf{F}_s^0(\mathbf{q}) = \frac{1}{2\Gamma_s^M(\mathbf{q})} \mathbf{v}_{\mathbf{q}}^s, \quad (63)$$

$$\mathbf{F}_s^{n+1}(\mathbf{q}) = \mathbf{F}_s^0(\mathbf{q}) - \frac{1}{2\Gamma_s^M(\mathbf{q})} \sum_{\mathbf{q}_2 s_2} \boldsymbol{\Xi}(\mathbf{q}s, \mathbf{q}_2 s_2) \mathbf{F}_{s_2}^n(\mathbf{q}_2). \quad (64)$$

This iterative approach is analogous to Omini's solution to the phonon Boltzmann equation [51]. In our implementation, convergence of the series is improved using a mixing prefactor α between iterations, where $0 < \alpha < 1$. As a tradeoff between memory usage and speed, the scattering matrix is retained throughout iterations, but only rows corresponding to the N_{irr} irreducible $\mathbf{q}$ points are stored. This results in a manageable storage size of $3N_{\mathrm{at}}N_{\mathrm{irr}} \times 3N_{\mathrm{at}}N_q$, *independent of the scattering order considered*, thereby avoiding the memory overhead associated with fourth-order terms when storing scattering processes independently [37,52] and allowing the use of the BLAS linear algebra library [53] to perform the matrix multiplication in Eq. (64).

B. Improving the computational cost

Calculating thermal conductivity can incur significant computational costs, especially when considering fourth-order interactions. In a naïve implementation, the computation of third-order interactions scales as $O(N_i \times N_q \times N_s^3)$, where

N_i is the number of irreducible $\mathbf{q}$ points in the Brillouin zone, N_q is the number of points in the full grid, and N_s is the number of modes. For fourth-order scattering, the scaling is even more demanding, at $O(N_i \times N_q^2 \times N_s^4)$.

In this subsection, we will demonstrate techniques to mitigate this computational cost.

1. Computing the scattering amplitude

The most time-consuming part of computing thermal conductivity is the calculation of the scattering matrix elements, which are needed for a large number of triplets or quartets of $\mathbf{q}$ points and modes. To reduce this computational cost, we divide the calculation into two steps. First, once a triplet of $\mathbf{q}$ point is selected, we Fourier transform the third-order IFC in reciprocal space, without projecting on mode:

$$\widetilde{\Psi}_{ijk}^{\alpha\beta\gamma}(\mathbf{q}_1, \mathbf{q}_2, \mathbf{q}_3) = \sum_{\mu\nu} \frac{\Psi_{ijk}^{\alpha\beta\gamma}(\mu, \nu)}{\sqrt{M_i M_j M_k}} e^{-i(\mathbf{q}_2 \mathbf{R}_{\mu,j} + \mathbf{q}_3 \mathbf{R}_{\nu,k})}. \quad (65)$$

Then, for each triplet of modes, corresponding to this triplet of $\mathbf{q}$ points, the third-order IFC in reciprocal space are projected onto the phonon modes using

$$\Psi_{\mathbf{q}_1 \mathbf{q}_2 \mathbf{q}_3}^{s_1 s_2 s_3} = \widetilde{\Psi}(\mathbf{q}_1, \mathbf{q}_2, \mathbf{q}_3) \times \widetilde{\boldsymbol{\varepsilon}}_{s_1}(\mathbf{q}_1) \times \widetilde{\boldsymbol{\varepsilon}}_{s_2}(\mathbf{q}_2) \times \widetilde{\boldsymbol{\varepsilon}}_{s_3}(\mathbf{q}_3) \quad (66)$$

with $\widetilde{\boldsymbol{\varepsilon}}_s(\mathbf{q}) = \boldsymbol{\varepsilon}_s(\mathbf{q})/\sqrt{\Omega_s(\mathbf{q})}$. This second step can be significantly accelerated by recognizing that it can be formulated as matrix-vector multiplications, allowing us to use optimized routines. The same approach can be applied to the fourth-order scattering matrix elements.

2. Irreducible triplet and quartet

To reduce both the time and memory cost of the calculations, it is essential to exploit the symmetry properties of the scattering matrix elements. These elements exhibit specific symmetries under permutations of both the q points and mode indices [47,54]

$$\Psi_{P(q_1, q_2, q_3)}^{P(s_1, s_2, s_3)} = \Psi_{q_1, q_2, q_3}^{s_1, s_2, s_3} \quad \forall P \in \mathcal{P}^{(3)},$$

$$\Psi_{P(q_1, q_2, q_3, q_4)}^{P(s_1, s_2, s_3, s_4)} = \Psi_{q_1, q_2, q_3, q_4}^{s_1, s_2, s_3, s_4} \quad \forall P \in \mathcal{P}^{(4)}, \quad (67)$$

where $\mathcal{P}^{(3)}$ represents the set of all the permutations of a triplet and $\mathcal{P}^{(4)}$ is the set of all permutations of a quartet. Utilizing these symmetries for any irreducible triplet reduces the number of third-order elements by about half and the fourth-order elements by about a factor of 6.

Furthermore, the number of elements can be further reduced by employing the symmetry operations of the crystal structure. For a rotation R belonging to the set of crystal symmetry operations $\mathcal{R}$ expressed for reciprocal space, the invariance is expressed as [47,54]

$$\Psi_{R\mathbf{q}_1, R\mathbf{q}_2, R\mathbf{q}_3}^{s_1, s_2, s_3} = \Psi_{\mathbf{q}_1, \mathbf{q}_2, \mathbf{q}_3}^{s_1, s_2, s_3},$$

$$\Psi_{R\mathbf{q}_1, R\mathbf{q}_2, R\mathbf{q}_3, R\mathbf{q}_4}^{s_1, s_2, s_3, s_4} = \Psi_{\mathbf{q}_1, \mathbf{q}_2, \mathbf{q}_3, \mathbf{q}_4}^{s_1, s_2, s_3, s_4}. \quad (68)$$

In our implementation, once a triplet or quartet of q points is selected, we check the possibility of reduction based on the aforementioned symmetries. If the triplet or quartet is reducible, the calculation of scattering matrix elements is skipped. The integration weights of the remaining irreducible

triplets or quartets are adjusted to reflect their multiplicity accordingly.

3. Monte Carlo integration for the scattering rates

Despite the improvements brought by the linear algebra formulation of the scattering matrix elements and the irreducible triplet and quartet, the computational cost remains significant due to the large number of elements involved, especially for fourth-order scattering.

This cost can be greatly reduced by recognizing that the computation of κ can be divided into distinct integrations. The first (outer) integration pertains to the contribution of each q point to the thermal conductivity, and can be written as a weighted sum over the irreducible q points

$$\kappa = \sum_{\mathbf{q}^{\mathrm{irr}}} w(\mathbf{q}^{\mathrm{irr}})\kappa(\mathbf{q}^{\mathrm{irr}}), \qquad (69)$$

where $w(\mathbf{q}^{\mathrm{irr}})$ is the integration weight of the irreducible q point $\mathbf{q}^{\mathrm{irr}}$ and $\kappa(\mathbf{q}^{\mathrm{irr}})$ represents the contribution of this q point to the thermal conductivity.

For each irreducible point and each vibrational mode, additional inner integrations are required to compute either the lifetime or the memory kernel at the isotopic, three-phonon, and/or four-phonon levels. Typically, a full grid is used for these integrations. However, the q-point grid densities needed to converge the different integrations are not necessarily the same. Specifically, the grid densities required to converge the linewidths are usually much lower than those needed for the outer integration for the thermal conductivity, as we will demonstrate in the applications section. Consequently, we implement a scheme to decouple these integrations, using a Monte Carlo method on the grids for the inner integrals. This decoupling significantly reduces the computational cost, with the only drawback being the introduction of (controllable, numerical) noise into the results.

Initially, a dense grid is generated, and all necessary harmonic quantities are computed on it. This grid, which will be used for the thermal conductivity integration, is referred to as the full grid. Then, for each scattering integration, we compute the contributions from a randomly selected subset of points of the dense grid, termed the Monte Carlo grid. To enhance the convergence of the integrals with respect to the Monte Carlo grid densities, the points are not selected entirely at random but rather using a stratified approach. In this approach, the full grid is subdivided into smaller sections, and points are randomly selected within these subdivisions. This ensures that the Monte Carlo grid samples the reciprocal space more uniformly, as shown in Fig. 2, thereby reducing the variance of the results.

It should be noted that a similar method has been proposed based on a maximum likelihood justification [55]. However, while the maximum likelihood approach is based on the relaxation time approximation (RTA), our Monte Carlo integration method is agnostic to the quantity computed and can be used for any approximation derived in this work. Moreover, our stratification step ensures that if the Monte Carlo and full grids have the same densities, all points on the full grid are used in the Monte Carlo grid, making the inner integrations
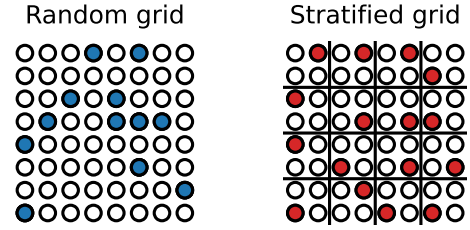

FIG. 2. Sketch of the method used to select q points for the Monte Carlo integrations. In this example, the full grid is 8×8 and we use a 4×4 grid for the Monte Carlo. For all grids, empty circles represent a point on the 8×8 full grid, while the colored circles represent the point selected for the Monte Carlo integration. When the Monte Carlo grid points are selected randomly, the distribution of points is less uniform and some part of reciprocal space can be left empty while others are "bunched" and oversampled. Moreover, the same point can be selected several times, reducing even more the uniformity of the distribution. With our stratified approach, represented on the bottom right, the subdivisions of the full grid ensure that reciprocal space is more uniformly sampled.

deterministic and yielding results equivalent to those obtained using the full grid in all steps.

Empirically we have found that this approach is more delicate for the computation of the off-diagonal terms of the scattering matrix. Indeed, if the terms that couple $\mathbf{q}$ points $(\mathbf{q}_1, \mathbf{q}_2)$ are skipped by the Monte Carlo scheme, then the corresponding entries of the matrix will be empty, thus neglecting coupling between the corresponding modes. While this should not be a problem for most systems, where collective effects contribute only a small fraction of the thermal conductivity, this neglect can be dramatic for materials such as graphene, where the collective contribution is the dominant source in heat transport [56]. Fortunately, the scattering matrix should respect some symmetries that can be enforced to alleviate this problem. For instance, given a rotation $\mathbf{R}$ belonging to the little group of $\mathbf{q}_1$, the scattering matrix should respect the relation

$$\Xi_{s_1 s_2}(\mathbf{R}\mathbf{q}_1, \mathbf{R}\mathbf{q}_2) = \Xi_{s_1 s_2}(\mathbf{q}_1, \mathbf{q}_2). \qquad (70)$$

In our implementation, we impose this symmetry in a way that fills the neglected entries of the scattering matrix with the average of the values of other equivalent entries.

V. APPLICATIONS

In this section, we demonstrate the performance and precision of the formalism and implementation detailed in this paper through various applications. To provide a comprehensive overview, we selected systems that represent the diverse regimes of thermal conductivity of thermal conductivity.

To quantify the different regimes of anharmonicity spanned by our sample materials, we use the anharmonicity measure introduced by Knoop *et al.* [13],

$$\sigma^{\mathrm{anh}}(T) = \sqrt{\frac{\sum_{i\alpha} \langle (\delta f_i^\alpha)^2 \rangle}{\sum_{i\alpha} \langle (f_i^\alpha)^2 \rangle}}, \qquad (71)$$

which, in the context of the mode-coupling theory, becomes a measure of the dissipative component of the dynamics of
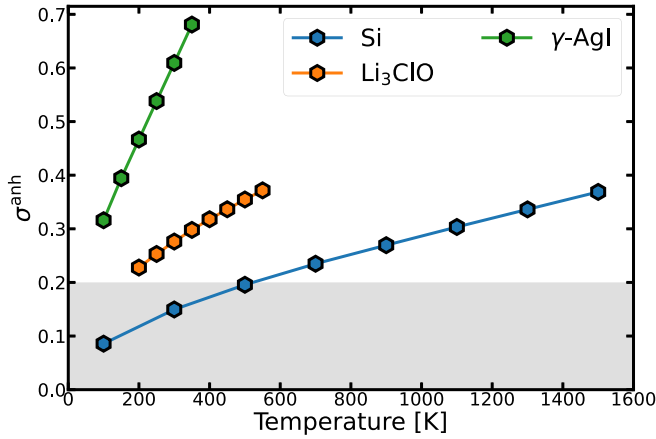
FIG. 3. Anharmonicity measure of the materials studied in this work. The gray zone indicates low anharmonicity.

the system [28]. In Fig. 3, we plot the anharmonicity measure for the different materials considered in this work. Going from low to high anharmonicity, our example systems are silicon [$\sigma^{\mathrm{anh}}(T = 300 \text{ K}) = 0.15$], Li$_3$ClO [$\sigma^{\mathrm{anh}}(T = 300 \text{ K}) = 0.28$]. and γ-AgI [$\sigma^{\mathrm{anh}}(T = 300 \text{ K}) = 0.61$].

A. Framework to compute the thermal conductivity and numerical details

The key components for computing the thermal conductivity tensor are the generalized IFC, which must be derived from molecular dynamics (MD), or path-integral molecular dynamics (PIMD) for systems with significant nuclear quantum effects. Performing MD simulations for each temperature with an *ab initio* description of the Born-Oppenheimer surface incurs substantial computational expense, even when using density functional theory (DFT). To mitigate this cost, we propose a comprehensive framework utilizing machine-learning interatomic potentials (MLIP) as surrogates for the *ab initio* Born-Oppenheimer surface in MD simulations.

Our framework consists of three main steps. First, starting from the crystal structure, a MLIP is trained using a self-consistent approach. In this method, the MLIP is iteratively trained and used to generate configurations, which are then added to a data set. It should be noted that configurations are added randomly, without any accuracy criterion, in order to sample uniformly the canonical ensemble of the systems. Using a variational principle, it can be shown that this approach yields an optimal MLIP according to the Kullback-Leibler divergence [57], enhancing accuracy for equilibrium properties at the expense of extrapolation capacity.

Once the MLIP is prepared, MD simulations in the NPT ensemble are conducted for each desired temperature to determine the system equilibrium volumes. This step is crucial because thermal expansion significantly affects the renormalization of phonon frequencies, thus impacting thermal conductivity. The equilibrated cell is then used for MD simulations in the NVT ensemble and configurations from these simulations are extracted to compute the generalized IFCs, which are subsequently used to calculate the thermal conductivity.

It should be noted that while we use classical MD in the remaining of this work, this scheme can easily be adapted to systems where nuclear quantum effects are important, by simply replacing classical MD with path-integral MD.

B. Computational parameters

For all applications, DFT calculations are performed with the ABINIT suite [58,59]. The MLIP employed in this work uses the moment tensor potential framework [60,61], with a level 22 and a 6-Å cutoff for every material. MD simulations are executed with the LAMMPS software [62], utilizing the Grønbech-Jensen-Farago (GJF) integrator [63] for Langevin dynamics. Finally, the computation of the generalized IFCs and the thermal conductivity tensor is carried out using the TDEP package [29]. More information on the computational details can be found in Appendix G.

For the NPT and NVT molecular dynamics, we used a $4 \times 4 \times 4$ supercell of Li$_3$ClO and AgI, totaling 350 and 512 atoms and a $3 \times 3 \times 3$ supercell for Si, with 216 atoms. The cutoff for the second-order generalized IFC was set at half the size of the supercell for all systems. For the third order, we used a cutoff of 7.3, 6.4, and 7.0 Å for Si, Li$_3$ClO, and AgI, respectively, while we used 4.0, 3.0, and 5.0 Å at the fourth order. These parameters were selected after careful convergence of the thermal conductivity tensor to below 1%.

All calculations for the thermal conductivity tensor were performed on the Lucia supercomputer of the CECI consortium in the Walloon region of Belgium. Each node in this cluster is equipped with two AMD EPYC 7763 processors, each featuring 64 cores with a clock speed of 2.45 GHz. For all timing measurements presented in this study, computations were conducted using a single node.

A direct comparison with experimental measurement could suffer from inaccuracies due to underlying DFT or MLIP biases. To better assess the accuracy of our theory for all systems, we also computed the thermal conductivity using approach-to-equilibrium molecular dynamics (AEMD) [64–68]. Being a nonequilibrium MD method, AEMD includes all orders of anharmonicity in its description of heat transport, with the drawback of a strong size dependence and absence of nuclear quantum effects. More details on our AEMD simulations are provided in Appendix H.

C. Silicon

We start our applications with silicon, a critical material in the semiconductor industry. Its thermal conductivity has been extensively researched both theoretically and experimentally, making it an ideal candidate for benchmarking the approaches developed in this work. Silicon is typically considered to exhibit low anharmonicity, and perturbation theory has been shown to accurately reproduce its transport properties, at least below room temperature. Due to the large mean-free path observed in this system at low temperature, which would require very large simulation boxes to obtain convergence, we only applied AEMD at 700, 1100, and 1500 K.

We begin with a demonstration of the speedup provided by using the linear algebra formulation of the scattering matrix of Eqs. (65) and (66). Figure 4 shows that the new formulation
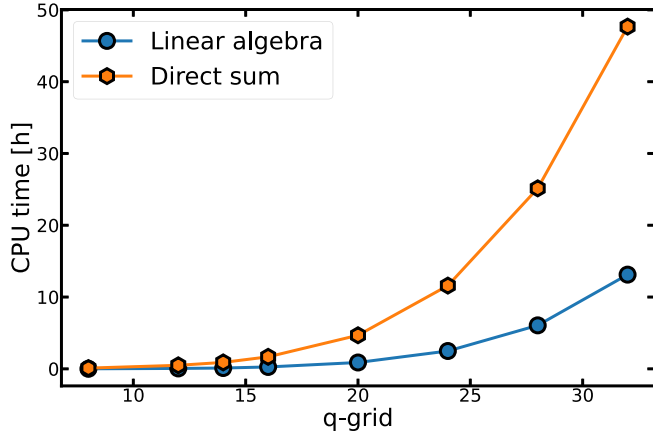
FIG. 4. Computational cost for the thermal conductivity of silicon with respect to the full grid density using third-order scattering. The blue dots show timings computed using the linear algebra scheme of Eqs. (65) and (66) while the timings using standard formulation of Eq. (32) are denoted by the orange hexagon.
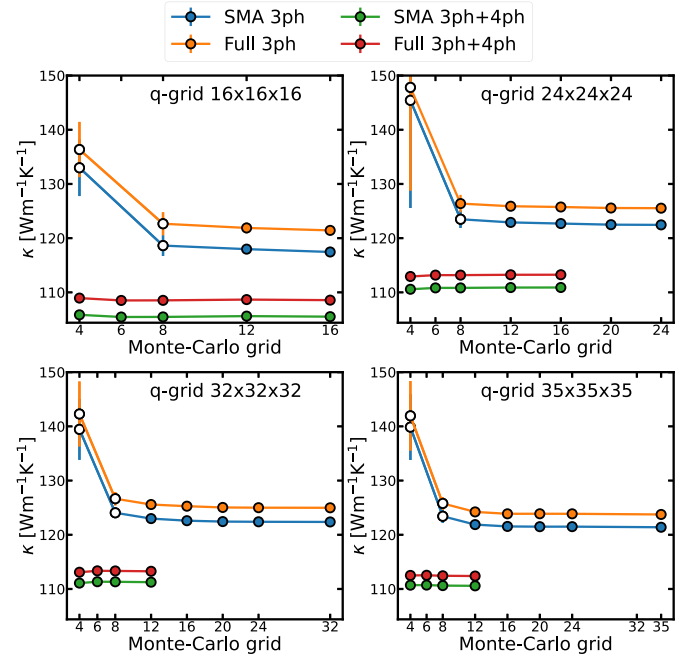

FIG. 5. Convergence of the thermal conductivity with respect to the Monte Carlo grid density for several full grid densities. Each point is the average over 10 calculations, except for the $12 \times 12 \times 12$ and $16 \times 16 \times 16$ grid with fourth order, and the error bars indicate the standard deviation. Results with fourth order including using the full grid as a Monte Carlo grid for the third order. SMA denotes results using the single-mode approximation and full grid denotes results computed using the full scattering matrix. Empty symbols indicate points with an error greater than 1 W/m/K compared to the largest grid.

allows for a drastic reduction of the CPU time, dividing for instance by more than 3 the computational cost with a **q**-point grid of $35 \times 35 \times 35$. It should be noted that, as the number of atoms in the unit cell or the order of the scattering matrix element increases, so does the speedup.

We continue with the improvement brought by the Monte Carlo integration scheme. Figure 5 illustrates the convergence of the thermal conductivity with respect to the Monte Carlo grid density, across several full grids. These results clearly demonstrate the decoupling between thermal conductivity and scattering integrations. For all the grids considered, an $8 \times 8 \times 8$ Monte Carlo grid achieves an error of less than 1% and a standard deviation of less than 1 W/m/K compared to scattering integration on the full grid. Notably, this convergence is independent of the type of approximation used, validating the effectiveness of our Monte Carlo scheme even for calculations beyond the single-mode approximation.

The efficiency of this scheme is further highlighted in Fig. 6, where it is shown that using a Monte Carlo grid of $12 \times 12 \times 12$ **q** points can reduce the wall time by an order of magnitude compared to a full grid. This acceleration becomes even more pronounced when fourth-order scattering processes are included. In such cases, even a $4 \times 4 \times 4$ grid is sufficient to converge the fourth-order contribution to thermal conductivity to less than 1 W/m/K, cutting computational cost by several orders of magnitude compared to full grid calculations.

The rapid convergence with smaller grids at the fourth order can be attributed to the combinatorially large number of scattering process it involves, combined with stochastic error cancellation. For instance, in a system like silicon, a $4 \times 4 \times 4$ grid incorporates a number of interactions on the same order of magnitude as the number of three-phonon processes within a $35 \times 35 \times 35$ **q**-point grid. While the specific grid densities required to converge the thermal conductivity tensor vary by system, this example demonstrates the significant computational acceleration achievable with our decoupling scheme.

Using a $35 \times 35 \times 35$ full grid along with a $16 \times 16 \times 16$ and a $8 \times 8 \times 8$ Monte Carlo grid for third- and fourth-order scattering, we computed the temperature dependence of silicon's lattice thermal conductivity. The results are displayed in Fig. 7. Our findings demonstrate good agreement with both
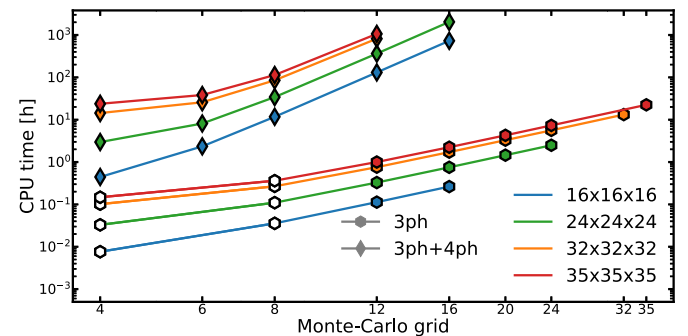

FIG. 6. Computational cost for the thermal conductivity of silicon with respect to the Monte Carlo grid density for different full grid densities. For the calculation involving fourth-order scattering, the Monte Carlo grid for the third-order contribution is set to the same density as the full grid. Each point is the average over 10 calculations (variance smaller than symbols), except for the $12 \times 12 \times 12$ and $16 \times 16 \times 16$ grid with fourth order. Empty symbols indicate points with an error greater than 1 W/m/K compared to the largest grid.
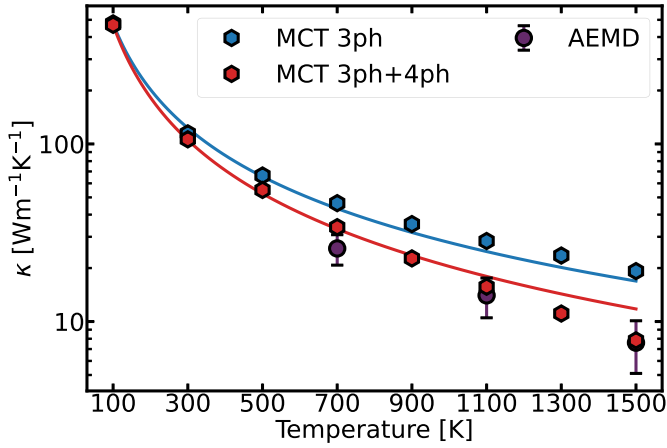
FIG. 7. Evolution of the thermal conductivity of silicon between 100 and 1500 K. Lines are fit of the results according to the model $\kappa(T) = A/T^C$, with A and C as fitting parameters.

FIG. 8. Evolution of the thermal conductivity of Li_3ClO with respect to temperature. Lines are fit of the results according to the model $\kappa(T) = A/T^C$, with A and C as fitting parameters. Full lines correspond to fit of MCT and AEMD results and the dashed lines denote the fit of results with temperature-independent IFC.

experimental [69] and theoretical results from the literature [37,70]. Notably, we observe an increasing significance of fourth-order scattering with rising temperatures, a trend corroborated by recent studies [70] and also reproduced with our AEMD simulations, with which the mode-coupling theory agrees very well.

It can be noted that our results show some discrepancy with previous results from the literature, both experimental [71] and theoretical [72,73]. Such discrepancies can be attributed to the MLIP used in this work. It has been shown that MLIP errors on the prediction of forces can introduce an underestimation of the thermal conductivity tensor through the introduction of an effective scattering channel [74,75]. While perturbative theory can be quite insensitive to the force's error, the mode-coupling theory is built on averages of thermally excited configurations and a similar mechanism could be at play in this case. However, setting up a correction scheme, such as the ones introduced for (non)equilibrium molecular dynamics methods, is out of the scope of this work, and the agreement between AEMD and the mode-coupling theory provides a clear validation of the latter.

D. Li_3ClO

The second system we studied is Li_3ClO, an antiperovskite with a rich lithium composition that makes it a candidate future generation electrolyte in solid-state batteries [76,77]. The thermal conductivity of this system has been studied using both lattice dynamics approaches, in the perturbative regime [38,78], and molecular dynamics within the Green-Kubo formalism [78]. Li_3ClO can be considered as a system with medium anharmonicity, as can be attested by its $\sigma^{\text{anh}}(T)$ going from 0.23 to 0.37 when increasing the temperature from 200 to 550 K.

For this system, we use a $24 \times 24 \times 24$ full grid alongside an $8 \times 8 \times 8$ Monte Carlo grid for third-order scattering and a $3 \times 3 \times 3$ grid for fourth-order interactions. This setup provides converged results with a computational cost of approximately 1.5 CPU hours when only third-order scattering is included, and around 120 CPU hours when fourth-order
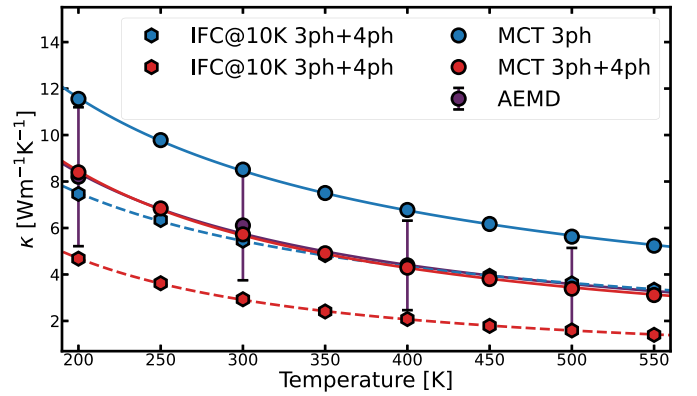
scattering is also accounted for. To examine the influence of generalized IFC, thermal conductivity was also calculated across all temperatures using IFCs extracted at 10 K. Although not exactly equivalent to purely harmonic or perturbative results, these results should give an indication of possible failures of perturbative theory.

Our findings, summarized in Fig. 8, reveal a significant contribution from fourth-order scattering, even at the lowest temperatures considered. At 200 K, the inclusion of fourth-order effects reduces thermal conductivity by approximately 37%. This impact of fourth-order scattering persists whether or not the temperature dependence of the IFCs is included in the heat transport calculations. However, incorporating this temperature dependence is critical for an accurate description of the system's thermal conductivity. When neglected, the third-order results yield a misleading agreement between AEMD and lattice dynamics calculations, and the inclusion of fourth-order scattering in the low-T harmonic model leads to a significant underestimation of κ across all temperatures. In contrast, mode-coupling theory restores agreement with molecular dynamics simulations, provided that fourth-order scattering is also taken into account.

E. γ-AgI

As an example of a strongly anharmonic material, we apply our formalism to silver iodide in its zinc-blende γ phase, a silver halide with applications in photovoltaic devices and solid-state batteries. Despite its simple crystal structure, AgI is known for its ultralow thermal conductivity, measured to be approximately 0.4 W/m/K at room temperature [26]. This value is significantly overestimated by conventional perturbation theory accounting only for three-phonon interactions, which predicts a thermal conductivity of 2.1 W/m/K [79]. Recent studies [26,80] have reconciled experimental and theoretical discrepancies by highlighting the critical role of phonon renormalization and high-order scattering processes. Reference [80] suggested that scattering processes beyond fourth order are necessary to accurately reproduce the ultralow thermal conductivity of AgI, even when
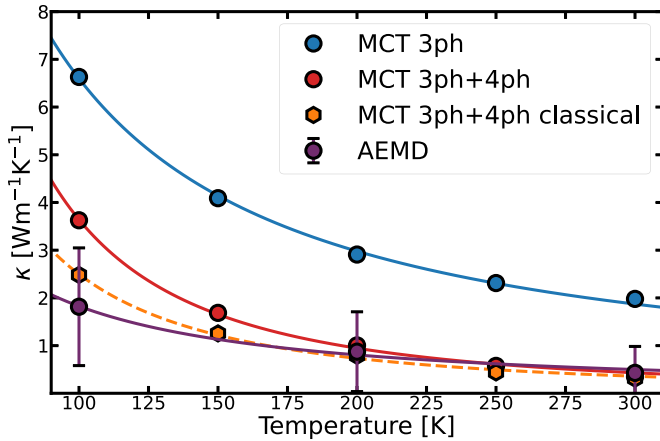
FIG. 9. Evolution of the thermal conductivity of AgI with respect to temperature. Lines are fit of the results according to the model $\kappa(T) = A/T^C$, with A and C as fitting parameters. The dashed lines are fit of the results using classical occupation for the computation of κ.

using anharmonic phonon theories. However, it is important to note that their work did not rely on the mode-coupling definition of anharmonic phonons. While they used a similar approach to mode-coupling theory (MCT) for calculating noninteracting phonons, the higher-order generalized IFC were computed using a different method, with all orders greater than second fitted simultaneously to molecular dynamics data instead of successively.

For this system, we employed a $32 \times 32 \times 32$ full grid, along with $16 \times 16 \times 16$ and $6 \times 6 \times 6$ Monte Carlo grids for third- and fourth-order scattering, yielding a computational cost of approximately 0.5 CPU hours and 14 CPU hours, respectively. Our results, shown in Fig. 9, demonstrate the the mode-coupling theory with fourth-order scattering is sufficient to produce converged results, yielding a thermal conductivity of about 0.3 W/m/K at room temperature, consistent with both experimental data and AEMD results. These findings underscore the importance of a correct definition for generalized IFCs. While second-order IFCs are crucial for accuracy, a consistent definition of higher-order IFCs is equally essential to capture the full anharmonic behavior of the system. In the end, using a classical distribution instead of the Bose-Einstein, our mode-coupling results are able to reproduce AEMD for the whole range of temperature considered, despite the strong anharmonicity of this system. A strong advantage of our mode coupling over MD techniques is the absence of finite-size artifacts and the insight in mode contributions and scattering mechanisms.

VI. CONCLUSION

In recent years, the limitations of the harmonic approximation have become more and more apparent, producing a surge in the use of temperature-dependent phonon theories. In this work, we provided a detailed derivation of the theory of thermal conductivity in the framework of the mode-coupling theory of anharmonic lattice dynamics, thus justifying the use of temperature-dependent phonons as a means to study heat transport in materials.

Following a summary of the mode-coupling theory for anharmonic crystals, the starting point of our derivation consists in the introduction of a consistent formulation of the heat current. Using the Green-Kubo formula, we obtain an equation for the thermal conductivity tensor involving correlation functions for the phonon operators. Our final result for the κ tensor includes single-mode, collective, and off-diagonal contributions, which makes it valid for a large range of systems, from simple to complex crystals with low or high anharmonicity.

Due to the extreme computational cost incurred in the computation of scattering processes, we also present numerical strategies to increase the efficiency of thermal conductivity calculations, and fully converge even the most advanced calculations with dense grids. This acceleration is enabled by reducing the cost of each scattering process, through the use of a linear algebra formulation of the scattering matrix elements, and by reducing the number of processes to be computed. For this second point, we implemented both symmetry reduction and Monte Carlo integration schemes. All these improvements result in a drastic reduction of the computational cost, and even enable the computation of thermal conductivity with up to fourth-order scattering, in complex systems for which it would otherwise be too expensive.

Finally, we apply our implementation to systems going from low to high anharmonicity. This demonstrates the validity of the mode-coupling theory of anharmonic lattice dynamics to compute transport properties, as well as the efficiency of our implementation.

Regarding the limitations of our work, we stress the two main approximations made. The first concerns the use of the Markovian limit, in which the full frequency-dependent phonon spectral functions are replaced by Lorentzians characterized only by their center [the frequency $\Omega_s(\mathbf{q})$] and width [the linewidths $\Gamma_s^M(\mathbf{q})$]. While this approximation is ubiquitous in the literature, the more complicated spectral functions observed in some anharmonic materials raise questions on the validity of the Markovian approximation in such cases. One should notice that in this work, we already derived Eq. (51), which goes beyond the Markovian limit. The other main approximation is the neglect of a part of the heat current operator involving the random force and memory kernel. As the anharmonicity of a material increases, their importance is expected to increase. However, these contributions have never been considered, and their importance in realistic materials is unknown: our work provides a starting point to quantify these terms.

APPENDIX A: RELATION BETWEEN SOME CORRELATION FUNCTIONS

If the definition of a classical correlation function is unambiguous, there exist an infinite number of ways to define a quantum correlation function. In this Appendix, we give the relation between the Kubo correlation function used throughout this work and other types of correlation functions used to obtain some of the relations appearing in the main text. Most of the equalities given here use properties of the Bose-Einstein distribution, in particular $n(-\omega) = -[n(\omega) + 1]$ or $e^{-\hbar\omega/k_B T} = n(\omega)/[n(\omega) + 1]$.

The first important relation is that between the Kubo correlation function and the generalized susceptibility, which stems from the fluctuation-dissipation theorem [28]

$$\chi''(\omega) = \frac{\omega}{2k_B T} G(\omega). \tag{A1}$$

Other important quantum correlation functions are the lesser and greater ones, which is defined for two operators A and B as

$$G^<(t) = \langle AB(t)\rangle\, \theta(t), \tag{A2}$$

$$G^>(t) = \langle AB(t)\rangle\, \theta(-t), \tag{A3}$$

where $\theta(t)$ is the Heaviside function. Decomposing the correlation functions on the eigenstates of the Hamiltonian into a Lehmann representation and using the properties of the Bose-Einstein distribution, one can show that the lesser, greater, and Kubo correlation functions are related by

$$G^<(\omega) = \frac{\hbar\omega}{k_B T} n(\omega) G(\omega) = n(\omega)\chi''(\omega), \tag{A4}$$

$$G^<(\omega) = \frac{\hbar\omega}{k_B T}[n(\omega) + 1] G(\omega) = [n(\omega) + 1]\chi''(\omega). \tag{A5}$$

APPENDIX B: DECOUPLING KUBO CORRELATION FUNCTIONS

In this Appendix, we formally derive the decoupling of four-point Kubo correlation functions of the form $(AB, C(t), D(t))$, where A, B, C, and D are arbitrary operators. In our previous work, we used the decoupling

$$(AB, C(t)D(t)) \approx (A, C(t))(B, D(t)) + \mathrm{perm} \tag{B1}$$

with perm being the permutations of the operators in the four-point correlation function. However, this decoupling corresponds to a semiclassical approximation mostly valid at

high temperature, and neglects some of the coupling between the decoupled two-point function's correlation due to the imaginary-time integration of the Kubo correlations. A more formal decoupling keeping this quantum coupling is given by

$$(AB, C(t)D(t)) = k_B T \int_0^\beta d\lambda\, \langle A(i\hbar\lambda)B(i\hbar\lambda)C(t)D(t)\rangle$$

$$\approx k_B T \int_0^\beta d\lambda[\langle A(i\hbar\lambda)C(t)\rangle\,\langle B(i\hbar\lambda)D(t)\rangle$$

$$+ \langle A(i\hbar\lambda)D(t)\rangle\,\langle B(i\hbar\lambda)C(t)\rangle$$

$$+ \langle A(i\hbar\lambda)B(i\hbar\lambda)\rangle\,\langle C(t)D(t)\rangle]. \tag{B2}$$

We can use the Fourier transform to express the first term of this equation in terms of the standard correlation function

$$\int_0^\beta d\lambda\, \langle A(i\hbar\lambda)C(t)\rangle\,\langle B(i\hbar\lambda)D(t)\rangle$$

$$= \int_{-\infty}^\infty d\omega_1 d\omega_2 G^<_{AC}(\omega_1) G^<_{BD}(\omega_2) e^{-i(\omega_1+\omega_2)t}$$

$$\times \int_0^\beta d\lambda\, e^{-\hbar(\omega_1+\omega_2)\lambda}$$

$$= \int_{-\infty}^\infty d\omega_1 d\omega_2 G^<_{AC}(\omega_1) G^<_{BD}(\omega_2) \frac{e^{\beta\hbar(\omega_1+\omega_2)} - 1}{\hbar(\omega_1 + \omega_2)}$$

$$\times e^{-i(\omega_1+\omega_2)t}$$

$$= \int_{-\infty}^\infty d\omega \frac{e^{\beta\hbar\omega} - 1}{\hbar\omega} e^{-i\omega t} \int_{-\infty}^\infty d\omega' G^<_{AC}(\omega') G^<_{BD}(\omega - \omega'). \tag{B3}$$

Going further, we can also integrate this result from $t = 0$ to infinity

$$\int_0^\infty dt\, \langle A(i\hbar\lambda)C(t)\rangle\,\langle B(i\hbar\lambda)D(t)\rangle$$

$$= \int d\omega \frac{e^{\beta\hbar\omega} - 1}{\hbar\omega} \int d\omega' G^<_{AC}(\omega') G^<_{BD}(\omega - \omega') \int_0^\infty dt\, e^{-i\omega t}$$

$$= \pi \int_{-\infty}^\infty d\omega' G^<_{AC}(\omega') G^<_{BD}(-\omega')$$

$$= \pi \int_{-\infty}^\infty d\omega' n(\omega')[n(\omega') + 1]\chi''_{AC}(\omega')\chi''_{BD}(\omega'), \tag{B4}$$

where we used $G^<(\omega) = n(\omega)\chi''(\omega)$ and $G^<(-\omega) = G^>(\omega) = [n(\omega) + 1]\chi''(\omega)$ from Appendix A.

APPENDIX C: DERIVATION OF THE MARKOVIAN APPROXIMATION

The Markovian approximation is founded on the assumption that the bath, represented by the memory kernel, follows a dynamic on a much slower timescale than the dynamical variable. Effectively, this assumption translates into taking the infinite-time limit of the convolution appearing in the generalized Langevin equation

$$\int_0^t ds\, \Gamma_s(\mathbf{q}, s)\dot{G}_s(\mathbf{q}, t - s) \to \lim_{t\to\infty} \int_0^t ds\, \Gamma_s(\mathbf{q}, t-s)\dot{G}_s(\mathbf{q}, s), \tag{C1}$$

where we used the symmetry of convolutions $\int_0^t ds\, f(s)g(t-s) = \int_0^t ds\, f(t-s)g(s)$. Furthermore, assuming that interactions with the bath are weak, the correlation function $\dot{G}_s(\mathbf{q}, t)$ in this equation can be approximated as acting as a delta function centered on $\Omega_s(\mathbf{q})$ in frequency space. Using these approximations in the memory kernel convolution gives

$$
\int_0^\infty ds\, \Gamma_s(\mathbf{q}, t-s)\dot{G}_s(\mathbf{q}, s)
$$
$$
= \int_{-\infty}^\infty d\omega_1 d\omega_2 \Gamma_s(\mathbf{q}, \omega_1) G_s(\mathbf{q}, \omega_2)\omega_2 \int_0^\infty ds\, e^{i\omega_1(t-s)}e^{i\omega_2 s}
$$
$$
= \int_{-\infty}^\infty d\omega\, \Gamma_s(\mathbf{q}, \omega) G_s(\mathbf{q}, \omega)\omega e^{i\omega t}
$$
$$
\approx \Gamma_s(\mathbf{q}, \Omega_s(\mathbf{q})) \int_{-\infty}^\infty d\omega\, G_s(\mathbf{q}, \omega)\omega e^{i\omega t}
$$
$$
= \Gamma_s^M(\mathbf{q})\dot{G}_s(\mathbf{q}, t), \tag{C2}
$$

where we defined the Markovian scattering rate $\Gamma_s^M(\mathbf{q}) = \Gamma_s(\mathbf{q}, \Omega_s(\mathbf{q}))$ found in the main text.

APPENDIX D: DERIVATION OF THE SCATTERING MATRIX

In this Appendix, we derive the scattering matrix by computing the time integral of the four-point correlation function

$$
(A_{s_1}(\mathbf{q}_1)B_{s_1}(\mathbf{q}_1), A_{s_2}(\mathbf{q}_2, t)B_{s_2}(\mathbf{q}_2, t)). \tag{D1}
$$

To facilitate the derivation, we introduce the composite operator

$$
C_s(\mathbf{q}, t) = A_s(\mathbf{q}, t)B_s(\mathbf{q}, t) \tag{D2}
$$

whose correlation function is denoted by

$$
Y_{s_1, s_2}(\mathbf{q}_1, \mathbf{q}_2, t) = (C_{s_1}(\mathbf{q}_1), C_{s_2}(\mathbf{q}_2)). \tag{D3}
$$

Our task is to compute the integral of this correlation function, which can be recognized as its zero-frequency Laplace transform.

From the definitions of the operators $A_s(\mathbf{q}, t)$ and $B_s(\mathbf{q}, t)$, and by projecting the Mori-Zwanzig equation of motion for $\dot{\mathbf{p}}$ [28] onto the phonon modes, we obtain the time derivative of these operators

$$
\dot{A}_s(\mathbf{q}, t) = -i\Omega_s(\mathbf{q})B_s(\mathbf{q}, t), \tag{D4}
$$

$$
\dot{B}_s(\mathbf{q}, t) = i\Omega_s(\mathbf{q})A_s(\mathbf{q}, t)
$$
$$
+ \frac{i}{\Omega_s(\mathbf{q})}\sum_{s'\mathbf{q}'}\int_0^t ds\, K_{ss'}(\mathbf{q}, \mathbf{q}', s)B_{s'}(\mathbf{q}', t-s)
$$
$$
+ \frac{i}{\Omega_s(\mathbf{q})}\delta A_s(\mathbf{q}, t). \tag{D5}
$$

The derivative of the composite operator $C_s(\mathbf{q}, t)$ can thus be expressed as

$$
\dot{C}_s(\mathbf{q}, t) = \dot{A}_s(\mathbf{q}, t)B_s(\mathbf{q}, t) + A_s(\mathbf{q}, t)\dot{B}_s(\mathbf{q}, t)
$$
$$
= -i\Omega_s(\mathbf{q})B_s(\mathbf{q}, t)B_s(\mathbf{q}, t) + i\Omega_s(\mathbf{q})A_s(\mathbf{q}, t)A_s(\mathbf{q}, t)
$$
$$
+ \frac{iA_s(\mathbf{q}, t)}{\Omega_s(\mathbf{q})}\sum_{s'\mathbf{q}'}\int_0^t ds\, K_{ss'}(\mathbf{q}\mathbf{q}', s)B_{s'}(\mathbf{q}', t-s)
$$

$$
- \frac{i}{\Omega_s(\mathbf{q})}\delta A_s(\mathbf{q}, t)A_s(\mathbf{q}, t). \tag{D6}
$$

Multiplying by $C_s(\mathbf{q})$, taking the Kubo average, and using the decoupling scheme, we obtain the following equation of motion for $Y_{s_1 s_2}(\mathbf{q}_1, \mathbf{q}_2, t)$:

$$
\dot{Y}_{s_1 s_2}(\mathbf{q}_1\mathbf{q}_2, t) = \sum_{s_3\mathbf{q}_3}\int_0^t ds\, K_{s_2 s_3}(\mathbf{q}_2\mathbf{q}_3, s)Y_{s_1 s_3}(\mathbf{q}_1\mathbf{q}_3, t-s) \tag{D7}
$$

or $\dot{\mathbf{Y}}(t) = \int_0^t ds\, \mathbf{K}(s)\mathbf{Y}(t-s)$ in matrix form. From this equation of motion, we find that the Laplace transform of $\mathbf{Y}(t)$ can be written $\widetilde{\mathbf{Y}}(\omega) = [\omega - \widetilde{\mathbf{K}}(\omega)]^{-1}\mathbf{Y}$, leading to the final result

$$
\widetilde{\mathbf{Y}}(0) = \widetilde{\mathbf{K}}(0)^{-1}\mathbf{Y}, \tag{D8}
$$

where $\widetilde{\mathbf{Y}}(\omega)$ and $\widetilde{\mathbf{K}}(\omega)$ are the Laplace transform of the four-point correlation function and the memory kernel, respectively. Applying the decoupling rule for the $\mathbf{Y}$ matrix, it can be shown that it is a diagonal matrix with entries

$$
Y_{ss}(\mathbf{q}, \mathbf{q}) = \Omega_s^2(\mathbf{q})n_s(\mathbf{q})[n_s(\mathbf{q}) + 1] = k_B T^2 c_s(\mathbf{q}). \tag{D9}
$$

Furthermore, we can recognize the scattering matrix of the main text as the Markovian limit of the memory kernel, including off-diagonal terms

$$
\Xi_{s_1 s_2}(\mathbf{q}_1, \mathbf{q}_2) = K_{s_1, s_2}(\mathbf{q}_1, \mathbf{q}_2, \Omega_{s_1}(\mathbf{q}_1))
$$
$$
= \Gamma_{s_1}^M(\mathbf{q}_1)\delta_{\mathbf{q}_1\mathbf{q}_2}\delta_{s_1 s_2}
$$
$$
+ \frac{\Omega_{s_2}(\mathbf{q}_2)}{\Omega_{s_1}(\mathbf{q}_1)}\Bigg[\sum_{\mathbf{q}_3 s_3}\big[\Gamma_{s_1 s_2 s_3}^{(3)}(\mathbf{q}_1, \mathbf{q}_2, \mathbf{q}_3, \Omega_{s_1}(\mathbf{q}_1))
$$
$$
+ \Gamma_{s_1 s_3 s_2}^{(3)}(\mathbf{q}_1, \mathbf{q}_3, \mathbf{q}_2, \Omega_{s_1}(\mathbf{q}_1))\big]
$$
$$
+ \sum_{\mathbf{q}_3 s_3 \mathbf{q}_4 s_4}\big[\Gamma_{s_1 s_2 s_3 s_4}^{(4)}(\mathbf{q}_1, \mathbf{q}_2, \mathbf{q}_3, \mathbf{q}_4, \Omega_{s_1}(\mathbf{q}_1))
$$
$$
+ \text{perm}\big]
$$
$$
+ \Gamma_{s_1 s_2}^{\text{iso}}(\mathbf{q}_1, \mathbf{q}_2, \Omega_{s_1}(\mathbf{q}_1))\Bigg], \tag{D10}
$$

where perm denotes all permutations of the second, third, and fourth phonons in $\Gamma_{s_1 s_2 s_3 s_4}^{(4)}(\mathbf{q}_1, \mathbf{q}_2, \mathbf{q}_3, \mathbf{q}_4, \Omega_{s_1}(\mathbf{q}_1))$.

APPENDIX E: COMPARISON WITH THE PHONON BOLTZMANN EQUATION

The central quantity in the phonon Boltzmann equation (PBE) is the phonon occupation $n_s(\mathbf{q}, t)$ [39]. To facilitate comparison with the results in the main text, we assume that the system is in a steady state with a homogeneous and constant temperature gradient. Under these conditions, the spatial and temporal derivatives of the phonon occupation vanish, allowing us to eliminate the time dependence and work directly with $n_s(\mathbf{q})$. Noting the equilibrium phonon occupation as $\bar{n}_s[\mathbf{q} = (e^{\beta\hbar\Omega_s(\mathbf{q})} - 1)^{-1}]$, the Boltzmann equation is expressed as a balance between the temperature gradient and phonon scattering processes

$$
\frac{\partial \bar{n}_s(\mathbf{q})}{\partial T}\mathbf{v}_\mathbf{q}^s \nabla T = -\sum_{s'\mathbf{q}'}\Xi(\mathbf{q}s, \mathbf{q}'s', s)\delta n_{s'}(\mathbf{q}'), \tag{E1}
$$

where $\delta n_s(\mathbf{q}) = n_s(\mathbf{q}) - \bar{n}_s(\mathbf{q})$ represents the deviation of the phonon occupation from equilibrium, and $\Xi(\mathbf{q}s, \mathbf{q}'s')$ is the phonon scattering matrix introduced in the main text.

Assuming a linearized form of the deviation

$$n_s(\mathbf{q}) = \bar{n}_s(\mathbf{q}) + \rho_s(\mathbf{q})\nabla T \qquad (E2)$$

the PBE reduces to

$$\frac{\partial \bar{n}_s(\mathbf{q})}{\partial T}\mathbf{v}_{\mathbf{q}}^s = -\sum_{s'\mathbf{q}'} \Xi(\mathbf{q}s, \mathbf{q}', s)\boldsymbol{\rho}_{s'}(\mathbf{q}'). \qquad (E3)$$

Recognizing this as a matrix equation, we solve for $\rho_s(\mathbf{q})$ by inverting the scattering matrix:

$$\rho_s(\mathbf{q}) = -\sum_{s'\mathbf{q}'} \frac{\partial n_s(\mathbf{q})}{\partial T} \Xi^{-1}(s\mathbf{q}, s'\mathbf{q}')\mathbf{v}_{\mathbf{q}'}^{s'}, \qquad (E4)$$

where we used the fact that the scattering matrix is positive definite, hence symmetric.

To compute the thermal conductivity tensor, we introduce the heat current operator in the harmonic approximation

$$\mathcal{J}^{\text{harm}}(t) = -\frac{1}{V}\sum_{\mathbf{q},s} \hbar\Omega_s(\mathbf{q})\mathbf{v}_{\mathbf{q}}^s \delta n_s(\mathbf{q}, t). \qquad (E5)$$

Applying Fourier's law, we express the thermal conductivity tensor as

$$\boldsymbol{\kappa}^{\text{PBE}} = \frac{\langle \mathcal{J}^{\text{harm}} \rangle}{\nabla T}$$

$$= -\frac{1}{V}\sum_{\mathbf{q},s} \hbar\Omega_s(\mathbf{q})\mathbf{v}_{\mathbf{q}}^s \boldsymbol{\rho}_s(\mathbf{q}). \qquad (E6)$$

Substituting our solution for $\rho_s(\mathbf{q})$, we obtain

$$\boldsymbol{\kappa}^{\text{PBE}} = -\frac{1}{V}\sum_{s\mathbf{q}}\sum_{s'\mathbf{q}'} \hbar\Omega_s(\mathbf{q})\frac{\partial n_s(\mathbf{q})}{\partial T}\mathbf{v}_{\mathbf{q}}^s \otimes \mathbf{v}_{\mathbf{q}'}^{s'} \Xi^{-1}(s\mathbf{q}, s'\mathbf{q}')$$

$$= \frac{1}{V}\sum_{s\mathbf{q}}\sum_{s'\mathbf{q}'} c_s(\mathbf{q})\mathbf{v}_{\mathbf{q}}^s \otimes \mathbf{v}_{\mathbf{q}'}^{s'} \Xi^{-1}(s\mathbf{q}, s'\mathbf{q}') \qquad (E7)$$

which coincide with Eq. (47) of the main text.

APPENDIX F: TREATMENT OF DEGENERACIES

In reciprocal space, the generalized group velocities can be seen through Hellman-Feynman theorem as the derivative of the dynamical matrix projected on phonons s and s' of the same $\mathbf{q}$ point. We can write this formally as

$$\mathbf{v}_{\mathbf{q}}^{ss'} = \frac{1}{2\sqrt{2\Omega_s(\mathbf{q})\Omega_{s'}(\mathbf{q})}} \langle s, \mathbf{q}| \nabla_{\mathbf{q}}\boldsymbol{\Phi}(\mathbf{q}) |s', \mathbf{q}\rangle, \qquad (F1)$$

where we introduced the notation

$$\langle s, \mathbf{q}| \mathbf{O} |s', \mathbf{q}\rangle = \sum_{i\alpha, j\beta} \varepsilon_s^{i\alpha*}(\mathbf{q})\varepsilon_{s'}^{j\beta}(\mathbf{q})O_{i\alpha}^{j\beta}, \qquad (F2)$$

where $\mathbf{O}$ is a $3N_{\text{at}} \times 3N_{\text{at}}$ matrix. For degenerate modes, a direct calculation with this formula is ill defined and we use instead degenerate perturbation theory. We start by computing the $N_{\text{degen}} \times N_{\text{degen}}$ matrix $\mathbf{h}$ composed of the derivative of the dynamical matrix only for modes s_i and s_j in the degenerate

TABLE I. Parameters for the DFT calculations for each of the systems used in the applications.

System	XC functional	**k**-point grid	Cutoff (Ha)
Si	PBEsol[a] [82]	$12 \times 12 \times 12$	25
Li$_3$ClO	PBE[b]	$8 \times 8 \times 8$	32
AgI	PBE[b]	$8 \times 8 \times 8$	32

[a]Norm conserving, from pseudodojo [83].
[b]PAW, from GPAW pseudopotential data set [84].

subspace

$$h_{ij}^{\alpha} = \langle s_i, \mathbf{q}| \frac{\partial}{\partial q^{\alpha}}\boldsymbol{\Phi}(\mathbf{q}) |s_j, \mathbf{q}\rangle. \qquad (F3)$$

Then, the diagonal components of the generalized group velocities for each of the degenerate modes are computed as the average of the eigenvalues λ_i of $\mathbf{h}$:

$$v_{\mathbf{q}}^{s,\alpha} = \frac{1}{2\Omega_s(\mathbf{q})}\frac{1}{N_{\text{degen}}}\sum_i \lambda_i \qquad (F4)$$

while the off-diagonal components vanish:

$$v_{\mathbf{q}}^{s_i s_j, \alpha} = 0. \qquad (F5)$$

APPENDIX G: ACCURACY OF THE MACHINE-LEARNING INTERATOMIC POTENTIALS

In this Appendix, we give the computational details for the fitting of the machine-learning interatomic potential used in the applications of Sec. V. In all cases, the MLIP were constructed by fitting on *ab initio* data computed with DFT using the ABINIT package [58,59], with the data set created following the scheme presented in Sec. V A. The functional, **k**-point grid and kinetic energy cutoff used for each system are detailed in Table I, with the parameters selected to give a total energy accuracy better than 1 meV/atom. For Li$_3$ClO and AgI, Born effective charges and dielectric constant were computed at the ground-state volumes using DFPT as implemented in ABINIT. The nonanalytical long-range corrections were then applied using the method described in the Supplemental Materials of [81].

On Fig. 10, we show the correlations between DFT and MLIP energy, forces and stress for each system while Table II compares ground-state lattice parameters and volume. For all materials studied here, the agreement is excellent, both for the error measure given by the root-mean-squared error and the mean absolute error and the comparison of the lattice parameters.

TABLE II. Comparison between the ground-state lattice constant computed with DFT and the MLIP.

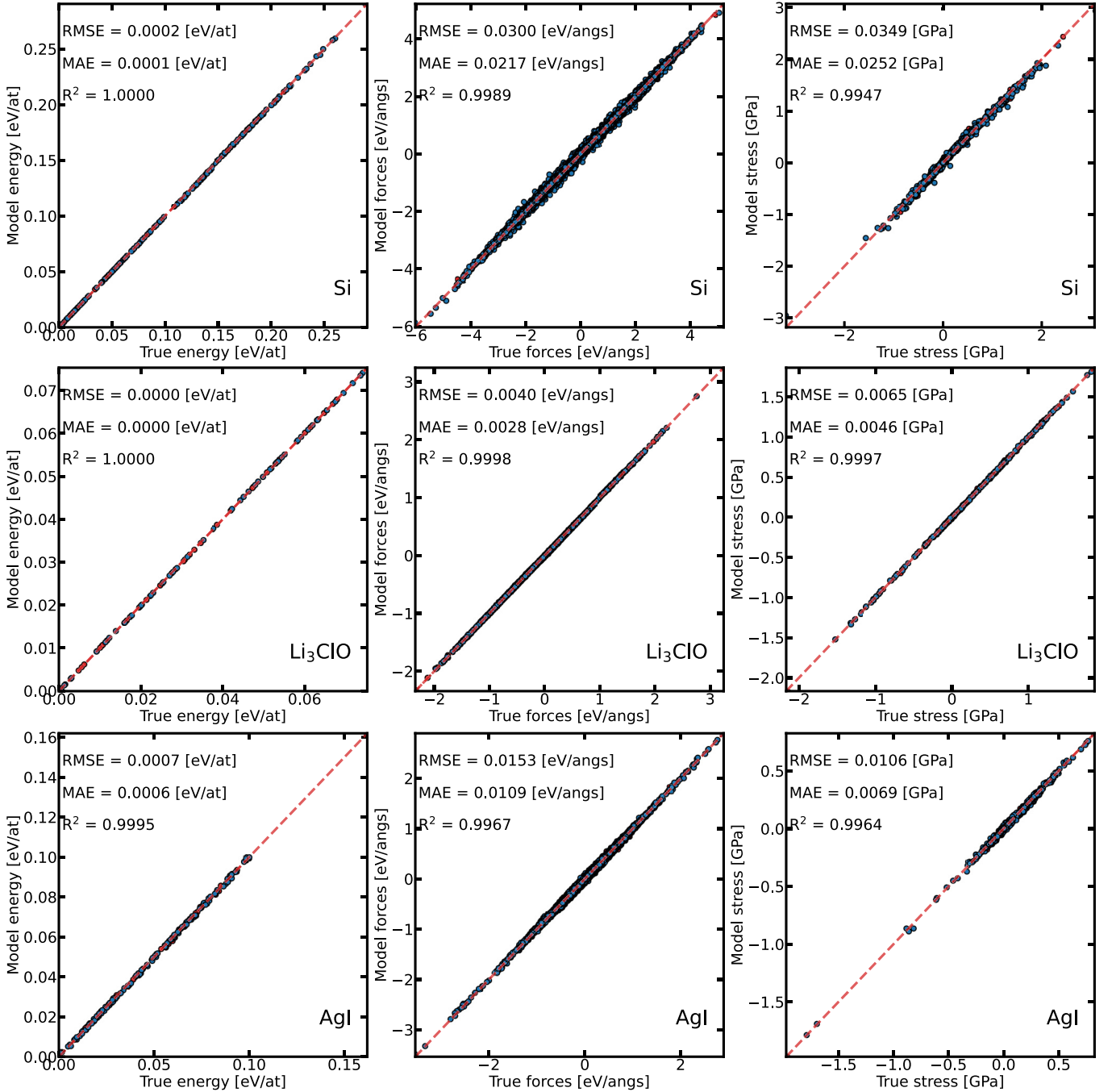| System	DFT		MLIP	
	a (Å)	Volume (Å^3)	a (Å)	Volume (Å^3)
Si	5.431	20.026	5.431	20.026
Li$_3$ClO	3.916	12.010	3.916	12.010
AgI	6.654	36.834	6.654	36.828

FIG. 10. Correlation between DFT and MLIP energy, forces, and stress for all the MLIP used in this work.

APPENDIX H: APPROACH TO EQUILIBRIUM MOLECULAR DYNAMICS

The approach-to-equilibrium molecular dynamics (AEMD) [64–68] method directly applies Fourier's law, utilizing the time evolution of temperature governed by the heat equation to estimate the thermal conductivity. In this approach, the simulation box is initially divided into two regions: a hot region and cold region, thermostatted at temperatures $T + \Delta T/2$ and $T - \Delta T/2$, respectively. After the regions reach constrained equilibrium, the thermostats are removed, allowing the system to relax towards a global equilibrium. During this relaxation, the time evolution of the temperature difference between the two regions is described by the heat equation

$$\Delta T(t) = \sum_{m=0}^{\infty} \frac{8\Delta T(0)}{(2m+1)^2 \pi^2} e^{-(2m+1)^2 t/\tau}, \quad \text{(H1)}$$

where τ is the decay time, which is related to the system's thermal conductivity through the equation

$$\kappa(L) = \frac{LC_v}{4\pi^2 S} \frac{1}{\tau}. \quad \text{(H2)}$$

Here, L is the length of the system along the temperature gradient, C_v is the heat capacity, and S is the cross-sectional area perpendicular to the heat flow.

As a real-space method, AEMD is subject to finite-size effects. Recently, Sheng *et al.* [64] used lattice dynamics analysis to derive a model that fits and extrapolates the size dependence of thermal conductivity from AEMD. Their model is expressed as

$$\hat{\kappa}(L) = \frac{\kappa_1}{1 + \left(\frac{2\pi \Lambda_1}{L}\right)^2} + \frac{\kappa_2}{1 + \left(\frac{2\pi \Lambda_2}{L}\right)^2}, \qquad \text{(H3)}$$

where κ_1, κ_2, Λ_1, and Λ_2 are fitting parameters.

In our simulations, we applied a temperature difference of $\Delta T = 200$ K. To fit the time evolution of the temperature difference, using 10 terms of Eq. (H1) was sufficient to accurately converge the decay time τ. For each system and temperature, thermal conductivity was computed for various systems length L, and the results were extrapolated to the bulk limit using Eq. (H3). The lengths of the system along the temperature gradient were 273, 546, 1092, 2731, 3278, 5463, and 8156 Å for Si, 40, 199, 398, and 795 Å for Li_3ClO, and 334, 1337, 2674, and 4679 Å for AgI. Our simulations were run for several hundred picoseconds, depending on the length of the system, with a time step of 1 fs and data gathered every 50 fs.

[1] B. Liu, Y. Liu, C. Zhu, H. Xiang, H. Chen, L. Sun, Y. Gao, and Y. Zhou, Advances on strategies for searching for next generation thermal barrier coating materials, J. Mater. Sci. Technol. **35**, 833 (2019).

[2] J. He and T. M. Tritt, Advances in thermoelectric materials research: Looking back and moving forward, Science **357**, eaak9997 (2017).

[3] M. T. Agne, T. Böger, T. Bernges, and W. G. Zeier, Importance of thermal transport for the design of solid-state battery materials, PRX Energy **1**, 031002 (2022).

[4] Y. Zeng, D. Chalise, S. D. Lubner, S. Kaur, and R. S. Prasher, A review of thermal physics and management inside lithium-ion batteries for high energy density and fast charging, Energy Storage Mater. **41**, 264 (2021).

[5] A. J. H. McGaughey, A. Jain, H.-Y. Kim, and B. Fu, Phonon properties and thermal conductivity from first principles, lattice dynamics, and the Boltzmann transport equation, J. Appl. Phys. **125**, 011101 (2019).

[6] L. Lindsay, First principles peierls-boltzmann phonon thermal transport: A topical review, Nanosc. Microscale. Therm. **20**, 67 (2016).

[7] L. Isaeva, G. Barbalinardo, D. Donadio, and S. Baroni, Modeling heat transport in crystals and glasses from a unified lattice-dynamical approach, Nat. Commun. **10**, 3853 (2019).

[8] G. P. Srivastava and M. Prasad, Diagonal and nondiagonal peierls contribution to the thermal conductivity of anharmonic crystals, Phys. Rev. B **23**, 4273 (1981).

[9] B. S. Semwal and P. K. Sharma, Thermal conductivity of an anharmonic crystal, Phys. Rev. B **5**, 3909 (1972).

[10] R. J. Hardy, Energy-flux operator for a lattice, Phys. Rev. **132**, 168 (1963).

[11] M. Simoncelli, N. Marzari, and F. Mauri, Wigner formulation of thermal transport in solids, Phys. Rev. X **12**, 041011 (2022).

[12] G. Caldarelli, M. Simoncelli, N. Marzari, F. Mauri, and L. Benfatto, Many-body greens function approach to lattice thermal transport, Phys. Rev. B **106**, 024312 (2022).

[13] F. Knoop, T. A. R. Purcell, M. Scheffler, and C. Carbogno, Anharmonicity measure for materials, Phys. Rev. Mater. **4**, 083809 (2020).

[14] F. Knoop, T. A. R. Purcell, M. Scheffler, and C. Carbogno, Anharmonicity in thermal insulators: An analysis from first principles, Phys. Rev. Lett. **130**, 236301 (2023).

[15] T. R. Koehler, Theory of the self-consistent harmonic approximation with application to solid Neon, Phys. Rev. Lett. **17**, 89 (1966).

[16] N. R. Werthamer, Self-consistent phonon formulation of anharmonic lattice dynamics, Phys. Rev. B **1**, 572 (1970).

[17] T. Tadano and S. Tsuneyuki, Self-consistent phonon calculations of lattice dynamical properties in cubic $SrTiO_3$ with first-principles anharmonic force constants, Phys. Rev. B **92**, 054301 (2015).

[18] L. Monacelli, R. Bianco, M. Cherubini, M. Calandra, I. Errea, and F. Mauri, The stochastic self-consistent harmonic approximation: Calculating vibrational properties of materials with full quantum and anharmonic effects, J. Phys.: Condens. Matter **33**, 363001 (2021).

[19] O. Hellman, I. A. Abrikosov, and S. I. Simak, Lattice dynamics of anharmonic solids from first principles, Phys. Rev. B **84**, 180301(R) (2011).

[20] O. Hellman, P. Steneteg, I. A. Abrikosov, and S. I. Simak, Temperature dependent effective potential method for accurate free energy calculations of solids, Phys. Rev. B **87**, 104111 (2013).

[21] O. Hellman and I. A. Abrikosov, Temperature-dependent effective third-order interatomic force constants from first principles, Phys. Rev. B **88**, 144301 (2013).

[22] O. Hellman and D. A. Broido, Phonon thermal transport in Bi_2Te_3 from first principles, Phys. Rev. B **90**, 134309 (2014).

[23] A. H. Romero, E. K. U. Gross, M. J. Verstraete, and O. Hellman, Thermal conductivity in PbTe from first principles, Phys. Rev. B **91**, 214310 (2015).

[24] T. Tadano and S. Tsuneyuki, Quartic anharmonicity of rattlers and its effect on lattice thermal conductivity of clathrates from first principles, Phys. Rev. Lett. **120**, 105901 (2018).

[25] B. Fu, G. Tang, and A. J. H. McGaughey, Finite-temperature force constants are essential for accurately predicting the thermal conductivity of rutile TiO_2, Phys. Rev. Mater. **6**, 015401 (2022).

[26] Y. Wang, Q. Gan, M. Hu, J. Li, L. Xie, and J. He, Anharmonic lattice dynamics and the origin of intrinsic ultralow thermal conductivity in AgI materials, Phys. Rev. B **107**, 064308 (2023).

[27] X. Yang, J. Tiwari, and T. Feng, Reduced anharmonic phonon scattering cross-section slows the decrease of thermal conductivity with temperature, Mater. Today Phys. **24**, 100689 (2022).

[28] A. Castellano, J. P. A. Batista, and M. J. Verstraete, Mode-coupling theory of lattice dynamics for classical and quantum crystals, J. Chem. Phys. **159**, 234501 (2023).

[29] F. Knoop, N. Shulumba, A. Castellano, J. P. A. Batista, R. Farris, M. J. Verstraete, M. Heine, D. Broido, D. S. Kim, J. Klarbring, I. A. Abrikosov, S. I. Simak, and O. Hellman,

TDEP: Temperature dependent effective potentials, JOSS **9**, 6150 (2024).

[30] R. Kubo, The fluctuation-dissipation theorem, Rep. Prog. Phys. **29**, 255 (1966).

[31] H. Mori, Transport, collective motion, and Brownian motion, Prog. Theor. Phys. **33**, 423 (1965).

[32] R. Zwanzig, Memory effects in irreversible thermodynamics, Phys. Rev. **124**, 983 (1961).

[33] S.-i. Tamura, Isotope scattering of dispersive phonons in Ge, Phys. Rev. B **27**, 858 (1983).

[34] A. Marcolongo, P. Umari, and S. Baroni, Microscopic theory and quantum simulation of atomic heat transport, Nat. Phys. **12**, 80 (2016).

[35] C. Carbogno, R. Ramprasad, and M. Scheffler, *Ab initio* Green-Kubo approach for the thermal conductivity of solids, Phys. Rev. Lett. **118**, 175901 (2017).

[36] D. Dangi, O. Hellman, S. Fahy, and I. Savi, The origin of the lattice thermal conductivity enhancement at the ferroelectric phase transition in GeTe, npj Computat. Mater. **7**, 57 (2021).

[37] Z. Han, X. Yang, W. Li, T. Feng, and X. Ruan, Fourphonon: An extension module to shengbte for computing four-phonon scattering rates and thermal conductivity, Comput. Phys. Commun. **270**, 108179 (2022).

[38] A. Fiorentino and S. Baroni, From Green-Kubo to the full Boltzmann kinetic approach to heat transport in crystals and glasses, Phys. Rev. B **107**, 054311 (2023).

[39] A. Cepellotti and N. Marzari, Thermal transport in crystals as a kinetic theory of relaxons, Phys. Rev. X **6**, 041013 (2016).

[40] I. R. Craig and D. E. Manolopoulos, Quantum statistics and classical mechanics: Real time correlation functions from ring polymer molecular dynamics, J. Chem. Phys. **121**, 3368 (2004).

[41] M. Rossi, M. Ceriotti, and D. E. Manolopoulos, How to remove the spurious resonances from ring polymer molecular dynamics, J. Chem. Phys. **140**, 234116 (2014).

[42] M. Shiga and A. Nakayama, Ab initio path integral ring polymer molecular dynamics: Vibrational spectra of molecules, Chem. Phys. Lett. **451**, 175 (2008).

[43] A. Witt, S. D. Ivanov, M. Shiga, H. Forbert, and D. Marx, On the applicability of centroid and ring polymer path integral molecular dynamics for vibrational spectroscopy, J. Chem. Phys. **130**, 194510 (2009).

[44] R. Ramírez, T. López-Ciudad, P. Kumar P, and D. Marx, Quantum corrections to classical time-correlation functions: Hydrogen bonding and anharmonic floppy modes, J. Chem. Phys. **121**, 3973 (2004).

[45] A. A. Maradudin and S. H. Vosko, Symmetry properties of the normal vibrations of a crystal, Rev. Mod. Phys. **40**, 1 (1968).

[46] W. Li, J. Carrete, N. A. Katcho, and N. Mingo, ShengBTE: A solver of the boltzmann transport equation for phonons, Comput. Phys. Commun. **185**, 1747 (2014).

[47] A. Togo, L. Chaput, T. Tadano, and I. Tanaka, Implementation strategies in phonopy and phono3py, J. Phys.: Condens. Matter **35**, 353001 (2023).

[48] J. R. Yates, X. Wang, D. Vanderbilt, and I. Souza, Spectral and fermi surface properties from Wannier interpolation, Phys. Rev. B **75**, 195121 (2007).

[49] W. Li, N. Mingo, L. Lindsay, D. A. Broido, D. A. Stewart, and N. A. Katcho, Thermal conductivity of diamond nanowires from first principles, Phys. Rev. B **85**, 195436 (2012).

[50] G. Barbalinardo, Z. Chen, N. W. Lundgren, and D. Donadio, Efficient anharmonic lattice dynamics calculations of thermal transport in crystalline and disordered solids, J. Appl. Phys. **128**, 135104 (2020).

[51] M. Omini and A. Sparavigna, Beyond the isotropic-model approximation in the theory of thermal conductivity, Phys. Rev. B **53**, 9064 (1996).

[52] Z. Han and X. Ruan, Thermal conductivity of monolayer graphene: Convergent and lower than diamond, Phys. Rev. B **108**, L121412 (2023).

[53] L. S. Blackford, A. Petitet, R. Pozo, K. Remington, R. C. Whaley, J. Demmel, J. Dongarra, I. Duff, S. Hammarling, G. Henry *et al.*, An updated set of basic linear algebra subprograms (BLAS), ACM Trans. Math. Software **28**, 135 (2002).

[54] L. Chaput, A. Togo, I. Tanaka, and G. Hug, Phonon-phonon interactions in transition metals, Phys. Rev. B **84**, 094302 (2011).

[55] Z. Guo, Z. Han, D. Feng, G. Lin, and X. Ruan, Sampling-accelerated prediction of phonon scattering rates for converged thermal conductivity and radiative properties, npj Comput. Mater. **10**, 31 (2024).

[56] G. Fugallo, A. Cepellotti, L. Paulatto, M. Lazzeri, N. Marzari, and F. Mauri, Thermal conductivity of graphene and graphite: Collective excitations and mean free paths, Nano Lett. **14**, 6109 (2014).

[57] A. Castellano, F. Bottin, J. Bouchet, A. Levitt, and G. Stoltz, *Ab initio* canonical sampling based on variational inference, Phys. Rev. B **106**, L161110 (2022).

[58] X. Gonze, B. Amadon, G. Antonius, F. Arnardi, L. Baguet, J.-M. Beuken, J. Bieder, F. Bottin, J. Bouchet, E. Bousquet, N. Brouwer, F. Bruneval, G. Brunin, T. Cavignac, J.-B. Charraud, W. Chen, M. Côté, S. Cottenier, J. Denier, G. Geneste *et al.*, The Abinitproject: Impact, environment and recent developments, Comput. Phys. Commun. **248**, 107042 (2020).

[59] A. H. Romero, D. C. Allan, B. Amadon, G. Antonius, T. Applencourt, L. Baguet, J. Bieder, F. Bottin, J. Bouchet, E. Bousquet, F. Bruneval, G. Brunin, D. Caliste, M. Côté, J. Denier, C. Dreyer, P. Ghosez, M. Giantomassi, Y. Gillet, O. Gingras *et al.*, ABINIT: Overview and focus on selected capabilities, J. Chem. Phys. **152**, 124102 (2020).

[60] A. V. Shapeev, Moment tensor potentials: A class of systematically improvable interatomic potentials, Multiscale Model. Simul. **14**, 1153 (2016).

[61] I. S. Novikov, K. Gubaev, E. V. Podryabinkin, and A. V. Shapeev, The MLIP package: Moment tensor potentials with MPI and active learning, Mach. Learn.: Sci. Technol. **2**, 025002 (2021).

[62] A. P. Thompson, H. M. Aktulga, R. Berger, D. S. Bolintineanu, W. M. Brown, P. S. Crozier, P. J. in 't Veld, A. Kohlmeyer, S. G. Moore, T. D. Nguyen, R. Shan, M. J. Stevens, J. Tranchida, C. Trott, and S. J. Plimpton, LAMMPS - a flexible simulation tool for particle-based materials modeling at the atomic, meso, and continuum scales, Comput. Phys. Commun. **271**, 108171 (2022).

[63] N. Grønbech-Jensen and O. Farago, A simple and effective verlet-type algorithm for simulating langevin dynamics, Mol. Phys. **111**, 983 (2013).

[64] Y. Sheng, Y. Hu, Z. Fan, and H. Bao, Size effect and transient phonon transport mechanism in approach-to-equilibrium molecular dynamics simulations, Phys. Rev. B **105**, 075301 (2022).

[65] E. Lampin, P. L. Palla, P.-A. Francioso, and F. Cleri, Thermal conductivity from approach-to-equilibrium molecular dynamics, J. Appl. Phys. **114**, 033525 (2013).

[66] E. Martin, G. Ori, T.-Q. Duong, M. Boero, and C. Massobrio, Thermal conductivity of amorphous SiO_2 by first-principles molecular dynamics, J. Non-Cryst. Solids **581**, 121434 (2022).

[67] A. Lambrecht, G. Ori, C. Massobrio, M. Boero, and E. Martin, Assessing the thermal conductivity of amorphous SiN by approach-to-equilibrium molecular dynamics, J. Chem. Phys. **160**, 094505 (2024).

[68] C. Melis, R. Dettori, S. Vandermeulen, and L. Colombo, Calculating thermal conductivity in a transient conduction regime: Theory and implementation, Eur. Phys. J. B **87**, 96 (2014).

[69] W. Fulkerson, J. P. Moore, R. K. Williams, R. S. Graves, and D. L. McElroy, Thermal conductivity, electrical resistivity, and seebeck coefficient of silicon from 100 to 1300°k, Phys. Rev. **167**, 765 (1968).

[70] X. Gu, S. Li, and H. Bao, Thermal conductivity of silicon at elevated temperature: Role of four-phonon scattering and electronic heat conduction, Int. J. Heat Mass Transfer **160**, 120165 (2020).

[71] A. V. Inyushkin, A. N. Taldenkov, A. M. Gibin, A. V. Gusev, and H. Pohl, On the isotope effect in thermal conductivity of silicon, Phys. Status Solidi C **1**, 2995 (2004).

[72] T. Feng and X. Ruan, Quantum mechanical prediction of four-phonon scattering rates and reduced thermal conductivity of solids, Phys. Rev. B **93**, 045202 (2016).

[73] D. A. Broido, M. Malorny, G. Birner, N. Mingo, and D. A. Stewart, Intrinsic lattice thermal conductivity of semiconductors from first principles, Appl. Phys. Lett. **91**, 231922 (2007).

[74] X. Wu, W. Zhou, H. Dong, P. Ying, Y. Wang, B. Song, Z. Fan, and S. Xiong, Correcting force error-induced underestimation of lattice thermal conductivity in machine learning molecular dynamics, J. Chem. Phys. **161**, 0213811 (2024).

[75] W. Zhou, N. Liang, X. Wu, S. Xiong, Z. Fan, and B. Song, Insight into the effect of force error on the thermal conductivity from machine-learned potentials, Mater. Today Phys. **50**, 101638 (2025).

[76] M. H. Braga, J. A. Ferreira, V. Stockhausen, J. E. Oliveira, and A. El-Azab, Novel Li_3ClO based glasses with superionic properties for lithium batteries, J. Mater. Chem. A **2**, 5470 (2014).

[77] X. Lü, G. Wu, J. W. Howard, A. Chen, Y. Zhao, L. L. Daemen, and Q. Jia, Li-rich anti-perovskite Li_3OCl films with enhanced ionic conductivity, Chem. Commun. **50**, 11520 (2014).

[78] P. Pegolo, S. Baroni, and F. Grasselli, Temperature- and vacancy-concentration-dependence of heat transport in Li_3ClO from multi-method numerical simulations, npj Comput. Mater. **8**, 24 (2022).

[79] A. Togo, L. Chaput, and I. Tanaka, Distributions of phonon lifetimes in Brillouin zones, Phys. Rev. B **91**, 094306 (2015).

[80] N. Ouyang, Z. Zeng, C. Wang, Q. Wang, and Y. Chen, Role of high-order lattice anharmonicity in the phonon thermal transport of silver halide AgX (X = Cl,Br,I), Phys. Rev. B **108**, 174302 (2023).

[81] J.-J. Zhou, O. Hellman, and M. Bernardi, Electron-phonon scattering in the presence of soft modes and electron mobility in $SrTiO_3$ perovskite from first principles, Phys. Rev. Lett. **121**, 226603 (2018).

[82] J. P. Perdew, A. Ruzsinszky, G. I. Csonka, O. A. Vydrov, G. E. Scuseria, L. A. Constantin, X. Zhou, and K. Burke, Restoring the density-gradient expansion for exchange in solids and surfaces, Phys. Rev. Lett. **100**, 136406 (2008).

[83] M. van Setten, M. Giantomassi, E. Bousquet, M. Verstraete, D. Hamann, X. Gonze, and G.-M. Rignanese, The PseudoDojo: Training and grading a 85 element optimized norm-conserving pseudopotential table, Comput. Phys. Commun. **226**, 39 (2018).

[84] J. J. Mortensen, A. H. Larsen, M. Kuisma, A. V. Ivanov, A. Taghizadeh, A. Peterson, A. Haldar, A. O. Dohn, C. Schäfer, E. O. Jónsson, E. D. Hermes, F. A. Nilsson, G. Kastlunger, G. Levi, H. Jónsson, H. Häkkinen, J. Fojt, J. Kangsabanik, J. Sødequist, J. Lehtomäki *et al.*, GPAW: An open Python package for electronic structure calculations, J. Chem. Phys. **160**, 092503 (2024).

Paper III

3.3 Fluctuation-dissipation and virtual processes in interacting phonon systems

Aloïs Castellano, JP Batista, Matthieu J Verstraete

Publication Report

Contributions Summary:*Contributed to theoretical derivations, physical understanding and manuscript review.*

Abstract

Phonon-phonon interactions are fundamental to understanding a wide range of material properties, including thermal transport and vibrational spectra. In conventional perturbative approaches, energy conservation during each microscopic phonon interaction is enforced using delta functions. We demonstrate that these delta functions stem from an incomplete treatment, that violates the fluctuation-dissipation theorem governing systems at equilibrium. By replacing delta functions with convolutions and introducing a self-consistency condition for the phonon spectral function, we provide a more accurate and physically consistent framework. For systems where phonon dynamics can be approximated as Markovian, we simplify this approach, reducing the dissipative component to a single parameter tied to phonon lifetimes. Applying this method to boron arsenide, we find that self-consistent linewidths better capture the phonon scattering processes, significantly improving agreement with experimental thermal conductivity values. These results also challenge the conventional view of four-phonon processes as dominant in BAs, demonstrating the adequacy of a three-phonon description, provided it is self-consistent. With this method we address critical limitations of perturbative approaches, offering new insights into dissipation and phonon-mediated processes, and enabling more accurate modeling of anharmonic materials.

Fluctuation-dissipation and virtual processes in interacting phonon systems

Aloïs Castellano,[1] J. P. Alvarinhas Batista,[1] and Matthieu J. Verstraete[1, 2]

[1]*Nanomat group, Q-MAT research center and European Theoretical Spectroscopy Facility,*
Université de Liège, allée du 6 août, 19, B-4000 Liège, Belgium
[2]*ITP, Physics Department, Utrecht University 3508 TA Utrecht, The Netherlands*

Phonon-phonon interactions are fundamental to understanding a wide range of material properties, including thermal transport, expansion and vibrational spectra. In all of the conventional perturbative approaches, energy conservation is enforced using Dirac delta functions at each microscopic phonon interaction. We demonstrate below that these delta functions stem from an incomplete treatment of the interacting problem, that violates the fluctuation-dissipation theorem governing systems at equilibrium. By replacing the deltas with convolutions of the phonon spectral functions, and introducing a self-consistency condition, we provide a more accurate and physically consistent framework. For systems where phonon dynamics can be approximated as Markovian, we simplify this approach, reducing the dissipative component to a single parameter tied to phonon lifetimes. Applying this method to boron arsenide, we find that self-consistent linewidths capture the phonon scattering processes better, significantly improving agreement with experimental thermal conductivity values. These results also challenge the conventional view of four-phonon processes as dominant in BAs, demonstrating a three-phonon description can explain most of the experimental value, provided it is self-consistent. With this method we address critical limitations of perturbative approaches, offering new insights into dissipation and phonon-mediated processes, and enabling more accurate modeling of anharmonic materials.

Phonons are quantized vibrational modes of a crystal lattice, and central to our understanding of a wide range of material properties. From mechanical stability and sound propagation to optical responses and thermal transport, phonons play a key role in determining the behavior of solids, and enable many functionalities and applications. As such, an accurate description of phonon dynamics is essential to advance our understanding of both fundamental physics and material functionality. In the harmonic approximation, phonons are treated as non-interacting quasiparticles with infinite lifetimes. This can naturally not be a complete description: in real systems, anharmonicity introduces phonon-phonon interactions, which lead to a broadening of phonon spectral lineshapes. These interactions are crucial to describe key material properties quantitatively and sometimes even qualitatively. For example, without interactions the phonon thermal conductivity is infinite, an inconsistency which is resolved with the introduction of anharmonicity.

In conventional perturbative approaches, phonon-phonon interactions are treated with strict energy conservation, enforced by Dirac delta functions of the energy difference before and after each scattering event [1–4]. In this letter, we show that while this formalism captures the idealized dynamics of non-interacting phonons, it employs a strong approximation that neglects the dissipative component of real phonon dynamics, and breaks the fluctuation-dissipation theorem. We show that a more exact formulation replaces delta functions with spectral function convolutions and a self-consistency condition, which can be interpreted as high-order effective interactions mediated by virtual phonons. Importantly, these are not subject to energy conservation. A practical implementation is introduced for cases where phonon dynamics are approximated as Markovian, reducing the dissipative component to a single parameter associated with phonon lifetimes.

We are interested in phonon correlation functions at finite temperature, which are linked to observables such as X-ray or neutron scattering. For the derivation, we place ourselves within our recently introduced mode-coupling theory of anharmonic lattice dynamics [5–7], but similar arguments will hold for all of the commonly used (perturbative) theories. Within this formalism, the phonon Kubo correlation functions (KCF) [8] obey the generalized Langevin equation of motion

$$\ddot{G}_\lambda(t) = -\Omega_\lambda^2 G_\lambda(t) - \int_0^t ds K_\lambda(s)\dot{G}_\lambda(t-s), \quad (1)$$

where we introduce the super-index $\lambda = (\mathbf{q}, s)$, with $\mathbf{q}$ the wave vector in reciprocal space and s the index of the phonon branch. This equation describes the dynamics as driven by a harmonic force with the spring magnitude given by the phonon frequency Ω_λ, and a time-dependent friction term. The latter is contained in a memory kernel $K_\lambda(t)$ which describes the dissipation of the phonon energy through a bath made up of all other phonons. Importantly, $K_\lambda(t)$ must respect the fluctuation-dissipation theorem [8–10], which states that $K_\lambda(t) = \big(\delta f_\lambda, \delta f_\lambda(t)\big)$, where $\delta f_\lambda(t)$ is the "random" force which describes the effects of neglected degrees of freedom on the dynamics. The dynamical susceptibility (or spectral function) is obtained through a Laplace transform of eq.(1), giving

$$\chi''_\lambda(\omega) = \frac{1}{\hbar\pi} \frac{4\omega\Omega_\lambda\Gamma_\lambda^2(\omega)}{(\omega^2 - \Omega_\lambda^2 - 2\omega\Delta_\lambda(\omega))^2 + 4\omega^2\Gamma_\lambda^2(\omega)}, \quad (2)$$

where $\Gamma_\lambda(\omega)$ and $\Delta_\lambda(\omega)$ are respectively the real and imaginary parts of its memory kernel (which are related

by a Kramers-Kronig transform). The main complication of eq.(2) lies in the expression of the memory kernel. Within the mode-coupling approximation, K is obtained by projecting the component of the "random" force onto multiple displacements, introducing interactions between phonons. To simplify our presentation, we will stay at the lowest order of phonon-phonon interaction, but it is important to note that our reasoning holds identically with higher orders. With only three-phonon interactions and after a decoupling of four-point correlations into products of two-point correlations [7], the real part of the memory kernel has the form

$$\Gamma_\lambda(\omega) = \frac{1}{16} \sum_{\lambda'\lambda''} |\Psi_{\lambda\lambda'\lambda''}|^2 S_{\lambda'\lambda''}(\omega). \quad (3)$$

In this equation, $\Psi_{\lambda\lambda'\lambda''}$ are third-order scattering matrix elements, and S is a function describing the effect of phonons λ' and λ'' on the memory kernel. S is expressed as

$$S_{\lambda'\lambda''}(\omega) = \frac{\hbar\Omega_\lambda}{n(\omega)\hbar\omega} \int_{-\infty}^{\infty} d\omega' G_{\lambda'}^<(\omega') G_{\lambda''}^<(\omega - \omega'), \quad (4)$$

where the lesser phonon correlation function $G_\lambda^<(\omega)$ is proportional to the KCF, and related to the dynamical susceptibility by the fluctuation-dissipation theorem, through $G_\lambda^<(\omega) = n(\omega)\chi_\lambda''(\omega)$. $n = (e^{\beta\hbar\omega} - 1)^{-1}$ is the Bose-Einstein distribution.

A common simplification involves approximating $S_{\lambda',\lambda''}(\omega)$ using the memory-less dynamical susceptibility of the phonons λ' and λ''. This results in $S_{\lambda',\lambda''}(\omega)$ being expressed as a sum of delta functions centered at sums or differences of phonon frequencies, weighted by phonon occupation numbers [7]

$$\begin{aligned}
S_{\lambda'\lambda''}(\omega) = &(n_{\lambda'} + n_{\lambda''} + 1)\delta(\omega - \Omega_{\lambda'} - \Omega_{\lambda''}) \\
&- (n_{\lambda'} + n_{\lambda''} + 1)\delta(\omega + \Omega_{\lambda'} + \Omega_{\lambda''}) \\
&+ (n_{\lambda'} - n_{\lambda''})\delta(\omega + \Omega_{\lambda'} - \Omega_{\lambda''}) \\
&- (n_{\lambda'} - n_{\lambda''})\delta(\omega - \Omega_{\lambda'} + \Omega_{\lambda''}),
\end{aligned} \quad (5)$$

where $n_\lambda = n(\Omega_\lambda)$. The delta functions in this equation have a clear physical interpretation: they represent energy conservation during each phonon interaction. However, this approach neglects a critical element: the memory kernel. In a memory-less framework, phonons are idealized as infinitely long-lived quasiparticles, with their dynamical susceptibility given by $\chi_\lambda''(\omega) \propto \delta(\omega - \Omega_\lambda)$. This idealization inherently assumes non-dissipative dynamics, so that energy conservation arises automatically from the system's behavior. Introducing the memory kernel fundamentally changes this picture. Phonons are no longer viewed as perfectly conserving energy through their dynamics; instead, the memory kernel accounts for the exchange of energy between interacting phonons. In this framework, the energy conservation for individual events is generalized to the detailed balance condition,
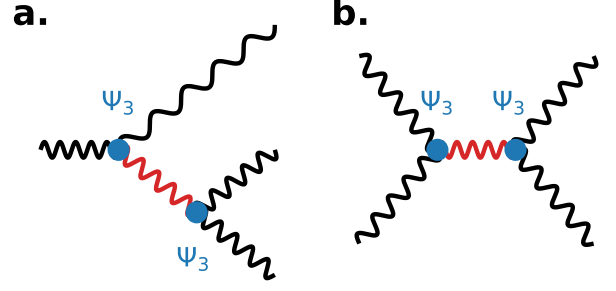

FIG. 1. Examples of second-order three-phonon Feynman diagrams for anharmonic systems. The black wiggly lines represent phonon propagators, the red ones representing intermediate virtual phonons and the blue dots represent 3-phonon vertices. **a.** Second order decay process. **b.** Second order redistribution process.

which gives rise to the fluctuation-dissipation theorem. Energy conservation should only be found between the initial and final states. Consequently, the delta functions, which cannot capture dissipation, are replaced by a convolution term in eq.(3), which is self-consistently linked to eq.(2). This convolution reflects the interplay between phonons and their self-created environment, where the memory kernel describes the "phonon bath" formed by the collective dynamics of all phonons. Modifying the memory kernel alters the phonon properties, which in turn reshape the bath—a feedback mechanism captured by the self-consistent framework.

In a diagrammatic framework, the convolution can be interpreted as introducing higher-order interactions mediated by virtual phonons [11, 12]. For instance, the process illustrated in FIG.1a. represents an effective four-phonon interaction, where one phonon decays into three phonons through an intermediate process involving a virtual phonon. Similarly, FIG.1b. depicts a second-order redistribution process in which two phonons merge to form a virtual phonon, which subsequently decays into two new phonons. In such higher-order interactions, energy and momentum conservation are strictly enforced only for the initial and final phonons. The virtual phonons, however, are not subject to these constraints, enabling phonon interactions that would otherwise be forbidden by strict energy conservation. When self-consistency is applied, even more complex higher-order interactions emerge, and at full convergence, an infinite series of such interactions contributes to the phonon linewidths. Consequently, these previously forbidden interactions, which are simply a manifestation of the fluctuation-dissipation condition, can have drastic consequences on the properties of systems where selection rules could restrict anharmonicity [13–17]. For instance, in systems with large mass differences - and thus a large acoustic-optical band gap - interactions between acoustic

and optical modes are no longer forbidden within a three-phonon truncation. This should modify substantially the scattering phase space and reduce, for example, the expected large conductivity in these systems.

The self consistency of the full frequency dependent dynamical susceptibility represents an important computational challenge due to the convolution appearing in $S_{\lambda',\lambda''}(\omega)$. However, phonons are often accurately described using a Markovian approximation, where the memory kernel reduces to a single number $\Gamma_\lambda = \Gamma_\lambda(\Omega_\lambda)$ and $\chi''_\lambda(\omega)$ to a sum of Lorentzian centered on $\pm\Omega_\lambda$ with widths Γ_λ. In this case, the $S_{\lambda',\lambda''}(\omega)$ function has the simple form [7]

$$
\begin{aligned}
S_{\lambda'\lambda''}(\omega) = {} & (n_{\lambda'} + n_{\lambda''} + 1)L(\omega, \Omega_{\lambda'} + \Omega_{\lambda''}, \Gamma_{\lambda'} + \Gamma_{\lambda''}) \\
& - (n_{\lambda'} + n_{\lambda''} + 1)L(\omega, -\Omega_{\lambda'} - \Omega_{\lambda''}, \Gamma_{\lambda'} + \Gamma_{\lambda''}) \\
& + (n_{\lambda'} - n_{\lambda''})L(\omega, \Omega_{\lambda'} - \Omega_{\lambda''}, \Gamma_{\lambda'} + \Gamma_{\lambda''}) \\
& - (n_{\lambda'} - n_{\lambda''})L(\omega, -\Omega_{\lambda'} + \Omega_{\lambda''}, \Gamma_{\lambda'} + \Gamma_{\lambda''}),
\end{aligned}
\tag{6}
$$

where L are Lorentzian functions defined as $L(\omega, \Omega, \Gamma) = \Gamma/((\omega - \Omega)^2 + \Gamma^2)/\pi$. Thus, within the Markovian approximation, the fluctuation-dissipation theorem can be simply enforced by using this equation in a self-consistent cycle involving equations (2), (3) and (6). This represents a simplification compared to the numerical implementation of delta functions [2–4, 18] as it avoids the need of introducing numerical convergence parameters and usually creates a broader smearing than would be used numerically, easing convergence. It does however bring an extra-cost related to the need to compute eq.(3) several times. It should be noted that the need for linewidth self-consistency has already been proposed in previous work [19, 20]. However, these works do not propose a formal justification for this self-consistency. Moreover, the smearing used in these works does not correspond to the convolution of the Lorentzian dynamical susceptibility appearing in eq.(6), breaking the relation between the dissipative component of the phonon dynamics and the memory kernel, and with it, the fluctuation-dissipation theorem.

To demonstrate the importance of the fluctuation-dissipation condition, we applied our approach to boron arsenide, a semiconductor renowned for its exceptionally high thermal conductivity [21–24]. A key feature of this material is its large band gap separating the acoustic and optical phonon branches, as shown in FIG.2a. This gap is sufficiently wide to forbid three-phonon coupling between acoustic and optical phonons if strict energy conservation is applied [15], making four-phonon interactions a requirement to accurately reproduce the thermal conductivity in this system [25]. However, when the energy conservation principle is replaced by the fluctuation-dissipation theorem, third-order acoustic-optical interactions are no longer strictly forbidden: through the Markovian approximation physically natural Lorentzian
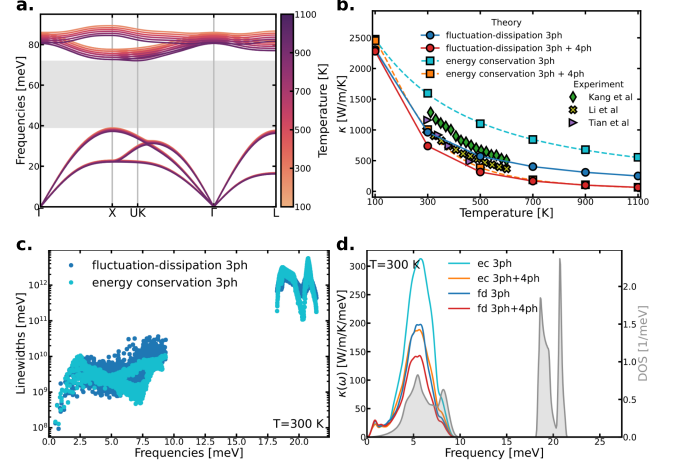

FIG. 2. **a.** T-dependent phonons in BAs from 100 to 1100 K. The large acoustic to optical band-gap is highlighted in grey. **b.** Thermal conductivity in BAs including 3 or 3+4 phonon interactions, with energy conservation enforced or using the fluctuation-dissipation condition. Experimental results from Kang *et al* [21], Li *et al* [22] and Tian *et al* [23] are shown for comparison. **c.** Comparison of the phonon linewidths at 300 K with 3-phonon interactions with energy conservation vs fluctuation-dissipation condition. **d.** Comparison of the spectral thermal conductivity at 300 K computed with energy conservation (ec) or after self-consistency to enforce the fluctuation-dissipation condition (fd). The phonon density of states is represented in grey.

functions [7] appear. Their long tails extend the scattering phase space, significantly altering the dynamics of both acoustic and optical phonons. This highlights BAs as an archetypal system where the fluctuation-dissipation theorem should play a critical role in capturing the true phonon scattering processes, and their impact on thermal transport.

Our results in FIG.2 were computed using machine-learning interatomic potentials constructed on *ab initio* data, whose details are provided in the SM [7]. At the three-phonon level, the impact of the fluctuation-dissipation condition is particularly striking. While enforcing strict energy conservation allows us to reproduce theoretical results from the literature [15, 24, 25], incorporating self-consistent linewidths consistently leads to lower thermal conductivity values, which are in closer agreement with experimental measurements [21–23]. This reduction can be attributed to a significant decrease in the thermal conductivity contribution from phonons with energies around 20 meV. Under strict energy conservation, these phonons are forbidden from interacting with optical modes, but the convolution in the self-consistent approach relaxes this restriction, thereby expanding the scattering phase space. This behavior is analogous to what occurs when four-phonon processes are included: the increased scattering phase space re-

sults in higher linewidths for these phonons and a corresponding reduction in their thermal conductivity contribution. Our findings challenge the prevailing view that four-phonon interactions are essential to explain the thermal conductivity in large phonon band gap materials like boron arsenide. While these interactions are not negligible, their importance appears to have been overestimated in previous literature. Remaining at the three-phonon level while enforcing the fluctuation-dissipation condition provides a reasonably accurate prediction of thermal transport in this material, consistent with its low anharmonicity. However, this accuracy should not be seen as an indication that the self-consistent determination of linewidth could avoid the need for four-phonon interactions. Instead, the fluctuation-dissipation condition should be seen as a new, superior framework to evaluate all scattering mechanisms. Its importance in the context of BAs stems from the constrained 3-phonon scattering phase-space produced by strict energy conservation. The FD approach removes this constraint, and shows the reproduction of the experimental thermal conductivity of BAs using energy conservation and the 4-phonon channel is actually a coincidence: the EC 3-phonon κ is too high, and the EC 4-phonon correction is too large, but happens to land near the experimental values.

The fluctuation-dissipation condition is universally applicable, but its impact on different materials varies, and requires quantitative evaluation. In the SM [7], we show the impact of the self-consistency for silicon, a highly harmonic system with low linewidths and no phonon band gap, and for silver iodide, which exhibits strong anharmonicity. In the former case, the difference in using the fluctuation-dissipation condition is negligible, both with three and four-phonon interactions. In AgI however, its impact is more pronounced. Including only three-phonon scattering, the self-consistency reduces the thermal conductivity by 15% to 25% between 100 to 300 K. When four phonon scattering is included, the impact of the fluctuation-dissipation condition is smaller, between 5% and 20 % in the same range of temperature, which is still significant for low thermal conductivity materials. Ultimately, the fluctuation-dissipation condition is a universal principle that applies to all materials, yet its impact on phonon dynamics appears to be highly system-dependent. Our findings highlight the need for broader investigations to determine how this condition interacts with anharmonicity and the available scattering phase space. In more complex or strongly interacting systems, additional factors, such as possible deviations from Markovian behavior, may also influence the outcome. Such studies will be essential for establishing when and how fluctuation-dissipation-consistent treatments are necessary for accurate modeling of lattice dynamics.

While our study focuses on phonons, similar self-consistent approaches should be relevant for other finite-temperature quasiparticles. Systems involving interactions between quasiparticles with vastly different energy scales, such as magnon-phonon or electron-phonon interactions, will be particularly affected by the relaxation of strict energy conservation. For instance, recent work [26, 27] demonstrates that incorporating self-consistent electronic linewidths resolves divergences previously expected in piezoelectric materials. This highlights the broader importance of capturing dissipative dynamics in a rigorous and consistent framework, extending the relevance of our approach beyond phonons to other complex quasiparticle systems.

[1] A. A. Maradudin and A. E. Fein, Scattering of neutrons by an anharmonic crystal, Phys. Rev. **128**, 2589 (1962).

[2] W. Li, N. Mingo, L. Lindsay, D. A. Broido, D. A. Stewart, and N. A. Katcho, Thermal conductivity of diamond nanowires from first principles, Phys. Rev. B **85**, 195436 (2012).

[3] W. Li, J. Carrete, N. A. Katcho, and N. Mingo, Shengbte: A solver of the boltzmann transport equation for phonons, Comput. Phys. Commun. **185**, 1747–1758 (2014).

[4] Z. Han, X. Yang, W. Li, T. Feng, and X. Ruan, Fourphonon: An extension module to shengbte for computing four-phonon scattering rates and thermal conductivity, Computer Physics Communications **270**, 108179 (2022).

[5] A. Castellano, J. P. A. Batista, and M. J. Verstraete, Mode-coupling theory of lattice dynamics for classical and quantum crystals, J. Chem. Phys. **159**, 0174255 (2023).

[6] A. Castellano, J. P. A. Batista, O. Hellman, and M. J. Verstraete, Mode-coupling formulation of heat transport in anharmonic materials, Phys. Rev. B **111**, 094306 (2025).

[7] See Supplemental Material at URL-will-be-inserted-by-

publisher for the derivation of the theory and the computational details, which include Refs [5, 6, 28–40].

[8] R. Kubo, The fluctuation-dissipation theorem, Rep. Prog. in Phys. **29**, 255–284 (1966).

[9] H. Mori, Transport, collective motion, and brownian motion, Prog. Theor. Phys. **33**, 423–455 (1965).

[10] R. Zwanzig, Memory effects in irreversible thermodynamics, Phys. Rev. **124**, 983 (1961).

[11] P. Carruthers, Resonance in phonon-phonon scattering, Phys. Rev. **125**, 123 (1962).

[12] A. J. Leggett and D. t. Haar, Finite linewidths and "forbidden" three-phonon interactions, Phys. Rev. **139**, A779 (1965).

[13] Y.-Q. Lin, S.-H. Cao, C.-E. Hu, H.-Y. Geng, and X.-R. Chen, Intrinsic scattering channels and selection rules in four-phonon interactions, Phys. Rev. B **110**, 075414 (2024).

[14] L. Lindsay, D. A. Broido, J. Carrete, N. Mingo, and T. L. Reinecke, Anomalous pressure dependence of thermal conductivities of large mass ratio compounds, Phys. Rev. B **91**, 121202 (2015).

[15] N. K. Ravichandran and D. Broido, Phonon-phonon interactions in strongly bonded solids: Selection rules and higher-order processes, Phys. Rev. X **10**, 021063 (2020).

[16] N. K. Ravichandran and D. Broido, Exposing the hidden influence of selection rules on phonon–phonon scattering by pressure and temperature tuning, Nat. Commun. **12**, 3473 (2021).

[17] R. Yang, S. Yue, Y. Quan, and B. Liao, Crystal symmetry based selection rules for anharmonic phonon-phonon scattering from a group theory formalism, Phys. Rev. B **103**, 184302 (2021).

[18] J. R. Yates, X. Wang, D. Vanderbilt, and I. Souza, Spectral and fermi surface properties from wannier interpolation, Phys. Rev. B **75**, 195121 (2007).

[19] X. Gu, Z. Fan, H. Bao, and C. Y. Zhao, Revisiting phonon-phonon scattering in single-layer graphene, Phys. Rev. B **100**, 064306 (2019).

[20] J. E. Turney, E. S. Landry, A. J. H. McGaughey, and C. H. Amon, Predicting phonon properties and thermal conductivity from anharmonic lattice dynamics calculations and molecular dynamics simulations, Phys. Rev. B **79**, 064301 (2009).

[21] J. S. Kang, M. Li, H. Wu, H. Nguyen, and Y. Hu, Experimental observation of high thermal conductivity in boron arsenide, Science **361**, 575–578 (2018).

[22] S. Li, Q. Zheng, Y. Lv, X. Liu, X. Wang, P. Y. Huang, D. G. Cahill, and B. Lv, High thermal conductivity in cubic boron arsenide crystals, Science **361**, 579–581 (2018).

[23] F. Tian, B. Song, X. Chen, N. K. Ravichandran, Y. Lv, K. Chen, S. Sullivan, J. Kim, Y. Zhou, T.-H. Liu, M. Goni, Z. Ding, J. Sun, G. A. G. Udalamatta Gamage, H. Sun, H. Ziyaee, S. Huyan, L. Deng, J. Zhou, A. J. Schmidt, S. Chen, C.-W. Chu, P. Y. Huang, D. Broido, L. Shi, G. Chen, and Z. Ren, Unusual high thermal conductivity in boron arsenide bulk crystals, Science **361**, 582–585 (2018).

[24] L. Lindsay, D. A. Broido, and T. L. Reinecke, First-principles determination of ultrahigh thermal conductivity of boron arsenide: A competitor for diamond?, Phys. Rev. Lett. **111**, 025901 (2013).

[25] T. Feng, L. Lindsay, and X. Ruan, Four-phonon scattering significantly reduces intrinsic thermal conductivity of solids, Phys. Rev. B **96**, 161201 (2017).

[26] J.-M. Lihm, S. Poncé, and C.-H. Park, Self-consistent electron lifetimes for electron-phonon scattering, Phys. Rev. B **110**, L121106 (2024).

[27] J.-M. Lihm and S. Poncé, Non-perturbative self-consistent electron-phonon spectral functions and transport, arxiv , 2501.00468 (2024).

[28] A. P. Thompson, H. M. Aktulga, R. Berger, D. S. Bolintineanu, W. M. Brown, P. S. Crozier, P. J. in 't Veld, A. Kohlmeyer, S. G. Moore, T. D. Nguyen, R. Shan, M. J. Stevens, J. Tranchida, C. Trott, and S. J. Plimpton, Lammps - a flexible simulation tool for particle-based materials modeling at the atomic, meso, and continuum scales, Comput. Phys. Commun. **271**, 108171 (2022).

[29] I. S. Novikov, K. Gubaev, E. V. Podryabinkin, and A. V. Shapeev, The mlip package: moment tensor potentials with mpi and active learning, Mach. Learn.: Sci. Technol. **2**, 025002 (2021).

[30] X. Gonze, B. Amadon, G. Antonius, F. Arnardi, L. Baguet, J.-M. Beuken, J. Bieder, F. Bottin, J. Bouchet, E. Bousquet, N. Brouwer, F. Bruneval, G. Brunin, T. Cavignac, J.-B. Charraud, W. Chen, M. Côté, S. Cottenier, J. Denier, G. Geneste, P. Ghosez, M. Giantomassi, Y. Gillet, O. Gingras, D. R. Hamann, G. Hautier, X. He, N. Helbig, N. Holzwarth, Y. Jia, F. Jollet, W. Lafargue-Dit-Hauret, K. Lejaeghere, M. A. Marques, A. Martin, C. Martins, H. P. Miranda, F. Naccarato, K. Persson, G. Petretto, V. Planes, Y. Pouillon, S. Prokhorenko, F. Ricci, G.-M. Rignanese, A. H. Romero, M. M. Schmitt, M. Torrent, M. J. van Setten, B. Van Troeye, M. J. Verstraete, G. Zérah, and J. W. Zwanziger, The abinit project: Impact, environment and recent developments, Comput. Phys. Commun. **248**, 107042 (2020).

[31] A. H. Romero, D. C. Allan, B. Amadon, G. Antonius, T. Applencourt, L. Baguet, J. Bieder, F. Bottin, J. Bouchet, E. Bousquet, F. Bruneval, G. Brunin, D. Caliste, M. Côté, J. Denier, C. Dreyer, P. Ghosez, M. Giantomassi, Y. Gillet, O. Gingras, D. R. Hamann, G. Hautier, F. Jollet, G. Jomard, A. Martin, H. P. C. Miranda, F. Naccarato, G. Petretto, N. A. Pike, V. Planes, S. Prokhorenko, T. Rangel, F. Ricci, G.-M. Rignanese, M. Royo, M. Stengel, M. Torrent, M. J. van Setten, B. Van Troeye, M. J. Verstraete, J. Wiktor, J. W. Zwanziger, and X. Gonze, Abinit: Overview and focus on selected capabilities, J. Chem. Phys. **152**, 5144261 (2020).

[32] J. P. Perdew, A. Ruzsinszky, G. I. Csonka, O. A. Vydrov, G. E. Scuseria, L. A. Constantin, X. Zhou, and K. Burke, Restoring the density-gradient expansion for exchange in solids and surfaces, Phys. Rev. Lett. **100**, 136406 (2008).

[33] M. van Setten, M. Giantomassi, E. Bousquet, M. Verstraete, D. Hamann, X. Gonze, and G.-M. Rignanese, The pseudodojo: Training and grading a 85 element optimized norm-conserving pseudopotential table, Comput. Phys. Commun. **226**, 39–54 (2018).

[34] O. Hellman, I. A. Abrikosov, and S. I. Simak, Lattice dynamics of anharmonic solids from first principles, Phys. Rev. B **84**, 180301 (2011).

[35] O. Hellman, P. Steneteg, I. A. Abrikosov, and S. I. Simak, Temperature dependent effective potential method for accurate free energy calculations of solids, Phys. Rev. B **87**, 104111 (2013).

[36] O. Hellman and I. A. Abrikosov, Temperature-dependent effective third-order interatomic force constants from first

principles, Phys. Rev. B **88**, 144301 (2013).

[37] F. Knoop, N. Shulumba, A. Castellano, J. P. A. Batista, R. Farris, M. J. Verstraete, M. Heine, D. Broido, D. S. Kim, J. Klarbring, I. A. Abrikosov, S. I. Simak, and O. Hellman, Tdep: Temperature dependent effective potentials, J. Open Source Softw. **9**, 6150 (2024).

[38] S.-I. Tamura, Isotope scattering of dispersive phonons in ge, Phys. Rev. B **27**, 858 (1983).

[39] A. Castellano, F. Bottin, J. Bouchet, A. Levitt, and G. Stoltz, ab initio canonical sampling based on variational inference, Phys. Rev. B **106**, L161110 (2022).

[40] A. Castellano, R. Béjaud, P. Richard, O. Nadeau, C. Duval, G. Geneste, G. Antonius, J. Bouchet, A. Levitt, G. Stoltz, and F. Bottin, Machine learning assisted canonical sampling (mlacs) (2024).

Supplementary material: Fluctuation-dissipation and virtual processes in interacting phonon systems

Aloïs Castellano,[1] J. P. Alvarinhas Batista,[1] and Matthieu J. Verstraete[1,2]

[1]*Nanomat group, Q-MAT research center and European Theoretical Spectroscopy Facility,
Université de Liège, allée du 6 août, 19, B-4000 Liège, Belgium*
[2]*ITP, Physics Department, Utrecht University 3508 TA Utrecht, The Netherlands*

S1. THE MODE-COUPLING THEORY OF ANHARMONIC LATTICE DYNAMICS

In this section, we describe briefly the mode-coupling theory of anharmonic lattice dynamics, and we refer the interested reader to references [S1] and [S2] for more details. For our purposes, we introduce the Kubo correlation function, defined as

$$\left(A, B(t)\right) = k_{\mathrm{B}}\mathrm{T} \int_0^\beta d\lambda \left\langle A(i\hbar\lambda)B(t)\right\rangle. \tag{S1}$$

We assume that atoms vibrate around equilibrium positions $\langle \mathbf{R}\rangle$ without diffusion, allowing the introduction of mass-weighted displacements $u_i = \sqrt{M_i}(R_i - \langle R_i\rangle)$, where i is a composite index for an atom I in a Cartesian direction α, $\langle R_i\rangle$ its average position and M_i is the mass of the corresponding atom. In these mass-scaled coordinates, the forces are expressed with $f_i = -\nabla_{\mathbf{R}_i}V(\mathbf{R})/\sqrt{M_i}$. The aim of the theory is to describe the displacement-displacement Kubo correlation function

$$G_{ij} = \left(u_i, u_j(t)\right). \tag{S2}$$

The first step in the derivation is built on the Mori-Zwanzig projection operator formalism, in which the projection operator $\mathcal{P}$ and its orthogonal projection $\mathcal{Q}$ are defined as

$$\mathcal{P} = \sum_{ij}\left[\frac{(u_j, \mathcal{O})}{(u_i, u_j)}u_i + \frac{(p_j, \mathcal{O})}{(p_i, p_j)}p_i\right], \tag{S3}$$

$$\mathcal{Q} = 1 - \mathcal{P}. \tag{S4}$$

Applying the identity $\mathcal{P} + \mathcal{Q} = 1$ on the forces separates out the "known" and "random" parts. Taking the Kubo correlation of the result with respect to displacements, one obtains an equation of motion for the displacement-displacement correlation function as the generalized Langevin equation

$$\ddot{G}_{ij}(t) = -\sum_k \Phi_{jk}G_{ik}(t) - \sum_k \int_0^t ds K_{jk}(s)\dot{G}_{ik}(t-s). \tag{S5}$$

In this equation, we introduced the frequency matrix

$$\Phi_{ij} = \sum_k \left(u_k, u_j\right)^{-1}\left(u_k, f_i\right) \tag{S6}$$

as well as the memory kernel,

$$K_{ij}(t) = \frac{1}{k_{\mathrm{B}}\mathrm{T}}\left(\delta f_i, \delta f_j(t)\right), \tag{S7}$$

which is the Kubo correlation function of the random forces

$$\delta f_j(t) = e^{i\mathcal{QL}t}\left(f_j + \sum_k \Phi_{jk}u_k\right). \tag{S8}$$

The generalized interatomic force constants can be Fourier transformed and diagonalized (note that the masses are already included in $\mathbf{\Phi}$ through the mass-scaled coordinates):

$$\mathbf{\Phi}(\mathbf{q})\varepsilon_\lambda = \Omega_\lambda^2\varepsilon_\lambda, \tag{S9}$$

allowing the introduction of phonons with frequency Ω_λ and eigenvectors ε_λ, where $\lambda = (\mathbf{q}, s)$ is a super-index with $\mathbf{q}$ the wavevector and s a phonon branch. Consequently, the dynamics of the system can be described in terms of phonon operators A_λ and random forces δA_λ, defined with the projection

$$A_\lambda(t) = \sqrt{\frac{2\Omega_\lambda}{\hbar}}\sum_i \varepsilon_\lambda^i u_i(t) \tag{S10}$$

$$\delta A_\lambda(t) = \sqrt{\frac{2\Omega_\lambda}{\hbar}}\sum_i \varepsilon_\lambda^i \delta f_i(t). \tag{S11}$$

The memory kernel in phonon coordinates becomes

$$K_\lambda(t) = \frac{\hbar}{2k_{\mathrm{B}}\mathrm{T}\Omega_\lambda}\left(\delta A_\lambda, \delta A_\lambda(t)\right), \tag{S12}$$

allowing to introduce the generalized Langevin equation for the motion of a phonon λ

$$\ddot{G}_\lambda(t) = -\Omega_\lambda^2 G_\lambda(t) - \int_0^t ds K_\lambda(s)\dot{G}_\lambda(t-s). \tag{S13}$$

The most complicated part of this equation is the expression of the memory kernel. In the mode-couping theory, the difficulties are alleviated by introducing higher-order projection on several displacements. To lowest order, the random forces in real space are approximated as

$$\begin{aligned}
\delta f_i &\approx -\frac{1}{2}\sum_{jklm}\frac{(u_l u_m, \delta f_i)}{(u_j u_k, u_l u_m)}u_j u_k \\
&= -\frac{1}{2}\sum_{jk}\Psi_{ijk}u_j u_k,
\end{aligned} \tag{S14}$$

where Ψ_{ijk} are generalized third-order force constants. Projecting on phonons, the random forces are expressed as

$$\delta A_\lambda(t) \approx \sqrt{\frac{\hbar}{2}} \frac{\Omega_\lambda}{2} \sum_{\lambda'\lambda''} \Psi_{\lambda\lambda'\lambda''} A_{\lambda'}(t) A_{\lambda''}(t), \quad (S15)$$

with the three-phonon scattering matrix elements

$$\Psi_{\lambda\lambda'\lambda''} = \frac{1}{\sqrt{\Omega_\lambda \Omega_{\lambda'} \Omega_{\lambda''}}} \sum_{ijk} \frac{\varepsilon_\lambda^i \varepsilon_{\lambda'}^j \varepsilon_{\lambda''}^k}{\sqrt{M_i M_j M_k}} \Psi_{ijk}$$
$$\times e^{i(\mathbf{R}_i\mathbf{q}_\lambda + \mathbf{R}_j\mathbf{q}_{\lambda'} + \mathbf{R}_k\mathbf{q}_{\lambda''})} \Delta_\mathbf{G}(\mathbf{q} + \mathbf{q}' + \mathbf{q}''). \quad (S16)$$

The resulting memory kernel for a phonon λ is finally written

$$K_\lambda(t) = \frac{1}{16} \frac{\hbar\Omega_\lambda}{k_B T} \sum_{\lambda'\lambda''\lambda'''\lambda''''} \Psi_{\lambda\lambda'\lambda''} \Psi_{\lambda\lambda'''\lambda''''}$$
$$\left(A_{\lambda'} A_{\lambda''}, A_{\lambda'''}(t) A_{\lambda''''}(t) \right). \quad (S17)$$

S2. THE S FUNCTION

To express the memory kernel, one needs to compute the four-point correlation of eq.(S17). Carefully accounting for the imaginary time integral of Kubo correlations, we perform a decoupling [S2] expressed through a Fourier transform as:

$$\int dt \left(A_{\lambda_1} A_{\lambda_2}, A_{\lambda_3}(t) A_{\lambda_4}(t) \right) e^{i\omega t}$$
$$\approx \frac{k_B T}{n(\omega)\hbar\omega} \int_{-\infty}^{\infty} d\omega' G_{\lambda_1}^<(\omega') G_{\lambda_2}^<(\omega - \omega') \quad (S18)$$
$$\times (\delta_{\lambda_1\lambda_3}\delta_{\lambda_2\lambda_4} + \delta_{\lambda_1\lambda_4}\delta_{\lambda_2\lambda_3}),$$

where

$$n(\omega) = \frac{1}{e^{\beta\hbar\omega} - 1} \quad (S19)$$

is the Bose-Einstein distribution function. Multiplying this result by $\hbar\Omega_\lambda/k_B T$, we can now introduce the S function of the main text as

$$S_{\lambda'\lambda''}(\omega) = \frac{\hbar\Omega_\lambda}{n(\omega)\hbar\omega} \int_{-\infty}^{\infty} d\omega' G_{\lambda'}^<(\omega') G_{\lambda''}^<(\omega - \omega'), \quad (S20)$$

where we also introduced the lesser correlation function

$$G_\lambda^<(\omega) = n(\omega)\chi_\lambda''(\omega) \quad (S21)$$

Injecting eq.(S20) into eq.(S17), the memory kernel is approximated as

$$\Gamma_\lambda(\omega) \approx \frac{1}{16} \sum_{\lambda'\lambda''} |\Psi_{\lambda\lambda'\lambda''}|^2 S_{\lambda'\lambda''}(\omega). \quad (S22)$$

With the presence of Kubo correlation functions in the definition of the S function, eq.(S22) has to be solved in a self-consistent cycle involving eq.(S13)

A. Memory-less approximation

As suggested by its name, the memory-less approximation consists in neglecting the phonon dissipation in their equation of motion, which becomes

$$\ddot{G}_\lambda(t) = -\Omega_\lambda^2 G_\lambda(t). \quad (S23)$$

Such an approximation corresponds to the usual non-interacting phonons, with a spectral function given by

$$\chi_\lambda''(\omega) = \frac{\omega}{4\hbar\Omega_\lambda} \left[\delta(\omega - \Omega_\lambda) + \delta(\omega + \Omega_\lambda) \right]. \quad (S24)$$

Introducing this equation into the S function gives rise to convolutions of the form

$$\int_{-\infty}^{\infty} d\omega' n(\omega')\delta(\omega \pm \Omega_{\lambda'}) n(\omega - \omega')\delta(\omega - \omega' \pm \Omega_{\lambda''})$$
$$= n(\mp\Omega_{\lambda'}) n(\mp\Omega_{\lambda''})\delta(\omega \pm \Omega_{\lambda'} \pm \Omega_{\lambda''}). \quad (S25)$$

For further simplification, we also use the identity of the Bose-Einstein distribution for sums of frequencies

$$n(\Omega_{\lambda'} + \Omega_{\lambda''}) = \frac{n_{\lambda'} n_{\lambda''}}{(n_{\lambda'} + 1)(n_{\lambda''} + 1) - n_{\lambda'} n_{\lambda''}}, \quad (S26)$$

where we introduced the notation $n_\lambda = n(\Omega_\lambda)$. Injecting all these results into the S function, we obtain finally

$$S_{\lambda'\lambda''}(\omega) = (n_{\lambda'} - n_{\lambda''})\delta(\omega + \Omega_{\lambda'} - \Omega_{\lambda''})$$
$$- (n_{\lambda'} - n_{\lambda''})\delta(\omega - \Omega_{\lambda'} + \Omega_{\lambda''})$$
$$+ (n_{\lambda'} + n_{\lambda''} + 1)\delta(\omega - \Omega_{\lambda'} - \Omega_{\lambda''})$$
$$- (n_{\lambda'} + n_{\lambda''} + 1)\delta(\omega + \Omega_{\lambda'} + \Omega_{\lambda''}), \quad (S27)$$

which is the usual result for phonon-phonon interactions with microscopic energy conservation.

An important thing to notice about this derivation is that the energy conservation is a direct consequence of the neglect of the memory-kernel and is consequently only exact for non-interacting phonons, hence in a purely (eventually effective) harmonic system.

B. Markovian approximation

The Markovian approximation is obtained by assuming that the phonons are fast compared to the random forces, and consists in taking the $t \to \infty$ limit in the convolution term of eq.(S13). In the mode-coupling approximation, this results in a Langevin equation of motion for the phonon Kubo correlation function

$$\ddot{G}_\lambda(t) = -\Omega_\lambda^2 G_\lambda(t) - \Gamma_\lambda \dot{G}_\lambda(t), \quad (S28)$$

where $\Gamma_\lambda = \Gamma_\lambda(\Omega_\lambda)$. In frequency space, the Markovian dynamical susceptibility has a Lorentzian shape:

$$\chi_\lambda''(\omega) = \frac{1}{\pi} \frac{4\omega\Omega_\lambda\Gamma_\lambda}{(\omega^2 - \Omega_\lambda^2)^2 + 4\omega^2\Gamma_\lambda^2}$$
$$\approx \frac{\omega}{\Omega_\lambda\pi} \left[\frac{\Gamma_\lambda}{(\omega - \Omega_\lambda)^2 + \Gamma_\lambda^2} + \frac{\Gamma_\lambda}{(\omega + \Omega_\lambda)^2 + \Gamma_\lambda^2} \right]. \quad (S29)$$

Introducing the following notation for the Lorentzian

$$L(\omega, \Omega, \Gamma) = \frac{1}{\pi} \frac{\Gamma}{(\omega - \Omega)^2 + \Gamma^2} \qquad (S30)$$

and assuming a small linewidth Γ_λ compared to the frequency Ω_λ, the lesser phonon correlation functions can be approximated as

$$G_\lambda^<(\omega) \approx n(\Omega_\lambda)L(\omega, \Omega_\lambda, \Gamma_\lambda) - n(-\Omega_\lambda)L(\omega, -\Omega_\lambda, \Gamma_\lambda). \qquad (S31)$$

Thus, the S function will be composed of convolutions of the form

$$n(\pm\Omega_{\lambda'})n(\pm\Omega_{\lambda''})\left(L(\cdot, \pm\Omega_{\lambda'}, \Gamma_{\lambda'}) * L(\cdot, \pm\Omega_{\lambda''}, \Gamma_{\lambda''}) \right)(\omega)$$

$$\approx \frac{n(\mp\Omega_{\lambda'})n(\mp\Omega_{\lambda''})}{n(\omega)}L(\omega, \pm\Omega_{\lambda'} \pm \Omega_{\lambda''}, \Gamma_{\lambda'} + \Gamma_{\lambda''}). \qquad (S32)$$

Assuming a small enough linewidth, so that the Lorentzian in this equation can be approximated as acting as a delta function, the prefactor of can be rewritten $n(\pm\Omega_{\lambda'})n(\pm\Omega_{\lambda''})/n(\pm\Omega_{\lambda'} \pm \Omega_{\lambda''})$. Collecting these results, the S function in the Markovian approximation is written

$$\begin{aligned} S_{\lambda'\lambda''}(\omega) = &(n_{\lambda'} + n_{\lambda''} + 1)L(\omega, \Omega_{\lambda'} + \Omega_{\lambda''}, \Gamma_{\lambda'} + \Gamma_{\lambda''}) \\ &- (n_{\lambda'} + n_{\lambda''} + 1)L(\omega, -\Omega_{\lambda'} - \Omega_{\lambda''}, \Gamma_{\lambda'} + \Gamma_{\lambda''}) \\ &+ (n_{\lambda'} - n_{\lambda''})L(\omega, \Omega_{\lambda'} - \Omega_{\lambda''}, \Gamma_{\lambda'} + \Gamma_{\lambda''}) \\ &- (n_{\lambda'} - n_{\lambda''})L(\omega, -\Omega_{\lambda'} + \Omega_{\lambda''}, \Gamma_{\lambda'} + \Gamma_{\lambda''}). \end{aligned} \qquad (S33)$$

The derivation so far only includes three phonon interactions. However, it can be important to consider other phonon-phonon contributions to the memory kernel, such as the four phonon or isotopic disorder scattering. Renaming the previously derived memory kernel as $\Gamma_\lambda^{3ph}(\omega)$, the memory kernel with these contributions is given by

$$\Gamma_\lambda(\omega) = \Gamma_\lambda^{iso}(\omega) + \Gamma_\lambda^{3ph}(\omega) + \Gamma_\lambda^{4ph}(\omega). \qquad (S34)$$

The isotopic contribution $\Gamma_\lambda^{iso}(\omega)$, corresponding to Tamura's model [S3], is written

$$\Gamma_\lambda^{iso}(\omega) = \sum_{\lambda'} g_i|\epsilon_\lambda^i \epsilon_{\lambda'}^i|^2 L(\omega, \Omega_{\lambda'}, \Gamma_{\lambda'}), \qquad (S35)$$

with g_i measuring the distribution of the isotope masses of element i and computed as $g_i = \sum_n \frac{d_{i,n}}{N}\left(\frac{\Delta M_{i,n}}{M_i}\right)^2$. In this equation, N is the number of isotopes, $d_{i,n}$ is the concentration of isotope n of element i, and $\Delta M_{i,n}$ is the mass difference between isotope n and the average mass of the element. The four phonon contribution Γ_λ^{4ph} is given by

$$\Gamma_\lambda^{4ph}(\omega) = \frac{\pi}{96} \sum_{\lambda'\lambda''\lambda'''} |\Psi_{\lambda\lambda'\lambda''\lambda'''}|^2 S_{\lambda'\lambda''\lambda'''}(\omega), \qquad (S36)$$

with $\Psi_{\lambda\lambda'\lambda''\lambda'''}$ the four-phonon scattering matrix elements. Following the same steps as for the three phonons, the S function for four phonons in the Markovian approximation is given by

$$\begin{aligned} S_{\lambda'\lambda''\lambda'''} = &\frac{n_{\lambda'}n_{\lambda''}n_{\lambda'''}}{n(\omega)}L(\omega, \Omega_{\lambda'} + \Omega_{\lambda''} + \Omega_{\lambda'''}, \Gamma_{\lambda'} + \Gamma_{\lambda''} + \Gamma_{\lambda'''}) \\ &+ \frac{(n_{\lambda'} + 1)n_{\lambda''}n_{\lambda'''}}{n(\omega)}L(\omega, -\Omega_{\lambda'} + \Omega_{\lambda''} + \Omega_{\lambda'''}, \Gamma_{\lambda'} + \Gamma_{\lambda''} + \Gamma_{\lambda'''}) \\ &+ \frac{n_{\lambda'}(n_{\lambda''} + 1)n_{\lambda'''}}{n(\omega)}L(\omega, \Omega_{\lambda'} - \Omega_{\lambda''} + \Omega_{\lambda'''}, \Gamma_{\lambda'} + \Gamma_{\lambda''} + \Gamma_{\lambda'''}) \\ &+ \frac{n_{\lambda'}n_{\lambda''}(n_{\lambda'''} + 1)}{n(\omega)}L(\omega, \Omega_{\lambda'} + \Omega_{\lambda''} - \Omega_{\lambda'''}, \Gamma_{\lambda'} + \Gamma_{\lambda''} + \Gamma_{\lambda'''}) \\ &+ \frac{(n_{\lambda'} + 1)(n_{\lambda''} + 1)n_{\lambda'''}}{n(\omega)}L(\omega, -\Omega_{\lambda'} - \Omega_{\lambda''} + \Omega_{\lambda'''}, \Gamma_{\lambda'} + \Gamma_{\lambda''} + \Gamma_{\lambda'''}) \\ &+ \frac{(n_{\lambda'} + 1)n_{\lambda''}(n_{\lambda'''} + 1)}{n(\omega)}L(\omega, -\Omega_{\lambda'} + \Omega_{\lambda''} - \Omega_{\lambda'''}, \Gamma_{\lambda'} + \Gamma_{\lambda''} + \Gamma_{\lambda'''}) \\ &+ \frac{n_{\lambda'}(n_{\lambda''} + 1)(n_{\lambda'''} + 1)}{n(\omega)}L(\omega, \Omega_{\lambda'} - \Omega_{\lambda''} - \Omega_{\lambda'''}, \Gamma_{\lambda'} + \Gamma_{\lambda''} + \Gamma_{\lambda'''}) \\ &+ \frac{(n_{\lambda'} + 1)(n_{\lambda''} + 1)(n_{\lambda'''} + 1)}{n(\omega)}L(\omega, -\Omega_{\lambda'} - \Omega_{\lambda''} - \Omega_{\lambda'''}, \Gamma_{\lambda'} + \Gamma_{\lambda''} + \Gamma_{\lambda'''}). \end{aligned} \qquad (S37)$$

S3. LORENTZIAN AND ENERGY CONSERVATION

With the energy conservation condition, the numerical approximation of the delta function becomes one of the most delicate parts for the implementation of phonon-
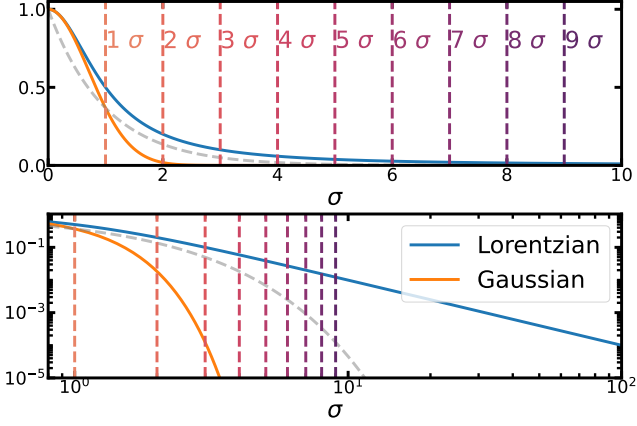
FIG. S1. Lorentzian and Gaussian functions centered on 0, with equal width $\sigma = 1$ and normalized to 1 at $x = 0$. Top is in a linear scale and bottom is a log-log scale. The grey dashed-line shows an exponential decay.
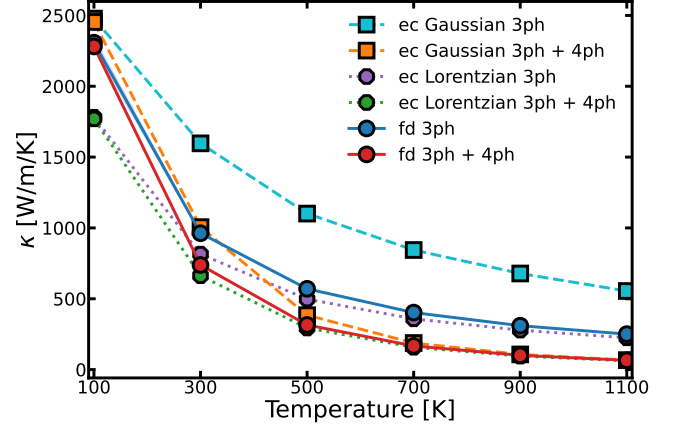

FIG. S2. Thermal conductivity in BAs using energy conservation (ec), with either Gaussian or Lorentzian approximation to delta functions or with the fluctuation-dissipation condition (fd).

phonon interactions. Usually, the delta are replaced by highly peaked symmetric functions which recover the delta function in the limit of vanishing width. In recent years, the use of Gaussians with adaptively parametrized widths has become the *de facto* standard, but other functions have been proposed, in particular the Lorentzian. For highly harmonic systems, in which the linewidths are small, the fact that both Gaussian and Lorentzian are approximations of delta functions seems to imply that the energy-conservation is still somewhat valid. The results for AgI and Si displayed on fig.S4 and S3 seem to confirm this intuition, with κ varying only slightly when going from the energy conservation to the fluctuation-dissipation condition.

However, the BAs result of the main text shows that the validity of energy conservation is more complex, allowing us to highlight an often overlooked but key difference between Lorentzians and Gaussians as numerical approximations for delta functions. Indeed, if both reduce to delta peaks in the limit of vanishing width, these function have a very different behavior once their width is finite. In particular, the Lorentzian is a long-tail distribution, decreasing exponentially slower than the Gaussian. For instance fig.S1 shows that one need to go to more than 56 σ to decrease the value of a Lorentzian to 10^{-4}. For phonon-phonon interactions this means that, when using Lorentzians, interactions between phonons with a large energy separation still have noticeable effects on Γ_λ, thus breaking energy-conservation.

This is illustrated on fig S2, which shows that for BAs, enforcing energy-conservation through Lorentzian functions results in a thermal conductivity close to that obtained with the physically exact fluctuation-dissipation condition. While this casts doubt on the Lorentzian's utility as a good numerical approximation for delta functions, it seems that the adaptive broadening scheme with Lorentzian functions can serve as an approximation for

the full self-consistent calculations for the fluctuation-dissipation, especially at high T.

S4. RESULTS IN SILICON AND AGI

To assess the effects of fluctuation-dissipation on other systems, we compute the thermal conductivity with self-consistent linewidths for silicon and AgI, using the generalized interatomic force constants calculated in ref [S2].

Similarly to BAs, silicon is a very harmonic material, presenting high frequencies and low linewidths, so that the phonon dynamical susceptibilities in this system are close to Lorentzian. However, being mono-elemental, the phonon dispersion in Si doesn't present a gap between the acoustic and optical bands as shown on fig.S3. As a result, the thermal conductivity computed with energy conservation or the fluctuation-dissipation condition are virtually indistinguishable, as can be seen in fig.S3.

The corresponding results for AgI are shown in fig.S4 and S5 Here anharmonicity is much stronger, as are the phonon frequency shifts with T. Compared to BAs, the variation observed when including the fluctuation dissipation conditions are smaller, but fig.S5 shows that the self-consistency still amounts to a sizable reduction in the thermal conductivity At the three-phonon level, the κ reduction is between 15 and 25% from 100 to 300 K, and with four-phonon interactions this reduction is still 5% to 20%.

S5. VALIDITY OF THE MARKOVIAN APPROXIMATION

Our computational approach to incorporate the fluctuation-dissipation theorem is constructed on the premise that the Markovian approximation (ignoring
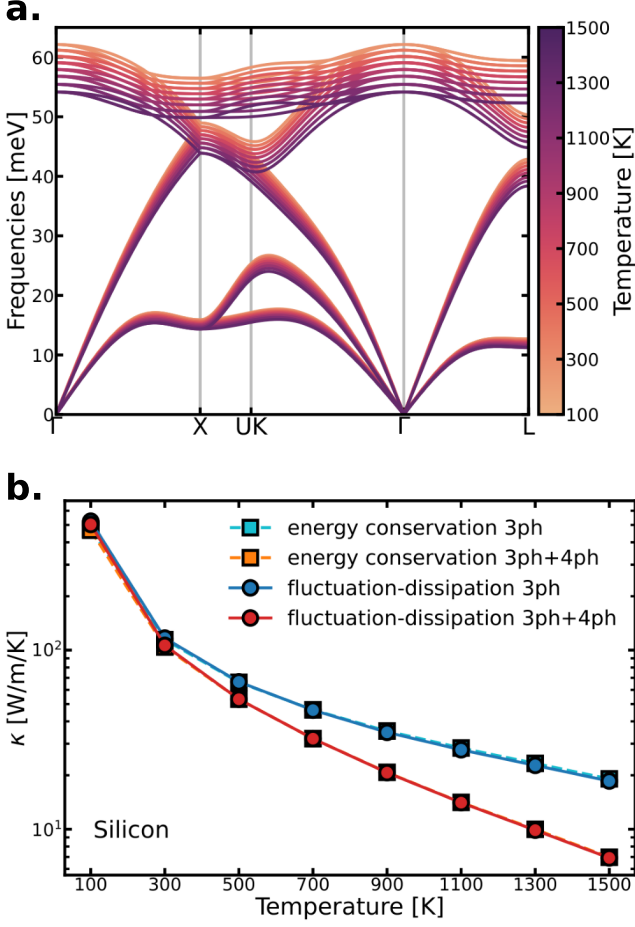
FIG. S3. **a.** Evolution of the phonons in silicon between 100 and 1500 K. **b.** Thermal conductivity of silicon computed with energy conservation or the fluctuation-dissipation condition.
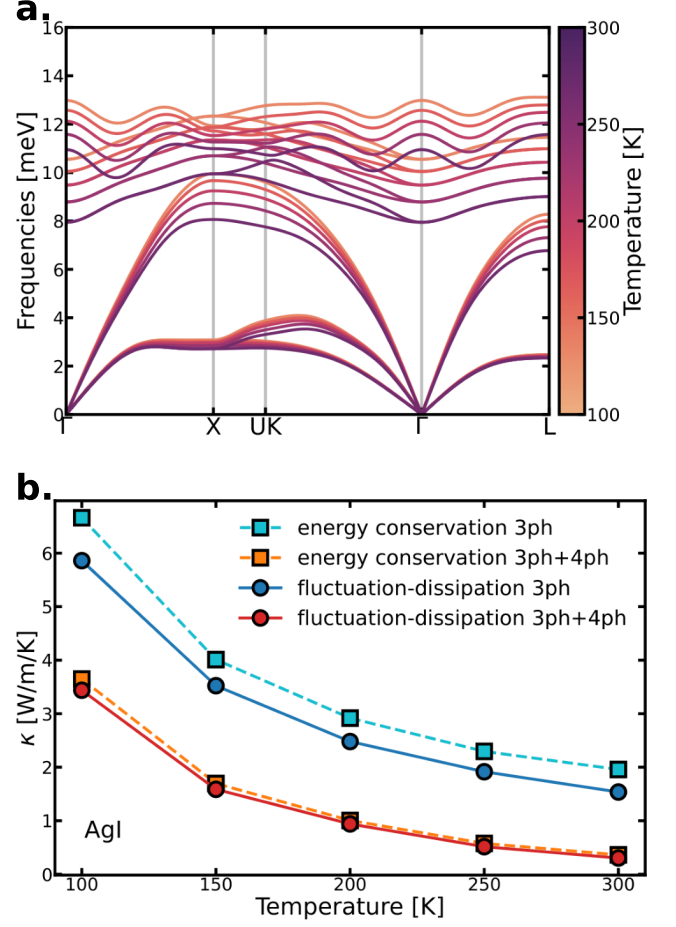

FIG. S4. **a.** Evolution of the phonons in AgI between 100 and 300 K. **b.** Thermal conductivity of AgI computed with energy conservation or the fluctuation-dissipation condition.

memory effects) accurately models thermal transport. Consequently, evaluating the correctness of this approximation is crucial. To this end, we calculated the thermal conductivity without the Markovian approximation in the single mode approximation framework (ignoring collective effects) and without the fluctuation dissipation theorem. Our non-Markovian expression for the thermal conductivity is given by

$$\boldsymbol{\kappa}_{\mathrm{SMA}}^{\mathrm{nM}} = \frac{\pi}{V} \sum_{\lambda\lambda'} \mathbf{v}_{\lambda\lambda'} \otimes \mathbf{v}_{\lambda\lambda'} \int_{-\infty}^{\infty} d\omega \chi_\lambda''(\omega)\chi_{\lambda'}''(\omega)c(\omega)$$
(S38)

where $c(\omega) = \omega^2 n(\omega)(n(\omega)+1)/k_\mathrm{B}\mathrm{T}^2$ is the frequency dependent heat capacity, and χ_λ is the full susceptibility generalizing Eq. S29. When taking the Markovian limit, the thermal conductivity tensor is given by:

$$\boldsymbol{\kappa}_{\mathrm{SMA}}^{\mathrm{M}} = \frac{\pi}{V} \sum_{\lambda\lambda'} \mathbf{v}_{\lambda\lambda'} \otimes \mathbf{v}_{\lambda\lambda'} c(\Omega_\lambda)\Gamma_{\lambda\lambda'}$$
(S39)

where we define

$$\Gamma_{\lambda\lambda'} = \frac{\Gamma_\lambda + \Gamma_{\lambda'}}{(\Omega_\lambda - \Omega_{\lambda'})^2 + (\Gamma_\lambda + \Gamma_{\lambda'})^2}.$$
(S40)

Focusing on the three-phonon scattering level, fig.S8 presents our findings for AgI, which is the most anharmonic material analyzed in this study. The minor discrepancy between $\boldsymbol{\kappa}^\mathrm{M}$ and $\boldsymbol{\kappa}^\mathrm{nM}$ (about $10^{-2}\mathrm{W/m/K}$) confirms the reliability of the Markovian approximation even in such highly anharmonic systems. For BAs fig.S9 shows that the impact of non-Markovian effects is similarly minimal. Indeed, the relative difference between calculations with and without Markovian effects is around a few percent at the highest temperature, where memory effects are expected to be more significant.

These tests are restricted to calculations with three-phonon interactions and omitted the collective phonon contributions. The structure of the thermal conductivity formulation suggests that four-phonon interactions should not change the analysis performed at the three
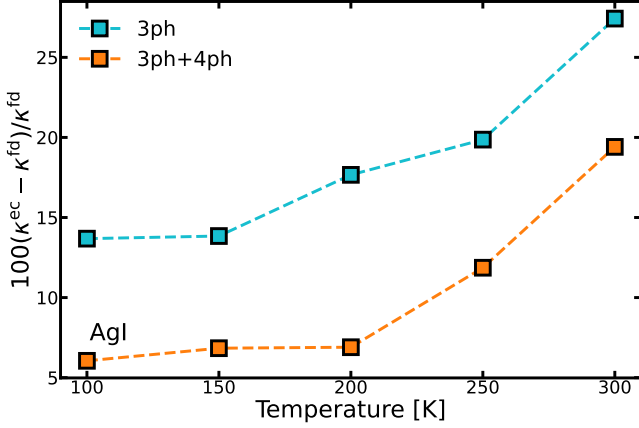
FIG. S5. Difference between the thermal conductivity of AgI computed with energy conservation or the fluctuation-dissipation condition.

phonon level. In particular, the Markovian limit of the thermal conductivity involves the substitution

$$\int_{-\infty}^{\infty} d\omega c(\omega)\chi_\lambda''(\omega)\chi_\lambda''(\omega) \to \frac{c(\Omega_\lambda)}{2\Gamma_\lambda}. \qquad (S41)$$

For modes that are strongly non-Markovian, the substituted formula involving the inverse of the scattering rates should be small, indicating a proportionally small contribution to the thermal conductivity. Furthermore, these contributions decrease even more when combined with group velocities, as non-Markovian modes are typically optical, and have low group velocities.

For the collective contribution, there is currently no formulation to our knowledge involving non-Markovian effects. Such a derivation would be very interesting but we also expect these to be minimal in our case, since collective contributions are mainly observed in fairly harmonic systems where the Markovian limit is accurate, as in BAs. For AgI, the collective effects in the Markovian approximation are even smaller than the memory contribution at the three-phonon level and we expect collective contributions to remain negligible also beyond the Markovian approximation.

We anticipate that incorporating four-phonon interactions and collective phonon contributions will not significantly alter the conclusions from three-phonon interactions in the single-mode approximation: the Markovian approximation remains applicable to the systems explored in this work.

S6. COMPUTATIONAL DETAILS

For the silicon and AgI results presented in this supplementary materials, we used the MLIP and parameters from reference [S2]. For BAs, all DFT calculations were performed with the Abinit suite [S4, S5] using PBEsol pseudopotentials [S6] from the Pseudo-dojo project [S7].

After carefully checking the convergence, the kinetic energy cutoff was set to 42 Hartree and a $10 \times 10 \times 10$ k-point grid was used for unit-cell calculations. Supercell DFT calculations were performed on $3 \times 3 \times 3$ repetitions of the conventional unit-cells with only Γ point sampling.

To reduce the computational cost, a machine learning interatomic potential (MLIP) was constructed using the Moment Tensor Potential framework [S8, S9]. The training dataset was generated self-consistently following the methodology described in ref [S2] and using the MLACS code [S10, S11], with temperatures generated randomly between 20 and 1300 K for the MLIP driven molecular dynamic simulations. Only 122 DFT configurations were necessary to converge the MLIP. Our resulting potential provide a very accurate representation of the DFT described Born-Oppenheimer surface for BAs, as shown by the low root mean squared error and high correlation displayed on fig.(S6). To further assess the accuracy of our MLIP, we also compare harmonic phonons computed with finite differences on fig.(S7). The MLIP and DFT dispersions are indistinguishable, giving a high confidence in the ability of our MLIP to describe the atomic motion in BAs crystals.

To compute the generalized interatomic force constants, NVT molecular dynamics simulations were performed on $4 \times 4 \times 4$ conventional supercells. The volume is obtained from averages of NPT MD runs, to account for the system's thermal expansion. All the MD calculation were performed with the LAMMPS package [S12], and the mode-coupling theory calculation were done with the TDEP package [S13–S16]. For BAs, the generalized interatomic force constants used cutoffs of 9.55, 6.0 and 3.5 Å for the second, third and fourth-order, respectively. For the thermal conductivity calculations, we used a full q-point grid of $32 \times 32 \times 32$ and the scattering were computed on $16 \times 16 \times 16$ and $6 \times 6 \times 6$ Monte-Carlo q-grid for the third and fourth order, using the implementation presented in ref [S2].

Fundamentally, the self-consistent algorithm involves iteratively performing thermal conductivity calculations using Lorentzians whose broadening is derived from previous iterations. In all instances, the initial iteration employs energy conservation within the adaptive Gaussian scheme [S2], although it has been observed that the starting point does not affect the final results. No mixing of the linewidths between iterations was used, as this approach did not enhance convergence. For all calculations, we conducted 10 iterations and averaged the results over the last 5 iterations, to help mitigate noise arising from the Monte-Carlo grid integration. In both the main and supplementary texts, all results incorporating the fluctuation-dissipation condition also display the variance of the thermal conductivity over these 5 iterations as a shaded area. However, the variance is usually smaller than the width of the lines. The self-consistent cycle is illustrated in Fig.S10, which depicts the evolution of the thermal conductivity with iterations for BAs at 300K at the three-phonon level.
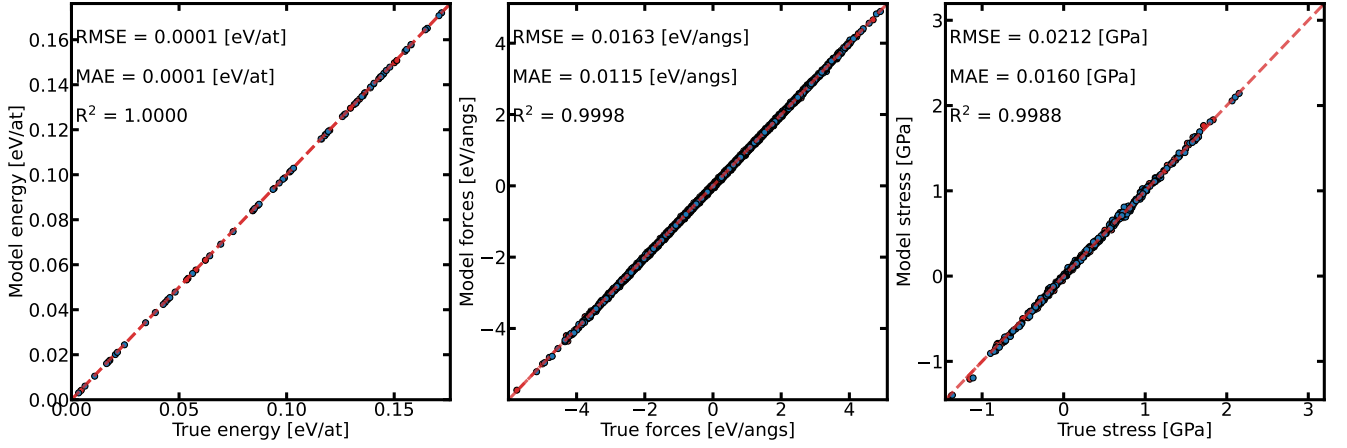
FIG. S6. Correlation between energy, forces and stress computed with DFT and our MLIP.
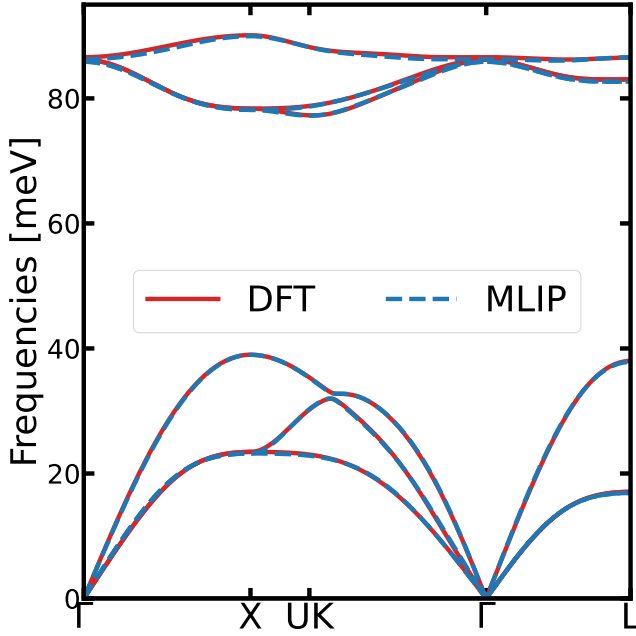

FIG. S7. Comparison between harmonic phonons computed with finite difference using DFT and our MLIP.

[S1] A. Castellano, J. P. A. Batista, and M. J. Verstraete, Mode-coupling theory of lattice dynamics for classical and quantum crystals, J. Chem. Phys. **159**, 0174255 (2023).

[S2] A. Castellano, J. P. A. Batista, O. Hellman, and M. J. Verstraete, Mode-coupling formulation of heat transport in anharmonic materials, Phys. Rev. B **111**, 094306 (2025).

[S3] S.-I. Tamura, Isotope scattering of dispersive phonons in ge, Phys. Rev. B **27**, 858 (1983).

[S4] X. Gonze, B. Amadon, G. Antonius, F. Arnardi, L. Baguet, J.-M. Beuken, J. Bieder, F. Bottin, J. Bouchet, E. Bousquet, N. Brouwer, F. Bruneval, G. Brunin, T. Cavignac, J.-B. Charraud, W. Chen, M. Côté, S. Cottenier, J. Denier, G. Geneste, P. Ghosez, M. Giantomassi, Y. Gillet, O. Gingras, D. R. Hamann, G. Hautier, X. He, N. Helbig, N. Holzwarth, Y. Jia, F. Jollet, W. Lafargue-Dit-Hauret, K. Lejaeghere, M. A. Marques, A. Martin, C. Martins, H. P. Miranda, F. Naccarato, K. Persson, G. Petretto, V. Planes, Y. Pouillon, S. Prokhorenko, F. Ricci, G.-M. Rignanese, A. H. Romero, M. M. Schmitt, M. Torrent, M. J. van Setten, B. Van Troye, M. J. Verstraete, G. Zérah, and J. W. Zwanziger, The abinit project: Impact, environ-
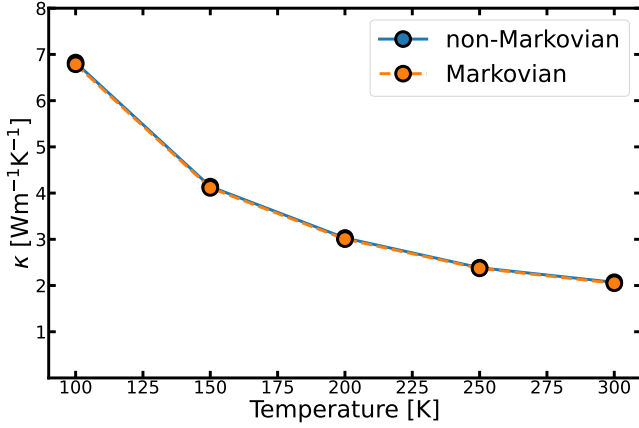
FIG. S8. Comparison of thermal conductivity for AgI, with and without applying the Markovian approximation, utilizing three-phonon scattering and maintaining strict energy conservation.
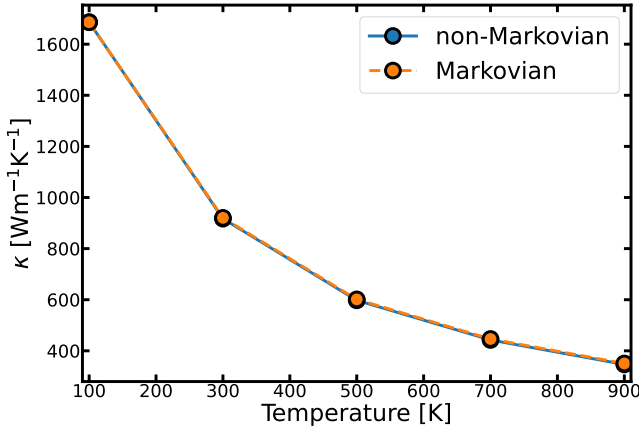

FIG. S10. Convergence of the thermal conductivity in BAs with FD iterations. The calculation only consider three-phonon interactions.

FIG. S9. Comparison of thermal conductivity for BAs, with and without applying the Markovian approximation, utilizing three-phonon scattering and maintaining strict energy conservation. It is important to note that the collective effects, which are important for BAs, are not included in the calculations.

ment and recent developments, Comput. Phys. Commun. **248**, 107042 (2020).

[S5] A. H. Romero, D. C. Allan, B. Amadon, G. Antonius, T. Applencourt, L. Baguet, J. Bieder, F. Bottin, J. Bouchet, E. Bousquet, F. Bruneval, G. Brunin, D. Caliste, M. Côté, J. Denier, C. Dreyer, P. Ghosez, M. Giantomassi, Y. Gillet, O. Gingras, D. R. Hamann, G. Hautier, F. Jollet, G. Jomard, A. Martin, H. P. C. Miranda, F. Naccarato, G. Petretto, N. A. Pike, V. Planes, S. Prokhorenko, T. Rangel, F. Ricci, G.-M. Rignanese, M. Royo, M. Stengel, M. Torrent, M. J. van Setten, B. Van Troeye, M. J. Verstraete, J. Wiktor, J. W. Zwanziger, and X. Gonze, Abinit: Overview and focus on selected capabilities, J. Chem. Phys. **152**, 5144261 (2020).

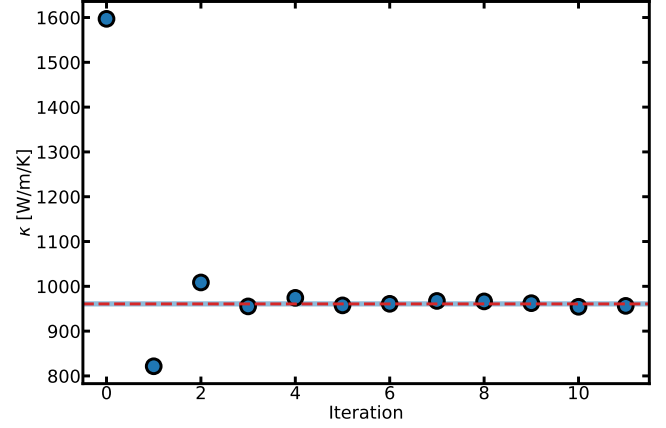[S6] J. P. Perdew, A. Ruzsinszky, G. I. Csonka, O. A. Vydrov, G. E. Scuseria, L. A. Constantin, X. Zhou, and K. Burke, Restoring the density-gradient expansion for exchange in solids and surfaces, Phys. Rev. Lett. **100**, 136406 (2008).

[S7] M. van Setten, M. Giantomassi, E. Bousquet, M. Verstraete, D. Hamann, X. Gonze, and G.-M. Rignanese, The pseudodojo: Training and grading a 85 element optimized norm-conserving pseudopotential table, Comput. Phys. Commun. **226**, 39–54 (2018).

[S8] A. V. Shapeev, Moment tensor potentials: A class of systematically improvable interatomic potentials, Multiscale Modeling Sim. **14**, 1153–1173 (2016).

[S9] I. S. Novikov, K. Gubaev, E. V. Podryabinkin, and A. V. Shapeev, The mlip package: moment tensor potentials with mpi and active learning, Mach. Learn.: Sci. Technol. **2**, 025002 (2021).

[S10] A. Castellano, F. Bottin, J. Bouchet, A. Levitt, and G. Stoltz, ab initio canonical sampling based on variational inference, Phys. Rev. B **106**, L161110 (2022).

[S11] A. Castellano, R. Béjaud, P. Richard, O. Nadeau, C. Duval, G. Geneste, G. Antonius, J. Bouchet, A. Levitt, G. Stoltz, and F. Bottin, Machine learning assisted canonical sampling (mlacs) (2024).

[S12] A. P. Thompson, H. M. Aktulga, R. Berger, D. S. Bolintineanu, W. M. Brown, P. S. Crozier, P. J. in 't Veld, A. Kohlmeyer, S. G. Moore, T. D. Nguyen, R. Shan, M. J. Stevens, J. Tranchida, C. Trott, and S. J. Plimpton, Lammps - a flexible simulation tool for particle-based materials modeling at the atomic, meso, and continuum scales, Comput. Phys. Commun. **271**, 108171 (2022).

[S13] O. Hellman, I. A. Abrikosov, and S. I. Simak, Lattice dynamics of anharmonic solids from first principles, Phys. Rev. B **84**, 180301 (2011).

[S14] O. Hellman, P. Steneteg, I. A. Abrikosov, and S. I. Simak, Temperature dependent effective potential method for accurate free energy calculations of solids, Phys. Rev. B **87**, 104111 (2013).

[S15] O. Hellman and I. A. Abrikosov, Temperature-dependent effective third-order interatomic force constants from first principles, Phys. Rev. B **88**, 144301 (2013).

[S16] F. Knoop, N. Shulumba, A. Castellano, J. P. A. Batista,

R. Farris, M. J. Verstraete, M. Heine, D. Broido, D. S. Kim, J. Klarbring, I. A. Abrikosov, S. I. Simak, and O. Hellman, Tdep: Temperature dependent effective potentials, J. Open Source Softw. **9**, 6150 (2024).

Paper IV

3.4 Thermal Conductivity Of Monolayer Hexagonal Boron Nitride: Four-Phonon Scattering And Quantum Sampling Effects

José Pedro Alvarinhas Batista, Matthieu J Verstraete, Aloïs Castellano

Publication Report

Contributions Summary:*Contributed to conceptualization, theory, simulations and manuscript writing*

Abstract

Monolayer hexagonal boron nitride is a prototypical planar 2-dimensional material and has been the subject of many investigations of its exceptional vibrational, spectroscopic and transport properties. The lattice thermal conductivity remains quite uncertain, with theoretical and experimental reports varying between 218 and 1060 Wm-1K-1. It has a strong temperature evolution and is sensitive to strain effects and isotope concentrations. While the impact of isotope scattering has been widely studied and is well understood, nuclear quantum effects and 4-phonon scattering have so far been neglected. Monolayer hexagonal boron nitride is composed of light elements, and further has its 3-phonon scattering phase space restricted by mirror plane symmetry, so these effects may be of similar order as isotope scattering, and would lead to a completely different understanding of the fundamental processes limiting the lattice thermal conductivity for this system. In this work, we use both classical and path-integral molecular dynamics, in conjunction with the Temperature Dependent Effective Potential method, to compute temperature-dependent renormalized phonons including isotope scattering, 3-phonon scattering, 4-phonon scattering and nuclear quantum effects. We show the impact of the latter two on the lattice thermal conductivity for a large temperature range, as well as their impact on the phonon lifetimes. Overall, our work provides a robust framework for calculations of the lattice thermal conductivity in solids, providing quantitative improvements and physical understanding that help explain the variety of results found in the literature.

Thermal Conductivity Of Monolayer Hexagonal Boron Nitride: Four-Phonon Scattering And Quantum Sampling Effects

José Pedro Alvarinhas Batista,[1, *] Matthieu J. Verstraete,[1, 2] and Aloïs Castellano[1]

[1]*Nanomat group, Q-MAT center, CESAM research unit and European Theoretical Spectroscopy Facility,*
Université de Liège, allée du 6 août, 19, B-4000 Liège, Belgium
[2]*ITP, Physics Department, Utrecht University 3508 TA Utrecht, The Netherlands*

Monolayer hexagonal boron nitride is a prototypical planar 2-dimensional system material and has been the subject of many investigations of its exceptional vibrational, spectroscopic and transport properties. The lattice thermal conductivity remains quite uncertain, with theoretical and experimental reports varying between 218 and 1060 $Wm^{-1}K^{-1}$. It has a strong temperature evolution and is sensitive to strain effects and isotope concentrations. While the impact of isotope scattering has been widely studied and is well understood, nuclear quantum effects and 4-phonon scattering have so far been neglected. Monolayer hexagonal boron nitride is composed of light elements, and further has its 3-phonon scattering phase space restricted by mirror plane symmetry, so these effects may be of similar order as isotope scattering, and would lead to a completely different understanding of the fundamental processes limiting the lattice thermal conductivity for this system. In this work, we use both classical and path-integral molecular dynamics, in conjunction with the Temperature Dependent Effective Potential method, to compute temperature-dependent renormalized phonons including isotope scattering, 3-phonon scattering, 4-phonon scattering and nuclear quantum effects. We show the impact of the latter two on the lattice thermal conductivity for a large temperature range, as well as their impact on the phonon lifetimes. Overall, our work provides a robust framework for calculations of the lattice thermal conductivity in solids, providing quantitative improvements and physical understanding that help explain the variety of results found in the literature.

I. INTRODUCTION

With the rise of energetic efficiency as a worldwide priority in recent years, new solutions for thermal management are being sought at all scales from macro to nano. The strongly anisotropic and tunable nature of 2-dimensional materials suggests a broad range of applications in this domain. In particular, systems with very large in-plane thermal conductivity (κ) have been highly sought after for the flexibility they provide in directed cooling of semiconductor microchips.

For over a decade, simulations of thermal conductivity for layered and 2D materials pointed to graphene and monolayer hexagonal boron nitride (h-BN) as the best candidates for thermal management applications [1–8]. Experimental work has mostly supported this idea [9–14], though results found in the literature can vary widely. The case of graphene is particularly extreme variance, though most studies report very high thermal conductivities.

These results have been, however, called into question more recently. Graphene's thermal conductivity has been shown to actually be lower than that of diamond if 4-phonon scattering effects are taken into account [15–17]. In the particular case of *strictly planar* 2D systems, the acoustic flexural mode was previously thought to be the main driver for the thermal conductivity. Its scattering phase space is suppressed due to mirror plane symmetry, which prevents scattering events containing an odd number of such modes [1, 18]. The result of this suppression

is that, despite the fact that the third-order interatomic force constants (IFCs) are still larger in amplitude than the fourth-order ones, the scattering phase space they span is so reduced that the sheer number of allowed 4-phonon interactions makes them dominant.

Another question that is raised for both graphene and h-BN systems is the role played by nuclear quantum effects (NQEs) in their thermal conductivities. Both are composed of light elements and have rather large Debye temperatures ($\sim$ 1680K for h-BN [19] and $\sim$ 1800K for graphene [20]). One standard approach to include NQEs in phonon simulations is the self-consistent harmonic approximation (SCHA), most commonly used in its stochastic form (sSCHA) [21–25], a non-perturbative, self-consistent anharmonic phonon theory. SCHA has an effective harmonic Hamiltonian as its basis, enforcing a Gaussian distribution whose mean and variance are temperature dependent. This restriction on the distribution means that the SCHA is usually very reliable for lower temperatures, where the Gaussian approximation is often appropriate, but can fail at higher temperatures or near phase transitions, where anharmonicity can increase drastically to the point where the phonon distribution takes a more complex form, and requires extra parameters like skewness and kurtosis. A solution to this problem is to instead employ an approach based on path-integral molecular dynamics (PIMD) [26–28] for sampling purposes: the MD will guarantee the correct canonical distribution, and the path integral is able to handle quantum effects at low T. Once sampled, the temperature dependent effective potential (TDEP) method [29–32] can extract the anharmonic phonons from the dynamics. Since TDEP works by fitting IFCs directly

from the snapshots it is provided with, if these come directly from MD the displacement distribution does not follow a pre-established functional form, and will remain accurate even in very anharmonic scenarios. It is worth noting that TDEP is not restricted to fitting IFCs from MD simulations, and can be used in its stochastic form as well (known as sTDEP) [33] as another variation of the SCHA.

The PIMD + TDEP approach has been applied to metallic hydrogen [34] and silicon [35], and we gave a formal treatment and justification in a previous paper [36], based on the Mori-Zwanzig projection operator formalism and the mode coupling approximation. The fcc phase of ^{4}He was chosen as a test case. We showed that the method provides remarkable agreement with inelastic neutron scattering experiments and how, even at low temperatures, the PIMD based approach differs from the SCHA when comparing 3rd order IFCs. This difference can prove essential when dealing with thermal conductivity calculations, where higher order IFCs are the crucial ingredients to obtain scattering amplitudes. Combined with the fact that at high temperature the PIMD sampling based results should match their classical MD counterparts, this unified approach allows us to not only directly investigate the importance of NQEs, but also study a wide temperature range using a single consistent method.

In this work, we use TDEP combined with both classical MD and PIMD, to study the impact of NQEs and 4-phonon scattering effects in the lattice thermal conductivity of monolayer hexagonal boron nitride. A machine learning interatomic potential (MLIP) based on the moment tensor potential (MTP) descriptor [37, 38] is used to accelerate the sampling process for both cases. The main results of this work are separated in 3 parts. In the first part, we demonstrate the accuracy of the MLIP and address the convergence of the lattice parameter and its temperature dependence, as well as how the system's pair distribution function changes with temperature in the classical and quantum cases. In the second part, we show the consequences of the NQEs on the TDEP fit, as well as in the temperature-dependent phonon band structures. Finally, in the third part we show our main result: how the thermal conductivity evolves with temperature when including classical MD or PIMD and either 3 or 3+4 phonon scattering. We show that the thermal conductivity is drastically overestimated using just 3-phonon interactions, highlighting the importance of 4-phonon effects in planar 2D materials. The restriction imposed by mirror-plane symmetry on the acoustic flexural phonons and their interactions is such that 4-phonon scattering is required for an accurate description of the thermal conductivity. This implies that both levels of theory are essential for a proper physical understanding of the phonon-phonon interactions in monolayer h-BN, calling into question previous results for systems with similar scattering constraints. We further show that, despite the very light masses, effects of NQEs are small in h-BN, and a classical approach therefore suffices for this system, provided full anharmonicity is taken into account.

II. METHODS

To build temperature dependent IFCs we rely on the TDEP method [29–32], which has been proven to provide a solution to the lattice dynamics problem, both in the classical and quantum cases[36] in the context of mode-coupling theory. In this approach, temperature-dependent second-order IFCs are computed from representative configurations of the canonical ensemble through a least-squares fit of the atoms' forces and displacements. Higher-order IFCs are built in succession with the residual forces, subtracting the previous order fits.

Sampling of the canonical ensemble is performed using classical and PI-MD driven by machine learning (ML). An order 22 MTP descriptor with a radial cutoff of 5.5 Å is employed as per Ref. [38]. Long range electrostatic effects are not accounted for explicitly in the MLIP, but we do not expect a significant effect on the thermal conductivity due to polar effects. In our calculations the LO and TO modes combined contribute less than 1% to the total thermal conductivity. The training of the MLIP is done using the machine learning assisted canonical sampling (MLACS) approach [39, 40] with PIMD. After each snapshot is added to the training set, the temperature of a Langevin thermostat is changed to a random value between 100K and 1200K. This allows us to train a single potential usable for all cases of interest. Density functional theory (DFT) calculations are done with the Abinit code [41, 42], using the PBE exchange-correlation functional [43] as well as D3 van der Waals corrections according to Ref. [44]. A plane wave energy cutoff of 40 Ha and a 2x2x1 k-point grid were sufficient to ensure convergence for our supercell (6x6x1 with 72 atoms) total energies to a 1 meV per atom accuracy.

Molecular dynamics simulations were performed using the LAMMPS software [45] with a 0.5 fs time-step. The GJF integrator [46] is used for the Langevin dynamics in the classical case, while the BAOAB integrator is used instead for the path-integral cases. The number of beads used in the PIMD simulations is determined by first converging the energy of the lowest temperature case (150K), and then maintaining $N_{beads} \times T$ constant. The converged value is found to be $N_{beads} = 80$, implying $N_{beads} \times T = 12000$ is imposed for all temperatures.

After convergence of the MLIP, NPT simulations are launched for temperatures between 150K and 1050K, with increasing steps of 150K, in order to obtain the equilibrium volumes of the supercells. The equilibrated cells are then used for sampling under NVT conditions to obtain representative configurations of the canonical ensemble for each temperature. In the PIMD case, an extra step is performed in which the beads are used to

construct a centroid trajectory where the quantum effects are implicitly included. The forces from the potential energy are averaged in the same way as the positions to obtain the centroid force (excluding the stochastic Langevin components of the force for each bead). This centroid allows us to build an approximation to the Kubo correlation function, the central object behind ensemble quantum effects in the TDEP method [36]. Finally, these configurations' displacements and forces are used in the TDEP method for the least-squares fits to obtain temperature-dependent IFCs. For the TDEP fits, the second-order IFC cutoff uses the full supercell, the third-order IFC cutoff is 5.1 Å and the fourth-order IFC cutoff is 2.51 Å.

Lattice thermal conductivities are computed using the TDEP software's in-built solver for the iterative Boltzmann transport equation (IBTE) [47–50]. The latest version of the solver is used as per [51], with the full grid being employed in every case. Isotopic effects are included in the scattering processes according to the Tamura model [52, 53] with a natural distribution of boron and nitrogen isotopes. These effects have been shown to be particularly important in h-BN, with substantial changes being seen in its vibrational [5], excitonic [54] and electronic [55] properties. q-point grids of up to 360x360x1 for 3-phonon scattering cases and 64x64x1 for 4-phonon scattering cases are used. The lattice thermal conductivity is then obtained for the infinitely dense q-point grid as the y-intersect of the linear extrapolation of the κ vs $1/q$ curve in the 3-phonon scattering cases. For 4-phonon scattering we use the κ obtained for the largest q-grid (64x64x1) as the extrapolation can be noisy in the lowest temperature cases. An effective thickness is used for each temperature such that the c/a ratio of 1.317 from bulk h-BN holds as in Ref. [56].

Finally, it is important to mention that no extra corrections have to be included due to the usage of MLIPs. It was reported in recent works [57] that an extra scattering channel is introduced when calculating the lattice thermal conductivity directly from MLIP-driven MD. This problem does not appear when using MLMD + TDEP to compute phonon properties. The reason behind this is simple: the TDEP method computes the IFCs from a linear least-squares fit of the forces and their residuals into increasing displacements. As a result, the addition of a gaussian error to the forces does not change the results of the fit, as the least-squares is the maximum likelihood estimator in this case [58]. This constitutes an advantage to computing the lattice thermal conductivity from a quasiparticle (in this case TDEP) approach instead of directly from the MD, as the correction due to the MLIPs is expensive and complex in the latter case (involving extrapolations and noise estimators) but unnecessary in the former. It is worth noting that the error does not need to be strictly Gaussian in order for the TDEP least squares fit to remain unchanged, as any distribution with zero mean and constant variance will not affect the peak of the force distribution.

III. RESULTS

A. Sampling the canonical ensemble

Our first goal is to establish that the ML driven MD accurately reproduces the true dynamics of our system. In particular, we want to ensure that we capture the correct temperature evolution of its lattice parameter, as the system's volume impacts its thermal conductivity, both directly through a $1/V$ factor, and indirectly through the IFCs.

We start by analyzing the quality of our MLIP. Our main goal is to guarantee that the forces reproduced by the MLIP are as close as possible to DFT, since they will be the key quantity to obtain the force constants within the TDEP approach, as well as ensuring an accurate time evolution of our system using molecular dynamics. The comparison between the energies, forces and stresses calculated with DFT and with our MLIP is shown in Fig.1.

Having a highly accurate MLIP in hand, we compute the system's temperature-dependent unit cell in a range from 150K to 1050K, in steps of 150K, both in the classical and quantum cases. In thermal equilibrium, the lattice parameter a for each of these unit cells is computed as the phase space average $\langle a \rangle = Tr[a\rho]$, with ρ the probability distribution function given by

$$\rho = \frac{e^{-\beta H}}{Z}, \tag{1}$$

where Z is the partition function, H the Hamiltonian and $\beta = \frac{1}{k_B T}$. Calculating the lattice parameter directly in this way is not realistic except for very simple cases. However, using the ergodic principle one can replace the phase space average by a discrete time average in the limit of infinite number of time-steps:

$$\langle a \rangle = \lim_{N \to \infty} \frac{1}{N} \sum_{t=1}^{N} a(t) \tag{2}$$

This is done in practice by performing MD simulations under NPT constraints at zero pressure and averaging out the resulting lattice parameters of the snapshots of each simulation for each of the temperatures under consideration.

For cases where the number of atoms is very large, ergodicity can be considered as an innate characteristic of the system's dynamics. In our case, however, the system has 200 atoms only, which opens up the possibility that not all position and momentum degrees of freedom are explored. It can also happen that our system becomes mode-locked, and therefore constrained to exploring a closed path in phase space. This can be circumvented by initiating several different MD simulations (NPT or NVT conditions depending on what we want to calculate) for each temperature with different initial conditions, and then averaging the resulting snapshots for all of them.
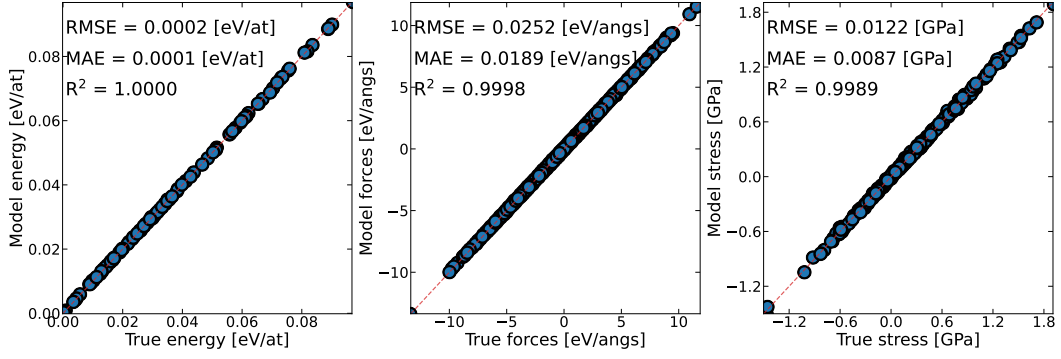
FIG. 1. Correlation plots for training and test sets. The x-axis pertains to the energies, forces and stresses calculated with DFT, while the y-axis pertains to those calculated with our MLIP. The dashed red-line is a visual aid to help track the data points where these two match. The agreement is excellent as quantified by the R^2 coefficients in the legends.

A large enough number of MD simulations with different starting configurations will span the full momentum phase space more efficiently, and therefore this number is a parameter to converge. Furthermore, the number of snapshots included in every MD instance also needs to be converged, as it dictates how well the phase space of that particular instance is sampled.

Together, the number of MD instances and their number of configurations control the shape and quality of our coverage of the phase space. The convergence study of these parameters is conducted directly through the temperature dependency of the lattice parameter in both classical and quantum cases. We find that convergence is achieved with 21 NPT instances with 1900 snapshots each in the classical case, and with 10 NPT instances with ~ 3000 snapshots in the quantum case. These very large numbers of snapshots, and in particular the need for multiple NPT instances, are a necessity we have only observed in planar 2D systems. This is the case in h-BN, and due to the presence of the very low frequency acoustic flexural mode and very high frequency optical vibrational modes, leading to the need of both small time steps and large simulation times. These are reflected in the unusually large sample size required for an accurate lattice parameter. The lattice parameters are then fit to a cubic polynomial function of temperature to smooth them and reduce the random noise arising from molecular dynamics. Comparing our results to experimental data in [59], we see that the larger changes in the lattice parameter a obtained with PIMD at higher temperatures are observed, indicating a need for NQEs to be included in MD simulations looking to accurately capture this observable's temperature evolution.

At this point, it is important to verify the need for using molecular dynamics versus stochastic sampling, and whether quantum effects are visible in the sampling to the extent that the path integral approach could be required. A key quantity that enables this analysis is the pair distribution function, which contains information on the distances between pairs of atoms in the simulation su-
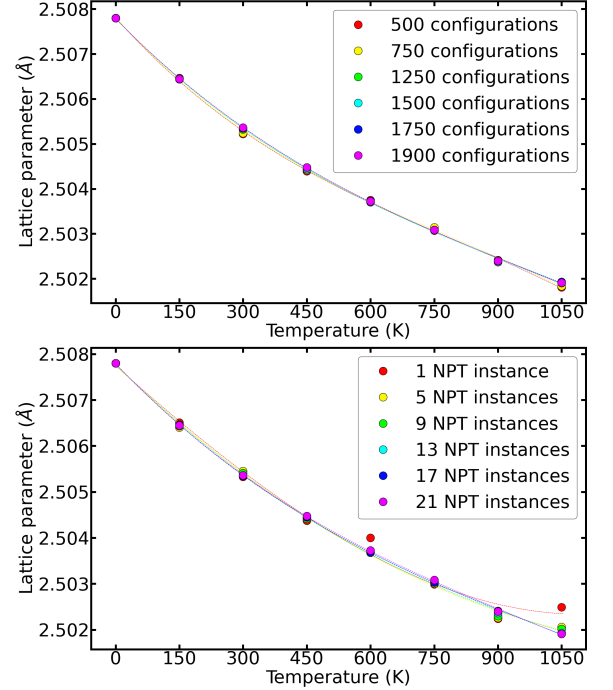

FIG. 2. Convergence of the temperature evolution of the lattice parameter a with respect to the number of NPT instances and snapshots for the classical MD case. The number of NPT instances is fixed at 21 for the convergence of the number of snapshots. The number of snapshots is fixed at 1900 for the convergence of NPT instances. The 0 K data point comes from the full relaxation of the system driven by the MLIP, and is not used in the cubic interpolation.

percell. If this function's shape is Gaussian, a stochastic method for sampling (e.g., the sSCHA or sTDEP) could be used without compromising accuracy; however, if it deviates substantially from a Gaussian, using molecular dynamics-based approaches becomes essential to capture the full anharmonicity of the system. Furthermore, one can compare the pair distribution functions arising from
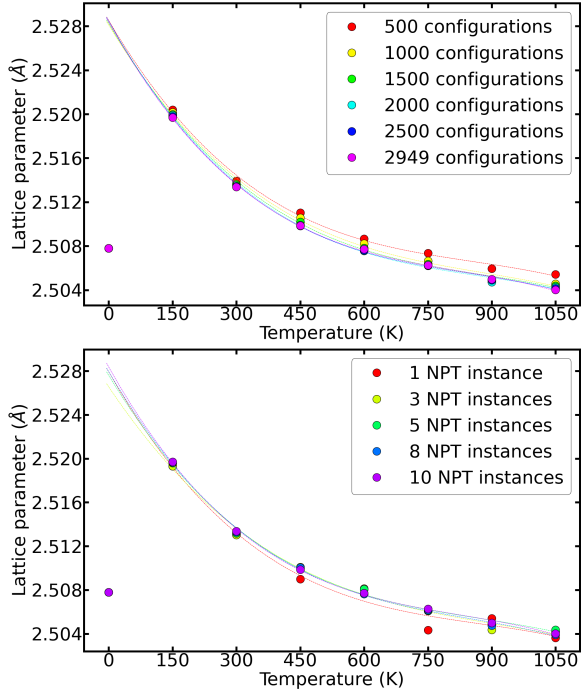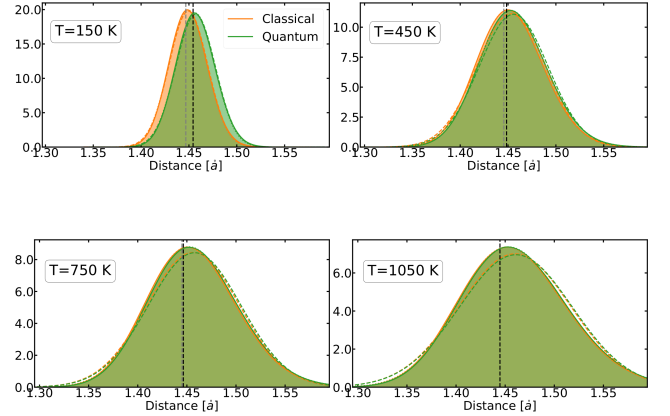
FIG. 4. Comparison between pair-distribution functions using classical and path-integral molecular dynamics. Dashed lines correspond to Gaussian fits, and dotted lines to skewed Gaussian fits. As temperature is increased the distributions deviate from Gaussians and approach each other.

FIG. 3. Convergence of the temperature evolution of the lattice parameter a with respect to the number of NPT instances and snapshots for the PIMD case. The number of NPT instances is fixed at 10 for the convergence of the number of snapshots. The number of snapshots is fixed at 2949 for the convergence of NPT instances. The 0 K data point comes from the relaxation of the system driven by the MLIP and is not used in the cubic interpolation. Its deviation relative to the PIMD data shows the importance of zero-point motion in monolayer h-BN.

classical and path integral molecular dynamics simulations, to directly observe the impact of quantum effects and determine at what temperatures they no longer affect the distribution.

In the case of monolayer h-BN, our simulations show that at the lowest temperature the classical and quantum distributions deviate in their means, but as temperature increases, they converge, becoming very similar at room temperature. At higher temperatures, the two distributions are indistinguishable, indicating that quantum sampling effects are negligible for the vibrational properties of the system. At low temperatures the distributions are well described by Gaussians (dashed lines in Fig. 4), but as the temperature increases, this is no longer the case, justifying the need for molecular dynamics-based sampling.

Finally, the pair distribution functions can be fit to skewed Gaussian distributions (dotted lines in Fig. 4). Surprisingly, this is sufficient to fully describe all the analyzed pair distribution functions, indicating that the second and third-order interatomic force constants are adequate to provide a complete understanding of the pairwise interactions. This topic will be revisited in Section

III C when we examine the impact of the fourth-order force constants on thermal conductivity.

B. Quantum effects in the force constants

With the converged lattice parameters for each temperature of interest, we can now perform (PI)MD simulations under NVT conditions and apply the TDEP method to obtain temperature-dependent second-order IFCs and phonon band structures. As the pair-distribution functions in Figure 4 already suggest, we confirm that the differences between phonon dispersions in the classical and quantum sampling cases are minimal at 150K and negligible at higher temperatures. Moreover, no significant changes in the shape of the dispersions are observed at any of the sampled temperatures. This suggests that important components of thermal conductivity, such as phonon frequencies and group velocities, will be largely unaffected by NQEs, which was not expected for very light elements such as boron and nitrogen.

Despite the minimal effects on the phonon band structures, the use of PIMD sampling in conjunction with TDEP significantly impacts another metric: the R^2 of the force-constant fit, plotted in Fig. 5. By obtaining the second, third, and fourth-order IFCs via least square fits, the R^2 value indicates how well the forces are described up to the order of the fit. Moreover, this value can indicate the degree of anharmonicity in the system, as a low R^2 value of the second-order IFC fit suggests that a significant component of the forces obtained from MD sampling is not harmonic in nature. The anharmonicity measure proposed by Knoop et al. in [60] can also be
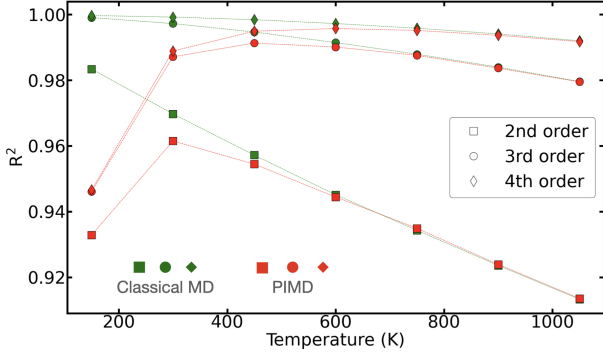
FIG. 5. Temperature evolution of the R^2 coefficients from the TDEP least-squares fits. In the classical MD sampling case, we observe a decrease in the R^2 values with temperature; nonetheless, when fitting up to 4th order the values for R^2 are always above 0.99 for all temperature data points. In the PIMD sampling case, the trend is very similar for $T > 450$ K. For lower temperatures, and especially in the $T = 150$ K case, the R^2 values are significantly lower than their classical counterparts, even including the fit up to 4th order. This is due to the fact that the averaged Born Oppenheimer surface generated in this case is less smooth than in the classical case due to the bead averaging required to construct the centroid dynamics.
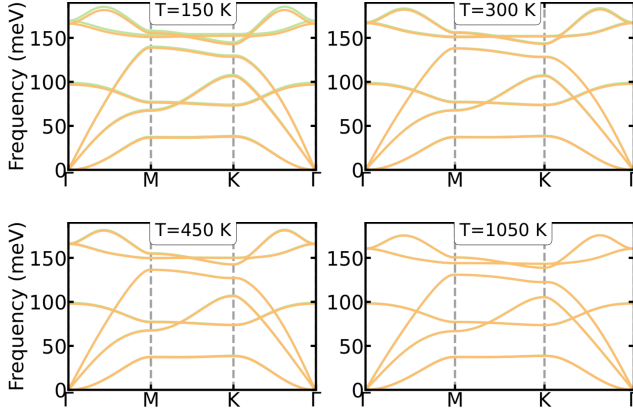
FIG. 6. Temperature evolution of the phonon band structure. Classical sampling data is presented in green while PIMD sampling data is presented in yellow. We observe negligible changes in all temperatures, with the only noticeable effect being a small vertical shift in the transversal and longitudinal optical modes for $T = 150$ K. No changes are visible in the shape of the phonon bands due to sampling.

used for the same purpose and is an output of the same routine used to calculate the IFCs in the TDEP code.

However, this is true only in the case of classical MD sampling. An illustrative example can be found in Figure 7. When performing the TDEP fit with classical MD sampling, the temperature-dependent Born-Oppenheimer surface for the system is indirectly reconstructed. This surface is well-defined as the forces and displacements from a single system's dynamics are used.
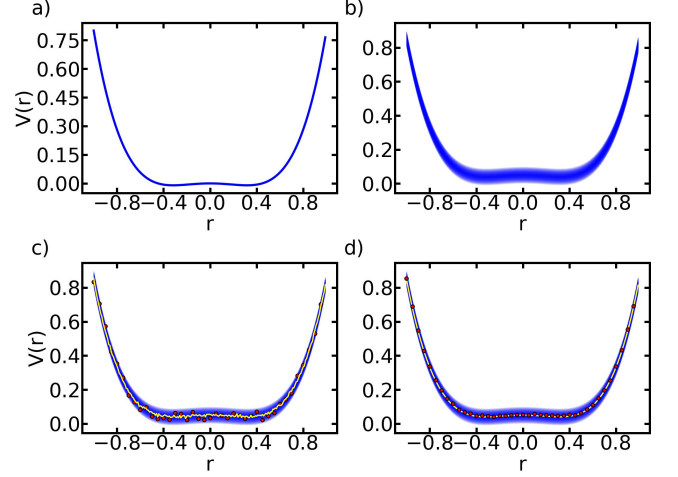

FIG. 7. Pictorial representation of the bead averaging effects on the Born-Oppenheimer potential energy surface (PES). Panel a) corresponds to the classical MD case, or equivalently 1 bead, where no averaging happens and the PES is smooth. In figure b) the spread of the quantum ion distribution is shown by the thickness of the color gradient. In c) multiple beads sample the NQE and are averaged to build the centroid. The dots correspond to the averages for each point in the centroid r-grid, with the yellow line being the new PES, now ragged due to noise in the averaging process. Panel d) corresponds to the same case as panel c) but with a very well converged number of beads, where enough data is present to ensure the final PES is again smooth like in panel a)'s case.

However, when PIMD sampling is used, a centroid needs to be constructed to approximate the system's Kubo correlation function. In practice, this centroid is constructed by averaging the dynamics of several replica of the physical system, corresponding to the number of beads used for a given temperature case. This averaging process is essential, but the limited number of beads can lead to a noisy description of the effective Born-Oppenheimer surface corresponding to the centroid compared to the smooth one generated in the classical case. This is reflected in the R^2 values and can introduce spurious effects, with the only countermeasure being increasing the number of beads for better averaging.

C. Thermal Conductivity

Figure 8 summarizes one of the main results of this work. We find that when performing classical MD sampling, the inclusion of 4-phonon scattering results in a substantial reduction of the lattice thermal conductivity for the full temperature range. This effect is particularly noticeable at lower temperatures, where the reduction reaches an order of magnitude for the $T = 150$ K data point. This result is in agreement with both the results presented in graphene [15–17] and other hexagonal boron-X compounds [61–64]. The mirror-plane symme-
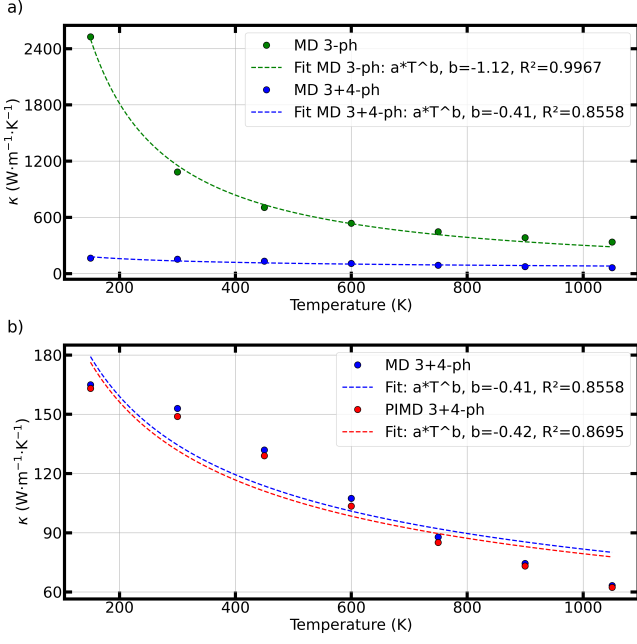
FIG. 8. Temperature evolution of the thermal conductivity for monolayer h-BN. Panel a) compares classical MD sampling results using 3-phonon and 3+4-phonon interactions. A drastic reduction is observed when 4-phonon interactions are included, especially at T = 150K where we obtain a reduction of an order of magnitude. In panel b) we compare the classical 3+4-phonon interaction result with it's PIMD counterpart. The results obtained are identical for all temperatures. Isotope scattering is present in all cases as described in the Methods section.

FIG. 9. Phonon lifetimes for the classical MD sampling case. Figures a) and b) correspond to the T = 150K case for a 60x60x1 q-point grid, while c) and d) correspond to the T = 1050 K case for the same grid. The y-axis is presented in a logarithmic scale. On a) and c) we show the lifetimes for all phonon modes; in b) and d) we single out the acoustic flexural mode, highlighting the difference in magnitude when 4-phonon scattering is included, and the lifetimes are reduced by several orders of magnitude.

FIG. 10. Phonon lifetimes including 3+4-phonon scattering for both classical MD and PIMD sampling for a 60x60x1 q-point grid. Panel a) corresponds to the T = 150 K case while panel b) corresponds to the T = 1050 K case. In both cases we observe that the scattering rates are very close regardless of sampling method, suggesting that quantum effects are negligible.

try limits the scattering at the 3-phonon level such that when 4-phonon scattering is included (and thus pairs and quartets of flexural phonons can now be included in interactions) all phonon modes' contributions to the thermal conductivity are reduced. To support the reasoning for this thermal conductivity reduction, we plot the phonon lifetimes for the classical MD case at T = 150 K and T = 1050 K in Figure 9. We find that the lifetimes of the acoustic flexural mode are severely reduced (2 orders of magnitude) when 4-phonon interactions are included. This is particularly noticeable at the lowest temperatures, where acoustic modes' contributions to the thermal conductivity are stronger.

The same trend is observed in panel b) of Fig. 8 when PIMD sampling is performed. Comparing the phonon lifetimes obtained with the classical case in Fig. 10, we find only very small differences even at the lowest temperatures, and the values obtained for the thermal conductivity match the classical sampling results. We can therefore conclude that, despite the low atomic numbers of both boron and nitrogen, one would have to go far below room temperature to potentially observe nuclear quantum effects in the thermal conductivity of monolayer h-BN.

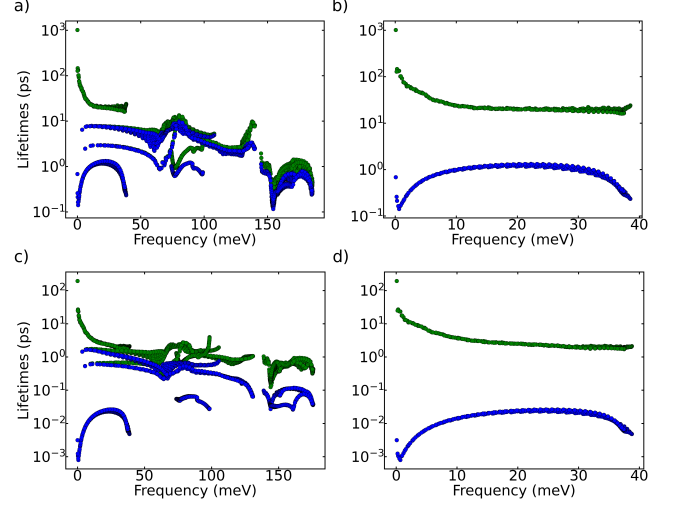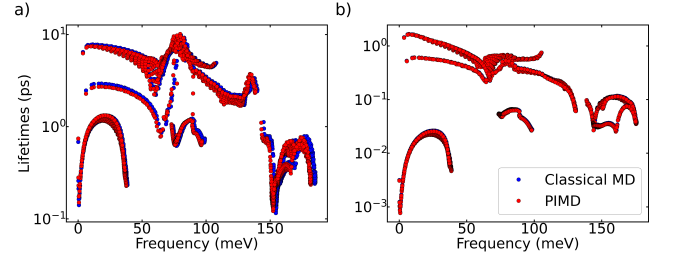We conclude that when computing the lattice thermal conductivity of monolayer h-BN one can safely operate within a classical sampling method without a loss in accuracy. On the other hand, 4-phonon effects are absolutely essential, due to the system's mirror-plane symmetry and to energy conservation restrictions as a consequence of the large gaps in its phonon band structure. It is important to highlight, however, that this need not be the case of other phonon related observables. Indeed as we have shown in Section III A one can fully reproduce the pair-distribution function with great accuracy staying within a 3rd order fit, as the 4th order IFCs are significantly smaller in amplitude than the 3rd order ones. In the thermal conductivity case, however, the suppression of

3rd order processes is such that however small the 4th order IFCs are, they contribute much more to the overall scattering, to the point that for the acoustic flexural mode even the curvature of the lifetimes as function of the frequency changes sign. We therefore expect only observables in which the restriction in scattering phase space is relevant to require 4-phonon scattering to be included.

It is at this point important to compare our results to previous works. Theoretical approaches to the thermal conductivity of monolayer h-BN can be broadly divided in two groups: BTE based approaches, where phonon IFCs are computed from density functional perturbation theory (DFPT), stochastic sampling, TDEP, etc.; and MD based approaches, such as equilibrium and non-equilibrium molecular dynamics (EMD and NEMD), where the thermal conductivity is directly computed via the Green-Kubo formula [65]. In the first case, the usual limitations of previous works consist of the lack of inclusion of isotope and/or 4-phonon scattering. In the second case, while all degrees of anharmonicity are in principle included, isotope effects are neglected. Furthermore, as Tersoff potentials are often used in these cases, results can be very sensitive to their parameterization and on how many nearest-neighbours are included. In both cases, important contributions to the thermal conductivity are systematically neglected, and to our knowledge the first result that included all relevant scattering channels is [66], where the room temperature thermal conductivity is reported.

Regarding EMD based approaches, [7] and [67] report values of approximately 290 and 218 $Wm^{-1}K^{-1}$ respectively for κ at room temperature, while [68] reports a much larger value of 471 $Wm^{-1}K^{-1}$. For NEMD based approaches, [69] reports a value for κ of 58 $Wm^{-1}K^{-1}$ also for room temperature. This result is significantly lower than for the EMD based approaches, which the authors attribute to a likely non-optimal parameterization of the Tersoff potential used. Regarding IBTE based approaches, Refs [6], [70] and [56] report values of 440, 771 and 1060 $Wm^{-1}K^{-1}$ respectively at room temperature, all of them using DFPT or finite differences to obtain the IFCs and restrict their scattering to isotope and 3-phonon level. More recently, [66] reported a value for κ of 1024.6 $Wm^{-1}K^{-1}$ including isotope and 3-phonon scattering, and 229.4 $Wm^{-1}K^{-1}$ when 4-phonon scattering is included, using IFCs from a finite difference approach. Their approach is more complete, but the authors do not specify the effective thickness used for the volume normalization of the thermal conductivity, making a direct comparison to our results more delicate. All other values reported above are renormalized with our convention, to reflect the effective thickness previously mentioned in section II and used in all of our own results.

In this work, we obtain within the standard energy conservation approach a value for κ at room temperature of 1303 $Wm^{-1}K^{-1}$ using only 3-phonon scattering, 1085 $Wm^{-1}K^{-1}$ using 3-phonon and isotope scattering, 180 $Wm^{-1}K^{-1}$ using 3 and 4-phonon scattering and finally 150 $Wm^{-1}K^{-1}$ using isotope, 3 and 4-phonon scattering. When comparing to values obtained from EMD approaches, our result using only 3 and 4-phonon scattering is very similar to previously reported values, with differences being easily attributable to the usage of approximate Tersoff potentials. Furthermore, the 20% decrease in κ when isotope scattering is included shows an important limitation of these methods. When comparing to IBTE results where isotope and 3-phonon scattering are used, our results match those reported in [56]. The drastic reduction in κ observed in our results when 4-phonon scattering is included shows this level of theory is essential to obtain an accurate, or even qualitatively correct, representation of the thermal conductivity. It is also worth noting that contrary to the previously mentioned results based on the IBTE, in this work temperature-dependent phonon IFCs are included through the TDEP method, while previous works' IFCs are inherently temperature-independent: renormalization is not included when using DFPT, formally at T = 0K. Finally, when comparing our results to those reported in [66], if one assumes they employed the commonly used effective thickness of 0.33 nm we obtain 745 $Wm^{-1}K^{-1}$ with isotope and 3-phonon scattering and 167 $Wm^{-1}K^{-1}$ with 4-phonon scattering, which agrees with our results in the latter case but not in the former.

The fact that our result points towards a lower value of κ than previously expected and measured experimentally in [9] and [10] shows a disconnect exists between experimental and theoretical works. One possible explanation for this difference could be the exposure of the samples to air or other atmospheres other than vacuum. This has been shown [71, 72] to have an effect on the thermal conductivity, by providing an extra cooling channel to the sample that is not accounted for in the equations used for κ and thus leads to a larger apparent value than the intrinsic one obtained when the experiment is done in vacuum. The amount of experimental works done regarding the thermal conductivity of monolayer h-BN is, however, very small and more detailed studies are needed before stronger conclusions can be drawn.

IV. CONCLUSIONS

In summary, the impact of nuclear quantum effects and 4-phonon scattering in the lattice thermal conductivity of monolayer hexagonal boron nitride is investigated using classical molecular dynamics and path-integral molecular dynamics as sampling methods combined with the temperature dependent effective potential approach to compute temperature dependent phonon properties. We show that while nuclear quantum effects are not pronounced for this system, 4-phonon scattering is crucial for a proper description of this quantity as well as its temperature evolution. We further show that these effects are relevant despite not being apparent in the phonon

pair distribution functions, as these are well described by skewed Gaussian distributions for all temperatures studied. The consequences of using path-integral molecular dynamics instead of classical molecular dynamics are also discussed, in particular by showcasing its effect on the R^2 coefficients of the temperature dependent effective potential's least-squares fits and how the bead averaging affects the Born-Oppenheimer potential energy surface, by first making it more ragged for small bead numbers and smoother as the number of beads increases. Finally, we compare our results to previous theoretical and experimental works. In the theoretical works, the lack of either isotope or 4-phonon scattering in the κ calculations provides an explanation as to why those values range from 550-650 $\mathrm{Wm^{-1}K^{-1}}$ at room temperature, instead of our 150 $\mathrm{Wm^{-1}K^{-1}}$ including both of those effects. Our results point towards a potential disconnect between theoretical and experimental results, and show that further studies are needed on monolayer hexagonal boron nitride to further clarify the origin of their differences.

As an outlook, both graphene and h-BN have particular band structures, where the acoustic and optical band widths are extremely large throughout most of their Brillouin zone. This further restricts the allowed 3-phonon scattering, in a way completely independent from the mirror plane symmetry, by now imposing a constraint based on the energy conservation in the scattering processes[73, 74]. This second kind of constraint is not exclusive to 2D systems, and has been shown to lead to major effects on the thermal conductivities of boron arsenide and boron phosphide, for example [61–64]. When energy conservation conditions are corrected to be compliant with the fluctuation-dissipation condition, how-

ever, the impact of this restriction on BAs has been shown to be drastically reduced, and the importance of 4-phonon scattering is greatly diminished when compared to isotope and 3-phonon scattering [75]. The energy conservation restriction, whether fluctuation-dissipation compliant or not, is independent of the mirror-plane symmetry constraint for planar materials. It will be important in the future to consider the interaction between the 2D effects imposing 4-phonon scattering and the fluctuation dissipation relaxation of the energy conservation. Work is ongoing in this direction.

[1] L. Lindsay, D. A. Broido, and N. Mingo, Flexural phonons and thermal transport in graphene, Physical Review B **82**, 10.1103/physrevb.82.115427 (2010).

[2] L. Lindsay, W. Li, J. Carrete, N. Mingo, D. A. Broido, and T. L. Reinecke, Phonon thermal transport in strained and unstrained graphene from first principles, Phys. Rev. B **89**, 155426 (2014).

[3] A. Alofi and G. P. Srivastava, Thermal conductivity of graphene and graphite, Phys. Rev. B **87**, 115421 (2013).

[4] G. Fugallo, A. Cepellotti, L. Paulatto, M. Lazzeri, N. Marzari, and F. Mauri, Thermal conductivity of graphene and graphite: Collective excitations and mean free paths, Nano Letters **14**, 6109 (2014), pMID: 25343716, https://doi.org/10.1021/nl502059f.

[5] C. Yuan, J. Li, L. Lindsay, D. Cherns, J. W. Pomeroy, S. Liu, J. H. Edgar, and M. Kuball, Modulating the thermal conductivity in hexagonal boron nitride via controlled boron isotope concentration, Communications Physics **2**, 10.1038/s42005-019-0145-5 (2019).

[6] L. Lindsay and D. A. Broido, Enhanced thermal conductivity and isotope effect in single-layer hexagonal boron nitride, Phys. Rev. B **84**, 155421 (2011).

[7] C. Sevik, A. Kinaci, J. B. Haskins, and T. Çağın, Charac-

terization of thermal transport in low-dimensional boron nitride nanostructures, Phys. Rev. B **84**, 085409 (2011).

[8] X. Wu and Q. Han, Thermal conductivity of monolayer hexagonal boron nitride: From defective to amorphous, Computational Materials Science **184**, 109938 (2020).

[9] Q. Cai, D. Scullion, W. Gan, A. Falin, S. Zhang, K. Watanabe, T. Taniguchi, Y. Chen, E. J. G. Santos, and L. H. Li, High thermal conductivity of high-quality monolayer boron nitride and its thermal expansion, Science Advances **5**, 10.1126/sciadv.aav0129 (2019).

[10] H. Ying, A. Moore, J. Cui, Y. Liu, D. Li, S. Han, Y. Yao, Z. Wang, L. Wang, and S. Chen, Tailoring the thermal transport properties of monolayer hexagonal boron nitride by grain size engineering, 2D Materials **7**, 015031 (2019).

[11] A. A. Balandin, S. Ghosh, W. Bao, I. Calizo, D. Teweldebrhan, F. Miao, and C. N. Lau, Superior thermal conductivity of single-layer graphene, Nano Letters **8**, 902–907 (2008).

[12] J.-U. Lee, D. Yoon, H. Kim, S. W. Lee, and H. Cheong, Thermal conductivity of suspended pristine graphene measured by raman spectroscopy, Physical Review B **83**, 10.1103/physrevb.83.081419 (2011).

[13] X. Xu, L. F. C. Pereira, Y. Wang, J. Wu, K. Zhang, X. Zhao, S. Bae, C. Tinh Bui, R. Xie, J. T. L. Thong, B. H. Hong, K. P. Loh, D. Donadio, B. Li, and B. Özyilmaz, Length-dependent thermal conductivity in suspended single-layer graphene, Nature Communications 5, 10.1038/ncomms4689 (2014).

[14] D. L. Nika and A. A. Balandin, Two-dimensional phonon transport in graphene, Journal of Physics: Condensed Matter 24, 233203 (2012).

[15] Z. Han and X. Ruan, Thermal conductivity of monolayer graphene: Convergent and lower than diamond, Physical Review B 108, 10.1103/physrevb.108.l121412 (2023).

[16] T. Feng and X. Ruan, Four-phonon scattering reduces intrinsic thermal conductivity of graphene and the contributions from flexural phonons, Physical Review B 97, 10.1103/physrevb.97.045202 (2018).

[17] Y. Han, C. Yang, X. Cheng, D. Han, W. Ding, and X. Wang, Investigation of the effect of four-phonon scattering on thermal transport in two-dimensional group-iv materials, ACS Applied Energy Materials 7, 649–656 (2023).

[18] E. Mariani and F. von Oppen, Flexural phonons in free-standing graphene, Physical Review Letters 100, 10.1103/physrevlett.100.076801 (2008).

[19] S. Illera, M. Pruneda, L. Colombo, and P. Ordejón, Thermal and transport properties of pristine single-layer hexagonal boron nitride: A first principles investigation, Phys. Rev. Mater. 1, 044006 (2017).

[20] Y. Xie, Z. Xu, S. Xu, Z. Cheng, N. Hashemi, C. Deng, and X. Wang, The defect level and ideal thermal conductivity of graphene uncovered by residual thermal reffusivity at the 0 k limit, Nanoscale 7, 10101–10110 (2015).

[21] I. Errea, M. Calandra, and F. Mauri, First-principles theory of anharmonicity and the inverse isotope effect in superconducting palladium-hydride compounds, Physical Review Letters 111, 10.1103/physrevlett.111.177002 (2013).

[22] I. Errea, M. Calandra, and F. Mauri, Anharmonic free energies and phonon dispersions from the stochastic self-consistent harmonic approximation: Application to platinum and palladium hydrides, Physical Review B 89, 10.1103/physrevb.89.064302 (2014).

[23] R. Bianco, I. Errea, L. Paulatto, M. Calandra, and F. Mauri, Second-order structural phase transitions, free energy curvature, and temperature-dependent anharmonic phonons in the self-consistent harmonic approximation: Theory and stochastic implementation, Physical Review B 96, 10.1103/physrevb.96.014111 (2017).

[24] L. Monacelli, I. Errea, M. Calandra, and F. Mauri, Pressure and stress tensor of complex anharmonic crystals within the stochastic self-consistent harmonic approximation, Physical Review B 98, 10.1103/physrevb.98.024106 (2018).

[25] L. Monacelli, R. Bianco, M. Cherubini, M. Calandra, I. Errea, and F. Mauri, The stochastic self-consistent harmonic approximation: calculating vibrational properties of materials with full quantum and anharmonic effects, Journal of Physics: Condensed Matter 33, 363001 (2021).

[26] I. R. Craig and D. E. Manolopoulos, Quantum statistics and classical mechanics: Real time correlation functions from ring polymer molecular dynamics, The Journal of Chemical Physics 121, 3368–3373 (2004).

[27] B. J. Braams and D. E. Manolopoulos, On the short-time limit of ring polymer molecular dynamics, The Journal of Chemical Physics 125, 10.1063/1.2357599 (2006).

[28] T. Morresi, L. Paulatto, R. Vuilleumier, and M. Casula, Probing anharmonic phonons by quantum correlators: A path integral approach, The Journal of Chemical Physics 154, 224108 (2021).

[29] O. Hellman, I. A. Abrikosov, and S. I. Simak, Lattice dynamics of anharmonic solids from first principles, Phys. Rev. B 84, 180301(R) (2011).

[30] O. Hellman, P. Steneteg, I. A. Abrikosov, and S. I. Simak, Temperature dependent effective potential method for accurate free energy calculations of solids, Phys. Rev. B 87, 104111 (2013).

[31] O. Hellman and I. A. Abrikosov, Temperature-dependent effective third-order interatomic force constants from first principles, Phys. Rev. B 88, 144301 (2013).

[32] F. Knoop, N. Shulumba, A. Castellano, J. P. A. Batista, R. Farris, M. J. Verstraete, M. Heine, D. Broido, D. S. Kim, J. Klarbring, I. A. Abrikosov, S. I. Simak, and O. Hellman, Tdep: Temperature dependent effective potentials, Journal of Open Source Software 9, 6150 (2024).

[33] N. Shulumba, O. Hellman, and A. J. Minnich, Intrinsic localized mode and low thermal conductivity of pbse, Physical Review B 95, 10.1103/physrevb.95.014302 (2017).

[34] H. Y. Geng, Full temperature-dependent potential and anharmonicity in metallic hydrogen: Colossal nqe and the consequences, The Journal of Physical Chemistry C 126, 19355–19366 (2022).

[35] D. A. Folkner, Z. Chen, G. Barbalinardo, F. Knoop, and D. Donadio, Elastic moduli and thermal conductivity of quantum materials at finite temperature, Journal of Applied Physics 136, 10.1063/5.0238723 (2024).

[36] A. Castellano, J. P. A. Batista, and M. J. Verstraete, Mode-coupling theory of lattice dynamics for classical and quantum crystals, The Journal of Chemical Physics 159, 10.1063/5.0174255 (2023).

[37] A. V. Shapeev, Moment tensor potentials: A class of systematically improvable interatomic potentials, Multiscale Modeling & Simulation 14, 1153 (2016), https://doi.org/10.1137/15M1054183.

[38] I. S. Novikov, K. Gubaev, E. V. Podryabinkin, and A. V. Shapeev, The mlip package: moment tensor potentials with mpi and active learning, Machine Learning: Science and Technology 2, 025002 (2021).

[39] A. Castellano, F. m. c. Bottin, J. Bouchet, A. Levitt, and G. Stoltz, ab initio canonical sampling based on variational inference, Phys. Rev. B 106, L161110 (2022).

[40] A. Castellano, R. Béjaud, P. Richard, O. Nadeau, C. Duval, G. Geneste, G. Antonius, J. Bouchet, A. Levitt, G. Stoltz, and F. Bottin, Machine learning assisted canonical sampling (mlacs) (2024).

[41] X. Gonze, B. Amadon, G. Antonius, F. Arnardi, L. Baguet, J.-M. Beuken, J. Bieder, F. Bottin, J. Bouchet, E. Bousquet, N. Brouwer, F. Bruneval, G. Brunin, T. Cavignac, J.-B. Charraud, W. Chen, M. Côté, S. Cottenier, J. Denier, G. Geneste, P. Ghosez, M. Giantomassi, Y. Gillet, O. Gingras, D. R. Hamann, G. Hautier, X. He, N. Helbig, N. Holzwarth, Y. Jia, F. Jollet, W. Lafargue-Dit-Hauret, K. Lejaeghere, M. A. Marques, A. Martin, C. Martins, H. P. Miranda, F. Naccarato, K. Persson, G. Petretto, V. Planes, Y. Pouillon, S. Prokhorenko, F. Ricci, G.-M. Rignanese, A. H. Romero, M. M. Schmitt, M. Torrent, M. J. van Setten, B. Van Troeye, M. J. Verstraete, G. Zérah, and

J. W. Zwanziger, The abinitproject: Impact, environment and recent developments, Computer Physics Communications **248**, 107042 (2020).

[42] A. H. Romero, D. C. Allan, B. Amadon, G. Antonius, T. Applencourt, L. Baguet, J. Bieder, F. Bottin, J. Bouchet, E. Bousquet, F. Bruneval, G. Brunin, D. Caliste, M. Côté, J. Denier, C. Dreyer, P. Ghosez, M. Giantomassi, Y. Gillet, O. Gingras, D. R. Hamann, G. Hautier, F. Jollet, G. Jomard, A. Martin, H. P. C. Miranda, F. Naccarato, G. Petretto, N. A. Pike, V. Planes, S. Prokhorenko, T. Rangel, F. Ricci, G.-M. Rignanese, M. Royo, M. Stengel, M. Torrent, M. J. van Setten, B. Van Troeye, M. J. Verstraete, J. Wiktor, J. W. Zwanziger, and X. Gonze, ABINIT: Overview and focus on selected capabilities, The Journal of Chemical Physics **152**, 124102 (2020), https://pubs.aip.org/aip/jcp/article-pdf/doi/10.1063/1.5144261/16711978/124102_1_online.pdf.

[43] J. P. Perdew, K. Burke, and M. Ernzerhof, Generalized gradient approximation made simple, Phys. Rev. Lett. **77**, 3865 (1996).

[44] S. Grimme, J. Antony, S. Ehrlich, and H. Krieg, A consistent and accurate ab initio parametrization of density functional dispersion correction (DFT-d) for the 94 elements h-pu, The Journal of Chemical Physics **132**, 154104 (2010).

[45] A. P. Thompson, H. M. Aktulga, R. Berger, D. S. Bolintineanu, W. M. Brown, P. S. Crozier, P. J. in 't Veld, A. Kohlmeyer, S. G. Moore, T. D. Nguyen, R. Shan, M. J. Stevens, J. Tranchida, C. Trott, and S. J. Plimpton, Lammps - a flexible simulation tool for particle-based materials modeling at the atomic, meso, and continuum scales, Computer Physics Communications **271**, 108171 (2022).

[46] N. Grønbech-Jensen and O. Farago, A simple and effective verlet-type algorithm for simulating langevin dynamics, Molecular Physics **111**, 983 (2013), https://doi.org/10.1080/00268976.2012.760055.

[47] M. Omini and A. Sparavigna, Beyond the isotropic-model approximation in the theory of thermal conductivity, Phys. Rev. B **53**, 9064 (1996).

[48] G. Fugallo, M. Lazzeri, L. Paulatto, and F. Mauri, Ab initio variational approach for evaluating lattice thermal conductivity, Phys. Rev. B **88**, 045430 (2013).

[49] D. A. Broido, M. Malorny, G. Birner, N. Mingo, and D. A. Stewart, Intrinsic lattice thermal conductivity of semiconductors from first principles, Applied Physics Letters **91**, 231922 (2007), https://pubs.aip.org/aip/apl/article-pdf/doi/10.1063/1.2822891/14384383/231922_1_online.pdf.

[50] O. Hellman and D. A. Broido, Phonon thermal transport in bi$_2$te$_3$ from first principles, Phys. Rev. B **90**, 134309 (2014).

[51] A. Castellano, J. P. A. Batista, O. Hellman, and M. J. Verstraete, Mode-coupling formulation of heat transport in anharmonic materials (2024).

[52] S.-i. Tamura, Isotope scattering of dispersive phonons in ge, Phys. Rev. B **27**, 858 (1983).

[53] N. H. Protik and C. Draxl, Beyond the tamura model of phonon-isotope scattering, Phys. Rev. B **109**, 165201 (2024).

[54] E. Janzen, H. Schutte, J. Plo, A. Rousseau, T. Michel, W. Desrat, P. Valvin, V. Jacques, G. Cassabois, B. Gil, and J. H. Edgar, Boron and nitrogen isotope effects on hexagonal boron nitride properties, Advanced Materials **36**, 10.1002/adma.202306033 (2023).

[55] T. Q. P. Vuong, S. Liu, A. Van der Lee, R. Cuscó, L. Artús, T. Michel, P. Valvin, J. H. Edgar, G. Cassabois, and B. Gil, Isotope engineering of van der waals interactions in hexagonal boron nitride, Nature Materials **17**, 152–158 (2017).

[56] A. Cepellotti, G. Fugallo, L. Paulatto, M. Lazzeri, F. Mauri, and N. Marzari, Phonon hydrodynamics in two-dimensional materials, Nature Communications **6**, 10.1038/ncomms7400 (2015).

[57] X. Wu, W. Zhou, H. Dong, P. Ying, Y. Wang, B. Song, Z. Fan, and S. Xiong, Correcting force error-induced underestimation of lattice thermal conductivity in machine learning molecular dynamics, The Journal of Chemical Physics **161**, 10.1063/5.0213811 (2024).

[58] R. Carter Hill, W. E. Griffiths, and G. C. Lim, *Principles of econometrics*, 5th ed. (John Wiley & Sons, Nashville, TN, 2024).

[59] M. A. Kriegel, K. M. Omambac, S. Franzka, F.-J. Meyer zu Heringdorf, and M. Horn-von Hoegen, Incommensurability and negative thermal expansion of single layer hexagonal boron nitride, Applied Surface Science **624**, 157156 (2023).

[60] F. Knoop, T. A. R. Purcell, M. Scheffler, and C. Carbogno, Anharmonicity measure for materials, Physical Review Materials **4**, 10.1103/physrevmaterials.4.083809 (2020).

[61] T. Feng and X. Ruan, Quantum mechanical prediction of four-phonon scattering rates and reduced thermal conductivity of solids, Physical Review B **93**, 10.1103/physrevb.93.045202 (2016).

[62] T. Feng, L. Lindsay, and X. Ruan, Four-phonon scattering significantly reduces intrinsic thermal conductivity of solids, Physical Review B **96**, 10.1103/physrevb.96.161201 (2017).

[63] J. S. Kang, M. Li, H. Wu, H. Nguyen, and Y. Hu, Experimental observation of high thermal conductivity in boron arsenide, Science **361**, 575–578 (2018).

[64] S. Bi, Z. Chang, K. Yuan, Z. Sun, X. Zhang, Y. Gao, and D. Tang, First-principles prediction of the lattice thermal conductivity of two-dimensional (2d) h-bx (x=p, as, sb) considering the effects of fourth-order and all-order scattering, Journal of Applied Physics **132**, 10.1063/5.0073473 (2022).

[65] R. Kubo, M. Yokota, and S. Nakajima, Statistical-mechanical theory of irreversible processes. ii. response to thermal disturbance, Journal of the Physical Society of Japan **12**, 1203–1211 (1957).

[66] G. Sun, J. Ma, C. Liu, Z. Xiang, D. Xu, T.-H. Liu, and X. Luo, Four-phonon and normal scattering in 2d hexagonal structures, International Journal of Heat and Mass Transfer **215**, 124475 (2023).

[67] B. Mortazavi, L. F. C. Pereira, J.-W. Jiang, and T. Rabczuk, Modelling heat conduction in polycrystalline hexagonal boron-nitride films, Scientific Reports **5**, 10.1038/srep13228 (2015).

[68] A. I. Khan, I. A. Navid, M. Noshin, and S. Subrina, Thermal transport characterization of hexagonal boron nitride nanoribbons using molecular dynamics simulation, AIP Advances **7**, 10.1063/1.4997036 (2017).

[69] B. Mortazavi and Y. Rémond, Investigation of tensile response and thermal conductivity of boron-nitride nanosheets using molecular dynamics simulations, Phys-

ica E: Low-dimensional Systems and Nanostructures **44**, 1846–1852 (2012).

[70] H. Fan, H. Wu, L. Lindsay, and Y. Hu, Ab initio investigation of single-layer high thermal conductivity boron compounds, Physical Review B **100**, 10.1103/physrevb.100.085420 (2019).

[71] D. Saleta Reig, S. Varghese, R. Farris, A. Block, J. D. Mehew, O. Hellman, P. Woźniak, M. Sledzinska, A. El Sachat, E. Chávez-Ángel, S. O. Valenzuela, N. F. van Hulst, P. Ordejón, Z. Zanolli, C. M. Sotomayor Torres, M. J. Verstraete, and K.-J. Tielrooij, Unraveling heat transport and dissipation in suspended mose2 from bulk to monolayer, Advanced Materials **34**, 2108352 (2022), https://onlinelibrary.wiley.com/doi/pdf/10.1002/adma.202108352.

[72] S. Chen, A. L. Moore, W. Cai, J. W. Suk, J. An, C. Mishra, C. Amos, C. W. Magnuson, J. Kang, L. Shi, and R. S. Ruoff, Raman measurements of thermal transport in suspended monolayer graphene of variable sizes in vacuum and gaseous environments, ACS Nano **5**, 321–328 (2010).

[73] N. K. Ravichandran and D. Broido, Phonon-phonon interactions in strongly bonded solids: Selection rules and higher-order processes, Phys. Rev. X **10**, 021063 (2020).

[74] N. K. Ravichandran and D. Broido, Exposing the hidden influence of selection rules on phonon–phonon scattering by pressure and temperature tuning, Nature Communications **12**, 10.1038/s41467-021-23618-7 (2021).

[75] A. Castellano, J. P. A. Batista, and M. J. Verstraete, Fluctuation-dissipation and virtual processes in interacting phonon systems (2025).

4

Temperature Dependent Phonon Properties Of Bulk Hexagonal Boron Nitride

4.1   Introduction

In this section we study the temperature evolution of dielectric properties of bulk hexagonal boron nitride, as well as its room temperature thermal conductivity. Bulk h-BN is an electric insulator, composed of AA' stacked h-BN layers bonded by van der Waals interactions. As a 2D layered crystal, it is highly anisotropic in nature, giving rise to interesting physical properties such as a lattice thermal conductivity whose in-plane component is significantly larger than the out-of-plane one, making it an enticing system for heat management applications. Furthermore, it shows two Raman active modes that are easily distinguishable by their large frequency separation. These modes, known as E_{2g}^{low} and E_{2g}^{high}, can provide a wide range of information about the system, as they can be used for the study of properties like the number of layers of the sample, its purity or even as a thermometer by studying their frequency and linewidth.

   In the work below we simulate the temperature dependence of the E_{2g}^{high} mode's Raman spectrum, as well as the dielectric tensor and optical coefficients of bulk h-BN from T=100K to T=500K. We also compute its room temperature lattice thermal conductivity with and without 4-phonon interactions to show their

importance in this system. We find that while the dielectric tensor and optical coefficients are largely unaffected by the temperature, the Raman spectrum shows an important decrease in the peak's frequency and linewidth which matches previous experimental works. We further find that 4-phonon interactions are crucial for an accurate description of the lattice thermal conductivity, in particular for its out-of-plane component which almost halves when this approximation is applied.

4.2   Methods

The sTDEP approach described in section 1.2 is used in order to compute temperature dependent second, third and fourth-order IFCs. The maximal radius inscribed in the super-cell is considered for the second-order IFCs, while cutoffs of 4.0 and 2.6 Å guarantee convergence of the thermal conductivity to less than 1% and are used for the third and fourth-order IFCs respectively. For all phonon related calculations we use the TDEP implementation [54]. A level 22 moment tensor potential (MTP) [73, 83] with a 5.5Å cutoff radius (converged to ensure 1 meV/atom accuracy) was trained with configurations generated with the machine learning assisted canonical sampling (MLACS) method [15, 18] in order to approximate the Born Oppenheimer potential energy surface. This MLIP was trained for a temperature range between 100 K and 600 K. Energies, forces and stresses are computed through DFT using the Abinit code [36, 79], using the PBE exchange-correlation functional [77] as well as D3 van der Waals corrections according to [37]. A plane wave energy cutoff of 50 Ha and an $8 \times 8 \times 4$ k-point grid were sufficient to ensure convergence for unit-cell calculations to 1 meV per atom accuracy on the total energy, while for supercells ($6 \times 6 \times 2$ with 288 atoms) a cutoff of 50 Ha and a $2 \times 2 \times 2$ k-point grid were used. The temperature-dependent lattice parameters are obtained using the quasi-harmonic approximation [93, 96], by finding the lattice parameters that minimize the TDEP harmonic free energy.

Thermal conductivity calculations are performed at 300K using the TDEP code's IBTE solver on converged Monte Carlo grids according to [17]. An $18 \times 18 \times 18$ Monte Carlo grid is used when the reciprocal-space grid $q > 18$ in the 3-phonon scattering case, with the full grid being used for the remaining grids. A $6 \times 6 \times 6$ Monte Carlo grid was found to be sufficient for 4-phonon scattering.
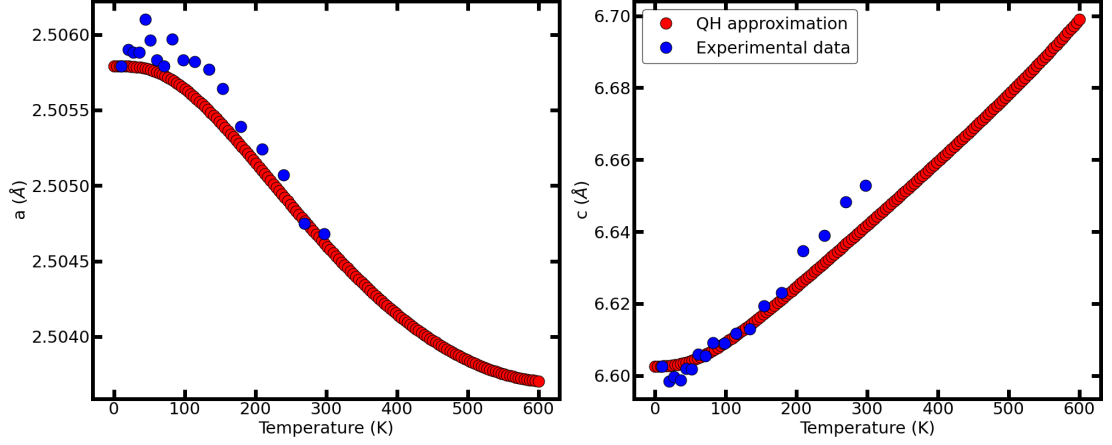
Figure 4.1: Temperature evolution of the in-plane and out-of-plane lattice parameters a and c under the quasi-harmonic approximation. Our results are compared with [75] and are found to match closely for the values within the available temperature range.

Isotope scattering according to the natural distribution was used in all cases following the Tamura model described in the end of section 2.3.

4.3 Temperature Dependent Dielectric Properties

The scattering cross section σ for the Raman effect is given by

$$\sigma(\omega) \propto \sum_{\alpha\beta\mu\nu} E_\alpha^{\text{out}} E_\beta^{\text{out}} I_{\alpha\beta\mu\nu(\omega)} E_\mu^{\text{in}} E_\nu^{\text{in}} \ , \tag{4.1}$$

with $\vec{E}^{\text{in}}$ and $\vec{E}^{\text{out}}$ are the electric fields associated with the incoming and outgoing photons. The Raman tensor $I_{\alpha\beta\mu\nu}(\omega)$ is the intrinsic quantity that determines the strength of the crystal susceptibility χ, the response function to the perturbing $\vec{E}$ field, given by the susceptibility autocorrelation function's Fourier transform [6, 22]:

$$I_{\alpha\beta\mu\nu}(\omega) = \int dt \langle \chi_{\alpha\beta}(t)\chi_{\mu\nu}(0)\rangle e^{i\omega t} \ . \tag{4.2}$$

117
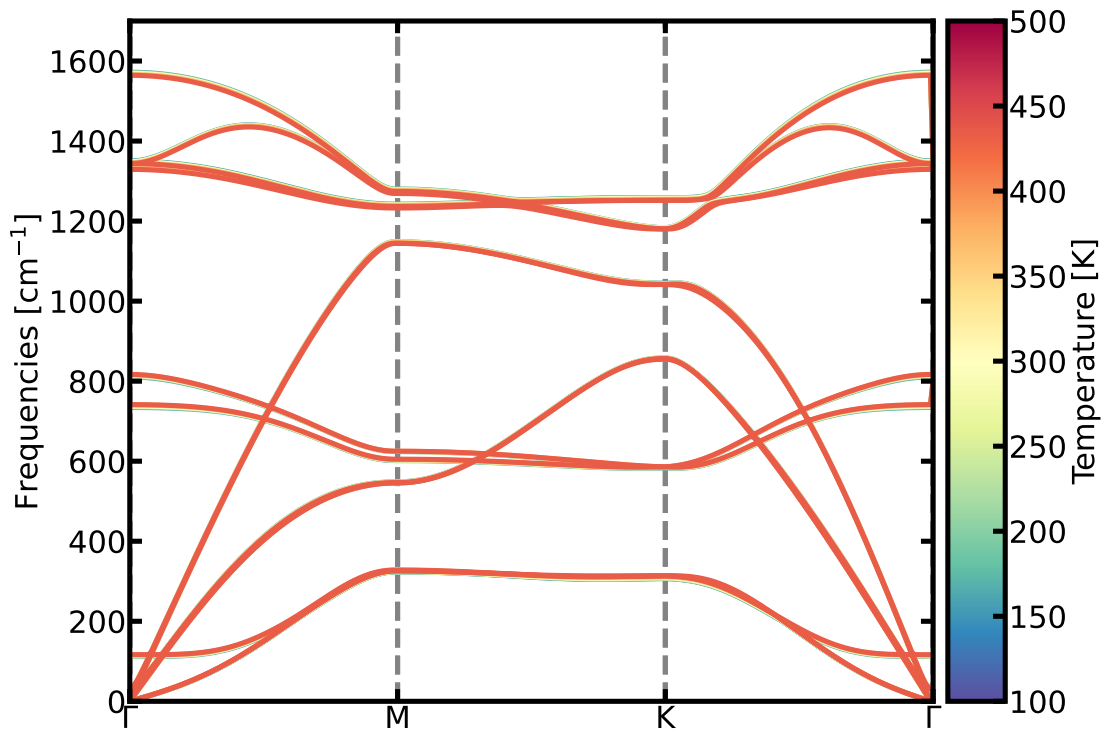
Figure 4.2: Temperature evolution of the phonon dispersion of bulk h-BN between
T=100K and T=500K. No major variations are found in this temperature range.

While this object contains the fluctuations in susceptibility to all orders, the autocorrelation function in 4.2 is computationally expensive to obtain. Instead, one can compute a simpler object, the first-order Raman tensor defined as [13, 53]

$$I_{\alpha\beta;s} = \frac{\partial \chi_{\alpha\beta}}{\partial u_s} \; , \tag{4.3}$$

where u_s is the atomic displacement according to phonon mode s. The contribution per mode to the scattering cross section is then given by

$$\sigma_s(\omega) = |\vec{e}_{\text{in}} \cdot I_s \cdot \vec{e}_{\text{out}}| J_s(\omega) \; , \tag{4.4}$$

with $\vec{e}_{\text{in}}$ and $\vec{e}_{\text{out}}$ are the incoming and outgoing light polarizations respectively and $J_s(\omega)$ is the mode-resolved phonon spectral function [16]

$$J_s(\omega) = \frac{\omega}{2k_B T} G_s(\omega) \; . \tag{4.5}$$

The Fourier-transformed Green's function can be written as a damped-harmonic oscillator

$$G_s(\omega) = \frac{2\Omega_s \Gamma_s(\omega)}{\left[\omega^2 - \Omega_s^2 - 2\Omega_s \Delta_s(\omega)\right]^2 + 4\Omega_s^2 \Gamma_s^2(\omega)} \; . \tag{4.6}$$

This object can be constructed from the IFCs (see Part I), and is temperature dependent if the IFCs are as well. The Raman tensor, on the other hand, can be obtained via finite differences by computing the susceptibility (e.g. using density functional perturbation theory [3, 35] for configurations representing all phonon mode displacements. With both components in hand, the Raman scattering cross-section can be formed and directly compared to experimental results.

In the case of AA' stacked bulk h-BN, 2 Raman active phonon modes are present: one low frequency mode, corresponding to the rigid gliding between the layers (the E_{2g}^{low} mode); and one higher frequency mode (the E_{2g}^{high} mode), corresponding to the in-plane anti-phase vibrations between the boron and nitrogen atoms. The E_{2g}^{high} mode is of particular interest as it is the most easily identifiable and simplest to detect, as it is a spectral fingerprint (for example in BN on a substrate), but also to assess the sample's quality and if its subject to external effects such as strain. The E_{2g}^{high} mode is the focus of this section.
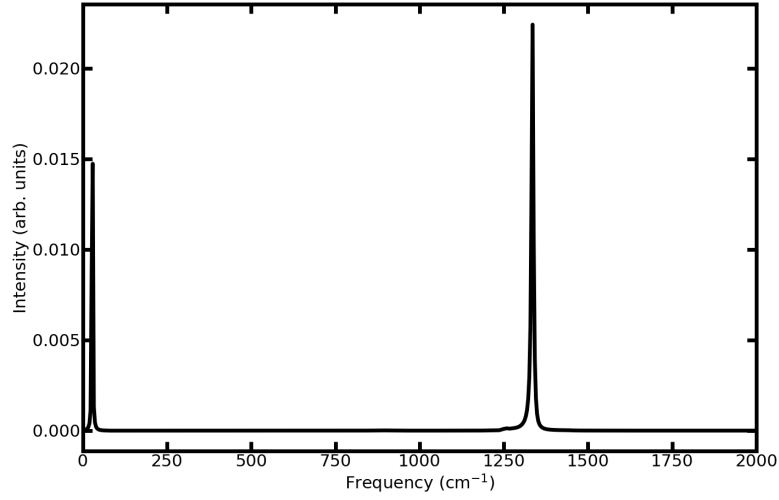
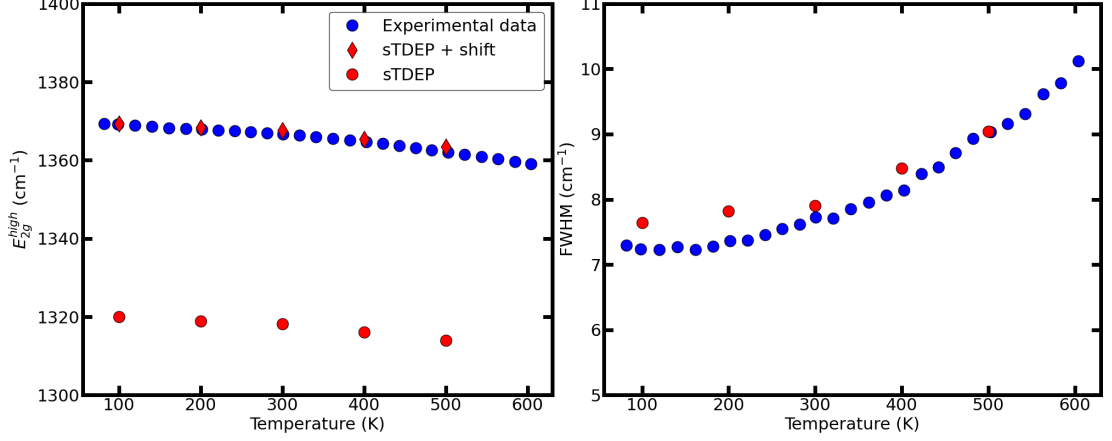**Figure 4.3:** Full Raman spectrum of bulk h-BN at T = 100K. The higher frequency peak corresponds to the E_{2g}^{high} mode, which is the subject of this study.
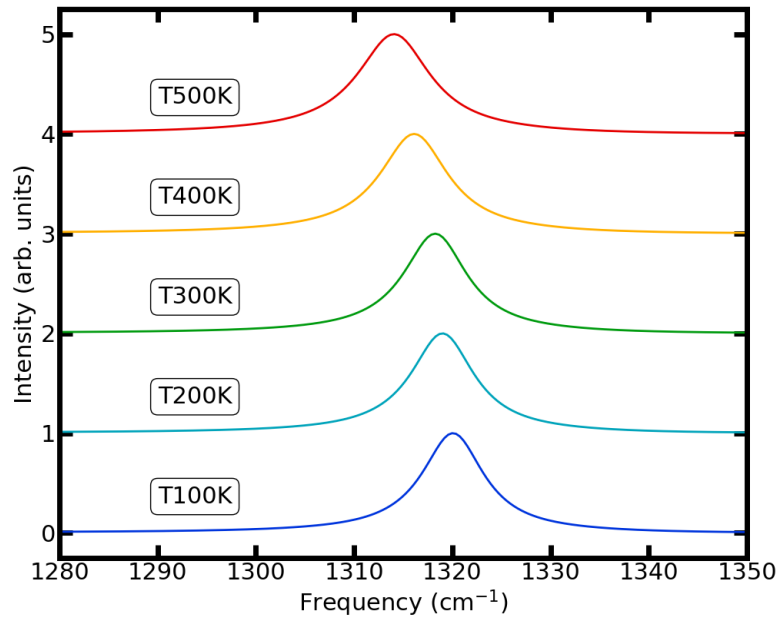
Figure 4.4: Temperature evolution of the Raman active E_{2g}^{high} mode of bulk hexagonal boron nitride.

Figure 4.5: Temperature evolution of the frequency and linewidth of the E_{2g}^{high} Raman mode. Values are obtained by fitting the spectra from Figure 4.4 to a Lorentzian distribution. The sTDEP frequency data points are shifted up by 49.36 cm^{-1} in order to match the experimental values at T = 100K.

As this mode is associated to the in-plane atomic motion of the boron and nitrogen atoms, one could expect that the contraction of the in-plane lattice parameter a with increasing temperature would lead to an increase in the mode's frequency. However, both experimental data and our simulations show that the contrary occurs, with a decrease of about 0.02 cm^{-1}K^{-1} being observed [24, 59, 89]. This can be understood if we recall that the Raman scattering cross-section depends on temperature only through the unit cell expansion (via the first-order Raman tensor) and through explicit anharmonicity in the phonon spectral function. If the lattice contraction sways the frequency evolution to be increasing but the total object shows it as decreasing, then the phonon anharmonicity must be strong enough that it overcomes the lattice's effect.

Figure 4.5 summarizes the results for the E_{2g}^{high} Raman spectrum's temperature evolution. We find that our results match those of Reference [24] both for the frequency and linewidths while only taking into account 3-phonon and isotope scattering. While seemingly contradicting their claim that 4-phonon interactions are essential to capture the correct temperature dependence, this can be explained by the difference in treatment of anharmonicity. The referenced work's simulations compute phonon IFCs using DFPT, which as mentioned in part I does not

4. TEMPERATURE DEPENDENT PHONON PROPERTIES OF BULK HEXAGONAL BORON NITRIDE

incorporate temperature renormalization. Our results with sTDEP have both anharmonic and nuclear quantum effects included. The accuracy of our results then suggest that the relevant 4th-order interactions are implicitly included in sTDEP's renormalization, bypassing the need for their explicit calculation. As for the temperature evolution of the linewidths, TDEP's successive fit of the forces and their residuals also ensures that the 3rd-order IFCs are as large as possible, which acts as to diminish the relative impact of 4th-order IFCs when compared to DFPT based (T=0K) calculations.

Bulk h-BN is further interesting from an optical perspective due to it being a naturally occurring hyperbolic material thanks to its high degree of anisotropy. This means that for a wide frequency range, commonly referred to as *reststrahlen* bands, the parallel and perpendicular real parts of its dielectric tensor have opposite signs, leading to the hyperbolic isofrequency surface in wave-vector space that names the class of materials. The frequency dependent dielectric tensor $\epsilon(\omega)$ can be written as a damped harmonic oscillator (also called the Lorentz model)

$$\epsilon(\omega) = \epsilon_\infty + \frac{S\Omega_0^2}{\Omega_0^2 - \omega^2 - \mathrm{i}\omega\gamma} \ , \tag{4.7}$$

where ϵ_∞ is the high frequency dielectric constant, Ω_0 is the frequency of the Raman mode and γ is its linewidth. From the dielectric tensor we can further compute the reflectance ($\mathcal{R}$) and transmittance ($\mathcal{T}$) as

$$n = \sqrt{\frac{|\epsilon| + \mathrm{Re}(\epsilon)}{2}}, \quad r = \left|\frac{\sqrt{\epsilon} - 1}{\sqrt{\epsilon} + 1}\right|^2, \quad t = \exp\left(-d\,\frac{\mathrm{Im}(\epsilon)}{n}\right) \tag{4.8}$$

$$\mathcal{T} = \frac{t(1-r)^2}{1 - r^2 t^2}, \quad \mathcal{R} = r(1 + t\mathcal{T}) \ . \tag{4.9}$$

In the above, n is the refractive index, d is the sample thickness and all functions are frequency dependent.
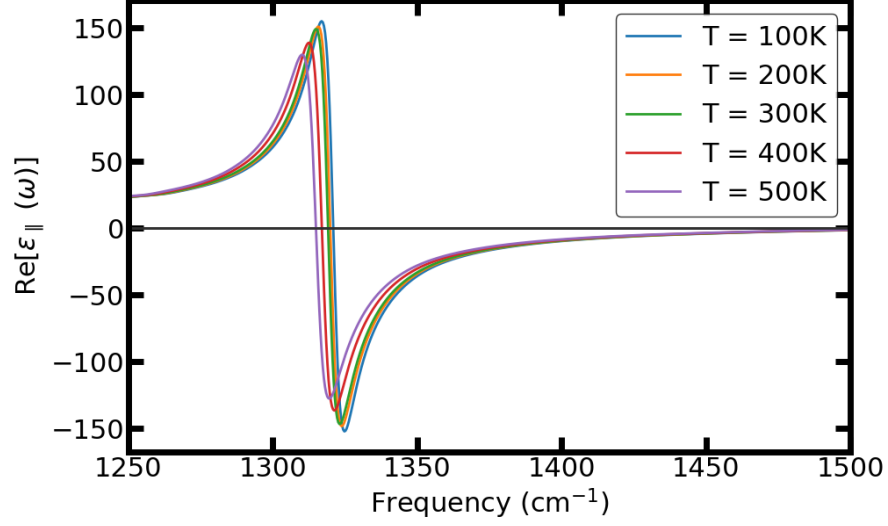
Figure 4.6: Temperature evolution of the real part of the parallel component of the dielectric tensor for the upper *reststrahlen* band of bulk h-BN. The horizontal line at the origin corresponds to the perpendicular component of the real part of the dielectric tensor.
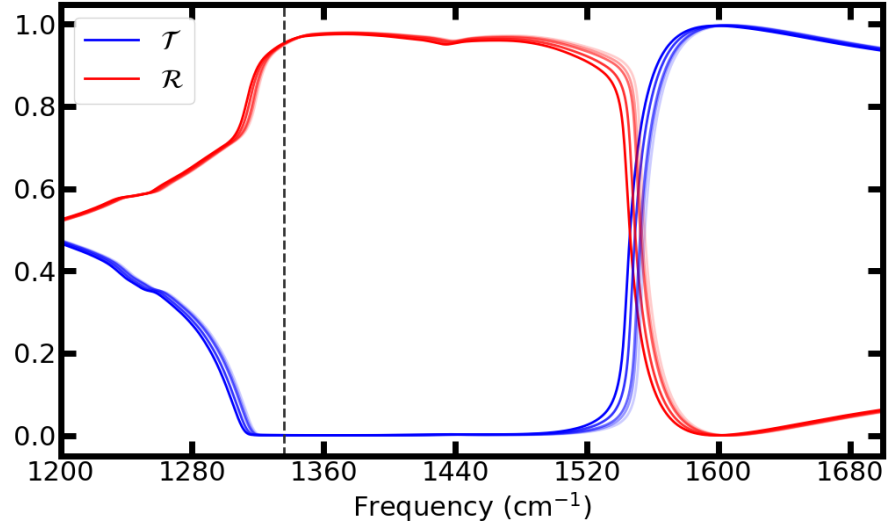
Figure 4.7: Temperature evolution of the transmission and reflectivity for the upper *reststrahlen* band of bulk h-BN. More opaque lines represent higher temperatures. The vertical dashed line corresponds to the frequency of the E_{2g}^{high} mode at T=100K

Our results show that both the hyperbolicity and optical coefficients are fairly insensitive to temperature. While the peak of the real part of the parallel component of the dielectric tensor contracts and has a frequency decrease, the impact is not very significant. A similar effect is seen on the optical coefficients in Figure 4.7, which both also move to lower frequencies. In turn, the reflectance decreases inside the *reststrahlen* band, leading to an increase of the transmittance.
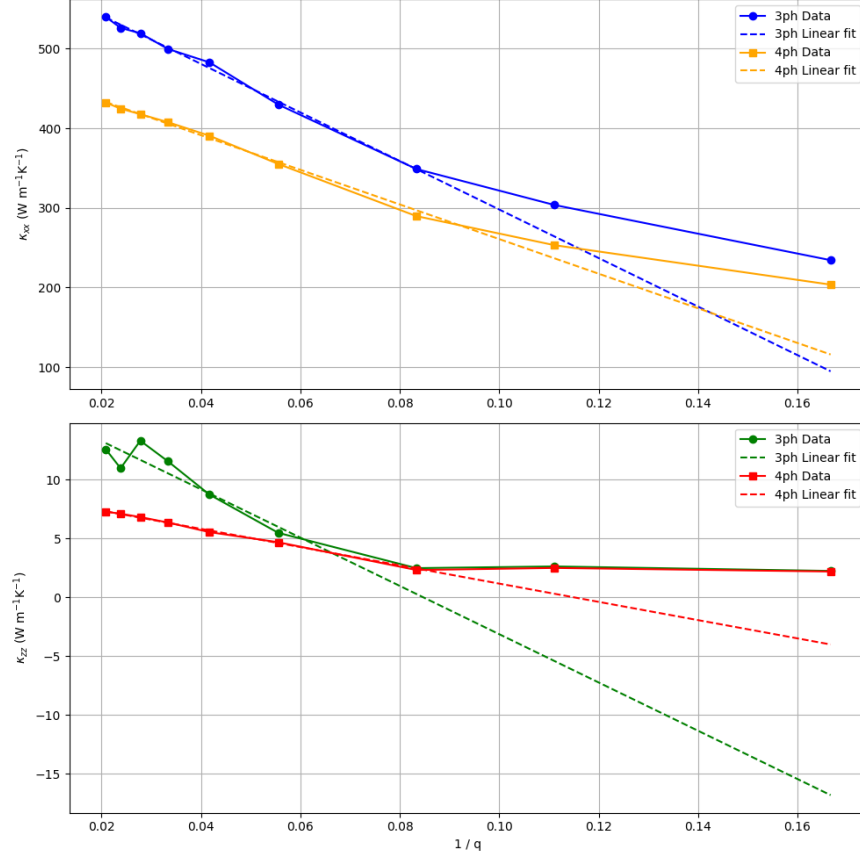
4.4 Lattice Thermal Conductivity

The IBTE is used to compute the thermal conductivity at room temperature for a set of q-point grids, which are then used to perform a linear extrapolation of κ vs $1/q$. The final values are then obtained at the limit $q \to \infty$, i.e. the extrapolation's y-intercept. The calculations are performed for both isotope + 3-phonon scattering and isotope + 3 + 4-phonon scattering. We observe that the in-plane thermal conductivity κ_{xx} is decreased by $\approx 25\%$ from 602.727 Wm^{-1}K^{-1} to 478.285 Wm^{-1}K^{-1} when 4-phonon effects are included. The out-of-plane component κ_{zz}, on the other hand, is affected much more significantly, with a decrease by almost a factor 2, from 17.391 Wm^{-1}K^{-1} to 8.933 Wm^{-1}K^{-1} being observed. This decrease in thermal conductivity can be understood by analyzing the change in phonon lifetimes. When 4-phonon interactions are included, we observe that at low frequency the largest phonon lifetimes are suppressed by the increased level of scattering.

Figure 4.8: In-plane and out-of-plane components of the thermal conductivity of bulk for q-grids ranging from $6 \times 6 \times 6$ to $48 \times 48 \times 48$. A Monte Carlo grid of $18 \times 18 \times 18$ is used in the 3-phonon case for $q < 18$, and $6 \times 6 \times 6$ for the 4-phonon case.
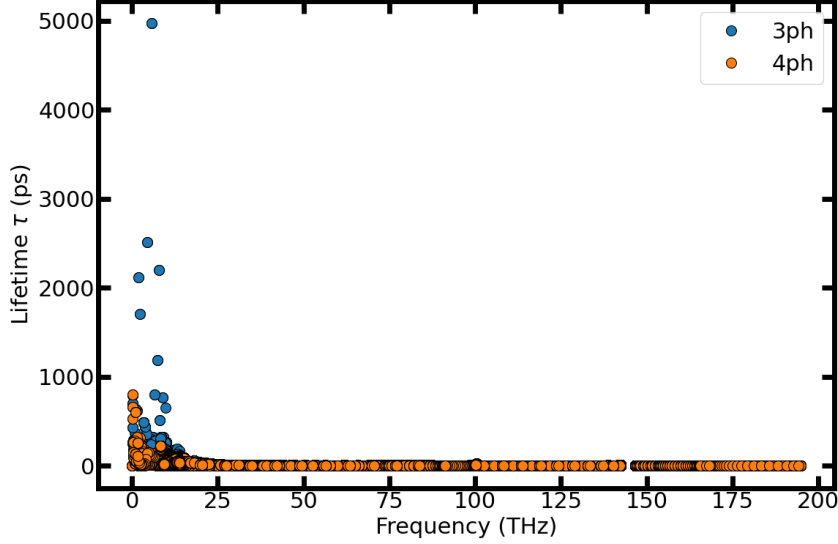
Figure 4.9: Phonon lifetimes with and without 4-phonon scattering in bulk h-
BN at room temperature. A massive decrease in the larger lifetimes is observed
at lower frequencies when 4-phonon effects are included, leading to a substantial
decrease in lattice thermal conductivity.

We find that our results match favorably with previous experimental and
theoretical works [47, 85, 102], with better agreement on the in-plane κ as well
as the out-of-plane component when carefully treated [46]. In particular, the
in-plane thermal conductivity obtained is manifestly lower than previous works
due to the inclusion of 4-phonon effects, highlighting the importance they have
for an accurate result. As for the out-of-plane component, despite higher-order
interactions we obtain a value which almost doubles that of previous works. A
potential reason for such a disparity can be the substantially larger integration
grids used in this work. If one computes κ_{zz} by interpolating only up to an
$18 \times 18 \times 18$ grid, for example, we obtain $\kappa_{zz} \approx 3$, a value much closer to that of
previously reported theoretical works.

4.5   Conclusions

In summary, the temperature evolution of the E_{2g} mode's Raman spectrum, optical coefficients and real part of the dielectric tensor of bulk hexagonal boron nitride were studied for the temperature range T = 100-500K. We find that while not very sensitive to temperature change in this region, our approach of sTDEP combined with first-order Raman via phonon mode-displacement matches experimental results accurately, as displayed in Figure 4.4. We further show that sTDEP renormalized phonons allow for this accuracy to be achieved without 4-phonon interactions, substantially reducing the computational cost of the simulations. We also compute boron nitride's lattice thermal conductivity at room temperature. For this property, we find agreement with experimental results both for the in-plane and out-of-plane components when 4-phonon interactions are included. Our results not only show our method's accuracy at reproducing temperature dependent dielectric properties, but also point towards the need for 4-phonon interactions to be included for similar systems when looking for accurate thermal conductivity simulations.

4. TEMPERATURE DEPENDENT PHONON PROPERTIES OF BULK HEXAGONAL BORON NITRIDE

Part III

Conclusions And Future Work

Conclusions And Future Work

Conclusions and Future work

In this thesis, we have dealt with the problem of anharmonic lattice dynamics, thermal conductivity and dielectric properties from the perspective of our novel Mori-Zwanzig projection operator formalism and mode-coupling theory approach.

In Part I we introduced the harmonic theory and renormalized phonon theories. Particular focus was given to the SCHA and TDEP approaches, with their respective advantages and limitations. Additionally, we presented an overview of the theory of lattice thermal conductivity, exploring the relaxation time approximation, the iterative solution to the Boltzmann equation and the Green-Kubo formalism. Finally, we explored the peculiarities of thermal transport in two-dimensional systems due to their symmetry constraints and presence of collective effects. An appendix is provided with supporting text on machine learning interatomic potentials and molecular dynamics.

In Part II we displayed the main results of this thesis. In 3.1 we presented our theory of lattice dynamics based on the Mori-Zwanzig projection operator formalism and mode-coupling theory. A generalized Langevin equation was derived describing the dynamics through a static conservative part and a dynamic dissipative one, where the first can be obtained exactly, leading to phonons renormalized to infinite order, and the second requiring approximations. To this effect, we derived a self-consistent set of equations for the memory kernel, requiring only static Kubo correlation functions as inputs. The theory lays a fundamental framework for the TDEP approach while also extending it to account for nuclear quantum effects (NQEs), allowing for vibrational properties to be derived from path-integral molecular dynamics. An application to fcc ^{4}He was provided, highlighting its ability to accurately describe the phonon spectra of systems with strongly anharmonic and nuclear quantum effects.

In 3.2 we derived a theory of lattice thermal conductivity within the mode-coupling formalism. Our derivation, based on the Green-Kubo formula, yields an equation that encompasses both single-mode, collective and off-diagonal contributions, making it valid for a wide range of systems regardless of their level of anharmonicity. A numerical technique based on Monte Carlo integration is introduced in order to reduce the cost of scattering matrix calculations, allowing for large reciprocal space grids to be studied as well as 4-phonon interactions to an otherwise prohibitive degree. Finally, the derivation and implementation are validated by successfully applying them to systems with varying degrees of anharmonicity.

In 3.3 we highlighted the deficiency of standard energy conservation conditions and provided an improvement by substituting the typical Dirac delta functions by convolutions of phonon spectral functions. While the former violate the fluctuation-dissipation theorem, the latter comply with it and, in the Markovian approximation, directly link the dissipative component of the dynamics to phonon lifetimes. These new conditions were applied to BAs, where the dominance of 4-phonon interactions and their crucial role in thermal conductivity simulations was previously attributed to its large acoustic-optical phonon band-gap. With fluctuation-dissipation compliant energy conservation conditions, however, we showed that this is not the case as they give rise to previously forbidden interactions via the now Lorentzian phonons, effectively decreasing the previously enormous band-gap. While reducing the impact of 4-phonon effects dramatically, this approach is not an indicator that such an approximation is unnecessary; instead, it provides a superior formalism at all levels of interaction. In the case of BAs, the new energy conservation conditions relax the previous constraints on the scattering phase space at the 3-phonon level, and it is the consequent increase of the number of scattering processes that leads to a relative decrease in importance of 4-phonon scattering.

In 3.4, we studied the impact of 4-phonon scattering and NQEs in the lattice thermal conductivity of monolayer hexagonal boron nitride (h-BN). Using classical and path-integral molecular dynamics (classical MD and PIMD) together with TDEP we found that while NQEs are negligible, 4-phonon scattering is crucial for an accurate prediction of the thermal conductivity. These results were explained

as a result of the crystal's mirror-plane symmetry, which limits scattering processes to include only even numbers of flexural modes. In the 3-phonon scattering approximation, this means that the interactions are constrained to include either 0 or 2 flexural phonons, severely limiting the scattering phase space, and consequently increasing the comparative importance of 4-phonon interactions. This result includes isotope, 3-phonon and 4-phonon scattering as well as NQEs and renormalized phonons, which makes it the first systematic study of the temperature evolution of the thermal conductivity of monolayer h-BN at this level of accuracy.

In 4 we studied the temperature evolution of dielectric properties of bulk h-BN, as well as its room temperature lattice thermal conductivity. Employing a first-order approximation to the Raman tensor together with sTDEP phonons, we achieved very good agreement with experimental results for both the frequency and linewidth of the E_{2g}^{high} mode, the highest frequency Raman active mode of the two present in this system. We found that staying at a 3-phonon scattering level we reproduce results that in the literature are argued to be only obtainable by considering 4-phonon interactions, as our IFCs include them naturally in their renormalization process. We further computed the real part of the dielectric tensor and the optical coefficients and their evolution with temperature, showing how small their variations are in the range T = 100-500 K. Finally, we obtained bulk h-BN's lattice thermal conductivity at room temperature with 4-phonon interactions. We showed that these are essential not only for a better agreement with experimental results for the in-plane component, providing a $\approx 25\%$ reduction, but also for the out-of-plane component, where the reduction is much larger at $\approx 50\%$. The study of the full temperature range will be the subject of future work.

While the developments to the theory of lattice dynamics and thermal transport presented provide a strong framework to compute temperature dependent properties of crystals, they also open many questions. The usage of PIMD in conjunction with TDEP, for example, is not a well understood concept in practice despite being physically well founded. In particular, the centroid construction process involves averaging over all the beads in the ring-polymer used in a PIMD simulation, which in turn leads to a ragged Born-Oppenheimer potential energy

surface. Consequently, the forces used to build the TDEP IFCs will contain statistical noise, potentially impeding an unbiased least-squares fit procedure. While in the limit where the number of beads is large enough this effect disappears, such calculations are often unfeasible, highlighting the need for a further understanding of its functional form and impact. Another point of interest arises in the thermal conductivity of monolayer h-BN. While our approach already includes NQEs and 4-phonon scattering, the impact of fluctuation-dissipation compliant energy conservation conditions is not studied. Given its phonon dispersion and some preliminary results, we expect that while the thermal conductivity at the 4-phonon scattering level changes only minimally, at the 3-phonon scattering level it will be greatly reduced when compared to their Dirac delta counterparts. This would constitute a different case than that of BAs, where there is no mirror-plane symmetry present and the 3-phonon + fluctuation dissipation compliance case yields similar values as the 4-phonon + standard energy conservation case. For monolayer h-BN, mirror plane symmetry constrains the 3-phonon scattering phase space to such a degree that the effect of fluctuation-dissipation compliance is only visible at that level. When 4-phonon interactions are included, the sheer number of extra processes fills the scattering phase space in a way that overshadows the previous impact on the 3-phonon scattering. This problem is currently still under study. Finally, while the mode-coupling theory and its applications to thermal properties have been discussed here, only cases of perfectly pure or isotopically impure crystals are studied. As the approach is dependent on the system's unit cell, treating systems with structural defects such as vacancies is a non-trivial problem. Due to the high degree of relevance these types of systems hold in thermal and optical applications, a re-derivation of the mode-coupling theory of lattice dynamics that can properly handle them is of high priority.

Part IV

Appendixes

Appendix A

Machine-Learning Interatomic Potentials

When performing *ab-initio* MD simulations, one computes energies, forces and stresses for a system from a quantum mechanical approach. While accurate and independent of empirical parameters, these methods are computationally expensive, scaling as $O(N^3)$ or worse with respect to the number of atoms in the system. Despite the power of modern high performance computers, this level of scaling means that a tradeoff often occurs, where the system's size or the simulation length are limited or even unconverged.

Empirical potentials (also known as force fields), such as the Tersoff [95] or Lennard-Jones [48], have existed and been used for a long time. Composed by analytical functions built based on physical principles, they are much faster than using *ab-initio* methods. They do, however, trade their speed and ability to handle large simulation cells and long time scales for their accuracy and flexibility, being often constrained to conditions very similar to those they were parameterized on.

As discussed in the main section of the manuscript, in order to obtain temperature dependent phonon properties one needs an accurate description of the potential energy surface. To obtain such a quantity from MD requires supercells and simulation lengths that are often too large to be computed in *ab-initio* fashion, and properties are often too sensitive to be accurately computed from empirical potentials. The rise of machine learning-interatomic potentials (MLIPs) comes as an approach aiming to overcome the issues with both empirical potential driven and *ab-initio* MD, by offering a paradigm where both accuracy and speed are preserved. The basic idea behind an MLIP is that given a sufficiently

complex machine learning model trained on *ab-initio* data, one can obtain the optimal point between precision and speed to compute the potential energy surface of a given system. In order to build such a model, three key components are required.

The first of these components is the input for the machine-learning model. These inputs are ideally independent of the system's size, in order for extrapolation to large super-cells to be allowed, and to be a vector of fixed length. To achieve this goal, a common approximation is to decompose the potential energy into its atomic contributions:

$$V(\vec{R}) = \sum_i V_i(\vec{R}) \ . \tag{4.10}$$

These inputs are known as descriptors, whose function is to be the representations of the atoms' local environment, such that for a specific atom i a descriptor vector ρ_i is created. While other approaches exist, these objects are often treated as representing a generalization of the density of atoms, which allows for the potential energy to be obtained as a functional:

$$V_i(\vec{R}) = \mathcal{F}\left[\rho_i(\vec{R})\right] \ . \tag{4.11}$$

In order to efficiently exploit the descriptor, one can enforce rotational, translational and permutation symmetry, as these are always present in potential energy surfaces. This means that for a given coordinate set $\vec{R} = R_1, R_2, ...$, permutation operator $\mathcal{P}(i \leftrightarrow j)$, translation $\vec{R} \to \vec{R} + \delta\vec{R}$ and rotation operators $\mathcal{R}$ yield an invariant descriptor,

$$\rho(\mathcal{P}(i \leftrightarrow j)\vec{R}) = \rho(\vec{R})$$
$$\rho(\vec{R} + \delta\vec{R}) = \rho(\vec{R})$$
$$\rho(\mathcal{R}\vec{R}) = \rho(\vec{R}) \ . \tag{4.12}$$

Applying these symmetries directly in the descriptor means they are automatically imposed in the potential energy as well.

An example of a descriptor is the Smooth Overlap of Atomic Positions (SOAP) [5], where the local atomic density around a central atom i is defined by a Gaussian

$$\rho_i(\vec{R}) = \sum_{i \neq j} \exp\left(-\frac{(\vec{R} - \vec{R}_{ij})^2}{2\sigma^2}\right) f_{\text{cut}}(\vec{R}_{ij} - \vec{R}_{cut}) , \qquad (4.13)$$

where $\vec{R}_{ij}$ is the distance between the central atom and atom j, σ establishes the spacial uncertainty, and f_{cut} is a cutoff function that ensures only atoms within $\vec{R}_{cut}$ are included. This density is then expanded in terms of spherical harmonics $Y_{lm}(\vec{R})$ and radial basis functions $g_n(\vec{R})$ as

$$\rho_i(\vec{R}) = \sum_{lmn} c_{lmn}^{(i)} g_n(\vec{R}) Y_{lm}(\vec{R}) . \qquad (4.14)$$

The coefficients $c_{lmn}^{(i)}$ are then obtained by projecting the density in 4.13 into this basis as

$$c_{lmn}^{(i)} = \int \rho_i(\vec{R}) g_n(\vec{R}) Y_{lm}^*(\vec{R}) d\vec{R} . \qquad (4.15)$$

As the coefficients $c_{lmn}^{(i)}$ are not rotationally invariant, the descriptor is built instead from the power spectrum obtained as

$$p_{lnn'}^{(i)} = \sum_{m=-l}^{l} \left(c_{lmn}^{(i)}\right)^* c_{lmn'}^{(i)} , \qquad (4.16)$$

with the sum over m averaging out the angular orientation. The indices l, n and n' define the components of the descriptor, and its complexity and resolution are controlled by the number of radial basis functions and the maximum angular momentum included in 4.14.

With a descriptor in hand, the second component required to build an MLIP according to 4.11 is a relationship between the density and the potential energy. While many functionals exist with varying levels of complexity, from polynomials to neural networks, linear relationships are often found to be sufficient for an accurate description. For a descriptor p, this means that the potential energy of atom i is given simply by

$$V_i(\vec{p}_i) = \sum_k w_k p_{i,k} \ , \tag{4.17}$$

where $\vec{w}$ is a vector of the weights that need to be determined. As we are presuming we can obtain the total energy by summing individual atomic energies, we obtain

$$V(\vec{R}) = \sum_k w_k \left(\sum_i p_{i,k} \right) \ , \tag{4.18}$$

showing how the total energy in this case is linear on the summed descriptor components from all atoms in the system, and the problem is now a simple linear regression one. The forces can be obtained by taking the gradient of the energy

$$\vec{F}_k = -\vec{\nabla}_k V(\vec{R}) = -\sum_k w_k \left(\sum_i \vec{\nabla} p_{i,k} \right) \ , \tag{4.19}$$

and are also linear now on the derivative of the descriptor.

Finally, the last key ingredient is the dataset on which the MLIP is trained. If this dataset is composed by data that is not accurate for the system under study, the MLIP will poorly reproduce the potential energy surface and yield the wrong lattice dynamics. One method to generate a physically informed dataset is the machine-learning assisted canonical sampling (MLACS) approach [18], which generates configurations in a self-consistent fashion based on the principle of variational inference. In order to optimize the $\vec{w}$ that minimize the difference between the predicted and the reference data, one can perform a least-squares fit, where the coefficients are minimized according to

$$\min_{\mathbf{w}} \left(\sum_n \left[\lambda_V (V^{\mathrm{MLIP}} - V^{\mathrm{DFT}})^2 + \lambda_F \sum_i |\vec{F}_i^{\mathrm{MLIP}} - \vec{F}_i^{\mathrm{DFT}}|^2 \right. \right.$$
$$\left. \left. + \lambda_\sigma \sum_\alpha |\sigma_\alpha^{\mathrm{MLIP}} - \sigma_\alpha^{\mathrm{DFT}}|^2 \right] + \lambda_R |\mathbf{w}|^2 \right) \ , \tag{4.20}$$

where the outer sum is on the configurations used for training, $\lambda_{V,F,\sigma}$ are hyperparameters that regulate the relative impact of the energies, forces and stresses

on the minimization procedure, and lastly λ_R is a regularization parameter that penalizes large coefficient values and prevents overfitting.

Appendix B

Molecular Dynamics

When computing temperature dependent properties for a given system, their corresponding thermodynamic ensemble needs to be taken into consideration. The expectation value for a given operator $\hat{O}$ for such a case is given by its thermodynamic average over all the possible configurations $\Gamma = \{\vec{q}, \vec{p}\}$ of the system, with $\vec{q}$ and $\vec{p}$ the canonical coordinates and momenta:

$$\langle \hat{O} \rangle = \int O(\Gamma)\rho(\Gamma)d\Gamma . \tag{4.21}$$

The trace is taken over all possible Γ, and each of these Γ corresponds to a phase-space point. The set of all phase-space points comprises the phase-space. The probability density function ρ is given by

$$\rho = \frac{e^{-\beta H}}{Z} , \tag{4.22}$$

where $Z = Tr(e^{-\beta H})$ is the partition function, H is the Hamiltonian and $\beta = \frac{1}{k_B T}$.

While general, calculating a thermodynamic average via 4.21 is not efficient except for very simple cases. One can, however, use the ergodic principle in order to replace the phase space average by a discrete time average in the infinite time-step limit:

$$\langle O \rangle = \lim_{N_t \to \infty} \frac{1}{N_t} \sum_{t=0}^{N_t} O(t) . \tag{4.23}$$

In summary, the ergodic hypothesis states that a given system trajectory will pass through all valid points in phase space for a sufficiently large propagation time, allowing us to effectively replace thermodynamic averages by time averages.

The ergodic hypothesis is the underlying idea behind molecular dynamics (MD), a computational method which simulates how a system of atoms or molecules propagates through time for a given potential energy surface. In this approach, each particle's trajectory is obtained by, for example, numerically solving Hamilton's equations:

$$
\frac{\partial H}{\partial \vec{p}_i} = \frac{\partial \vec{R}_i}{\partial t} = \frac{\vec{p}_i}{m_i}
$$
$$
-\frac{\partial H}{\partial \vec{R}_i} = \frac{\partial \vec{p}_i}{\partial t} = -\frac{\partial V(\vec{r})}{\partial \vec{R}_i} = \vec{F}_i \ . \tag{4.24}
$$

In practice, time evolution of the positions $\vec{R}$ and velocities $\vec{v}$ of the particles in the system are obtained by solving Hamilton's equations via an algorithm like the velocity Verlet one [91, 97]:

$$
\vec{R}_i(t + \Delta t) = \vec{R}_i(t) + \vec{v}_i(t)\Delta t + \vec{F}_i(t)\frac{\Delta t^2}{2m_i} + \mathcal{O}(\Delta t^4)
$$
$$
\vec{v}_i(t + \Delta t) = \vec{v}_i(t) + \left(\vec{F}_i(t) + \vec{F}_i(t + \Delta t) \right) \frac{\Delta t^2}{2m_i} + \mathcal{O}(\Delta t^4) \ . \tag{4.25}
$$

While other algorithms exist, the velocity Verlet is widely used due to its time-reversibility and energy conservation properties.

While sufficient for simulations under NVE thermodynamic conditions, where the phase-space is isoenergetic, the above equations are incomplete in the case where the canonical ensemble is considered and NVT conditions apply. In this circumstances, a thermostat that manipulates the kinetic energy in order to preserve a target temperature is required. An example of a popular thermostat is the Langevin one, which modifies the equations of motion by adding a friction term and a stochastic force to the canonical momentum's Hamilton equation:

$$
\frac{\partial \vec{p}_i}{\partial t} = \vec{F}_i - \gamma m_i \vec{v}_i + F_i^s \ , \tag{4.26}
$$

The friction coefficient γ governs the strength of the friction term, that acts as the source of dissipative kinetic energy loss to the environment. The stochastic forces F_i^s, on the other hand, a friction term and a stochastic force, acts as a random source of energy injections back into the system from the surrounding heat bath, and counterbalances the kinetic losses due to friction. This force is typically normally distributed, and obeys

$$\langle F_i^s(t)\rangle = 0$$
$$\langle F_i^s(t)F_j^s(t')\rangle = \sqrt{\frac{2m_i\gamma}{\beta}}\delta_{ij}\delta(t-t') \ . \tag{4.27}$$

The addition of the Langevin thermostat ensures that the fluctuation-dissipation theorem holds, and thus allows us to sample the canonical ensemble.

Since for every time-step in 4.25 the potential energy surface needs to be computed, it becomes very apparent why *ab-initio* MD is such an expensive calculation and why one resorts to MLIPs in order to obtain simulation lengths that allow for the ergodic hypothesis to hold.

Despite its tremendous success and wide range of applicability, the formulation of MD described above is still limited by its classical treatment of the particles and their trajectories. In order to include quantum effects, a reformulation is required: path-integral molecular dynamics (PIMD) [10, 23, 68]. The basic idea behind PIMD lies on the isomorphism between the path-integral quantum-mechanical partition function and the classical partition function of a fictitious ring-polymer, consisting of multiple replicas (beads) of the physical system connected by fictitious springs. This isomorphism allows for the canonical partition function $Z = Tr(e^{-\beta H})$ to be re-written exactly as $\lim_{P\to\infty} Z_P$, with P the number of beads and

$$Z_P = \frac{1}{2\pi\hbar}\int d\vec{q}d\vec{p}\,e^{-\beta_P H_P(\vec{q},vecp)} \ , \tag{4.28}$$

where $\beta_P = \beta/P$ and H_P the classical Hamiltonian of a harmonic ring-polymer with external potential $V(\vec{q})$ and subject to the cyclic boundary condition $\vec{q}_0 = \vec{q}_P$:

$$H_P(\vec{q}, \vec{p}) = \sum_{j=1}^{P} \frac{\vec{p}_j^2}{2m} + \frac{m}{2\beta_P^2 \hbar^2} \sum_{j=1}^{P} (\vec{q}_j - \vec{q}_{j-1})^2 + \sum_{j=1}^{P} V(\vec{q}_j), \qquad (4.29)$$

This construction relies on the Trotter product formula $e^{A+B} = \lim_{P\to\infty}(e^{A/P}e^{B/P})^P$. For $P = 1$ the partition function is the classical one.

Within this approach, the thermodynamic average of an operator O is given by $\langle O \rangle = \lim_{P\to\infty} \langle O \rangle_P$ with

$$\langle O \rangle_P = \frac{1}{(2\pi\hbar)^P Z_P} \int d\vec{q} \int d\vec{p} e^{-\beta_P H_P(\vec{q}, \vec{p})} O_P(\vec{q}) \qquad (4.30)$$

and $O_P(\vec{q}) = \frac{1}{P} \sum_{j=1}^{P} O(\vec{q}_j)$, i.e. the expectation value is the classical one for each bead, but is then averaged for the ring-polymer. The Hamiltonian H_n generates the equations of motion

$$\frac{\partial \vec{q}}{\partial t_j} = \frac{\vec{p}_j}{m_j}$$
$$\frac{\partial \vec{p}}{\partial t_j} = -\frac{m}{\beta_P^2 \hbar^2}[2\vec{q}_j - \vec{q}_{j-1} - \vec{q}_{j+1}] - \frac{\partial V(\vec{q}_j)}{\partial \vec{q}_j} , \qquad (4.31)$$

where the second equation is the effective force for the ring-polymer, with the first term representing the harmonic interactions between adjacent beads in the ring polymer, and the second term is the physical force experienced by each bead. In order to further include Langevin dynamics, many integration algorithms exist. An example of such an integrator is the BAOAB (bend-accelerate-operate-accelerate-bend) [57], which includes the thermostat's effect via a five-step procedure that not only allows for accurate temperature control but also maintains the energy conservation and time-reversibility present in the classical velocity Verlet algorithm.

Bibliography

[1] N. W. Ashcroft and N. Mermin. *Solid State Physics*. Brooks/Cole, Florence, KY, Jan. 1976. 23

[2] A. A. Balandin, S. Ghosh, W. Bao, I. Calizo, D. Teweldebrhan, F. Miao, and C. N. Lau. Superior thermal conductivity of single-layer graphene. *Nano Letters*, 8(3):902–907, Feb. 2008. ISSN 1530-6992. doi: 10.1021/nl0731872. URL http://dx.doi.org/10.1021/nl0731872. 34

[3] S. Baroni, S. de Gironcoli, A. Dal Corso, and P. Giannozzi. Phonons and related crystal properties from density-functional perturbation theory. *Rev. Mod. Phys.*, 73(2):515–562, July 2001. 119

[4] S. Baroni, R. Bertossa, L. Ercole, F. Grasselli, and A. Marcolongo. *Heat Transport in Insulators from Ab Initio Green-Kubo Theory*, page 809–844. Springer International Publishing, 2020. ISBN 9783319446806. doi: 10.1007/978-3-319-44680-6_12. URL http://dx.doi.org/10.1007/978-3-319-44680-6_12. 31

[5] A. P. Bartók, R. Kondor, and G. Csányi. On representing chemical environments. *Physical Review B*, 87(18), May 2013. ISSN 1550-235X. doi: 10.1103/physrevb.87.184115. URL http://dx.doi.org/10.1103/PhysRevB.87.184115. 141

[6] N. Benshalom, G. Reuveni, R. Korobko, O. Yaffe, and O. Hellman. Dielectric response of rock-salt crystals at finite temperatures from first principles. *Physical Review Materials*, 6(3), Mar. 2022. ISSN 2475-9953.

doi: 10.1103/physrevmaterials.6.033607. URL http://dx.doi.org/10.1103/PhysRevMaterials.6.033607. 30, 117

[7] R. Bianco, I. Errea, L. Paulatto, M. Calandra, and F. Mauri. Second-order structural phase transitions, free energy curvature, and temperature-dependent anharmonic phonons in the self-consistent harmonic approximation: Theory and stochastic implementation. *Physical Review B*, 96 (1), July 2017. ISSN 2469-9969. doi: 10.1103/physrevb.96.014111. URL http://dx.doi.org/10.1103/PhysRevB.96.014111. 15

[8] M. Born and K. Huang. *Dynamical theory of crystal lattices*. Oxford Classic Texts in the Physical Sciences. Clarendon Press, Oxford, England, June 1998. 10

[9] M. Born and R. Oppenheimer. Zur quantentheorie der molekeln. *Annalen der Physik*, 389(20):457–484, Jan. 1927. ISSN 1521-3889. doi: 10.1002/andp.19273892002. URL http://dx.doi.org/10.1002/andp.19273892002. 8

[10] B. J. Braams and D. E. Manolopoulos. On the short-time limit of ring polymer molecular dynamics. *The Journal of Chemical Physics*, 125(12), Sept. 2006. ISSN 1089-7690. doi: 10.1063/1.2357599. URL http://dx.doi.org/10.1063/1.2357599. 147

[11] W. Cai, A. L. Moore, Y. Zhu, X. Li, S. Chen, L. Shi, and R. S. Ruoff. Thermal transport in suspended and supported monolayer graphene grown by chemical vapor deposition. *Nano Letters*, 10(5):1645–1651, Apr. 2010. ISSN 1530-6992. doi: 10.1021/nl9041966. URL http://dx.doi.org/10.1021/nl9041966. 34

[12] C. Carbogno, R. Ramprasad, and M. Scheffler. Ab initio green-kubo approach for the thermal conductivity of solids. *Physical Review Letters*, 118 (17), Apr. 2017. ISSN 1079-7114. doi: 10.1103/physrevlett.118.175901. URL http://dx.doi.org/10.1103/PhysRevLett.118.175901. 31

[13] M. Cardona and G. Güntherodt. *Light Scattering in Solids II: Basic Concepts and Instrumentation*. Number dl. 2 in Light Scattering in Solids

II: Basic Concepts and Instrumentation. Springer-Verlag, 1982. ISBN 9783540113805. URL `https://books.google.be/books?id=OHMsAAAAYAAJ`. 119

[14] A. Castellano. *Étude des effets de la température sur les combustibles nucléaires par une approche ab initio*. PhD thesis, Sorbonne Université, 2022. 22

[15] A. Castellano, F. m. c. Bottin, J. Bouchet, A. Levitt, and G. Stoltz. *ab* initio canonical sampling based on variational inference. *Phys. Rev. B*, 106: L161110, Oct 2022. doi: 10.1103/PhysRevB.106.L161110. URL `https://link.aps.org/doi/10.1103/PhysRevB.106.L161110`. 116

[16] A. Castellano, J. P. A. Batista, and M. J. Verstraete. Mode-coupling theory of lattice dynamics for classical and quantum crystals. *The Journal of Chemical Physics*, 159(23), Dec. 2023. ISSN 1089-7690. doi: 10.1063/5.0174255. URL `http://dx.doi.org/10.1063/5.0174255`. 21, 22, 119

[17] A. Castellano, J. P. A. Batista, O. Hellman, and M. J. Verstraete. Mode-coupling formulation of heat transport in anharmonic materials. *Physical Review B*, 111(9), Mar. 2025. ISSN 2469-9969. doi: 10.1103/physrevb.111.094306. URL `http://dx.doi.org/10.1103/PhysRevB.111.094306`. 26, 116

[18] A. Castellano, R. Béjaud, P. Richard, O. Nadeau, C. Duval, G. Geneste, G. Antonius, J. Bouchet, A. Levitt, G. Stoltz, and F. Bottin. Machine learning assisted canonical sampling (mlacs). *Computer Physics Communications*, 316:109730, Nov. 2025. ISSN 0010-4655. doi: 10.1016/j.cpc.2025.109730. URL `http://dx.doi.org/10.1016/j.cpc.2025.109730`. 116, 142

[19] A. Cepellotti, G. Fugallo, L. Paulatto, M. Lazzeri, F. Mauri, and N. Marzari. Phonon hydrodynamics in two-dimensional materials. *Nature Communications*, 6(1), Mar. 2015. ISSN 2041-1723. doi: 10.1038/ncomms7400. URL `http://dx.doi.org/10.1038/ncomms7400`. 34, 36

[20] S. Chen, Q. Wu, C. Mishra, J. Kang, H. Zhang, K. Cho, W. Cai, A. A. Balandin, and R. S. Ruoff. Thermal conductivity of isotopically modified graphene. *Nature Materials*, 11(3):203–207, Jan. 2012. ISSN 1476-4660. doi: 10.1038/nmat3207. URL http://dx.doi.org/10.1038/nmat3207. 32, 34

[21] Y.-C. Chen, S.-C. Lee, T.-H. Liu, and C.-C. Chang. Thermal conductivity of boron nitride nanoribbons: Anisotropic effects and boundary scattering. *International Journal of Thermal Sciences*, 94:72–78, Aug. 2015. ISSN 1290-0729. doi: 10.1016/j.ijthermalsci.2015.02.005. URL http://dx.doi.org/10.1016/j.ijthermalsci.2015.02.005. 34

[22] R. A. Cowley. The theory of raman scattering from crystals. *Proceedings of the Physical Society*, 84(2):281–296, Aug. 1964. ISSN 0370-1328. doi: 10.1088/0370-1328/84/2/311. URL http://dx.doi.org/10.1088/0370-1328/84/2/311. 117

[23] I. R. Craig and D. E. Manolopoulos. Quantum statistics and classical mechanics: Real time correlation functions from ring polymer molecular dynamics. *The Journal of Chemical Physics*, 121(8):3368–3373, Aug. 2004. ISSN 1089-7690. doi: 10.1063/1.1777575. URL http://dx.doi.org/10.1063/1.1777575. 147

[24] R. Cuscó, B. Gil, G. Cassabois, and L. Artús. Temperature dependence of raman-active phonons and anharmonic interactions in layered hexagonal bn. *Physical Review B*, 94(15), Oct. 2016. ISSN 2469-9969. doi: 10.1103/physrevb.94.155435. URL http://dx.doi.org/10.1103/PhysRevB.94.155435. 121

[25] D. Dangić, O. Hellman, S. Fahy, and I. Savić. The origin of the lattice thermal conductivity enhancement at the ferroelectric phase transition in gete. *npj Computational Materials*, 7(1), Apr. 2021. ISSN 2057-3960. doi: 10.1038/s41524-021-00523-7. URL http://dx.doi.org/10.1038/s41524-021-00523-7. 30

[26] D. Dangić, G. Caldarelli, R. Bianco, I. Savić, and I. Errea. Lattice thermal conductivity in the anharmonic overdamped regime. *Physical Review B*,

111(10), Mar. 2025. ISSN 2469-9969. doi: 10.1103/physrevb.111.104314. URL `http://dx.doi.org/10.1103/PhysRevB.111.104314`. 27

[27] O. Delaire, J. Ma, K. Marty, A. F. May, M. A. McGuire, M.-H. Du, D. J. Singh, A. Podlesnyak, G. Ehlers, M. D. Lumsden, and B. C. Sales. Giant anharmonic phonon scattering in pbte. *Nature Materials*, 10(8): 614–619, June 2011. ISSN 1476-4660. doi: 10.1038/nmat3035. URL `http://dx.doi.org/10.1038/nmat3035`. 14

[28] L. Ercole, A. Marcolongo, P. Umari, and S. Baroni. Gauge invariance of thermal transport coefficients. *Journal of Low Temperature Physics*, 185 (1–2):79–86, Apr. 2016. ISSN 1573-7357. doi: 10.1007/s10909-016-1617-6. URL `http://dx.doi.org/10.1007/s10909-016-1617-6`. 28

[29] I. Errea, B. Rousseau, and A. Bergara. Anharmonic stabilization of the high-pressure simple cubic phase of calcium. *Physical Review Letters*, 106 (16), Apr. 2011. ISSN 1079-7114. doi: 10.1103/physrevlett.106.165501. URL `http://dx.doi.org/10.1103/PhysRevLett.106.165501`. 14

[30] H. Fan, H. Wu, L. Lindsay, and Y. Hu. Ab initio investigation of single-layer high thermal conductivity boron compounds. *Physical Review B*, 100 (8), Aug. 2019. ISSN 2469-9969. doi: 10.1103/physrevb.100.085420. URL `http://dx.doi.org/10.1103/PhysRevB.100.085420`. 34

[31] T. Feng and X. Ruan. Four-phonon scattering reduces intrinsic thermal conductivity of graphene and the contributions from flexural phonons. *Physical Review B*, 97(4), Jan. 2018. ISSN 2469-9969. doi: 10.1103/ physrevb.97.045202. URL `http://dx.doi.org/10.1103/PhysRevB.97.045202`. 34

[32] G. Fugallo, M. Lazzeri, L. Paulatto, and F. Mauri. Ab initiovariational approach for evaluating lattice thermal conductivity. *Physical Review B*, 88(4), July 2013. ISSN 1550-235X. doi: 10.1103/physrevb.88.045430. URL `http://dx.doi.org/10.1103/PhysRevB.88.045430`. 26

BIBLIOGRAPHY

[33] G. Fugallo, A. Cepellotti, L. Paulatto, M. Lazzeri, N. Marzari, and F. Mauri. Thermal conductivity of graphene and graphite: Collective excitations and mean free paths. *Nano Letters*, 14(11):6109–6114, Nov. 2014. ISSN 1530-6992. doi: 10.1021/nl502059f. URL `http://dx.doi.org/10.1021/nl502059f`. 32, 34

[34] S. Ghosh, I. Calizo, D. Teweldebrhan, E. P. Pokatilov, D. L. Nika, A. A. Balandin, W. Bao, F. Miao, and C. N. Lau. Extremely high thermal conductivity of graphene: Prospects for thermal management applications in nanoelectronic circuits. *Applied Physics Letters*, 92(15), Apr. 2008. ISSN 1077-3118. doi: 10.1063/1.2907977. URL `http://dx.doi.org/10.1063/1.2907977`. 34

[35] X. Gonze and J. Vigneron. Density-functional approach to nonlinear-response coefficients of solids. *Phys. Rev. B Condens. Matter*, 39(18):13120–13128, June 1989. 119

[36] X. Gonze, B. Amadon, G. Antonius, F. Arnardi, L. Baguet, J.-M. Beuken, J. Bieder, F. Bottin, J. Bouchet, E. Bousquet, N. Brouwer, F. Bruneval, G. Brunin, T. Cavignac, J.-B. Charraud, W. Chen, M. Côté, S. Cottenier, J. Denier, G. Geneste, P. Ghosez, M. Giantomassi, Y. Gillet, O. Gingras, D. R. Hamann, G. Hautier, X. He, N. Helbig, N. Holzwarth, Y. Jia, F. Jollet, W. Lafargue-Dit-Hauret, K. Lejaeghere, M. A. Marques, A. Martin, C. Martins, H. P. Miranda, F. Naccarato, K. Persson, G. Petretto, V. Planes, Y. Pouillon, S. Prokhorenko, F. Ricci, G.-M. Rignanese, A. H. Romero, M. M. Schmitt, M. Torrent, M. J. van Setten, B. Van Troeye, M. J. Verstraete, G. Zérah, and J. W. Zwanziger. The abinitproject: Impact, environment and recent developments. *Computer Physics Communications*, 248:107042, 2020. ISSN 0010-4655. doi: https://doi.org/10.1016/j.cpc.2019.107042. URL `https://www.sciencedirect.com/science/article/pii/S0010465519303741`. 116

[37] S. Grimme, J. Antony, S. Ehrlich, and H. Krieg. A consistent and accurate ab initio parametrization of density functional dispersion correction (DFT-d) for the 94 elements h-pu. *The Journal of Chemical Physics*, 132(15):

154104, April 2010. ISSN 0021-9606, 1089-7690. doi: 10.1063/1.3382344. URL https://doi.org/10.1063/1.3382344. 116

[38] M. Guo, Y. Qian, H. Qi, K. Bi, and Y. Chen. Experimental measurements on the thermal conductivity of strained monolayer graphene. *Carbon*, 157: 185–190, Feb. 2020. ISSN 0008-6223. doi: 10.1016/j.carbon.2019.10.027. URL http://dx.doi.org/10.1016/j.carbon.2019.10.027. 34

[39] Z. Han and X. Ruan. Thermal conductivity of monolayer graphene: Convergent and lower than diamond. *Physical Review B*, 108(12), Sept. 2023. ISSN 2469-9969. doi: 10.1103/physrevb.108.l121412. URL http://dx.doi.org/10.1103/PhysRevB.108.L121412. 34

[40] R. J. Hardy. Energy-flux operator for a lattice. *Physical Review*, 132(1): 168–177, Oct. 1963. ISSN 0031-899X. doi: 10.1103/physrev.132.168. URL http://dx.doi.org/10.1103/PhysRev.132.168. 28, 30

[41] O. Hellman and I. A. Abrikosov. Temperature-dependent effective third-order interatomic force constants from first principles. *Physical Review B*, 88(14), Oct. 2013. ISSN 1550-235X. doi: 10.1103/physrevb.88.144301. URL http://dx.doi.org/10.1103/PhysRevB.88.144301. 19

[42] O. Hellman, I. A. Abrikosov, and S. I. Simak. Lattice dynamics of anharmonic solids from first principles. *Physical Review B*, 84(18), Nov. 2011. ISSN 1550-235X. doi: 10.1103/physrevb.84.180301. URL http://dx.doi.org/10.1103/PhysRevB.84.180301. 19

[43] O. Hellman, P. Steneteg, I. A. Abrikosov, and S. I. Simak. Temperature dependent effective potential method for accurate free energy calculations of solids. *Physical Review B*, 87(10), Mar. 2013. ISSN 1550-235X. doi: 10.1103/physrevb.87.104111. URL http://dx.doi.org/10.1103/PhysRevB.87.104111. 19

[44] A. V. Inyushkin, V. G. Ralchenko, A. P. Bolshakov, A. A. Khomich, D. A. Chernodubov, A. N. Taldenkov, V. V. Saraykin, and S. Y. Kilin. Thermal

conductivity of chemical vapor deposition diamond enriched with 13c isotope. *Journal of Applied Physics*, 137(12), Mar. 2025. ISSN 1089-7550. doi: 10.1063/5.0255049. URL `http://dx.doi.org/10.1063/5.0255049`. 32

[45] L. Isaeva, G. Barbalinardo, D. Donadio, and S. Baroni. Modeling heat transport in crystals and glasses from a unified lattice-dynamical approach. *Nature Communications*, 10(1), Aug. 2019. ISSN 2041-1723. doi: 10.1038/s41467-019-11572-4. URL `http://dx.doi.org/10.1038/s41467-019-11572-4`. 30

[46] G. R. Jaffe, K. J. Smith, K. Watanabe, T. Taniguchi, M. G. Lagally, M. A. Eriksson, and V. W. Brar. Thickness-dependent cross-plane thermal conductivity measurements of exfoliated hexagonal boron nitride. *ACS Applied Materials & Interfaces*, 15(9):12545–12550, Feb. 2023. ISSN 1944-8252. doi: 10.1021/acsami.2c21306. URL `http://dx.doi.org/10.1021/acsami.2c21306`. 126

[47] P. Jiang, X. Qian, R. Yang, and L. Lindsay. Anisotropic thermal transport in bulk hexagonal boron nitride. *Physical Review Materials*, 2(6), June 2018. ISSN 2475-9953. doi: 10.1103/physrevmaterials.2.064005. URL `http://dx.doi.org/10.1103/PhysRevMaterials.2.064005`. 126

[48] J. Jones. On the determination of molecular fields. —ii. from the equation of state of a gas. *Proceedings of the Royal Society of London. Series A, Containing Papers of a Mathematical and Physical Character*, 106(738): 463–477, Oct. 1924. ISSN 2053-9150. doi: 10.1098/rspa.1924.0082. URL `http://dx.doi.org/10.1098/rspa.1924.0082`. 139

[49] J. Kang and L.-W. Wang. First-principles green-kubo method for thermal conductivity calculations. *Physical Review B*, 96(2), July 2017. ISSN 2469-9969. doi: 10.1103/physrevb.96.020302. URL `http://dx.doi.org/10.1103/PhysRevB.96.020302`. 31

[50] A. I. Khan, I. A. Navid, M. Noshin, and S. Subrina. Thermal transport characterization of hexagonal boron nitride nanoribbons using molecular

dynamics simulation. *AIP Advances*, 7(10), Oct. 2017. ISSN 2158-3226. doi: 10.1063/1.4997036. URL `http://dx.doi.org/10.1063/1.4997036`. 34

[51] M. L. Klein and G. K. Horton. The rise of self-consistent phonon theory. *Journal of Low Temperature Physics*, 9(3–4):151–166, Nov. 1972. ISSN 1573-7357. doi: 10.1007/bf00654839. URL `http://dx.doi.org/10.1007/BF00654839`. 15

[52] F. Knoop, M. Scheffler, and C. Carbogno. Ab initio green-kubo simulations of heat transport in solids: Method and implementation. *Physical Review B*, 107(22), June 2023. ISSN 2469-9969. doi: 10.1103/physrevb.107.224304. URL `http://dx.doi.org/10.1103/PhysRevB.107.224304`. 31

[53] F. Knoop, N. Benshalom, M. Menahem, P. Gartner, T. Salzillo, O. Yaffe, and O. Hellman. Ab initio theory of the non-resonant raman effect in crystals at finite temperature in comparison to experiment: The examples of gan and bazrs3, 2024. URL `https://arxiv.org/abs/2412.17711`. 119

[54] F. Knoop, N. Shulumba, A. Castellano, J. P. A. Batista, R. Farris, M. J. Verstraete, M. Heine, D. Broido, D. S. Kim, J. Klarbring, I. A. Abrikosov, S. I. Simak, and O. Hellman. Tdep: Temperature dependent effective potentials. *Journal of Open Source Software*, 9(94):6150, Feb. 2024. ISSN 2475-9066. doi: 10.21105/joss.06150. URL `http://dx.doi.org/10.21105/joss.06150`. 116

[55] R. Kubo, M. Toda, and N. Hashitsume. *Statistical Physics II*. Springer Berlin Heidelberg, 1991. ISBN 9783642582448. doi: 10.1007/978-3-642-58244-8. URL `http://dx.doi.org/10.1007/978-3-642-58244-8`. 29

[56] T. Lanigan-Atkins, X. He, M. J. Krogstad, D. M. Pajerowski, D. L. Abernathy, G. N. M. N. Xu, Z. Xu, D.-Y. Chung, M. G. Kanatzidis, S. Rosenkranz, R. Osborn, and O. Delaire. Two-dimensional overdamped fluctuations of the soft perovskite lattice in cspbbr3. *Nature Materials*, 20 (7):977–983, Mar. 2021. ISSN 1476-4660. doi: 10.1038/s41563-021-00947-y. URL `http://dx.doi.org/10.1038/s41563-021-00947-y`. 27

[57] B. Leimkuhler and C. Matthews. Rational construction of stochastic numerical methods for molecular sampling. *Applied Mathematics Research eXpress*, June 2012. ISSN 1687-1197. doi: 10.1093/amrx/abs010. URL `http://dx.doi.org/10.1093/amrx/abs010`. 148

[58] C. W. Li, O. Hellman, J. Ma, A. F. May, H. B. Cao, X. Chen, A. D. Christianson, G. Ehlers, D. J. Singh, B. C. Sales, and O. Delaire. Phonon self-energy and origin of anomalous neutron scattering spectra in snte and pbte thermoelectrics. *Phys. Rev. Lett.*, 112:175501, Apr 2014. doi: 10.1103/PhysRevLett.112.175501. URL `https://link.aps.org/doi/10.1103/PhysRevLett.112.175501`. 14

[59] X. Li, J. Liu, K. Ding, X. Zhao, S. Li, W. Zhou, and B. Liang. Temperature dependence of raman-active in-plane e2g phonons in layered graphene and h-bn flakes. *Nanoscale Research Letters*, 13(1), Jan. 2018. ISSN 1556-276X. doi: 10.1186/s11671-018-2444-2. URL `http://dx.doi.org/10.1186/s11671-018-2444-2`. 121

[60] C. Lin, S. Poncé, and N. Marzari. General invariance and equilibrium conditions for lattice dynamics in 1d, 2d, and 3d materials. *npj Computational Materials*, 8(1), Nov. 2022. ISSN 2057-3960. doi: 10.1038/s41524-022-00920-6. URL `http://dx.doi.org/10.1038/s41524-022-00920-6`. 33

[61] L. Lindsay and D. A. Broido. Enhanced thermal conductivity and isotope effect in single-layer hexagonal boron nitride. *Physical Review B*, 84(15), Oct. 2011. ISSN 1550-235X. doi: 10.1103/physrevb.84.155421. URL `http://dx.doi.org/10.1103/PhysRevB.84.155421`. 34

[62] L. Lindsay, D. A. Broido, and N. Mingo. Flexural phonons and thermal transport in graphene. *Physical Review B*, 82(11), Sept. 2010. ISSN 1550-235X. doi: 10.1103/physrevb.82.115427. URL `http://dx.doi.org/10.1103/PhysRevB.82.115427`. 34

[63] L. Lindsay, D. A. Broido, and N. Mingo. Flexural phonons and thermal transport in multilayer graphene and graphite. *Physical Review B*, 83(23),

June 2011. ISSN 1550-235X. doi: 10.1103/physrevb.83.235428. URL `http://dx.doi.org/10.1103/PhysRevB.83.235428`. 34

[64] A. Marcolongo, P. Umari, and S. Baroni. Microscopic theory and quantum simulation of atomic heat transport. *Nature Physics*, 12(1):80–84, Oct. 2015. ISSN 1745-2481. doi: 10.1038/nphys3509. URL `http://dx.doi.org/10.1038/nphys3509`. 28

[65] A. Marcolongo, L. Ercole, and S. Baroni. Gauge fixing for heat-transport simulations. *Journal of Chemical Theory and Computation*, 16 (5):3352–3362, Apr. 2020. ISSN 1549-9626. doi: 10.1021/acs.jctc.9b01174. URL `http://dx.doi.org/10.1021/acs.jctc.9b01174`. 28

[66] M. A. Marques, N. T. Maitra, F. M. Nogueira, E. Gross, and A. Rubio. *Fundamentals of Time-Dependent Density Functional Theory*. Springer Berlin Heidelberg, 2012. ISBN 9783642235184. doi: 10.1007/978-3-642-23518-4. URL `http://dx.doi.org/10.1007/978-3-642-23518-4`. 9

[67] L. Monacelli, R. Bianco, M. Cherubini, M. Calandra, I. Errea, and F. Mauri. The stochastic self-consistent harmonic approximation: calculating vibrational properties of materials with full quantum and anharmonic effects. *Journal of Physics: Condensed Matter*, 33(36):363001, July 2021. ISSN 1361-648X. doi: 10.1088/1361-648x/ac066b. URL `http://dx.doi.org/10.1088/1361-648X/ac066b`. 15

[68] T. Morresi, L. Paulatto, R. Vuilleumier, and M. Casula. Probing anharmonic phonons by quantum correlators: A path integral approach. *The Journal of Chemical Physics*, 154(22):224108, June 2021. ISSN 1089-7690. doi: 10.1063/5.0050450. URL `http://dx.doi.org/10.1063/5.0050450`. 147

[69] B. Mortazavi and Y. Rémond. Investigation of tensile response and thermal conductivity of boron-nitride nanosheets using molecular dynamics simulations. *Physica E: Low-dimensional Systems and Nanostructures*, 44(9): 1846–1852, June 2012. ISSN 1386-9477. doi: 10.1016/j.physe.2012.05.007. URL `http://dx.doi.org/10.1016/j.physe.2012.05.007`. 34

[70] B. Mortazavi, L. F. C. Pereira, J.-W. Jiang, and T. Rabczuk. Modelling heat conduction in polycrystalline hexagonal boron-nitride films. *Scientific Reports*, 5(1), Aug. 2015. ISSN 2045-2322. doi: 10.1038/srep13228. URL `http://dx.doi.org/10.1038/srep13228`. 34

[71] D. L. Nika and A. A. Balandin. Two-dimensional phonon transport in graphene. *Journal of Physics: Condensed Matter*, 24(23):233203, May 2012. ISSN 1361-648X. doi: 10.1088/0953-8984/24/23/233203. URL `http://dx.doi.org/10.1088/0953-8984/24/23/233203`. 34

[72] D. L. Nika, E. P. Pokatilov, A. S. Askerov, and A. A. Balandin. Phonon thermal conduction in graphene: Role of umklapp and edge roughness scattering. *Physical Review B*, 79(15), Apr. 2009. ISSN 1550-235X. doi: 10.1103/physrevb.79.155413. URL `http://dx.doi.org/10.1103/PhysRevB.79.155413`. 34

[73] I. S. Novikov, K. Gubaev, E. V. Podryabinkin, and A. V. Shapeev. The mlip package: moment tensor potentials with mpi and active learning. *Machine Learning: Science and Technology*, 2(2):025002, Jan. 2021. ISSN 2632-2153. doi: 10.1088/2632-2153/abc9fe. URL `http://dx.doi.org/10.1088/2632-2153/abc9fe`. 116

[74] M. Omini and A. Sparavigna. An iterative approach to the phonon boltzmann equation in the theory of thermal conductivity. *Physica B: Condensed Matter*, 212(2):101–112, July 1995. ISSN 0921-4526. doi: 10.1016/0921-4526(95)00016-3. URL `http://dx.doi.org/10.1016/0921-4526(95)00016-3`. 26

[75] W. Paszkowicz, J. Pelka, M. Knapp, T. Szyszko, and S. Podsiadlo. Lattice parameters and anisotropic thermal expansion of hexagonal boron nitride in the 10-297.5 k temperature range. *Applied Physics A: Materials Science & Processing*, 75(3):431–435, Sept. 2002. ISSN 1432-0630. doi: 10.1007/s003390100999. URL `http://dx.doi.org/10.1007/s003390100999`. 117

[76] R. Peierls. Zur kinetischen theorie der wärmeleitung in kristallen. *Annalen der Physik*, 395(8):1055–1101, Jan. 1929. ISSN 1521-3889. doi: 10.1002/ andp.19293950803. URL http://dx.doi.org/10.1002/andp.19293950803. 28

[77] J. P. Perdew, K. Burke, and M. Ernzerhof. Generalized gradient approximation made simple. *Phys. Rev. Lett.*, 77:3865–3868, Oct 1996. doi: 10.1103/PhysRevLett.77.3865. URL https://link.aps.org/doi/10.1103/ PhysRevLett.77.3865. 116

[78] H. Rezgui. Phonon hydrodynamic transport: Observation of thermal wave-like flow and second sound propagation in graphene at 100 k. *ACS Omega*, 8(26):23964–23974, June 2023. ISSN 2470-1343. doi: 10.1021/ acsomega.3c02558. URL http://dx.doi.org/10.1021/acsomega.3c02558. 36

[79] A. H. Romero, D. C. Allan, B. Amadon, G. Antonius, T. Applencourt, L. Baguet, J. Bieder, F. Bottin, J. Bouchet, E. Bousquet, F. Bruneval, G. Brunin, D. Caliste, M. Côté, J. Denier, C. Dreyer, P. Ghosez, M. Giantomassi, Y. Gillet, O. Gingras, D. R. Hamann, G. Hautier, F. Jollet, G. Jomard, A. Martin, H. P. C. Miranda, F. Naccarato, G. Petretto, N. A. Pike, V. Planes, S. Prokhorenko, T. Rangel, F. Ricci, G.-M. Rignanese, M. Royo, M. Stengel, M. Torrent, M. J. van Setten, B. Van Troeye, M. J. Verstraete, J. Wiktor, J. W. Zwanziger, and X. Gonze. ABINIT: Overview and focus on selected capabilities. *The Journal of Chemical Physics*, 152 (12):124102, 03 2020. ISSN 0021-9606. doi: 10.1063/1.5144261. URL https://doi.org/10.1063/1.5144261. 116

[80] P. K. Schelling, A. M. Margolles, and L. P. Echazabal. Thermal response functions and second sound in single-layer hexagonal boron nitride. *Physical Review B*, 112(2), July 2025. ISSN 2469-9969. doi: 10.1103/2jqd-9fsd. URL http://dx.doi.org/10.1103/2jqd-9fsd. 36

[81] J. H. Seol, I. Jo, A. L. Moore, L. Lindsay, Z. H. Aitken, M. T. Pettes, X. Li, Z. Yao, R. Huang, D. Broido, N. Mingo, R. S. Ruoff, and L. Shi. Two-dimensional phonon transport in supported graphene. *Science*, 328

(5975):213–216, Apr. 2010. ISSN 1095-9203. doi: 10.1126/science.1184014. URL http://dx.doi.org/10.1126/science.1184014. 34

[82] C. Sevik, A. Kinaci, J. B. Haskins, and T. undefinedağın. Characterization of thermal transport in low-dimensional boron nitride nanostructures. *Physical Review B*, 84(8), Aug. 2011. ISSN 1550-235X. doi: 10.1103/ physrevb.84.085409. URL http://dx.doi.org/10.1103/PhysRevB.84.085409. 34

[83] A. V. Shapeev. Moment tensor potentials: A class of systematically improvable interatomic potentials. *Multiscale Modeling & Simulation*, 14(3): 1153–1173, Jan. 2016. ISSN 1540-3467. doi: 10.1137/15M1054183. URL https://doi.org/10.1137/15M1054183. 116

[84] N. Shulumba, O. Hellman, and A. J. Minnich. Intrinsic localized mode and low thermal conductivity of pbse. *Physical Review B*, 95(1), Jan. 2017. ISSN 2469-9969. doi: 10.1103/physrevb.95.014302. URL http://dx.doi.org/ 10.1103/PhysRevB.95.014302. 22

[85] E. K. Sichel, R. E. Miller, M. S. Abrahams, and C. J. Buiocchi. Heat capacity and thermal conductivity of hexagonal pyrolytic boron nitride. *Physical Review B*, 13(10):4607–4611, May 1976. ISSN 0556-2805. doi: 10.1103/ physrevb.13.4607. URL http://dx.doi.org/10.1103/PhysRevB.13.4607. 126

[86] M. Simoncelli, N. Marzari, and F. Mauri. Unified theory of thermal transport in crystals and glasses. *Nature Physics*, 15(8):809–813, May 2019. ISSN 1745-2481. doi: 10.1038/s41567-019-0520-x. URL http: //dx.doi.org/10.1038/s41567-019-0520-x. 30

[87] J. M. Skelton, L. A. Burton, S. C. Parker, A. Walsh, C.-E. Kim, A. Soon, J. Buckeridge, A. A. Sokol, C. R. A. Catlow, A. Togo, and I. Tanaka. Anharmonicity in the high-temperature *Cmcm* phase of snse: Soft modes and three-phonon interactions. *Physical Review Letters*, 117(7), Aug. 2016. ISSN 1079-7114. doi: 10.1103/physrevlett.117.075502. URL http: //dx.doi.org/10.1103/PhysRevLett.117.075502. 14

[88] G. P. Srivastava. *The physics of phonons*. Institute of Physics Publishing, London, England, Jan. 1990. 24

[89] I. Stenger, L. Schué, M. Boukhicha, B. Berini, B. Plaçais, A. Loiseau, and J. Barjon. Low frequency raman spectroscopy of few-atomic-layer thick hbn crystals. *2D Materials*, 4(3):031003, June 2017. ISSN 2053-1583. doi: 10.1088/2053-1583/aa77d4. URL `http://dx.doi.org/10.1088/2053-1583/aa77d4`. 121

[90] G. Sun, J. Ma, C. Liu, Z. Xiang, D. Xu, T.-H. Liu, and X. Luo. Four-phonon and normal scattering in 2d hexagonal structures. *International Journal of Heat and Mass Transfer*, 215:124475, Nov. 2023. ISSN 0017-9310. doi: 10.1016/j.ijheatmasstransfer.2023.124475. URL `http://dx.doi.org/10.1016/j.ijheatmasstransfer.2023.124475`. 34

[91] W. C. Swope, H. C. Andersen, P. H. Berens, and K. R. Wilson. A computer simulation method for the calculation of equilibrium constants for the formation of physical clusters of molecules: Application to small water clusters. *The Journal of Chemical Physics*, 76(1):637–649, Jan. 1982. ISSN 1089-7690. doi: 10.1063/1.442716. URL `http://dx.doi.org/10.1063/1.442716`. 146

[92] T. Tadano and W. A. Saidi. First-principles phonon quasiparticle theory applied to a strongly anharmonic halide perovskite. *Physical Review Letters*, 129(18), Oct. 2022. ISSN 1079-7114. doi: 10.1103/physrevlett.129.185901. URL `http://dx.doi.org/10.1103/PhysRevLett.129.185901`. 14

[93] T. Tadano and S. Tsuneyuki. Self-consistent phonon calculations of lattice dynamical properties in cubic srtio$_3$ with first-principles anharmonic force constants. *Phys. Rev. B*, 92:054301, Aug 2015. doi: 10.1103/PhysRevB.92.054301. URL `https://link.aps.org/doi/10.1103/PhysRevB.92.054301`. 14, 116

[94] S.-i. Tamura. Isotope scattering of dispersive phonons in ge. *Physical Review B*, 27(2):858–866, Jan. 1983. ISSN 0163-1829. doi: 10.1103/physrevb.27.858. URL `http://dx.doi.org/10.1103/PhysRevB.27.858`. 31

[95] J. Tersoff. Empirical interatomic potential for silicon with improved elastic properties. *Physical Review B*, 38(14):9902–9905, Nov. 1988. ISSN 0163-1829. doi: 10.1103/physrevb.38.9902. URL http://dx.doi.org/10.1103/PhysRevB.38.9902. 139

[96] A. Togo, L. Chaput, I. Tanaka, and G. Hug. First-principles phonon calculations of thermal expansion in ti_3sic_2, ti_3alc_2, and ti_3gec_2. *Phys. Rev. B*, 81:174301, May 2010. doi: 10.1103/PhysRevB.81.174301. URL https://link.aps.org/doi/10.1103/PhysRevB.81.174301. 116

[97] L. Verlet. Computer "experiments" on classical fluids. i. thermodynamical properties of lennard-jones molecules. *Physical Review*, 159(1):98–103, July 1967. ISSN 0031-899X. doi: 10.1103/physrev.159.98. URL http://dx.doi.org/10.1103/PhysRev.159.98. 146

[98] Q. Wang, Z. Zeng, and Y. Chen. Revisiting phonon transport in perovskite $SrTiO_3$: Anharmonic phonon renormalization and four-phonon scattering. *Physical Review B*, 104(23), Dec. 2021. ISSN 2469-9969. doi: 10.1103/physrevb.104.235205. URL http://dx.doi.org/10.1103/PhysRevB.104.235205. 14

[99] A. Ward, D. A. Broido, D. A. Stewart, and G. Deinzer. Ab initiotheory of the lattice thermal conductivity in diamond. *Physical Review B*, 80 (12), Sept. 2009. ISSN 1550-235X. doi: 10.1103/physrevb.80.125203. URL http://dx.doi.org/10.1103/PhysRevB.80.125203. 27

[100] X. Wu, V. Varshney, J. Lee, Y. Pang, A. K. Roy, and T. Luo. How to characterize thermal transport capability of 2d materials fairly? – sheet thermal conductance and the choice of thickness. *Chemical Physics Letters*, 669:233–237, Feb. 2017. ISSN 0009-2614. doi: 10.1016/j.cplett.2016.12.054. URL http://dx.doi.org/10.1016/j.cplett.2016.12.054. 36

[101] X. Wu, W. Zhou, H. Dong, P. Ying, Y. Wang, B. Song, Z. Fan, and S. Xiong. Correcting force error-induced underestimation of lattice thermal conductivity in machine learning molecular dynamics. *The Journal of Chemical*

Physics, 161(1), July 2024. ISSN 1089-7690. doi: 10.1063/5.0213811. URL `http://dx.doi.org/10.1063/5.0213811`. 32

[102] C. Yuan, J. Li, L. Lindsay, D. Cherns, J. W. Pomeroy, S. Liu, J. H. Edgar, and M. Kuball. Modulating the thermal conductivity in hexagonal boron nitride via controlled boron isotope concentration. *Communications Physics*, 2(1), May 2019. ISSN 2399-3650. doi: 10.1038/s42005-019-0145-5. URL `http://dx.doi.org/10.1038/s42005-019-0145-5`. 126

[103] W. Zhou, N. Liang, X. Wu, S. Xiong, Z. Fan, and B. Song. Insight into the effect of force error on the thermal conductivity from machine-learned potentials. *Materials Today Physics*, 50:101638, Jan. 2025. ISSN 2542-5293. doi: 10.1016/j.mtphys.2024.101638. URL `http://dx.doi.org/10.1016/j.mtphys.2024.101638`. 32

[104] T. Zhu and E. Ertekin. Resolving anomalous strain effects on two-dimensional phonon flows: The cases of graphene, boron nitride, and planar superlattices. *Physical Review B*, 91(20), May 2015. ISSN 1550-235X. doi: 10.1103/physrevb.91.205429. URL `http://dx.doi.org/10.1103/PhysRevB.91.205429`. 34

[105] X. Zhu and D. A. Egger. Effect of overdamped phonons on the fundamental band gap of perovskites. *Physical Review Letters*, 134(1), Jan. 2025. ISSN 1079-7114. doi: 10.1103/physrevlett.134.016403. URL `http://dx.doi.org/10.1103/PhysRevLett.134.016403`. 27

[106] J. Ziman. *Electrons and Phonons*. Oxford University Press, Feb. 2001. ISBN 9780198507796. doi: 10.1093/acprof:oso/9780198507796.001.0001. URL `http://dx.doi.org/10.1093/acprof:oso/9780198507796.001.0001`. 10